VNIVERSITAT DE VALÈNCIA

Departament de Física Aplicada i Electromagnetisme

Analysis of the multipactor effect in microwave waveguides and transmission lines

Tesis presentada para optar al grado de

DOCTOR EN FÍSICA

presentada por

Daniel González Iglesias

Dirigida por:

Dr. Benito Gimeno Martínez

Dr. Vicente Enrique Boria Esbert

Mayo 2017

Analysis of the multipactor effect in microwave waveguides and transmission lines

Tesis Doctoral de Daniel González Iglesias

Dirigida por:
Dr. Benito Gimeno Martínez
Dpto. Física Aplicada y Electromagnetismo-ICMUV (UVEG)

Dr. Vicente Enrique Boria Esbert
Dpto. Comunicaciones-iTEAM (UPV)

Mayo 2017

D. Benito Gimeno Martínez, Catedrático del Departamento de Física Aplicada y Electromagnetismo de la Universitat de València, y D. Vicente Enrique Boria Esbert, Catedrático del Departamento de Comunicaciones de la Universitat Politécnica de València,

CERTIFICAN que la presente memoria: "Analysis of the multipactor effect in microwave waveguides and transmission lines", resume el trabajo de investigación realizado, bajo su dirección, por D. Daniel González Iglesias, y constituye su Tesis Doctoral para optar al título de Doctor en Física.

Y para que conste y en cumplimiento de la legislación vigente, firman el presente certificado en Valencia, a veintinueve de mayo de dos mil diecisiete.

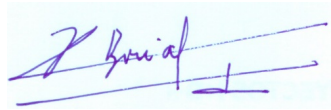

Fdo: Prof. Benito Gimeno Martínez

Fdo: Prof. Vicente Enrique Boria Esbert

Agradecimientos

Deseo expresar mi agradecimiento a los directores de este trabajo, Benito Gimeno Martínez y Vicente Enrique Boria Esbert. Sin su apoyo, esfuerzo y dedicación el desarrollo de esta tesis doctoral no hubiera sido posible. El camino se recorre más facilmente cuando te señalan en la dirección correcta.

También me gustaría dar las gracias a David Raboso García-Baquero, Director del Laboratorio conjunto de la Agencia Espacial Europea y el Consorcio Espacial Valenciano, y a David Argilés Ortiz, Gerente del Consorcio Espacial Valenciano, por buscarnos ambos siempre un hueco en la apretada agenda del laboratorio para poder llevar a cabo nuestras medidas. De igual manera, agradecer a toda la gente del laboratorio (Laura, Rocío, Davide, Marta, Máriam, María José) por su colaboración e inestimable ayuda tanto para preparar los intrincados montajes experimentales como con las mediciones propiamente dichas, mención especial para Óscar Monerris, quien se ha encargado de poner a punto todos los experimentos relacionados con el bloque de multipactor con señales moduladas digitalmente.

Merece la pena mencionar que este trabajo ha sido posible gracias a la colaboración con un grupo personas de gran valía, tanto a nivel de investigación como de calidad humana. Especialmente valiosa ha sido la ayuda prestada por la gente de Aurorasat (Sergio Anza, Carlos Vicente, Jordi Gil), tanto a nivel de discusiones técnicas como por permitirme usar el software FEST3D que tan necesario ha sido para elaborar algunos apartados de la tesis. Un recuerdo para la gente de la Universidad de Cantabria (Álvaro Gómez y Ángel Vegas), que han conseguido lidiar con éxito el problema de los campos electromagnéticos en las estructuras con ferritas. Gracias también a Pablo Soto de la Universidad Politécnica de Valencia, por su inestimable ayuda con el mundo de las guías *ridge*. Así mismo, quisiera mencionar también a Petronilo Martín Iglesias de la Agencia Espacial Europea, por su contribución en la generación de las señales moduladas digitalmente que se han analizado en la presente tesis doctoral. Gracias también a Fernando Casas, de la Universidad Jaime I de Castellón, por su ayuda para optimizar el método de *Velocity-Verlet* empleado para resolver las ecuaciones diferenciales del movimiento del electrón, dotando de una mayor robustez a nuestro simulador de multipactor. Recuerdo también con gratitud la ayuda de Antonio María Pérez Pastor, con quien pasé amenos ratos analizando el movimiento de los electrones inmersos en un campo magnético.

Agradecer también a los proyectos de la Agencia Espacial Europea "Development of a Software Tool for the Study of RF Breakdown for Realistic Scenarios: Multicarrier and Modulated Signals" (número de contrato 4000111147/14/NL/GLC), y "Novel Investigation in Multipactor Effect in Ferrite and other Dielectrics used in high power RF Space Hardware" (número de contrato AO 1-7551/13/NL/GLC), por contribuir parcialmente a la financiación de la presente tesis doctoral.

Un agradecimiento también para Rafa Mata, compañero de trabajo y quién ha medido muchas de las curvas del SEY que se han usado para las simulaciones que se presentan a lo largo de este trabajo.

Finalmente, quiero también hacer una mención especial de agradecimiento a mis padres. Habéis sido una fuente inagotable de apoyo en todo momento, por ello gracias de todo corazón.

Resumen

El trabajo desarrollado en la presente tesis doctoral tiene por objeto el estudio del efecto multipactor en guías de microondas. La descarga de multipactor es un fenómeno que aparece en componentes que operan en condiciones de alto vacío, y en presencia de campos electromagnéticos de gran intensidad en el rango de la radiofrecuencia (RF) y las microondas. El efecto multipactor aparece en un amplio rango de dispositivos como son los componentes pasivos de los satélites de telecomunicaciones espaciales, los aceleradores de partículas, y los amplificadores tipo klystron. Este fenómeno se produce debido a la presencia de electrones libres en el interior del dispositivo que son acelerados por el campo eléctrico de RF, de manera que al impactar con las paredes del componente pueden liberar electrones secundarios de la superficie. Si se dan las condiciones de sincronía necesarias con el campo eléctrico, se inicia una reacción en cadena que provoca un crecimiento exponecial de la población de electrones dentro del dispositivo, conduciendo finalmente a la aparición de una corriente eléctrica que constituye la descarga de multipactor. Existen una serie de efectos derivados de la descarga como son el aumento del nivel de ruido y de la potencia reflejada, calentamiento térmico local, desintonización de cavidades resonantes, y daños físicos en las superficies. Todos estos fenómenos provocan una degradación del funcionamiento del dispositivo, por lo que la descarga de multipactor debe de evitarse a toda costa. Esto implica una restricción en la potencia máxima a la que puede funcionar el componente.

En la presente tesis doctoral nos centraremos en el estudio del efecto multipactor en el ámbito de los componentes pasivos de los satélites de telecomunicaciones. En este escenario es crucial asegurarse de que la descarga no se pueda producir en ningún componente a lo largo de toda su vida útil, ya que de lo contrario esto supondría una grave amenanza para el correcto funcionamiento de todo el conjunto del satélite o de una parte del mismo. Evidentemente, si algún dispositivo fallara debido a una descarga, sería imposible efectuar ningún tipo de reparación del mismo. Es por ello que el estudio del efecto multipactor es un tema de gran interés, tanto para las industrias de fabricación de componentes de satélites como para las agencias espaciales. La correcta comprensión del efecto multipactor a través de herramientas de simulación permite estimar la potencia umbral a la que se inicia la descarga, información que es empleada para el diseño de componentes libres de este perjudicial fenómeno.

El objetivo de este trabajo es profundizar en el conocimiento del efecto multipactor en diferentes casos que, a pesar de ser de interés práctico, aún no habían sido abordados en la bibliografía existente hasta el momento. Como resultado de este estudio, se dispondrá de márgenes más rigurosos para la predicción de la descarga de multipactor que podrán ser aprovechados por las industrias destinadas a la fabricación de componentes espaciales, permitiendo de esta manaera incrementar la capacidad de manejo de potencia en dichos dispositivos.

En cuanto a la metodología para el estudio del efecto multipactor en guías de microondas en diferentes escenarios específicos, se ha desarrollado una herramienta eficiente para la simulación numérica de este fenómeno. La idea básica en la cual se basa el algoritmo de simulación es el estudio de las trayectorias de un conjunto de electrones en el interior del dispositivo, que son acelerados por el campo electromagnético total que hay dentro del mismo. Dependiendo del caso concreto que estemos tratando existen dos posibilidades diferentes para simular el comportamiento de los electrones: el modelo de electrón efectivo y el modelo de electrón individual. El modelo de electrón efectivo considera el seguimiento de un número fijo de partículas que se define en el instante inicial. El incremento de la población electrónica, debido a la emisión secundaria de electrones por parte de la superficie, se tiene en cuenta mediante la acumulación de carga y masa por parte de cada electrón efectivo. A pesar de que esta consideración supone una simplificación de la esencia física del problema, puesto que en la situación real se absorben o se crean nuevos electrones en las colisiones, los resultados proporcionados por este modelo son buenos cuando se comparan con los datos experimentales en un amplio abanico de escenarios, siempre que la señal de RF sea armónica en el tiempo. Sin embargo, cuando la envolvente de la señal de RF varía con el tiempo (como ocurre en el caso de las señales moduladas digitalmente) se obtienen resultados más precisos si se implementa un modelo de electrón individual. El modelo de electrón individual permite la creación de nuevas partículas en el transcurso de la simulación en el caso de que se generen electrones secundarios en las colisiones. De forma similar, si el electrón resulta absorbido por la superficie es eliminado de la simulación. El único inconveniente que presenta el modelo de electrón individual respecto al de electrón efectivo es que en este último caso es posible obtener fácilmente las trayectorias de los electrones en el interior del dispositivo; mientras que para el caso de electrón individual es mucho más complicado, ya que los electrones se crean y se destruyen continuamente en las numerosas colisiones con las paredes del componente. En cualquier caso, independientemente de la elección de un modelo u otro,

el funcionamiento del algorimo de simulación es muy similar en ambas situaciones. Inicialmente el código toma en consideración un cierto número de electrones individuales o efectivos que son emitidos con velocidades aleatorias, desde uno o varios puntos espaciales del interior del componente. Entonces, la trayectoria y la velocidad de cada electrón se obtiene resolviendo numéricamente su ecuación diferencial de movimiento, que es el resultado de la acción del campo electromagnético total al que se ve sometido. Como método de resolución numérica de la ecuación diferencial del movimiento usaremos un algoritmo *Velocity-Verlet*. Cada vez que se actualiza la posición y velocidad de un electrón se comprueba si se ha producido un impacto con las paredes del dispositivo. En caso de que esto ocurra, se calcula la función de emisión de electrones secundarios (conocida como SEY, del inglés *Secondary Electron Yield coefficient*), que da cuenta de la interacción del electrón con la superficie, y permite determinar tanto si se emiten electrones secundarios como si el electron primario incidente es absorbido por la misma. Hecho esto se actualiza la población de electrones y el electrón impactante (en caso de que no sea absorbido o si está implementado el modelo de electrón efectivo) es lanzado de nuevo hacia el interior del componente desde la posición de impacto. El código se detiene cuando se ha simulado un tiempo (expresado en número de periodos de RF) predefinido, o si se alcanza un cierto nivel crítico de número de electrones (asociado al criterio de descarga de multipactor). El dato de salida del simulador es la evolución de la población de electrones en el dispositivo en función del tiempo, siendo ésta la información necesaria para poder decidir si se ha producido la descarga para un nivel determinado del voltaje de RF de la señal.

El contenido de esta tesis doctoral se puede dividir en cuatro areas temáticas diferentes que pretenden abordar aspectos particulares del fenómeno de multipactor: mitigación del efecto multipactor por medio de campos magnéticos estáticos, multipactor en guías *ridge* y *multiridge*, multipactor con señales moduladas digitalmente, y multipactor en guías rellenadas parcialmente con ferrita. A continuación se hará un breve resumen de la motivación y los resultados obtenidos en cada caso.

El primer bloque trata sobre las técnicas de mitigación del efecto multipactor cuyo objetivo es prevenir la aparición de la descarga en el dispositivo ya que, como se ha comentado anteriormente, ésta comporta una serie de efectos negativos que degradan el funcionamiento del mismo. Existen diferentes técnicas con el propósito de inhibir la descarga. Por una parte, tenemos aquellos métodos que pretenden disminuir el número de electrones emitidos por la superficie aplicando diversos tratamientos físico-químicos sobre la misma: pulido químico, trazado de surcos, recubrimientos,

etc. Sin embargo, los tratamientos superficiales se degradan con el tiempo, y el surcado de la superficie puede empeorar el funcionamiento del dispositivo. Por otra parte, algunos autores proponen el uso de campos magnéticos estáticos para lograr una mitigación parcial o total del mismo. En nuestro caso, exploramos la posibilidad de suprimir la descarga de multipactor en una línea de transmisión coaxial sometida a un campo magnético estático orientado en la dirección axial de la guía. En una primera etapa, se analizó el caso de un campo magnetico espacialmente uniforme sobre la guía coaxial. La presencia de un campo magnetostático de tales características tiende a curvar las trayectorias de los electrones haciéndolas girar alrededor de las líneas de campo magnético, empujando al electrón de vuelta hacia el conductor de partida y perturbando las típicas trayectorias resonantes de doble superficie entre los conductores. Este hecho quedó constatado al examinar las trayectorias resultantes de las simulaciones numéricas, donde se observó la aparición de trayectorias resonantes de una sola superficie para algunos valores de intensidad del campo magnético aplicado. El principal parámetro que afecta al tiempo de vuelo de los electrones entre dos impactos sucesivos con los conductores del coaxial es el cociente entre la frecuencia de ciclotrón (que es proporcional a la amplitud del campo magnético) y la frecuencia de RF. Concretamente, cuanto mayor es dicho cociente menor es el tiempo entre colisiones. Cuando se excede un valor crítico del cociente frecuencia de ciclotrón frente a frecuencia de RF, el tiempo de vuelo se hace tan corto que el electrón no puede sincronizarse con el campo eléctrico de RF, dando como resultado impactos muy poco energéticos que inhiben por completo la descarga. Como consecuencia se demuestra que la descarga de multipactor puede suprimirse completamente en una línea de transmisión coaxial, siempre que se disponga de un campo magnético suficientemente intenso. El valor concreto del ratio frecuencia de ciclotron frente a frecuencia de RF necesario para inhibir la descarga depende a su vez del valor de la frecuencia de RF. Sin embargo, se puede tomar como regla aproximada que la descarga de multipactor no puede ocurrir cuando la frecuencia de ciclotrón excede a la de RF. Esta aproximación constituye un buen punto de inicio en la mayoría de los casos, antes de realizar las simulaciones numéricas propiamente dichas. Para validar los resultados teóricos obtenidos en las simulaciones numéricas se llevó a cabo una campaña de medidas experimentales, obteniéndose unos resultados satisfactorios en la comparacion entre teoría y experimento.

Una vez comprendido satisfactoriamente el caso de mitigación de la descarga de multipactor en guía coaxial con un campo magnetostático uniforme, se analizó en una

segunda etapa de este estudio la presencia de un campo magnetostático no uniforme sobre la guía. Este segundo caso supone una situación más realista desde el punto de vista de una implementación práctica, ya que un campo magnético de estas características puede lograrse con un imán permanente de neodimio en forma de cilindro hueco insertando la guía coaxial en su interior. En esta configuración, además del campo magnético axial, existe una componente en la dirección radial, siendo ambas espacialmente no uniformes. En concreto, la componente axial del campo magnético presenta una cierta uniformidad en la región central del cilindro imantado, pero su intensidad desciende rápidamente en la vecindad de las tapas del cilindro. Este hecho es importante desde el punto de vista de la mitigación de la descarga puesto que, tal y como se comprobó en el caso de campo magnetostático axial uniforme, se requiere una intensidad alta de campo magnético para suprimir la descarga. Sin embargo, tras examinar las trayectorias de los electrones en la guía coaxial sometida al campo no uniforme del imán, se constató que la componente radial del campo magnético tendía a expulsar al electrón de las regiones de bajo campo magnético axial, que es donde podría iniciarse la descarga en primera instancia. Gracias a este fenómeno, el efecto de mitigación de multipactor de un imán cilíndrico hueco resultó muy similar al del campo magnetostático axial y uniforme considerado en la primera etapa del estudio. Este hecho se verificó con una campaña experimental de medidas. Como consecuencia, se puede asumir que la aproximación de que el multipactor se ve mitigado para frecuencias de RF por debajo del valor de la frecuencia de ciclotrón también es válido en el caso del imán cilíndrico hueco.

El segundo bloque temático de esta tesis doctoral tiene como objetivo el estudio del efecto multipactor en guías *ridge* y *multiridge*. Este tipo de guías tiene muchas aplicaciones en dispositivos de microondas y RF. Por ejemplo, se usan tanto en aplicaciones de baja como de alta potencia, conformando las secciones de filtros pasobanda o pasobajo. A su vez, esta clase de filtros son buenos candidatos para aplicaciones destinadas a las telecomunicaciones espaciales, debido a su tamaño compacto y a una buena respuesta en la banda eliminada. Algunas de sus ventajas son amplio rango espectral de funcionamiento en régimen monomodo, baja impedancia característica y una alta longitud de onda de corte para el modo fundamental. Algunas aplicaciones concretas de estos filtros son, por ejemplo, como filtros preselectores antes de la entrada a multiplexores, o como filtros supresores de armónicos después de transmisores y amplificadores, especialmente en componentes a bordo de satélites.

Para llevar a cabo el estudio del efecto multipactor en este tipo de estructuras, se

han elaborado las cartas de susceptibilidad de multipactor para diferentes configuraciones de guías *ridge* y *multiridge*. En estas cartas de susceptibilidad se representa el voltaje umbral de multipactor en función del producto de frecuencia de RF por gap (típicamente el gap se mantiene fijo y es la frecuencia la que varía). Las simulaciones numéricas requeridas para elaborar las cartas de susceptibilidad se han realizado con un software de uso comercial denominado FEST3D. Respecto a las estructuras consideradas para las guías *ridge* y *multiridge*, las alturas del gap elegidas suelen ser mucho menores que las dimensiones transversales, lo que implica que las estructuras simuladas se aproximan bastante a una guía de placas plano-paralelas. A pesar de esto el análisis cubre un amplio rango de alturas del gap que son interesantes en aplicaciones prácticas. Con respecto al número de *ridges* (inserciones metálicas), se han considerado tres tipos de estructuras diferentes: *ridge* (un *ridge*), *ridge* doble (dos *ridges*), y *multiridge* (tres *ridges*). Además, existe otra clasificación posible en función de las dos configuraciones posibles: asimétrica (el *ridge* o *ridges* se sitúan solo en la superficie superior de la guía) y simétrica (el *ridge* o *ridges* se sitúan tanto en la cara superior como inferior de la guía). Las cartas de susceptibilidad exploran la variación del umbral de multipactor con los dos parámetros fundamentales que caracterizan la geometría de la guía *ridge*: la altura del gap y la anchura del *ridge*. Así mismo, se presenta un método sencillo para predecir el voltaje umbral de multipactor en estructuras complejas que contengan varias secciones de guías *ridge* o *multiridge*. Este procedimiento se constituye como una alternativa a la simulación precisa del efecto multipactor sobre todo el componente, que puede requerir bastante tiempo de cálculo. Mediante el uso de las cartas de susceptibilidad, y con el conocimiento de la distibución espacial del campo electromagnético en el dispositivo, se puede obtener el voltaje umbral de multipactor en el puerto de entrada del componente así como la localización en el interior del mismo donde se prevee la descarga. Este método aproximado se aplicó a un filtro de modos evanescente y a un filtro en banda S para alta potencia, encontrándose buena concordancia cuando los resultados obtenidos de esta forma fueron comparados con la simulación del dispositivo completo en FEST3D. En consecuencia, el uso de las cartas de susceptibilidad de las guías *ridge* y *multiridge* permite incrementar la capacidad de manejo de potencia del componente, en comparación con las predicciones dadas por aproximaciones más simplistas como la guía de placas plano-paralelas, que tiende a ser bastante conservativa para geometrías que difieren de dicha situación ideal. De hecho, de acuerdo con las cartas de susceptibilidad obtenidas, la potencia umbral de la descarga para los filtros de modo evanescente

y para el filtro en banda S están 4 dB y 3.3 dB por encima de los valores obtenidos mediante las aproximaciones de placas plano-paralelas, respectivamente.

El tercer tema a tratar es el análisis del efecto multipactor con señales moduladas digitalmente. Cabe mencionar que la mayor parte de las publicaciones relacionadas con el efecto multipactor centran su interés en el análisis de señales de RF armónicas en el tiempo con una sola señal portadora. Sin embargo, los sistemas reales de comunicaciones espaciales mediante satélites trabajan con señales multiportadora, donde a su vez cada una de las portadoras está modulada para usar eficientemente el espectro frecuencial disponible. Estas señales pueden llegar a ser muy diferentes de una señal no modulada (es decir, de una señal armónica pura) y, por lo tanto, las conclusiones provenientes de estudios de multipactor basados en señales armónicas de una sola portadora podrían no ser aplicables cuando se emplean señales moduladas. A pesar de este hecho, existe muy poca bibliografía que estudie multipactor con esta clase de señales. Por ello, en este apartado se pretende estudiar el fenómeno multipactor en una guía de transmisión coaxial excitada con una señal modulada digitalmente. Con este propósito se consideran algunos de los tipos de modulación digital más empleados como son la *Phase-Shift Keying* (PSK), la *Quadrature Amplitude Modulation* (QAM), y la *Amplitude and Phase-Shift Keying* (APSK).

Cabe destacar que el estudio del efecto multipactor con señales moduladas ha revelado un alto grado de complejidad en relación con el resto de temas tratados a lo largo de esta tesis doctoral. En las señales moduladas digitalmente, en contraste con el caso armónico, la envolvente de la señal varía en el transcurso de la transmisión. Por tanto, la amplitud de la envolvente puede subir y bajar por encima del voltaje umbral de multipactor del caso armónico en repetidas ocasiones. En aquellos intervalos de tiempo en que el voltaje excede el umbral del caso armónico, la población de electrones en el interior del coaxial aumentará. Sin embargo, en la situación opuesta, el número de electrones disminuirá, ya que serán principalmente absorbidos por las paredes del componente. Debido a esto, en las simulaciones de multipactor es necesario tener en cuenta y analizar cuidadosamente la forma de toda la señal transmitida, cuya duración suele ser muy larga si la comparamos con los tiempos en los que se realizan las simulaciones para un escenario típico de una señal armónica. Una consecuencia inmediata de este hecho es que se requieren tiempos de computación muy grandes si se pretende simular el efecto multipactor a lo largo de toda la señal. Además de esto, la elección del criterio teórico de multipactor para esclarecer si se ha producido la descarga llega a ser crítica cuando se trata con señales moduladas. Para el caso

de señales armónicas, la evolución en el tiempo del número de electrones adquiere un comportamiento bien definido (crecimiento o decrecimiento exponencial) después de un breve transitorio temporal. Por lo tanto, si se observa una tendencia creciente de estas características, la población siempre seguirá aumentando hasta que la descarga sea detectada por los instrumentos de medida. Teniendo en cuenta que la señal se extiende indefinidamente en el tiempo, no importa cómo de lento sea el ritmo de crecimiento, la población (o densidad) electrónica requerida para la detección de la descarga se alcanzará finalmente. Sin embargo, cuando está presente una señal modulada típicamente habrá intervalos alternos de crecimiento y decrecimiento del número de electrones, dependiendo de la forma de la envolvente de la señal. Así pués, la elección de la población (o densidad) electrónica que desencadena la descarga, es decir, el criterio de multipactor, será decisivo a la hora de obtener teóricamente el voltaje umbral. A pesar de la importancia que conlleva el conocimiento de la densidad electrónica crítica, que se traduce en la detección de la descarga en el laboratorio, este tema aún no ha sido abordado con suficiente profundidad. De hecho, tan sólo existen algunas publicaciones que tratan este asunto, pero desde un punto de vista meramente teórico y sin el soporte de resultados experimentales. Para intentar sortear este inconveniente, se ha propuesto un método indirecto para estimar la densidad electrónica existente durante la detección de la descarga en el laboratorio, basándose en resultados de medidas del voltaje umbral de multipactor con señales de RF pulsadas. Una vez conocido y establecido dicho valor como población límite de electrones para el criterio de multipactor, se realizaron simulaciones de multipactor para un amplio rango de señales moduladas con los tipos de modulación digital enumerados anteriormente. Los resultados teóricos obtenidos se contrastaron posteriormente con una serie de medidas experimentales, observándose un buen acuerdo entre ambos. De esta forma, se permitió validar tanto el algoritmo de simulación basado en el modelo de electrón individual, como el nivel de población elegido como criterio de descarga. Además de las simulaciones númericas que permiten obtener el voltaje umbral de multipactor con precisión, también se desarrolló un método aproximado, basado en la integración de la envolvente de la señal, que permite estimar el umbral de multipactor. Este procedimiento tan sólo requiere como datos de entrada los resultados de simulaciones de multipactor para el caso de una señal armónica a la frecuencia de la portadora de RF. La principal ventaja que presenta este otro método es que es mucho más rápido que las simulaciones de multipactor: las simulaciones numéricas requieren varias horas de tiempo computacional, mientras que el método aproximado es capaz de reducir esta

cantidad a unos pocos minutos. Además, puede ser aplicado a cualquier tipo de señal modulada, independientemente del tipo de modulación.

Finalmente, es importante mencionar que, hasta el momento actual, el estándar adoptado por la Agencia Espacial Europea para estimar el umbral de multipactor en un componente excitado con una señal no armónica pura se basa en la conocida como regla del "*20-gap-crossing*". Tras comparar las predicciones de esta regla con los resultados tanto teóricos como experimentales presentados en esta tesis doctoral, se comprueba la ineficacia de esta regla en el ámbito de las señales moduladas digitalmente.

El cuarto bloque temático de la presente tesis doctoral versa sobre el análisis del efecto multipactor en guías de placas plano-paralelas que contienen una lámina de ferrita magnetizada. Este estudio pretende ser un primer paso hacia la compresión del multipactor en estructuras más complejas que contienen ferritas magnetizadas, como es el caso de algunos tipos de circuladores, aislantes y variadores de fase. De hecho, hasta hoy en día no existe un conocimiento profundo de la fenomenología de multipactor en dispositivos que contengan ferritas. La industria europea suele usar grandes márgenes de potencia (para evitar la aparición del multipactor) cuando en el dispositivo hay presencia de dielectricos o ferritas. Así pues, los componentes que contienen ferritas sólo se pueden analizar en base a aproximaciones cuya validez no ha sido aún demostrada.

Las propiedades magnéticas anisótropas de las ferritas, junto con el campo magnético estático externo que se emplea para su magnetización, tienen efectos notorios en las trayectorias de los electrones y, por consiguiente, en el voltaje umbral de multipactor del dispositivo. En este trabajo se han considerado dos direcciones diferentes para el campo externo de magnetización: paralelo y normal a la lámina de ferrita. En ambos casos se han encontrado cambios sustanciales en el umbral de voltaje de multipactor con respecto al caso sin lámina de ferrita ni campo magnético externo. Además, la forma de las curvas de susceptibilidad depende de la orientación del campo de magnetización.

Por una parte, con la orientación del campo magnético paralela a la lámina de ferrita se observa una mitigación de la descarga para valores bajos del producto frecuencia por gap. Sin embargo, si aumenta el producto frecuencia por gap, el efecto multipactor hace su aparición incluso a valores del voltaje de RF inferiores al caso clásico de placas plano-paralelas. Además, se observa que cuanto mayor es la intensidad del campo de magnetización mayor es el rango en el que se suprime la descarga.

Por otro lado, cuando el campo magnético se orienta en la dirección normal a la lámina de ferrita no se aprecia ninguna región de mitigación de la descarga. De hecho, para valores bajos del producto frecuencia por gap la curva de umbrales de multipactor del caso con ferrita y sin ferrita se solapan. Sin embargo, a medida que aumenta el producto frecuencia por gap la curva del caso con ferrita tiende a situarse por debajo del caso sin ferrita. Así mismo, se registra una considerable disminución en el voltaje umbral de multipactor cuando la frecuencia de RF se aproxima al valor de la frecuencia de ciclotrón. Este efecto es debido al fenómeno de la resonancia de ciclotrón, que permite al electrón maximizar su energía cinética a expensas del campo eléctrico de RF cuando se satisfacen las condiciones de resonancia. La profundidad del mínimo en el umbral de multipactor es mayor conforme mayor sea el valor del producto frecuencia por gap al cual ocurre. Por ejemplo, se pueden encontrar diferencias de hasta 37 dB con respecto a la situación sin ferrita. Estos valores pueden llegar a exceder incluso los márgenes de seguridad más conservadores, provocando el riesgo de que aparezca una descarga en el dispositivo durante su funcionamiento si no se ha hecho un estudio adecuado.

Resum

El treball desenvolupat en la present tesi doctoral té com a objecte l'estudi de l'efecte multipactor en guies de microones. La descàrrega de multipactor és un fenomen que apareix en components que operen en condicions d'alt buit, i en presència de camps electromagnètics de gran intensitat en el rang de la radiofreqüència i les microones. L'efecte multipactor apareix en un ampli rang de dispositius com són els components passius dels satèl·lits de telecomunicacions espacials, els acceleradors de partícules, i els amplificadors tipus klystron. Aquest fenomen es produïx a causa de la presència d'electrons lliures en l'interior del dispositiu que són accelerats pel camp elèctric de RF, de manera que a l'impactar amb les parets del component poden alliberar electrons secundaris de la superfície. Si es donen les condicions de sincronia necessàries amb el camp elèctric, s'inicia una reacció en cadena que provoca un creixement exponecial de la població d'electrons dins del dispositiu, conduint finalment a l'aparició d'un corrent elèctric que constituïx la descàrrega de multipactor. Hi ha una sèrie d'efectes derivats de la descàrrega com són l'augment del nivell de soroll i de la potència reflectida, calfament tèrmic local, desintonització de cavitats ressonants, i danys físics en les superfícies. Tots aquests fenòmens provoquen una degradació del funcionament del dispositiu pel que la descàrrega de multipactor deu de ser evitada a tota costa. Això implica una restricció en la potència màxima a què pot funcionar el component.

Per al desenvolupament d'aquesta tesi doctoral ens centrarem en l'estudi del fenomen de multipactor en l'àmbit dels components passius dels satèl·lits de telecomunicacions. En aquest escenari és crucial assegurar-se de que la descàrrega no es puga produir en cap component al llarg de tota la seua vida útil, ja que en cas contrari això suposaria una greu amenaça per al funcionament correcte de tot el conjunt del satèl·lit o d'una part del mateix. Evidentment, si algun dispositiu fallara a causa d'una descàrrega, seria impossible efectuar cap tipus de reparació del mateix, comportant una important pèrdua econòmica a l'inutilitzar-se el conjunt del satèl·lit. És per això que l'estudi de l'efecte multipactor és un tema de gran interés tant per a les indústries de manufacturació de components de satèl·lits com per a les agències espacials. La correcta comprensió de l'efecte multipactor mitjançant ferramentes de simulació permet estimar la potència llindar a la que s'inicia la descàrrega, informació que és emprada per al disseny de components lliures d'aquest perjudicial fenomen.

L'objectiu d'aquest treball és aprofundir en el coneixement de l'efecte multipactor en diferents casos que, tot i ser d'interés pràctic, encara no havien sigut abordats en la bibliografia existent fins al moment. En concret, es consideren diferents geometries típiques en guies d'ones com són el cable coaxial, la guia de plaques pla-paral·leles, o les guies *ridge* i *multi-ridge*. Val la pena destacar que, encara que el contingut presentat és majoritàriament de tipus teòric, molts d'aquests resultats van ser posteriorment validats mitjançant mesures experimentals, demostrant així la validesa dels models teòrics proposats. Pel que fa a la temàtica tractada, aquesta tesi doctoral s'estructura en quatre grans blocs. En el primer bloc s'estudia la possibilitat de mitigar la descàrrega de multipactor en una guia coaxial per mitjà de l'aplicació d'un camp magnetostàtic extern orientat en la direcció axial de la guia. El segon bloc té com a objectiu presentar una sèrie de cartes de susceptibilitat de l'efecte multipactor per a guies de tipus *ridge* i *multi-ridge*, així com un procediment simple per al maneig d'estes cartes amb vista a la seva utilització per a estimar el voltatge llindar de multipactor en estructures més complexes compostes de diverses seccions de guies *ridge* o *multi-ridge*. En el tercer bloc s'estudia l'efecte multipactor en components amb ferrites. En concret s'analitza el cas d'una guia de plaques pla-paral·leles amb una làmina de ferrita magnetitzada per un camp magnetostàtic extern. Finalment, en el quart bloc, s'aborda un estudi de la fenomenologia de multipactor en guies de transmissió coaxial excitades per senyals modulades digitalment.

Abstract

The work performed throughout this PhD Thesis is aimed to study the multipactor effect in microwave waveguides. Multipactor breakdown is a phenomenon that takes place in devices operating in conditions of high vacuum, under the presence of high power electromagnetic fields within the Radiofrequency and microwave regions. The multipactor effect appears in a wide range of devices such as the satellite passive components devoted to spacial telecommunications, particle accelerators, and klystrons. This phenomenon is produced due to the presence of free electrons inside the component, which are accelerated by the RF electric field, impacting with the device walls and releasing new secondary electrons from the surface. If certain conditions are fulfilled to ensure the synchronism between the RF electric field and the electron, then a chain reaction is started, leading to an exponential growth of the electron population and, eventually, the discharge appears in the form of an electric current which is established between the walls of the device. The multipactor discharge has several negative effects that degrade the device performance, such as increasing signal noise and reflected power, local heating up of the walls, detuning of resonant cavities, and even physical damages in the surfaces. To avoid these undesirable effects, the maximum handling power of the device must be restricted, in order to ensure that the discharge does not appear during its operation.

This PhD Thesis is focused on the study of the multipactor effect in RF passive components employed for space telecommunications. In this scenario, it is crucial to avoid the appearance of the discharge, since replacement of damaged devices is not possible once the satellite has been launched. Due to this, the study of the multipactor effect is of great interest for both industries devoted to the manufacture of space components and space institutions. A proper knowledge of the multipactor effect by means of the numerical simulation tools allows to predict the multipactor RF power threshold which triggers the discharge, thus this information can be applied to the design of multipactor-free components.

The aim of this work is to reach a deeper understanding of the multipactor effect in certain specific scenarios which, despite of its remarkable interest, they had not been treated properly in the technical literature until the present moment. Specifically, several typical microwave component topologies will be considered such as the parallel-plate waveguide, the coaxial transmission line, as well as ridge and multi-

ridge waveguides. It is worth to mention that, despite most of this work is theoretical, a great number of these results were assessed by means of experimental measurements, thus demonstrating the validity of the theoretical frame proposed. With regard to the structure of this PhD Thesis, it is divided into four main thematic areas. The first topic analyzes the multipactor mitigation or suppression by means of an external magnetic field oriented along the axis of a coaxial transmission line. The second thematic area presents a bunch of multipactor susceptibility charts for ridge and multi-ridge waveguides, as well as a simple procedure to obtain the multipactor threshold in complex structures based on several sections of ridge and multi-ridge waveguides. The third topic is an study about the multipactor effect in ferrite-loaded components. In particular, it is examined the case of a parallel-plate waveguide with a magnetized ferrite slab. Finally, the fourth thematic area studies the multipactor effect in coaxial transmission lines excited with digital modulated signals.

Index

Chapter 1

Introduction

In present and near future space sector applications, higher power handling capabilities, as well as larger component integration, are being increasingly demanded. These harder requirements result in extremely high electromagnetic field densities within the devices, thus leading to major risks of RF breakdown. By RF breakdown, two basic phenomena are meant: corona and multipactor discharge effects.

The corona effect consists in the ionization of the gas molecules inside a device as a consequence of a high power electromagnetic field. The outer electrons in the gas molecules are released and collide with other molecules extracting more electrons. This phenomenon produces a chain reaction that increases the electron charge density, distorting the transmission of the RF signal, and eventually leading to a destructive electric current within the device. As the pressure in the component diminishes towards the vacuum, the electrons free path increases allowing them to cross the distance between walls without impacting with gas molecules. Then, the multipactor effect can appear.

Multipactor is a high-power radio frequency (RF) electromagnetic field phenomenon that appears on devices operating under high vacuum conditions. It is present in a wide range of different scenarios, such as passive components of satellite communication payloads, travelling wave tubes, or particle accelerators [1]. In a vacuum environment, free electrons inside a microwave device are accelerated by the RF electric field, impacting against its metallic walls. If the electron impact energy is high enough, one or more secondary electrons might be released from the surface. When some resonant conditions are satisfied, secondary electrons get synchronized with the

RF electric field, and the electron population inside the device grows exponentially leading to a multipactor discharge. The onset of the multipactor discharge degrades the device performance by several negative effects, such as increasing the signal noise and reflected power, heating up the device walls, outgassing, detuning of resonant cavities, vacuum window failure, and even resulting in the total destruction of the component. Due to that, multipactor phenomenon is revealed as a crucial limitation in the maximum RF power handling.

Focusing on spacial communications, special attention must be paid to multipactor in satellite components, where replacement of damaged devices is not possible. In fact, space environment surrounding satellites is heavily populated by high energetic particles (mostly protons and electrons) coming from the solar wind, and which are trapped by the Earth's magnetic field around the Van Allen belts. These particles constitute a source of free electrons that can trigger a multipactor discharge. Therefore, it is crucial to be sure that RF breakdown does not occur during the satellite life, since it can be catastrophic for its operation. Presently, the achievement of sufficient RF breakdown security margins, which are hardly achievable, implies long and high cost design and test campaigns for space sector companies. In addition, the lack of reliable theoretical models and software tools for the prediction of these phenomena does not help to alleviate the design process of components for space applications, which should minimize the risk of RF breakdown effects. In practice, companies presently developing microwave hardware for space applications are applying design margins of at least 3 dB (in some complex topologies, i.e. those involving dielectrics, margins between 6 and 10 dB are even forced) [2], which means a reduction of the satellite operating power of at least half the breakdown level tested experimentally.

Recently, more attention is being paid to these phenomena through research and technological activities promoted either by space institutions (i.e. the European Space Agency, and specially the European Space and Research Technology Centre, ESTEC, The Netherlands) and companies devoted to design and manufacture of space RF and microwave hardware.

Multipactor, when initially discovered by Farnsworth in 1934 [3], was briefly studied as a beneficial effect for signal amplification in cold-tube for TV applications. It took until the 1940s to appear the first multipactor theory aimed to understand this effect observed in many gaseous breakdown experiments at very low pressures. This early multipactor theory was proposed by Gill and von Engel [4] for an infinite metallic parallel-plate waveguide excited by a single-carrier harmonic signal. In such a

case, the RF electric field is homogeneous along the separation between the plates, which is commonly referred as the gap of the device. The results obtained for the parallel-plate scenario can be extrapolated to real structures provided the gap is small compared to the rest of the device dimensions. The Gill and von Engel theory considers the presence of double-surface electron trajectories, and makes the assumption that there is a constant ratio (k) between the impacting velocities of the primary electrons and the releasing velocities of the secondaries. However, this hypothesis has a lack of physical basis. According to Gill and von Engel, there are three conditions for the onset of a multipactor discharge. First, in order to achieve synchronism between the electron and the RF electric field, the electron time of flight between two consecutive impacts with the plates must be equal to an odd number of half-periods, this number is known as the multipactor order. Secondly, the departure phase of the electrons from the plates must be in a certain range with regard to the RF electric field phase in order to ensure that the released electrons can cross the gap, since if the RF electric field points in the wrong direction electrons are pushed back towards the originating wall. Thirdly, the impacting energy of the electrons must be in a certain energy range (that depends on the material) in order to extract secondary electrons.

Later in the 1950s, Hatch and Williams reformulated the Gill and von Engel theory to explain their own multipactor experiments. Since the constant "k" assumption was retained, the modified theory became known as "constant-k" theory, and for decades it remained as the classical theory for obtaining the multipactor susceptibility curves. It was not until the late 1980s when Vaughan removed the baseless "k"-constant assumption, and presented a new multipactor theory based on the most realistic hypothesis of a mono-energetic non-zero initial velocity for the secondary electrons [1]. Because of this assumption the theory was known as the "constant-v" theory. Moreover, Vaughan also provided the first attempt to analytically estimate the level of electron population at the saturation. The saturation phenomenon occurs when the electron population becomes very high, and the space charge electric field due to the coulombian repulsion is able to counteract the RF electric field, thus breaking the electron resonant trajectories.

Since then, Vaughan's multipactor theory was adopted by many researchers. Riyopoulos et al. included the presence of a crossed DC magnetic field [5], and described the appearance of the single-surface resonant trajectories related with multipactor modes that exhibit an even number of half-periods between consecutive impacts. In [5] it is also adressed for first time the effect of the realistic random emission velocities

of the secondaries, demonstrating that whenever the spread of the initial velocities is sufficiently small, the phase focusing effect from the RF electric field will overcome the dispersive effect of the random emission, thus the stability of the resonant trajectories is ensured. Besides, it is worth to mention the extension of the Vaughan's theory to other geometries such as rectangular waveguides [6], coaxial waveguides [7], waveguide irises [8], [9], and helix antennas [10].

More recently, the availability of more powerful computational resources led the emergence of many computer codes to model numerically the multipactor effect and aid in the design of multipactor-free structures. Firstly, such simulation codes were mainly based on the known as effective electron model [11], [12], which consists on the tracking of one or several of these called effective electrons that accumulate or lose charge and mass in each of the impacts with the device walls. Nowadays, there are also many computer algorithms that consider individual electrons, i. e., each tracked particle represents a real electron, which after colliding with the component surfaces can lead to the release of more tracked electrons throughout the simulation [13]. This latter model constitutes a more realistic approach to the underlying physics of the phenomenon, where electrons are being continuously absorbed and emitted by the device walls.

Whilst for the classical multipactor theories the only required data about the electron emission mechanism from the surfaces is the impacting energy range that ensures the emission of secondaries, for the computational simulation codes a more detailed information about the interaction of the electron with the material is required. In fact, when a primary electron strikes on a surface, it can be elastically backscattered, inelastically backscattered, absorbed, or secondary electrons can be released. The Secondary Electron Yield (SEY) coefficient δ gives the mean number of emitted electrons per impacting electron in the surface [14]. The SEY value at each impact depends mainly on the impact kinetic energy and angle. Despite the particular values of the SEY curve strongly vary depending on the specific material, the shape of the SEY curve is universal for all of them. For very low energies the SEY is slightly below the unity and the incident electrons are mainly elastically backscattered. As the energy increases the SEY diminishes until a minimum is reached, then the SEY starts to grow and, when the energy reaches the so-called first crossover point (W_1), the SEY value becomes equal to one. In this region the absorption process is dominant. Above W_1 it starts the optimum zone for electron multiplication. The SEY continues increasing until the maximum (δ_{max}) is reached for a certain energy (W_{max}). Then

the SEY curve starts to decrease, and eventually drops below the unity in the known as second crossover point (W_2). According to what it was stated above, classical multipactor theories only require the knowledge of W_1 and W_2. In any case, the concrete data of the SEY curve for each material must be obtained from measurements. This point is crucial since, even for a particular material, different SEY curves can arise depending on the manufacturing or coating process. Moreover, air exposure degrades surface properties with time, due to oxidation of metals and adsorption of contaminants. Therefore, accurate information of the SEY curve of the material is essential in order to perform accurate numerical simulations that could properly match with the multipactor experimental results. Once this material information is gathered, the SEY curve can be described by one of the several existing models in the technical literature that provide explicit mathematical expressions. A commonly employed SEY parametrization was proposed by Vaughan in [15] and [16], which allows fitting the experimental data by providing the values of W_{max} and δ_{max}. However, Vaughan's SEY curve only provides the total SEY and does not distinguish among the different contributions (elastic, inelastic, true secondaries). More important is the fact that Vaughan's SEY formulas tend to zero at such region, neglecting the effect of the elastic backscattered electrons which is predominating. With the aim of overcoming that inconvenience, Vaughan's model was later modified by C. Vicente et al. [17] to include a constant SEY value (ranging from 0 to 1) at very low energies. Another relevant SEY model was proposed by Furman and Pivi [18]. In this case, all the possible interactions with the surface are considered by means of different contributions to the total SEY. This implies that the Furman and Pivi model provides a more realistic approach to the SEY curve than the previous models based on Vaughan's formulation.

The development of the numerical simulation codes has allowed to go further in the understanding of the multipactor phenomenon, exploring in detail many cases that are out of the reach of the classical multipactor theories. In particular, the coaxial waveguide has been deeply examined by several works [7]-[23] and some interesting conclusions have been extracted. Udiljak et al., in [7] and [20], outlined that when the inner conductor radius is less than a certain threshold value in comparison with the outer one, it is expected the presence of single-surface multipactor modes in the outer wall. On the other hand, if the inner and outer radii dimensions are similar, then the multipactor properties are very similar to those of its counterpart in the parallel-plate geometry. It is worth to mention the article published by Pérez et al. in [22], where a bunch of multipactor susceptibility charts are computed for coaxial waveguides

operating in different regimes: travelling wave (TW), standing wave (SW) and mixed wave (MW). The computed multipactor curves show the differences in the multipactor threshold depending on the specific type of excitation, specially for high multipactor orders. This effect is explained in terms of the electron drifting along the axis of the coaxial waveguide, which is produced by the presence of the purely azimuthal RF magnetic field of the fundamental TEM mode. In the MW and SW regimes, the axial drift pushes the electrons towards the low RF electric field zones of the interference pattern, extinguish the discharge in some circumstances.

Multipactor phenomenon does not only appear when metallic surfaces are present but also in dielectric materials. Multipactor discharge in dielectrics has the peculiarity that the dielectric surface becomes charged when electrons are absorbed or emitted in an unbalanced way. On the one hand, if secondary electrons are released, the appearance of a positive charge in the surface originates a DC electric field that tends to attract the free space electrons. On the other hand, if impacting electrons are absorbed by the dielectric, the DC electric field originated by the negative charge repels the electrons from the surface. A particular case of structures affected by multipactor are the dielectric windows. In these kind of devices, the RF electric field is parallel to the dielectric surface and the electrons are accelerated along that direction. As a consequence, an electron released from the dielectric surface requires the presence of a certain DC electric field in order to come back to the departure surface. Hence this single-surface multipactor is expected to be considerably different from its double-surface counterpart. Concretely, this single-surface multipactor does not need the synchronism between the electron and the RF electric field for the onset of the discharge [24]. This greatly widens the parameter range for the discharge, and makes the dielectric surface much more susceptible to the multipactor. In [24], with the aid of computer simulations it is constructed a bunch of generic multipactor susceptibility curves taking into account both the SEY material properties, as well as the RF and DC electric field strengths. An important issue related with the multipactor in dielectric windows is the amount of power absorbed by the dielectric as a consequence of the discharge. Since thermal conductivity in dielectrics is lower than in metals, warming of dielectrics can lead to more harmful effects. Due to this, different authors have studied this phenomenon [24]-[26] arriving to the conclusion that, for a wide range of parameters, the multipactor RF power delivered to the dielectric is around 1 percent or less. Besides the dielectric windows, multipactor has also been analyzed in parallel-plate waveguides partially filled with a dielectric slab placed on the top (or

the bottom) of one of the metallic plates [27]-[29]. In [27] it is studied the time evolution of the multipactor discharge in such kind of structures. Initially, it is assumed the absence of any DC polarization electric field, and the multipactor behaves very similar to the classical pure metallic parallel-plate case with double-surface electron trajectories. However, as the electron cloud grows, the dielectric layer charges negatively, arising a noticeable DC electric field which repels the electrons from the dielectric and forces the appearance of single-surface trajectories in the metallic wall before turning off the multipactor discharge itself. This self-mitigation of the discharge where dielectric surfaces are involved is extensively investigated in [29], where susceptibility charts of a parallel-plate dielectric-loaded waveguide are presented for different typical geometrical and electrical parameters.

Most of the multipactor studies available in the technical literature are referred to single-carrier harmonic signals. In fact, all the results outlined above (classical multipactor theory, results for coaxial and dielectric loaded waveguides) are valid for such scenario. Nevertheless, realistic satellite communication systems are based on multicarrier operation and modulated carriers to efficiently use the available frequency spectrum. A typical multicarrier signal is composed of several modulated carriers with small frequency separation. Each of these carriers is modulated according to a certain pattern. As a result, the envelope of the resulting signal varies with time and differs notoriously from the constant envelope single-carrier harmonic case. This phenomenon makes much more complex the prediction of the multipactor discharge when modulated or multicarrier signals are considered. In the non-modulated single-carrier scenario, the criterion for the multipactor discharge is straightforward. When the voltage amplitude of the RF signal exceeds the multipactor threshold, the electron population increases exponentially with time and no matter how fast or slow is the growth rate, the critical electron density required to detect the discharge in the laboratory will be reached sooner or later. As a result, the multipactor criterion for numerical simulations with single-carrier harmonic signal is the observation of an exponential trend in the electron population. On the other hand, when the signal is modulated or multicarrier, the signal envelope is very likely to go above and below the single-carrier harmonic multipactor voltage threshold many times and, consequently, there will be intervals where the electron population will raise (“on” intervals) followed by time lapses in which the number of electrons diminishes (“off” intervals). Depending on the growth rate and time duration at the “on” intervals, different scenarios can be found. A high growth rate or sufficient long “on” interval might allow the discharge

to rise in a single-peak of the signal. However, in other case, the electron population will not be able to reach a high enough value in a single-peak of the signal to trigger the multipactor diagnostic methods, but there will be an electron accumulation from one "on" interval to the next. In this scenario, the discharge appears as a consequence of a "long term" multipactor [30], which requires the consideration of big pieces of the transmitted signal for the numerical simulations. Since the duration of a standard telecommunication signal is much greater in comparison with the typical multipactor simulation times for a single-carrier harmonic signal, the computational time to analyze modulated or multicarrier signals becomes much longer.

With regard to the technical literature, multipactor in multicarrier operation has been extensively considered. In [31] Morrison et al. present both numerical simulations and experimental results with the aim of providing a new criterion for predicting the maximum power operation before the discharge occurs. The results of the simulations shown that the time varying nature of the multicarrier signal is crucial in the multipactor discharge event. Concretely, according to their results, a multipactor discharge is not expected to take place if the multicarrier envelope does not exceed the single carrier threshold for a time equal or greater to the time corresponding to 20 transitions between the plates of a resonant electron. This statement is known as the "20-gap-crossing" rule and, despite it has not been either verified or denied by the experimental results presented within the aforementioned report, it has been adopted by the European Space Agency as the standard for assessing the multipactor risk when multicarrier or modulated signals are involved [2]. In the last decade, Anza et al. have addressed a number of interesting studies dealing with multicarrier, even developing an extension of the classical multipactor theory for multicarrier signals. Prior to that, in [32] the multipactor classical theory in parallel-plate waveguides with time-harmonic signal is extended in order to consider the effect of the spread in the velocities of the secondary electrons. A more realistic theory arises when the random nature of the electron emission is taken into account. In fact, if the velocity spread becomes large enough the flight time of electrons can strongly vary from impact to impact, even intercalated with single surface impacts and still having an overall SEY above the unity. This statistical treatment of the multipactor phenomenon called "non-resonant multipactor" provides results which are closer to the experiments. Later, in [33] the non-stationary multipactor theory is extended in order to consider multicarrier signals. Specifically, it is valid for signals with an arbitrary number of carriers with different amplitude, arbitrary frequency and phase conditions and for any material SEY proper-

ties. This theory has been contrasted with an extensive set of numerical simulations based on Particle-in-Cell (PIC) software tools, finding good agreement between them, thus validating the proposed theory. As an alternative to that full-complete formulation theory for multipactor prediction with multi-carrier signals, in [34] it is proposed a simplified procedure named as the Quasi-Stationary (QS) method. This algorithm relies on the non-stationary theory applied to a single-carrier scenario. It takes sophisticated simplifications on the multi-carrier signal and develops a specific growth electron model. By applying the single-carrier theory, the number of parameters of the problem is reduced significantly. The results from the QS method have been compared with experimental results, finding very good agreement. It is worth to mention that experimental results for multipactor measurements with multicarrier signals presented in [34] show discrepancies with the standard "20-gap-crossing" rule.

Despite multipactor in multicarrier scenarios has been studied by many authors, very few have focused their interest in the analysis of multipactor with modulated signals [35]-[37]. The most relevant of the aforementioned works is the one of Semenov et al. [35], who investigated the effect of a Quadrature Phase Shift-Keying (QPSK) modulation on the multipactor discharge. Numerical simulations showed that the multipactor threshold is affected when the time between phase shifts is below ten RF periods. The main effect observed is a certain suppression in the multipactor discharge with regard to the non-modulated scenario. However, the authors did not consider the effect of the signal filtering after the modulation process, which changes considerably the final signal waveform.

Due to the negative effects of the multipactor discharge on the device performance, several different strategies have been developed in order to suppress or mitigate the appearance of this harmful phenomenon. These techniques attempt either breaking the resonant conditions, or reducing the emission properties of the surfaces in order to avoid the release of secondary electrons. Next, the most relevant methods are outlined:

- Changing the shape of the RF structure. This is aimed to reduce the maximum voltage in the gap of the device, thus breaking the resonant condition for the multipactor.

- Pressurization. By increasing the pressure the mean free path of the electrons is reduced. Then, free electrons have a higher probability of being absorbed by the gas molecules before reaching the component walls. As a counterpart,

increasing the pressure enhances the risk of a corona discharge.

- Dielectric filling. Introducing dielectrics allows to decrease the mean free path of the electrons. However, it increases the losses of the component.

- Slot of broad walls. It consists of opening one or several slots to allow electrons exiting from the structure, and also perturbing the resonance conditions. Nevertheless, there is risk of RF leakage.

- Coatings. Special coatings and surface treatments can reduce the SEY of the surfaces [38]-[42]. The most commonly employed coatings are alodine, TiN, CrN, and CN. However, surface treatments increase the losses and degrade with time.

- DC biasing. It consists on the superposition of a DC electric or magnetic field to disturb the electron trajectories and break the resonance. In rectangular waveguides the orientation of DC magnetic field along the axis of the waveguide has been explored in [43]-[46] finding that a strong enough magnetic field is able to avoid the onset of the multipactor. For coaxial transmission lines a DC magnetic field oriented along the transverse plane of the devices has been intended [47], leading to partial mitigation of the negative effects of the discharge such as the decrease of the RF reflected power. As an alternative to the DC magnetic fields, the application of a DC electric field for mitigating the discharge in coaxial transmission lines was also investigated in [48].

The aim of this PhD thesis is to cover some existing problems in different topics related with the multipactor effect which, according to the author's knowledge, have not been treated extensively in the technical literature until that moment. As a result of these multipactor studies, more rigorous and suitable design margins for predicting multipactor discharges are provided to the space communications industries, thus easing the design of novel components with higher power handling features. In particular, four different topics are considered throughout this work. The first one analyzes the feasibility of inhibiting the multipactor discharge in a coaxial transmission line, by means of an external magnetostatic field oriented along the axial direction of the waveguide. Firstly, it is assumed the most simple scenario of a spatial uniform magnetic field over all the coaxial sample. Secondly, the more realistic case of a non-uniform magnetic field is explored by means of the magnetic field produced by a permanent

magnet. In the two cases, both theoretical and experimental results are presented. The second topic discussed is about the multipactor effect in ridge and multi-ridge waveguides. With this purpose, multipactor susceptibility charts for a wide range of practical cases of interest are presented. Moreover, a procedure to employ the susceptibility charts for assessing the multipactor risk in more complex RF structures, containing several sections of ridge or multi-ridge waveguides, is outlined. Some high power band-pass filters are suitable to be treated with this method. With regard to the third thematic area of this PhD thesis, it is focused on the multipactor analysis of coaxial waveguides excited with digitally modulated RF signals. Typical multipactor studies are devoted to the consideration of pure time-harmonic carriers. However, in practical applications for spacial telecommunications, the transmitted signals are digital modulated, resulting in signal waveforms more complex than the harmonic scenario. Due to this, it is essential to consider the proper transmitted signal in the multipactor analysis, in order to get accurate and reliable results that could be applied to a realistic case. In this work, several of the most employed digital modulation schemes such as the Binary Phase-Shift Keying (BPSK), Quadrature Phase-Shift Keying (QPSK), Quadrature Amplitude Modulation (QAM), and Amplitude and Phase-Shift Keying (APSK) are considered. Thus, theoretical results are assessed by a bunch of experimental measurements. Finally, the fourth and last topic treats about the multipactor phenomenon in RF devices containing ferrites. Ferrites are ferromagnetic materials which exhibit magnetic anisotropy when are immersed in a static magnetic bias field. The magnetic anisotropy of ferrites gives place to a non-reciprocal behavior of the component, which in fact is the basis of the working principle of some types of circulators, isolators and phase-shifters. In this work, the case of a parallel-plate waveguide partially filled with a ferrite slab magnetized by an external magnetic field is investigated. Two different directions of the magnetization field are considered in order to explore the anisotropic effects of the ferrite.

With regard to the PhD thesis structure, it is organized as follows:

This first Chapter is devoted to the introduction. Next, Chapter 2 presents some multipactor basic concepts, such as the classical multipactor theory for a parallel-plate waveguide, the standard “20-gap-crossing” rule for multipactor prediction in scenarios with non-pure time-harmonic signal, and the typical experimental set-up used for multipactor measurements. Afterwards, Chapter 3 describes the main features of the multipactor algorithm that has been developed for the theoretical analysis and simulations. The following two Chapters (4 and 5) contain a list of the most relevant pu-

blications that have resulted from this PhD thesis. There are a total of eight published articles. The first two articles deal with the topic of multipactor mitigation in coaxial lines by means of an external static magnetic field. The third article is related to the multipactor analysis of the ridge and multi-ridge waveguides. The next three articles are devoted to the study of multipactor with digital modulations in coaxial transmission lines. Finally, the remaining two papers are about the multipactor phenomenon in parallel-plate waveguides partially loaded with a magnetized ferrite slab.

Chapter 6 contains a general discussion about the main findings of the work presented in Chapters 4 and 5. This Chapter is splitted into four subsections, each of them linked to its correspondent thematic area as described above in this introductory chapter.

Finally, Chapter 7 presents the most relevant conclusions of this work.

Chapter 2

Multipactor basics

The multipactor effect is an electron avanche-like discharge occurring in devices operating under vacuum conditions and high-power Radiofrequency (RF) electromagnetic fields. In Fig. 2.1, we show the basic steps that lead to the onset of a multipactor discharge for the special case of single-carrier time harmonic signal in a parallel-plate waveguide scenario. First, free electrons pre-existing in the device are accelerated by the RF electric field towards one of the metallic walls. After colliding, if the impact kinetic energy of these called primary electrons is high enough, additional electrons (called secondaries) will be released from the surface. If the impact occurs when the RF electric field reverses its direction, the secondary electrons are driven towards the opposite side impacting in the same way as the primary ones, and generating more secondary electrons. The process is repeated many times finally creating an electron avalanche.

2.1. Multipactor theory in parallel-plate waveguide

In this subsection the most simple scenario for the multipactor effect is described, namely, the parallel-plate waveguide theory. Such kind of structure is depicted in Fig. 2.2 and consists of two infinite metallic parallel plates separated by a gap d. A time harmonic RF voltage is applied to the surfaces in the form $V_{RF}(t) = -V_0 \sin(\omega t)$, where $\omega = 2\pi f$, f is the frequency, and V_0 is the voltage amplitude. As a consequence of the applied voltage, a uniform and vertical RF electric field $\vec{E}_{RF} = \frac{V_{RF}(t)}{d}\hat{x}$ is

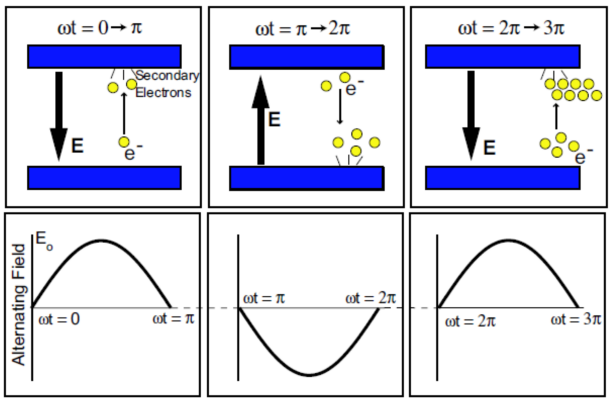

Figura 2.1: Basic steps of a multipactor discharge in a simple parallel-plate waveguide scenario. After each electron impact, secondary electrons are emitted from the surface, increasing the electron population in the waveguide. Synchronization between electrons and RF electric field is accomplished when electrons go across the gap in each half RF period.

generated between the plates. This yields to a one-dimensional model in terms of the electron motion.

The differential equation that governs the electron motion in the parallel-plate waveguide is derived from the non-relativistic Lorentz Force and the Newton's Second Law. In the following expresions, no relativistic effects are taken into account, only classical motion equations are presented. This is a good approximation, since in many multipacting scenarios electrons velocities are below enough to the speed of light in vacuum. Under these assumptions, the differential equation of motion for an electron is given by

$$\ddot{x} = \frac{eV_0}{m_e d}\sin(\omega t) \tag{2.1}$$

where m_e and $-e$ are the electron mass and charge, respectively.

Equation (2.1) can be solved analytically. Following initial conditions are imposed:

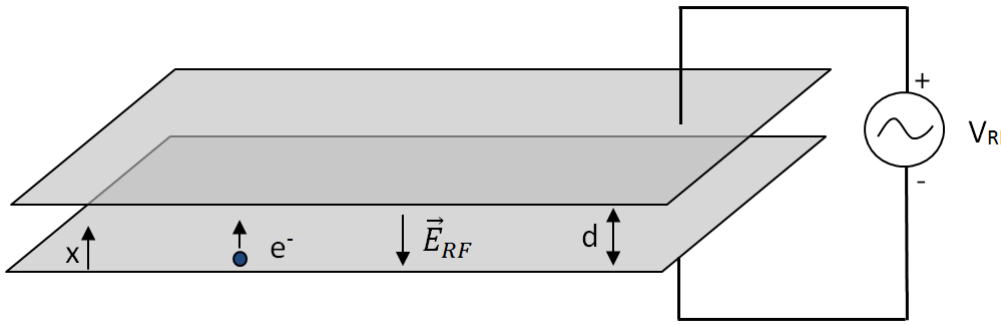

Figura 2.2: Parallel-plate waveguide with an RF electric field $\vec{E}_{RF}$ between surfaces.

$$\begin{aligned} \omega t_0 &\equiv \phi \\ \dot{x}(t_0) &\equiv v_0 \\ x(t_0) &\equiv x_0 \end{aligned} \tag{2.2}$$

where t_0 is the time when the electron starts interacting with the electric field, v_0 is the initial speed of the electron, and x_0 its initial position.

After solving the differential equation (2.1), and imposing the previous initial conditions (2.2), the following expressions for the electron velocity and trajectory are easily found:

$$v = v_0 + \frac{eV_0}{m_e \omega d}(\cos(\phi) - \cos(\omega t)) \tag{2.3}$$

$$x = x_0 + \frac{v_0}{\omega}(\omega t - \phi) + \frac{eV_0}{m_e \omega^2 d}((\omega t - \phi)\cos(\phi) - \sin(\omega t) + \sin(\phi)) \tag{2.4}$$

2.1.1. "constant-v" theory

In the "constant-v" theory proposed by Vaughan, all electrons are assumed to depart with the same initial velocity v_0. In order to get the multipactor discharge, it is

necessary that certain resonant conditions between the electron trajectory and the RF electric field are satisfied. The synchronism condition was reported in [49], [50], and states that the electron emitted from one of the plates shall reach the opposite surface in a time equal to an odd number of RF semicycles of the RF signal. Consequently, the resonant conditions can be expressed as

$$\omega t_i = \phi + m\pi; m = 1, 3, 5, 7, ... \tag{2.5}$$

where t_i represents the electron impacting time and m is the multipactor order. As an example, in Fig. 2.3 the electron trajectory and velocity for an $m = 1$ multipactor order are shown.

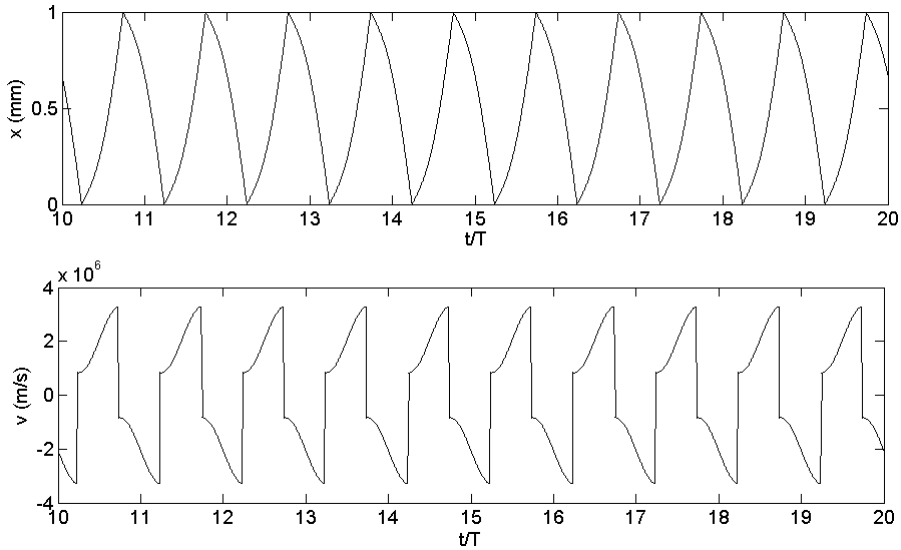

Figura 2.3: Trajectory and velocity of an electron as a function of the time normalized to the RF period ($T = 1/f$), for a harmonic multipacting of order $m = 1$. The parameters used in the simulation are $\phi = 0^o$, $V_0 = 44$ V, $d = 1$ mm, $f = 1$ GHz, $v_0 = 2$ eV.

Given the resonance condition (2.5), it is possible to obtain expresions of the impact velocity v_f and for the amplitude of the resonant voltage V_0. Substituting (2.5) in (2.3), we have

$$v_f = \frac{2eV_0}{m_e \omega d} \cos\phi + v_0 \tag{2.6}$$

In the same way, replacing (2.5) in (2.4) when the electron reaches the upper plate ($x = d$), we can obtain

$$V_0 = \frac{m_e}{e} \frac{\omega d(\omega d - m\pi v_0)}{m\pi \cos\phi + 2\sin\phi} \tag{2.7}$$

The previous expressions for the impact velocity and amplitude voltage depend on the initial launching phase ϕ. Not any initial phase of the released electron may accomplish synchronization with the electric field. In fact, if the electron departs when the electric field polarity points in the wrong direction, the electron will be accelerated towards the originating wall. There is a certain range with the initial phase values that are suitable for reaching resonance with the electric field:

$$\phi_{min} \leq \phi \leq \phi_{max} \tag{2.8}$$

Regarding the minimum phase value ϕ_{min}, when the electron starts with negative phase from the lower surface ($x = 0$), acceleration becomes also negative (see expression (2.1)), so the electron tends to be pushed back to the departure plate and a certain recoil in the electron trajectory is found (see Fig. 2.4). However, assuming that the initial velocity of the electron is greater than zero, the electron still may be able to reach the opposite wall for phase values above ϕ_{min}. An electron released with ϕ_{min} (also called the non-return point) will impact with the departure wall before reaching the opposite side. In order to obtain ϕ_{min}, the following conditions have to be fulfilled

$$\dot{x} = 0$$
$$x = 0$$

An analytical solution to this system of equations is not possible and has to be solved numerically. With respect to the maximum allowed departure phase ϕ_{max}, is the one that minimizes (2.7), hence it is obtained searching the maximum of the denominator of such expression:

$$\frac{d}{d\phi}(m\pi \cos\phi + 2\sin\phi) = -m\pi \sin\phi + 2\cos\phi$$

$$-m\pi \sin\phi_{max} + 2\cos\phi_{max} = 0$$

$$\phi_{max} = \arctan\left(\frac{2}{m\pi}\right) \tag{2.9}$$

since the optimum departure phase must be comprised within the range $[0, \phi]$, it can be easily demonstrated that the previous ϕ_{max} maximizes the denominator of (2.7) by substituting in the second derivative.

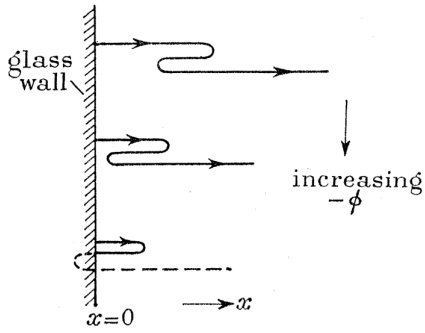

Figura 2.4: Electron trajectories for negative departure phases extracted from [4].

Finally, an extra condition related with the release of secondary electrons from the surfaces is also required . The secondary electron yield (SEY) coefficient is defined as the mean number of released electrons per impacting electron. Every material has two characteristic energies called first cross-over and second cross-over points (W_1 and W_2, respectively) that delimit the electron impacting energy range favorable for the electron multiplication within the waveguide, and hence necessary for the onset of the multipactor discharge. These impact energies can be related with the impact velocities ($W = \frac{1}{2}mv^2$) and, substituting in (2.6), the next condition for the voltage amplitude range arises

$$(v_1 - v_0)\frac{m_e\omega d}{2e\cos\phi} \leq V_0 \leq (v_2 - v_0)\frac{m_e\omega d}{2e\cos\phi} \tag{2.10}$$

The multipactor regions that satisfy the above conditions can be plotted in a V_0 versus $f \times d$ graph; these plots are very useful as an initial engineering model, and

are called susceptibility charts. This representation is very useful since for the parallel-plate geometry, all the magnitudes involved with the multipactor resonance are related only with the $f \times d$ product (recall (2.7), (2.10)). In Fig. 2.5 we depict an example of a typical multipactor chart for the first resonant modes (from $m = 1$ to $m = 9$). The envelope curve that fits the lower boundary of the multipactor modes delimits the multipactor RF voltage threshold.

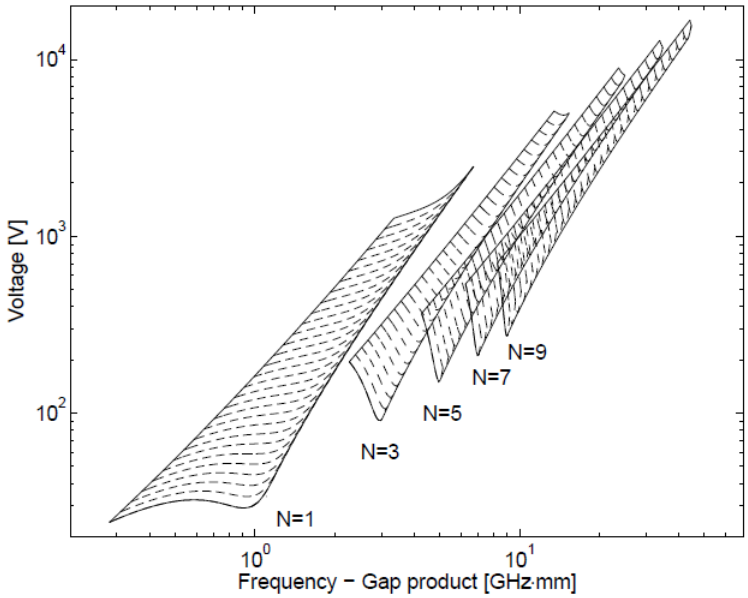

Figura 2.5: Multipactor susceptibility chart for the Vaughan's "constant-v" parallel-plate theory. Parameters used are: v_0 =3.68 eV, $W_1 = 23$ eV, and $W_2 = 1000$ eV. Figure extracted from [51].

2.1.2. "constant-k" theory

The "constant-k" theory takes the baseless assumption that there is a fixed ratio between the electron impact velocity and the initial velocity for all of them,

$$k = \frac{v_f}{v_0} \tag{2.11}$$

After imposing the multipactor synchronism condition (2.5), together with the "constant-k" assumption (2.11) in the velocity equation (2.3), it is obtained the following expression for the impact velocity

$$v_f = \frac{k}{k-1}\frac{2eV_0}{m_e\omega d}\cos(\phi) \tag{2.12}$$

Proceeding similarly with (2.4), the resonant voltage is calculated:

$$V_0 = \frac{4\pi^2(f\,d)^2}{(e/m_e)\Phi_m} \tag{2.13}$$

$$\Phi_m = \frac{k+1}{k-1}m\,\pi\cos(\phi) + 2\sin(\phi) \tag{2.14}$$

The maximum departure phase that minimizes the resonant voltage for the multipactor is obtained by maximizing (2.14):

$$\phi_{max} = \arctan\left(\frac{k-1}{k+1}\frac{2}{m\pi}\right) \tag{2.15}$$

Finally, the condition that ensures that the resonant electron impacts with an energy between W_1 and W_2 is expressed as

$$v_1\frac{k-1}{k}\frac{m_e\omega d}{2e\cos\phi} \leq V_0 \leq v_2\frac{k-1}{k}\frac{m_e\omega d}{2e\cos\phi} \tag{2.16}$$

Similarly as it was discussed for the "constant-v" theory, using the above resonance conditions it is possible to compute the multipactor susceptibility charts for the "constant-k" theory, as it is shown in Fig. 2.6.

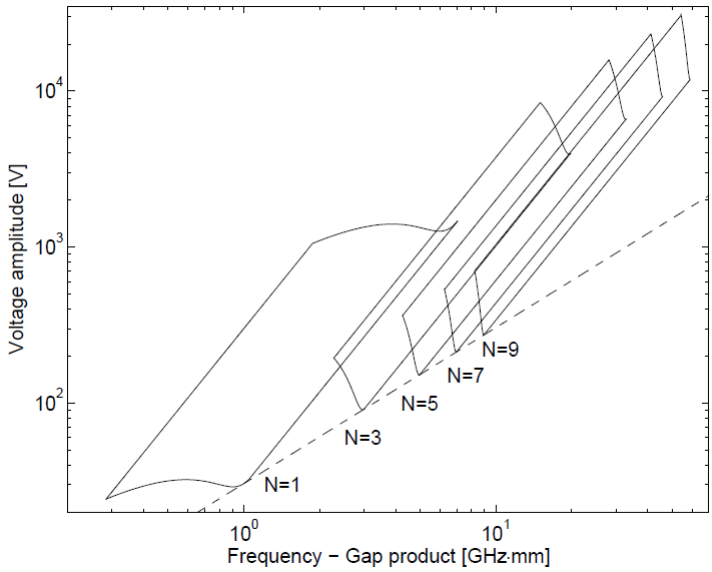

Figura 2.6: Multipactor susceptibility chart for the Hatch and Williams "constant-k" parallel-plate theory. Parameters used are: $k = 2.5$ (corresponding with an initial v_0 =3.68 eV when $v_i = W_1$), $W_1 = 23$ eV, and $W_2 = 1000$ eV. Figure extracted from [51].

2.1.3. Simple model for electron growth

When the electrons get synchronized with the RF electric field, the electron flight time between successive impacts with the waveguide walls is well defined by the multipactor order m. Moreover, the electron trajectories are periodic, as well as the electron velocities. This fact allows to define an average SEY coefficient δ_{av} in the impacts. Assuming that at the time instant $t = 0$ we have a bunch of N_0 electrons synchronized with the RF electric field, the number of electrons within the waveguide after n collisions, N_n, can be calculated as follows:

$$\begin{gathered} N_1 = N_0\delta_{av} \\ N_2 = N_1\delta_{av} = N_0\delta_{av}^2 \\ \cdots \\ N_n = N_0\delta_{av}^n = N_0\exp(n\,\ln\delta_{av}) \end{gathered}$$

Thus, the electron population increases exponentially with time. Alternatively, it can be expressed the number of electrons as a function of the time of the n-th impact, $t_n = n(m/(2f))$, in the following manner:

$$N(t_n) = N_0 \exp\left(t_n \frac{2f}{m} \ln \delta_{av}\right) = N_0 \exp(\alpha t_n) \tag{2.17}$$

where $\alpha = \frac{2f}{m} \ln \delta_{av}$.

2.2. "20-gap-crossing" rule for multipactor prediction

The semi-empirical "20-gap-crossing" rule is a rule-of-thumb adopted by the European Space Agency (ESA) for assessing the risk of multipactor breakdown for non-pure harmonic signals such as in multi-carrier scenarios [2]. This rule is based on the dependency of the multipactor discharge on the signal envelope, stating that multipactor occurs when the multi-carrier signal envelope exceeds the single carrier multipactor threshold for an interval equal or higher than the time that an electron needs to cross the gap 20 times.

2.3. Multipactor experimental set-up

The multipactor measurements presented throughout this PhD Thesis were carried out at the RF High Power Laboratory of European Space Agency and Val Space Consortium [52]. The standard experimental set-up for typical multipactor measurements is detailed in Fig. 2.7. The Device Under Test (DUT), which is the sample to be tested, is placed in a vacuum chamber that provides a high vacuum environment (below 10^{-6} mbar) monitored continuously during the experiment. The DUT is fed by a signal generator and a high power amplifier (TWTA) which provides the desired signal level. The signal can be Continuous Wave (CW) or pulsed with a certain duty cycle (typically within $2-5\,\%$, the pulse total length ranges between 20 - 40μs). Pulsed operation is often preferred due to overheating of the amplifier and power consumption.

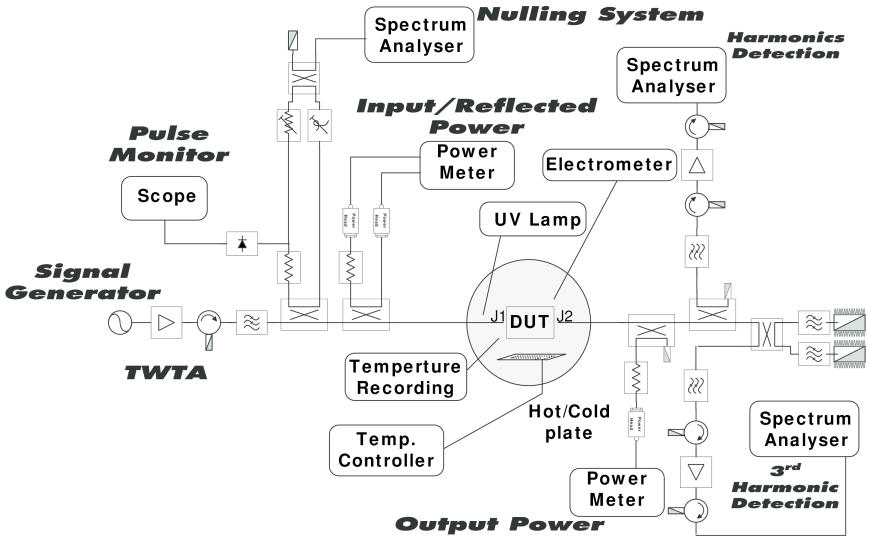

Figura 2.7: Standard set-up used for multipactor measurements.

Despite the fact that there are free electrons in the space that can reach the device critical areas, in the laboratory it is required an external source of electrons in order to trigger the electron multiplication that may eventually lead to the multipactor discharge. Regarding with the electron seeding, three kind of sources are typically employed: radioactive sources, Ultra-Violet (UV) lamp, and Regulated Electron Gun (REG). The radioactive sources consist of a certain amount of radioactive material that presents β-decay (typically a 1 mCi activity strontium-90 source is employed) and consequently, emit electrons. The radioactive source is placed outside the DUT but close to the critical zone where the discharge is expected. Then, electrons can arrive to the discharge area in two ways: by directly penetrating through the walls of the component, or by means of secondary electrons that are generated inside the device wall as the impacting electron penetrates and looses energy. The UV lamp extracts electrons from the inner metallic surface of the device by means of the photoelectric effect. To do this, the UV light is guided from the UV lamp; it is placed outside the vacuum chamber and it is inserted to the interior of the DUT through an optical fiber through a venting hole near to the critical region. The Regulated Electron Gun is a device that provides an electron beam with a controlled energy and current density. This is quite an advan-

tage, since these parameters can be set to the optimum value to trigger the multipactor discharge. However, it presents the disadvantage that the mechanism is bulky and it requires straight line of view to the critical gap.

With regard to the methods for detecting the discharge they can be classified in two types: local and global ones. On the one hand, the local methods are able to seek the discharge only in the surrounding place where they are located. An example of local method is the electron probe, which consists of a metallic wire biased with a positive voltage and placed close to a venting hole or a slot near the critical area, in order to catch the electrons produced during the discharge by means of a microamperimeter. On the other hand, the global methods are able to detect the multipactor discharge occurred in any area of the whole DUT. Two common global detection methods are the nulling system and the third harmonic detection. The nulling system consists of the interference of the incident and reflected signals. To proceed, a fraction of the incident and reflected signal are extracted from the set-up by means a directional coupler. Then, the incident signal is passed through a variable attenuator whilst the reflected signal is passed through a variable phase shifter. After that, both signals are combined by means of a 3 dB hybrid, and the spectrum of the interference signal is monitored in an spectrum analyzer. The variable attenuator and the phase shifter must be tuned prior to the multipactor testing in order to have a minimum in the superimposition of the two signals. This minimum is very sensitive to any variation of the amplitude or phase of the two composing signals and, when the discharge occurs, the RF power noise radiated by the electron cloud will distort the minimum, and a sharp variation of the superimposed signal level will be observed in the spectrum analyzer (see Fig. 2.8). With regard to the third harmonic technique, it is based on the detection of the RF noise generated by the discharge at a frequency of three times the frequency of the RF carrier signal. Proceeding in a similar way to the nulling system, a fraction of the output signal is extracted by means of a directional coupler, passed through a low noise amplifier and then monitored by a spectrum analyzer. At the moment of the multipactor discharge, a sudden increase at the third harmonic signal level occurs; other harmonics as the second one can also be registered but with lower intensity than the third one.

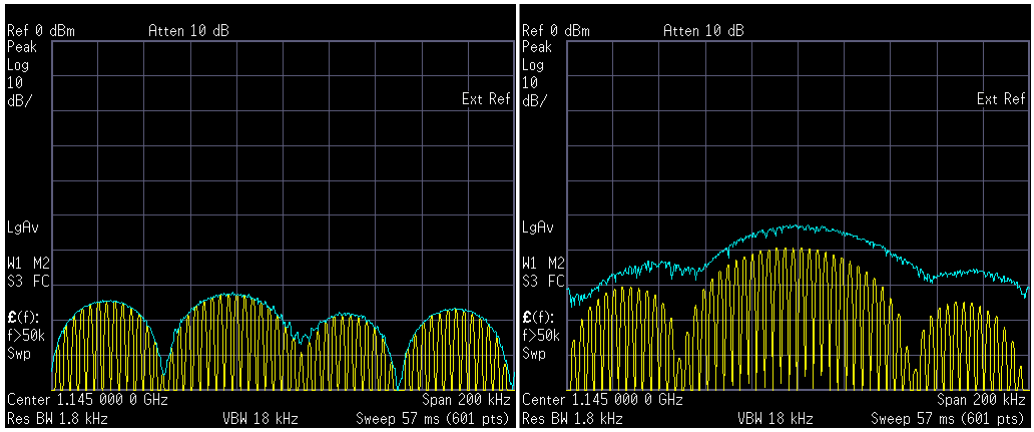

Figura 2.8: View of the spectrum analyzer monitoring the nulling system. Left: before the multipactor discharge. Right: after the discharge has taken place.

Chapter 3

Multipactor simulation algorithm

3.1. Overview

In order to study the multipactor phenomenon in several RF waveguides under different specific scenarios, an efficient multipactor prediction tool based on the Monte-Carlo method has been implemented. Briefly, Monte-Carlo methods are a class of computational algorithms that rely on repeated random sampling to obtain numerical results. Their basic idea is using randomness to solve problems that might be deterministic in principle. They are often used in physical and mathematical problems, and are most useful when it is difficult or impossible to use other approaches. Three different problem classes are treated with Monte-Carlo method [53]: optimization, numerical integration, and generating draws from a probability distribution. In physics-related problems, Monte-Carlo methods are useful for simulating systems with many coupled degrees of freedom, such as fluids, disordered materials, strongly coupled solids, and cellular structures.

The developed multipactor prediction tool simulates the electron behavior within the RF structure under the influence of the existing electromagnetic fields, and allows to estimate the multipactor RF voltage threshold in the component. Depending on the specific case to be analyzed, two different simulation algorithms are employed: the effective electron model and the individual electron model. The effective electron model constitutes a more simple approach to the underlying physics of the multipactor phenomenon than the individual electron model, since the number of tracked particles remain fixed during the simulation. The increase in the electron population during

the successive impacts of the electrons with the device walls is taken into account by the charge and mass accumulation of each effective electron. Despite this, good performance is found when comparing with experimental results for a wide range of scenarios with pure harmonic single-carrier signals. However, when time-varying envelope signals are transmitted (for example single-carrier digital modulated signals or multicarrier signals), more accurate results (in terms of the multipactor RF voltage threshold determination) are found if the individual electron model is implemented. In the individual electron model, new particles are generated throughout the simulation if secondary electrons are released after an impact, or the impacting electron can be removed from the simulation if it is absorbed by the surface. The counterpart of this individual electron model is that, whilst obtaining the electron resonant trajectories is quite straightforward with the effective electron model, it becomes hard in this case (since the tracked electrons are continuously created and destroyed at every collision with the device walls).

Despite the choice of the electron model implemented in the multipactor tool, there are many common aspects in the performance for both of them. The code starts considering a set of initial electrons that are emitted with random initial velocities from one or several spatial points within the waveguide. Then, the electron motion governed by the total electromagnetic field is obtained by solving numerically the equation of motion for each of the tracked electrons. When one of those electrons impacts with the device walls, it is computed the SEY coefficient that takes into account the release of secondary electrons from the colliding surface. Then, different treatment is done depending on the electron model implemented. On the one hand, in the individual electron model, the electron can be absorbed, backscattered by the surface, or secondary electrons might be released. In the two latter cases, the electron(s) is (are) re-emitted towards the waveguide. On the other hand, in the effective electron model, the absorption or emission of secondary electrons is taken into account by upgrading the charge and mass of the effective electron. Then, the effective electron is always launched back to the waveguide. The code runs until the simulation has lapsed a predefined number of RF periods, or until a certain critical population level (attached to the multipactor discharge criteria) is reached. The final output of the multipactor tool is the temporal evolution of the electron population within the device, which allows to decide whether the multipactor discharge will be present or not at such RF voltage level.

In the following subsections, the aspects of the multipactor algorithm outlined

previously are extensively detailed. First, in subsection 3.2 we present the differential equations that describe the electron motion in presence of the electromagnetic field, and also the numerical procedure to integrate such equations. In subsection 3.3 we discuss about the space charge effect that arises from the coulombian repulsion among electrons, that becomes important as the electron density increases in the device. Next, in subsection 3.4 two different SEY models that are employed for characterizing the interaction between the impacting electron and the colliding surface are described. Finally, the particularities of the effective and the individual electron models are examined in subsections 3.5 and 3.6, respectively.

3.2. Electron dynamics

The electron dynamics is governed by the relativistic Lorentz Force:

$$\vec{F}_L = q(\vec{E} + \vec{v} \times \vec{B}) = \frac{d\vec{p}}{dt}$$

$$\vec{p} = m_e \gamma \vec{v}; \qquad \gamma = \frac{1}{\sqrt{1 - \left(\frac{v}{c}\right)^2}}$$

where m_e is the electron mass at rest, $q = -e$ is the electron charge, v is the magnitude of the velocity vector $\vec{v}$, γ is the relativistic factor, $\vec{p}$ is the relativistic linear momentum, t is the time, c is the speed of light in vacuum, and $\vec{E}$ and $\vec{B}$ are the total electric and magnetic fields inside the device, respectively.

The typical electron velocity values reached in space communication systems are considerably lower than the speed of light in vacuum, due to this the relativistic formulation can be approached considering that $\gamma \approx 1$,

$$\vec{F}_L = \frac{d\vec{p}}{dt} \approx m_e \frac{d\vec{v}}{dt} = m_e \frac{d^2\vec{r}}{dt^2}$$

Finally the problem can be expressed as a coupled differential equations system of second order,

$$\frac{d^2\vec{r}}{dt^2} = \frac{q}{m_e}\left(\vec{E} + \vec{v} \times \vec{B}\right)$$

Regarding the total electric and magnetic fields experienced by the electron, it is the superposition of the RF electromagnetic field plus the electric field due to the space-charge effect (that takes into account the coulombian repulsion among electrons), plus an electric field that arises in dielectric surfaces (if present in the waveguide) due to its polarization when electrons are emitted or absorbed. Additionally, a static magnetic field has been considered in certain sections of the present work.

$$\vec{E} = \vec{E}_{RF} + \vec{E}_{sc} + \vec{E}_{pol}; \qquad \vec{B} = \vec{B}_{RF} + \vec{B}_{DC}$$

In most of the practical cases, the above differential equation system has not analytic solution, and it has to be numerically solved. To do this, we have employed a velocity-Verlet 2^{nd} order time-symmetric method suitably adapted to our particular problem [54]. This allows an improvement with respect to other integration methods for ordinary differential equations in terms of computational speed and accuracy. Moreover, it ensures other important properties in physical systems such as time reversibility of the solution. For the cases under analysis in this PhD thesis, convergent electron trajectories are found for 300 time steps per RF period. The expressions that provide the actualization of the position and velocity vectors of the electron from the current integration step to the next one are the following:

$$\frac{d\vec{v}}{dt} = \vec{a}(\vec{r}, \vec{v}, t)$$

$$(\vec{r}_n, \vec{v}_n) \rightarrow (\vec{r}_{n+1}, \vec{v}_{n+1})$$

$$\vec{v}_{n+\frac{1}{2}} = \vec{v}_n + \frac{\Delta t}{2}\vec{a}(\vec{r}_n, \vec{v}_{n+\frac{1}{2}}, t_n)$$

$$\vec{r}_{n+1} = \vec{r}_n + \Delta t \vec{v}_{n+\frac{1}{2}}$$

$$\vec{v}_{n+1} = \vec{v}_{n+\frac{1}{2}} + \frac{\Delta t}{2}\vec{a}(\vec{r}_{n+1}, \vec{v}_{n+\frac{1}{2}}, t_{n+1})$$

where $\vec{r}_n$ and $\vec{v}_n$ are current position and velocity vector of the electron, respectively; $\vec{r}_{n+1}$ and $\vec{v}_{n+1}$ are the position and velocity vectors at the next integration step, respectively; Δt is the time step, $\vec{a}$ is the acceleration vector, and $\vec{v}_{n+\frac{1}{2}}$ is an intermediate step velocity calculation.

3.3. Space-charge effect

When the electron population within the device becomes high, electric repulsion among adjacent electrons becomes noticeable. As a consequence, space-charge effect must be taken into consideration in order to get accurate results. In this work, coulombian repulsion has been considered by means of a model based on a single electron sheet of negligible thickness, in a similar way as it was successfully used in [28], [55], [56]. This electron sheet accumulates the total charge of the secondary electrons emitted when the primary electron impacts on the component walls. As a consequence, the electron sheet charge must be upgraded after each effective electron impact and will vary in time. The position of the electron sheet is assumed to be fixed in the middle of the device gap. Other authors considered the electron sheet movement across the gap in their analysis, but no relevant changes in the multipactor picture were found regarding the fixed position sheet case. The electric field due to the space charge, according to the proposed electron sheet model, can be derived from the Gauss' Law in vacuum. Analytical expressions can be obtained for simple geometries such as coaxial transmission lines and ferrite loaded parallel-plate waveguides, as it will be shown in subsections 3.3.1 and 3.3.2, respectively.

3.3.1. Space-charge effect in coaxial transmission lines

For a coaxial transmission line, the electric field due to the space-charge according to the single electron sheet model (see Fig. 3.1) is given by

$$\vec{E}_{sc}(\vec{r},t) = \begin{cases} -\frac{r_s}{r}\frac{\rho_s(t)}{\varepsilon_0}\frac{\ln\left(\frac{b}{r_s}\right)}{\ln\left(\frac{b}{a}\right)}\hat{r} & a \leq r \leq r_s \\ \frac{r_s}{r}\frac{\rho_s(t)}{\varepsilon_0}\frac{\ln\left(\frac{r_s}{a}\right)}{\ln\left(\frac{b}{a}\right)}\hat{r} & r_s \leq r \leq b \end{cases}$$

$$\rho_s(t) = -\frac{eN(t)}{2\pi r_s h}$$

where r is the radial cylindrical coordinate, $\rho_s(t)$ is the surface charge density of the electron sheet, a and b are the inner and outer radius of the coaxial, respectively; r_s is the radial position of the electron sheet (in our study we take $r_s = (a+b)/2$), ε_0 is the vacuum dielectric permittivity, h is the sheet length along the axial coordinate, and $N(t)$ is the electron population within the waveguide at that time instant.

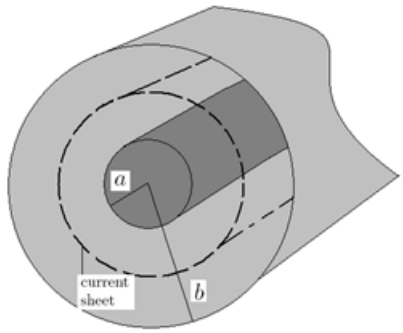

Figura 3.1: Coaxial transmission line with the single electron sheet that takes into account the space charge effect.

3.3.2. Space-charge effect in ferrite-loaded parallel-plate waveguides

For a parallel-plate ferrite-loaded waveguide (see Fig. 3.2), when calculating the space charge electric field, it must be also taken into account the appearance of a surface charge density $\rho_{sd}(t)$ in the top of the ferrite slab, due to the polarization of the dielectric whenever electrons are emitted or absorbed in an unbalanced way. On the one hand, if more electrons are emitted from the ferrite surface than those which are absorbed, then the surface acquires a positive charge because the lack of the negative charge is not almost instantly replaced as in the metals case, where high electric conductivity allows free mobility of the electrons between different spatial points of the material. On the other hand, if more electrons are absorbed than those which are emitted, then the surface becomes negatively charged. In both cases, a polarization electric field $\vec{E}_{pol}$ arises which must be taken into account, as well as the space charge electric field in order to describe the multipactor behavior within the component. The expressions for such space charge and polarization electric fields, assuming that the single electron space charge sheet is placed in the middle-gap of the waveguide, are given by the following expressions

$$\vec{E}_{sc}(\vec{r},t) = \begin{cases} -\dfrac{\rho_{sc}(t)}{2\varepsilon_0\left(1+\frac{h}{\varepsilon_r d}\right)}\hat{y} & h \leq y \leq h+\frac{d}{2} \\ \dfrac{\rho_{sc}(t)}{\varepsilon_0}\left[1-\dfrac{1}{2\left(1+\frac{h}{\varepsilon_r d}\right)}\right]\hat{y} & h+\frac{d}{2} \leq r \leq h+d \end{cases}$$

$$\rho_{sc}(t) = -\frac{eN(t)}{A}$$

$$\vec{E}_{pol} = \frac{\rho_{sd}(t)}{\varepsilon_0}\left[1 - \frac{1}{1+\frac{h}{\varepsilon_r d}}\right] \qquad h \leq y \leq d+h$$

$$\rho_{sd}(t) = \frac{e\Delta N_{ferr}(t)}{A}$$

where h is the height of the ferrite slab, d is the vacuum gap between the ferrite slab and the upper metallic wall, ε_r is the relative dielectric permittivity of the ferrite, A is the transversal area to the gap direction where the discharge is foreseen, $N(t)$ is the electron population within the waveguide, and $\Delta N_{ferr}(t)$ is the balance between the number of electrons emitted and absorbed by the ferrite slab.

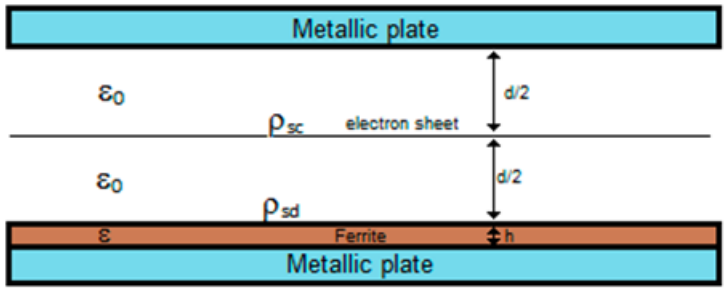

Figura 3.2: Scheme of the ferrite-loaded parallel-plate waveguide with the single electron sheet for space charge effect consideration.

3.4. Secondary electron emission

Secondary electron emission is a phenomenon where primary incident electrons of sufficient energy, when hitting a surface, induce the emission of secondary electrons. To characterize this process, it is defined the total Secondary Electron Yield coefficient (SEY) δ_t, as the mean number of secondary electrons emitted per incident one:

$$\delta_t = \frac{\text{mean number of secondary electrons released}}{\text{1 impacting electron}}$$

When SEY is larger than one extra electrons are generated, whilst for SEY lower than one, a portion of the colliding electrons is absorbed by the material (totally if SEY were equal to zero).

Three different phenomena can arise after a primary electron hits a material surface (see Fig. 3.3): the electron is elastically or inelastically backscattered, one or more true secondaries are released, or it can be absorbed. Elastically backscattered electrons do not penetrate in the surface and are released with an energy and departure angle equal to those of the impact, whereas inelastically backscattered ones lose some energy before they are re-emitted from the surface. On the other hand, emission energies and angles of true secondary electrons are totally independent of the electron impact conditions.

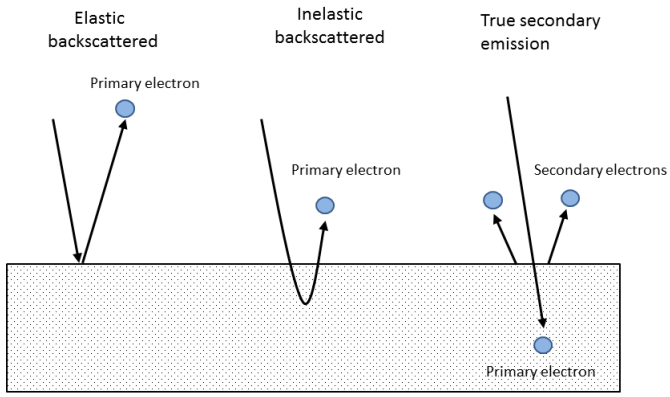

Figura 3.3: Scheme of the different kinds of electron interaction with matter.

The SEY value mainly depends on the impacting kinetic energy and angle of the primary electron. Although each material has its specific SEY properties, there is a common shape of the SEY curve for all materials. In Fig. 3.4, a typical SEY curve measured in the laboratory is shown.

At low impact energies, almost all electrons are elastically backscattered, which implies that the value of the SEY curve is slightly below 1. As the kinetic energy of the impacting electrons increases, it is observed an absorption process, and consequently the SEY decreases. However, for higher values of the energy, the true secondary emission is activated and becomes the main SEY contribution. In fact, there is an

energy interval in which the SEY value is greater than 1. This is the favorable range in terms of electron energy to the onset of a multipactor discharge. The minimum and maximum energies that delimit this interval are called the first cross-over point W_1 and the second cross-over point W_2, respectively. In both energy boundary values the SEY value is equal to 1. The maximum value of the SEY is known as δ_{max}, and it is reached when the impacting energy is W_{max}. For higher energies than W_2 the SEY drops monotonically, and inelastically backscattered electrons are predominant. SEY does not only depend on the impacting energy of the electron, but also depends on the incidence angle measured from the normal to the surface, ξ. Basically, the SEY value increases as the incidence angle ξ does.

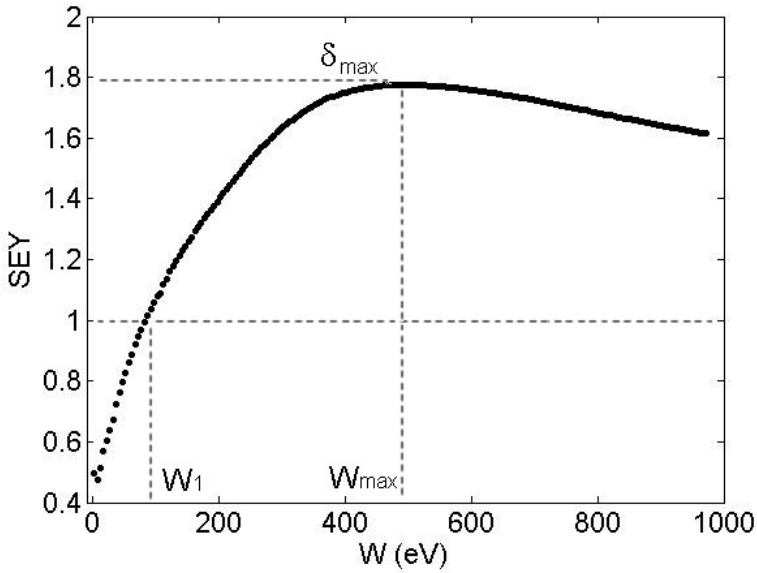

Figura 3.4: Experimental platinum SEY curve measured at the ESA-VSC High Power Space Materials Laboratory.

There are several theoretical models to characterize the SEY coefficient. In this

PhD Thesis, two different SEY models have been implemented in the multipactor simulation tool. For the simulation algorithm based on the effective electron model, the modified Vaughan's model is selected. Otherwise, for the code relying on the individual electron model, the Furman and Pivi SEY model has been employed.

3.4.1. Modified Vaughan's model

This SEY model was presented by C. Vicente et al. in [17] as a modification of the original formulation presented by Vaughan [1], [15], [16]. This model proposes the following expressions for the total SEY curve,

$$\delta_t(W,\xi) = \begin{cases} \delta_{low} & \text{for} \quad \gamma < 0 \\ \delta_{max}(\xi)\left(\gamma e^{1-\gamma}\right)^{0.25} & \text{for} \quad 0 \leq \gamma \leq 3.6 \\ \delta_{max}(\xi)\frac{1.125}{\gamma^{0.35}} & \text{for} \quad \gamma \geq 3.6 \end{cases}$$

$$\gamma = \frac{W - W_0}{W_{max}(\xi) - W_0}$$

$$\delta_{max}(\xi) = \delta_{max}(0)\left(1 + \frac{k_W \xi^2}{2\pi}\right)$$

$$W_{max}(\xi) = W_{max}(0)\left(1 + \frac{k_\xi \xi^2}{2\pi}\right)$$

where W is the electron kinetic energy, ξ is the incidence angle with regard to the normal of the impacting surface, $\delta_{max}(0)$ is the maximum SEY value at normal incidence, $W_{max}(0)$ is the impact kinetic energy at $\delta_{max}(0)$, W_0 is a parameter obtained from continuity conditions of the SEY curve and physically related to the work function of the material, δ_{low} is the SEY value at low impacting energies (within the range from 0 to 1), k_W and k_ξ are factors related to the surface roughness (normally taken equal to 1).

According to the above expressions, the main input parameters needed for this SEY model are $\delta_{max}(0)$, $W_{max}(0)$, W_1, and δ_{low}, which are extracted from the experimental measurement of the SEY coefficient. In Fig. 3.5 a typical SEY curve given by the modified Vaughan's model for normal incidence of the electron is shown.

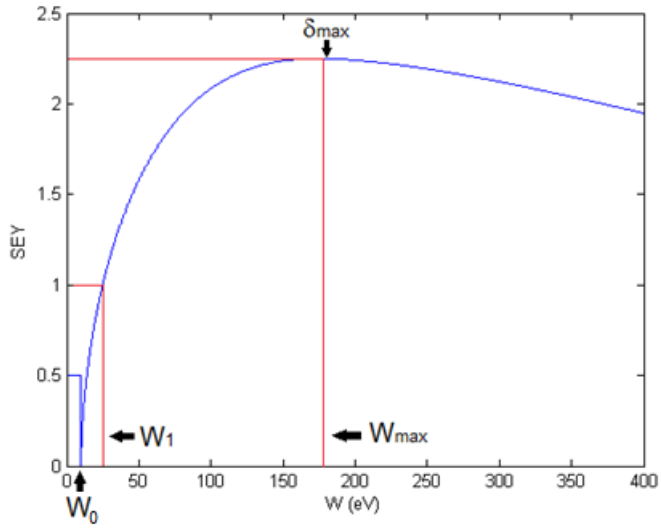

Figura 3.5: SEY curve as a function of the electron kinetic energy at normal incidence for the modified Vaughan's model. SEY parameters: $W_1 = 25$ eV, $W_{max} = 175$ eV, $\delta_{max} = 2.25$, $\delta_{low} = 0.5$

3.4.2. Furman and Pivi model

The SEY model formulated by Furman and Pivi, described in [18] and [57], takes into account the contributions of the elastically backscattered, inelastically backscattered, and true secondary electrons to the total SEY coefficient. The contribution of the inelastically backscattered electrons is modeled by

$$\eta(E_p) = a(1 - bE_p)E_p^{\gamma} \exp\left(-\left(\frac{E_p}{E_b}\right)^{\mu}\right)$$

$$E_b = c + dZ$$

where E_p is the primary electron kinetic energy, Z is the atomic number of the surface material, a is a property of the material, usually in the range $[7 \times 10^{-3}, 10 \times 10^{-3}]$, $b = 3.0 \times 10^{-5}$, $c = 300$, $d = 175$, $\gamma = 0.50$, $\mu = 0.70$. The contribution from elastically backscattered electrons is given by

$$\varepsilon(E_p) = \frac{\varepsilon_1}{1 + \frac{E_p}{E_{e1}}} + \frac{\varepsilon_2}{1 + \frac{E_p}{E_{e2}}}$$

where $\varepsilon_1 = \varepsilon_0 - \varepsilon_2$, ε_0 is the value of the elastic contribution for $E_p = 0$, which is within the range $[0, 1]$ but typically close to the unity, $\varepsilon_2 = 0.07$, $E_{e1} = g/\sqrt{Z}$, $E_{e2} = hZ^2$, $g = 50$, $h = 0.25$.

Finally, the contribution due to true secondary electrons is

$$\delta(E_p) = \delta_m \frac{s\frac{E_p}{E_m}}{s - 1 + \left(\frac{E_p}{E_m}\right)^s}$$

where δ_m, E_m, and s are parameters of the material that are extracted from the experimental measurement of the total SEY curve.

The angular dependence with regard to the impact angle measured from the normal of the colliding surface for the three previous expressions is given by

$$\delta(E_p, \varphi) = \delta(E_p)\frac{k+1}{k + \cos\varphi}$$

where $k = pZ + r$, $p = 0.0027$.

$$\eta(E_p, \varphi) = \eta(E_p)^{\cos\varphi} C_1^{1-\cos\varphi}$$

$$C_1 = \chi \frac{\eta(E_p)}{\eta(E_p) + \varepsilon(E_p)}$$

$$\varepsilon(E_p, \varphi) = \varepsilon(E_p)^{\cos\varphi} C_1^{1-\cos\varphi} C_2^{1-\cos\varphi}$$

$$C_2 = \chi \frac{\varepsilon(E_p)}{\eta(E_p) + \varepsilon(E_p)}$$

where $\chi = 0.89$, and note that $C_1 + C_2 = \chi$. For a clean surface, $r = 0$. For rough surfaces, $2.5 < r < 10$; typically, $r = 5$. In Fig. 3.6 an example with the different SEY contributions is shown, as well as the total SEY value, according to the Furman and Pivi model.

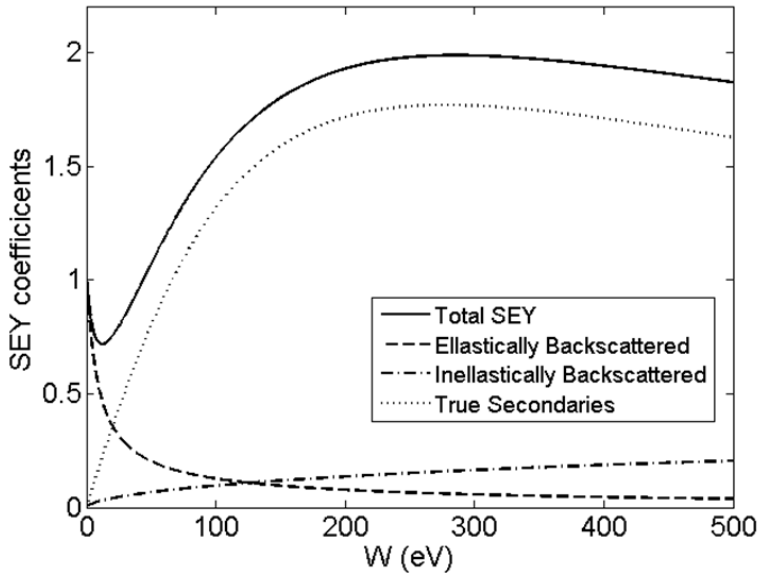

Figura 3.6: Typical Furman and Pivi SEY curve with the different kinds of emission contributions.

When an electron collides with the device walls, the probability for each kind of emission is thus given by

$$P_e(E_p, \varphi) = \varepsilon(E_p, \varphi)$$

$$P_b(E_p, \varphi) = \eta(E_p, \varphi)$$

$$P_s(E_p, \varphi) = 1 - P_e(E_p, \varphi) - P_b(E_p, \varphi)$$

The probabilities of a collision producing elastic or inelastically backscattered electrons are $P_e(W, \varphi)$ and $P_b(W, \varphi)$, respectively. Both types of collisions produce one emitted electron. In the first case (elastic), the incoming electron is perfectly reflected. In the second case (inelastic), there is an energy loss between the incident and the departure electron. In the true secondary emission case, the electrons interact with the material in a more complicated way. This collision has a probability $P_s(W, \varphi)$,

and a random number of electrons are produced. The mean number of true secondary electrons emitted per impacting electron is

$$\lambda(E_p, \varphi) = \frac{\delta(E_p, \varphi)}{1 - \varepsilon(E_p, \varphi) - \eta(E_p, \varphi)}$$

The way to determine the exact output number of true electrons is explained next. The factor λ is divided in two parts: the integer λ_i part and the fractional one λ_f. Then, a random number u with a uniform distribution within the range $[0, 1]$ is generated. Then, the number of true secondaries n is

$$n = \begin{cases} \lambda_i & \text{if} \quad u < \lambda_f \\ \lambda_i + 1 & \text{if} \quad u > \lambda_f \end{cases}$$

Note that the particular case $n = 0$ means that the incident electron has been absorbed by the surface.

3.5. Primary electrons

In order to get accurate results in the multipactor power threshold prediction, more than one effective (or individual) electron is required to be analyzed. The desirable total number of initial primary electrons N_e depends on the specific characteristics of the problem investigated. The most crucial factors are the waveguide geometry, the electromagnetic fields uniformity along the gap, and the presence or not of external bias electric or magnetic field. In fact, when RF electromagnetic fields are quite inhomogeneous or an external electric/magnetic field is applied, more electrons are needed in order to explore several initial launching positions because electromagnetic fields can trap electrons in certain spatial regions. For the effective electron case, even though the waveguide geometry is simple and the electromagnetic fields are uniform, it is required to launch several effective electrons at different initial phases of the RF electric field. Effective electrons starting at an initial phase in which the RF electric field points in the wrong direction will be pushed back to the departure surface, and will not be able to meet the resonant conditions that allow the electron multiplication. On the other hand, it is found that the individual electrons do not have such limitation, all of them can be launched at the same RF phase of the electromagnetic field (or equivalently at the same time), since they are able to reach the resonant conditions for any arbitrary initial phase of the RF electric field.

In this PhD Thesis, mainly coaxial transmission lines and ferrite loaded parallel-plate waveguides are analyzed. Regarding the coaxial line, the RF electric field is inhomogeneous and depends on the radial coordinate. In such a case, it is preferable to launch the electrons from the maximum RF electric field location, which is the inner conductor. However, in the presence of an external DC magnetic field, it has been found necessary lo launch electron from both the inner and outer conductor due to the trap effect of the magnetic field in the electron orbits. For the ferrite loaded parallel-plate waveguides, there is also an external DC magnetic field present (in order to magnetize the ferrite) and, in a similar way, it is mandatory to launch primary electrons from both the bottom and the upper walls of the waveguide. Regarding the proper initial number of effective (or individual) electrons, it has been checked that convergent and accurate results (in terms of the multipactor RF voltage threshold) are found for values within the range of 300-500.

With regard to the velocity vectors (magnitude and direction) of the initial electrons, the computing procedure is the same that employed for the released true secondary electrons, as it is shown in the next subsection.

3.6. Effective electron model

This model is based on the 3D tracking of a set of N_e effective electrons [11] whose motion is governed by the total electromagnetic field within the device, as described in subsection 3.2. The number of effective electrons tracked throughout of the simulation remains fixed from the beginning. Each *i-th* effective electron has associated an electron population which varies with time, i.e. $N_i(t)$, and which is upgraded when the effective electron collides with a surface. This is done by multiplying the total SEY coefficient at the impact δ_t by the accumulated electron population of such electron before the impact:

$$N_i(t + \Delta t) = N_i(t)\delta_{t,i}$$

where $N_i(t)$ and $N_i(t+\Delta t)$ are the accumulated electron populations before and after the collision, respectively. Thus, the accumulated electron population for an effective electron that has impacted k-times at the time t is given by

$$N_i(t) = \prod_{j=1}^{k} \delta_{t,i}^{(j)}$$

where $\delta_{t,i}^{(j)}$ represents the SEY value at the $j-th$ impact of the $i-th$ effective electron. In Fig. 3.7, an scheme of the charge and mass accumulation process for the effective electron algorithm is shown.

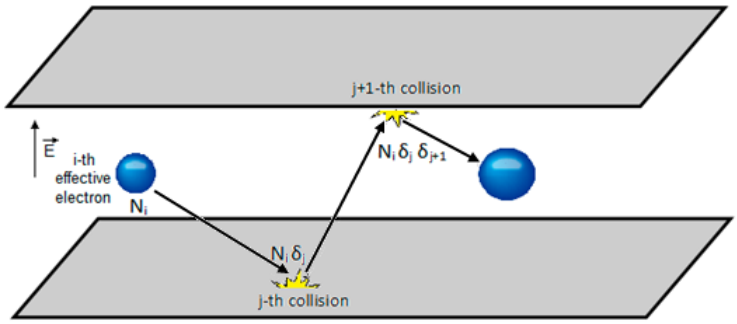

Figura 3.7: Scheme of the accumulation population process in the effective electron model.

Finally, the total electron population within the device is obtaining by adding all the contributions of the N_e effective electrons,

$$N(t) = \sum_{i=1}^{N_e} N_i(t)$$

In the developed multipactor tool based on the effective electron algorithm, it has been implemented the modified Vaughan's SEY model which, as was already discussed in subsection 3.5, only considers the total SEY coefficient. After any effective electron impacts on a wall of the component, it is launched back to the waveguide from the colliding position. If the impact kinetic energy of the effective electron is $W < W_0$, where W_0 is the SEY parameter related with the material work function, it is treated as elastically backscattered and the departure energy is equal to the impacting energy. Regarding to the angle, specular reflection is assumed, i. e., the impact

and departure angle measured from the normal to the surface are equal. In the remaining case, i.e. when $W > W_0$, the departure electron is treated as a true secondary electron. As discussed previously, the launching energy of a true secondary electron does not depend on the primary electron conditions. Actually, the departure energy is calculated by means of the following Rayleigh probability distribution density:

$$f(W_s) = \frac{W_s}{W_g^2} \exp\left(-\frac{W_s^2}{2W_g^2}\right)$$

where W_s is the departure energy of the secondary electron, $f(W_s)$ is the probability of releasing a secondary electron with a departure energy of W_s, and W_g is the standard deviation value of the distribution. An example of the Rayleigh distribution is depicted in Fig. 3.8. The probability density distribution satisfies the following normalization condition

$$\int_0^\infty f(W_s) dW_s = 1$$

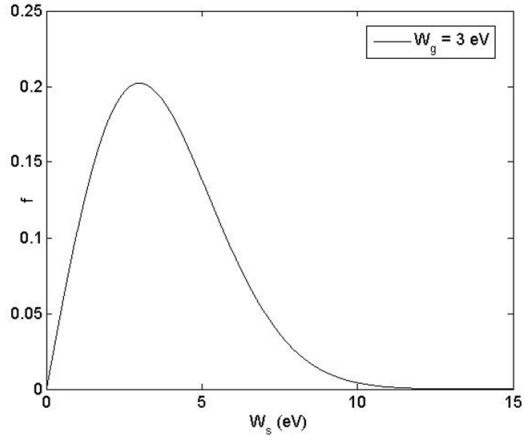

Figura 3.8: Rayleigh probability distribution density with $W_g = 3$ eV.

In order to implement this concept in the simulation code, the algorithm generates a random real number $u \in [0, 1]$, and the departure energy is calculated

$$W_s = W_g\sqrt{-2\ln u}$$

The code checks if the energy conservation principle is satisfied for the obtained energy W_s, i. e., the output energy of the secondary electron cannot exceed the energy of the primary electron.

Regarding the direction of the velocity vector of the secondary electron, it is calculated in a local spherical coordinate system centered at the impact point (see Fig. 3.9).

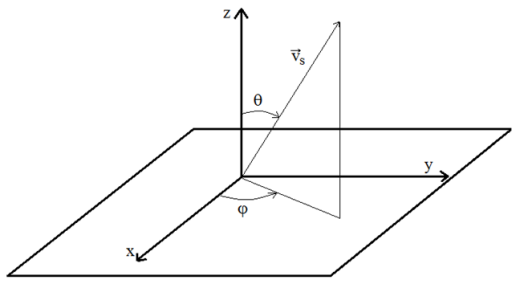

Figura 3.9: Local spherical coordinate system centred at the impact point of the electron.

The azimuthal angle $\varphi \in [0, 2\pi[$ is easily calculated by means of a uniform probability density

$$\varphi = 2\pi u$$

The elevation angle θ with regard to the normal of the surface is computed by means of the cosine law [58]

$$\theta = \sin^{-1}\sqrt{u}$$

Note that random numbers u used for computing W_s, φ, and θ are different.

3.7. Individual electron model

In the individual electron model, the number of tracked particles is not fixed and it can vary with the evolution of the simulation. This allows a more realistic approach to

the real scenario, where electrons are continuously being absorbed and emitted from the device walls. Actually, this version of the code has implemented the Furman and Pivi SEY model, that takes into account the three different contributions to the total SEY coefficient: elastic backscattering, inelastic backscattering, and true secondary emission. When an individual electron hits a surface, the code calculates the probabilities for each kind of electron interaction with the surface ($P_e(E_p, \varphi)$, $P_b(E_p, \varphi)$, $P_s(E_p, \varphi)$), and one of them is chosen with the aid of a random number u generated with a uniform probability between 0 and 1:

$$\begin{aligned} u < P_e(E_p, \varphi) &\longrightarrow \text{Elastic backscattered electron} \\ P_e(E_p, \varphi) \leq u < P_e(E_p, \varphi) + P_b(E_p, \varphi) &\longrightarrow \text{Inelastic backscattered electron} \\ u \geq P_e(E_p, \varphi) + P_b(E_p, \varphi) &\longrightarrow \text{True secondary electron} \end{aligned}$$

If the electron interaction type is elastic or inelastic, there is neither creation nor destruction of particles in such events. Elastically backscattered electrons depart with energy and angle equal to those at the impact moment. Inelastically backscattered electrons are released with the same colliding angle, but with a loss of the output energy with regard to the incident one. However, in the true secondaries case, there will be creation of new tracked particles whenever the number of secondary electrons is greater than one. The output energy and angle of each of these secondary electrons is given by the Rayleigh probability distribution and cosine law, respectively, both described in subsection 3.6. The conservation energy principle is now referred to the sum of the output energies of all the secondary electrons released in the collision, that has to be equal or lower than the primary electron energy. It must be also mentioned that the electron absorption by the surface is considered as a particular case of true secondary emission with number of secondaries equal to zero, in such scenario the individual electron is automatically removed from the simulation.

Finally, it must be mentioned that with the individual electron model the total electron population within the device is simply obtained as the sum of the number of tracked electrons.

3.8. Multipactor onset criteria

A particular criterion has to be established in order to decide if, for a given plot of the electron population evolution with time, the multipactor discharge will be ex-

pected or not. Mainly, there are two different possible multipactor criteria. The first one is based on the detection of a certain growth in the electron population within the component with regard to the initial level or, alternatively, with the exceed of a predefined number of electrons. The other multipactor criterion relies on the detection of the saturation in the electron population, which reaches a steady state due to the space-charge effect when the number of electrons in the device becomes very high. Fig. 3.10 shows a particular example of the time evolution of the total electron population normalized to the initial number of effective electrons, for two different values of the RF voltage amplitude. In the left-hand side of Fig. 3.10 it is perceived the overall decrease in the electron population as the number of RF periods increases and, consequently, no multipactor discharge is expected for that RF voltage amplitude. On the other hand, the right-hand side of Fig. 3.10 shows a multipactor breakdown scenario since, an increase in the electron population is found and a saturation level of the electron population is achieved.

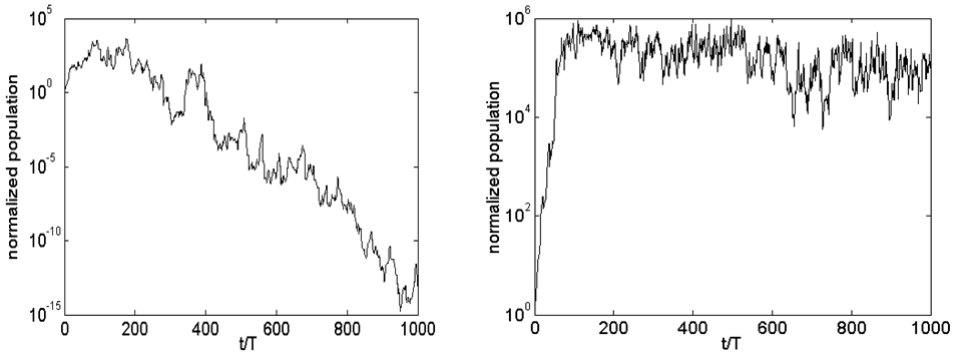

Figura 3.10: Total electron population normalized to the initial number of effective electrons as a function of the time normalized to the RF period, for two different RF voltages (in the left figure the discharge has not been predicted, whereas a multipactor discharge occurs in the right side).

Chapter 4

Article index

4.1. Multipactor in a coaxial line under the presence of an axial DC magnetic field

4.1.1. Bibliography record

- Authors: D. González-Iglesias, A. M. Pérez, S. Anza, J. Vague, B. Gimeno, V. E. Boria, D. Raboso, C. Vicente, J. Gil, F. Caspers, L. Conde
- Publication: IEEE Electron Device Letters, vol. 33, no. 5
- Year: 2012
- Pages: 727-729
- Keywords: coaxial transmission line, DC magnetic field, multipactor effect, RF breakdown

4.1.2. Abstract

The main goal of this letter is the analysis of the multipactor effect within a coaxial waveguide structure when an external axial DC magnetic field is applied. We have designed and manufactured a coaxial waveguide sample that has been immersed within a long solenoid. Numerical and experimental results confirm a significant change in

the RF breakdown behavior with regard to the case without the axial DC magnetic field, as well as the existence of single- and double-surface multipactor regimes. Good agreement between theory and experimental data has been found.

4.2. Multipactor mitigation in coaxial lines by means of permanent magnets

4.2.1. Bibliography record

- Authors: D. González-Iglesias, A. M. Pérez, S. Anza, J. Vague, B. Gimeno, V. E. Boria, D. Raboso, C. Vicente, J. Gil, F. Caspers, L. Conde
- Publication: IEEE Transactions on Electron Devices, vol. 61, no. 12
- Year: 2014
- Pages: 4224-4231
- Keywords: coaxial waveguide, DC magnetic field, multipactor effect, multipactor mitigation, permanent magnet, RF breakdown

4.2.2. Abstract

The main aim of this paper is the analysis of the feasibility of employing permanent magnets for the multipactor mitigation in a coaxial waveguide. First, the study of a coaxial line immersed in a uniform axial magnetic field shows that multipactor can be suppressed at any RF if the external magnetic field is strong enough. Both theoretical simulations and experimental tests validate this statement. Next, multipactor breakdown of a coaxial line immersed in a hollow cylindrical permanent magnet is analyzed. Numerical simulations show that multipactor can be suppressed in a certain RF range. The performed experimental test campaign demonstrates the capability of the magnet to avoid the multipactor electron multiplication process.

4.3. Multipactor susceptibility charts for ridge and multiridge waveguides

4.3.1. Bibliography record

- Authors: D. González-Iglesias, P. Soto, S. Anza, B. Gimeno, V. E. Boria, C. Vicente, J. Gil
- Publication: IEEE Transactions on Electron Devices, vol. 59, no. 12
- Year: 2012
- Pages: 3601–3607
- Keywords: Multipactor effect, multiridge waveguide, radio frequency (RF) breakdown, ridge waveguide

4.3.2. Abstract

The aim of this paper is to study the multipactor radio-frequency breakdown voltage in several ridge and multiridge waveguide configurations. First, multipactor susceptibility charts for several types of ridged waveguides have been computed using the commercial software FEST3D. Next, these charts have been used to predict multipactor threshold values for a bandpass filter and a quasi-low-pass filter both containing ridge waveguide sections. Furthermore, multipactor simulations using FEST3D are carried out to calculate the multipactor threshold of the aforementioned structures. A good agreement between predictions and simulations has been found for both filter examples.

4.4. Analysis of multipactor effect using a Phase-Shift Keying single-carrier digital modulated signal

4.4.1. Bibliography record

- Authors: D. González-Iglesias, M. P. Belloch O. Monerris, B. Gimeno, V. E. Boria, D. Raboso, V. E. Semenov

- Publication: IEEE Transactions on Electron Devices, vol. 60, no. 8
- Year: 2013
- Pages: 2664-2670
- Keywords: Binary phase-shift keying (BPSK), coaxial waveguides, digitally modulated signals, multipactor effect RF breakdown, quadrature phase-shift keying (QPSK), space charge

4.4.2. Abstract

The main aim of this paper is the analysis of the multipactor effect within a coaxial waveguide structure excited by a phase-shift keying single-carrier digital modulated signal. To reach this aim, we developed an in-house a software code which is able to predict the RF multipactor input voltage threshold. This code is based on the single effective electron model, and considers the space charge effect. Numerical simulations are performed for binary phase-shift keying and quadrature phase-shift keying modulated signals. In addition, an experiment is carried out to validate the proposed theoretical model. We have demonstrated that the digital modulation of the single-carrier signal may modify the RF voltage threshold in comparison to the non-modulated scenario. Good agreement between theory and experimental data is found.

4.5. Experimental analysis of the multipactor effect with RF pulsed signals

4.5.1. Bibliography record

- Authors: D. González-Iglesias, O. Monerris Belda, E. Díaz, B. Gimeno, V. E. Boria, D. Raboso
- Publication: IEEE Electron Device Letters, vol. 36, no. 10
- Year: 2015
- Pages: 1085-1087

- Keywords: multipactor effect, RF breakdown, coaxial waveguide, RF pulse, “20-gap-crossing” rule.

4.5.2. Abstract

The main goal of this letter is the analysis of the multipactor effect within a coaxial waveguide excited by an RF pulsed signal. The variation of the multipactor RF voltage threshold with the ON interval length of the pulse has been analyzed. To reach this aim, an in-house multipactor simulation code based on the Monte-Carlo algorithm has been implemented. The numerical simulations show that the multipactor RF voltage threshold increases as the ON pulse interval diminishes. In addition, an experiment was carried out to validate the proposed theoretical model, and demonstrating the excellent agreement between the theory and the experimental data. Finally, the results are compared with the 20-gap-crossing rule used in the space standard document (ECSS-E20-1A).

4.6. Multipactor RF breakdown in coaxial transmission lines with digitally modulated signals

4.6.1. Bibliography record

- Authors: D. González-Iglesias, Ó. Monerris, B. Gimeno, M. E. Díaz; V. E. Boria; P. Martín
- Publication: IEEE Transactions on Electron Devices, vol. 63, no. 10
- Year: 2016
- Pages: 4096-4103
- Keywords: “20-gap-crossing” rule, amplitude and phase-shift keying (APSK), coaxial waveguides, digital modulations, multipactor effect, quadrature amplitude modulation (QAM), quadrature phase-shift keying (QPSK), RF breakdown, root-raised-cosine filter.

4.6.2. Abstract

The aim of this paper is the study of the RF multipactor breakdown in coaxial transmission lines excited by a single carrier with a digitally modulated signal. Employing an in-house developed code, numerical simulations are performed to determine the RF multipactor voltage threshold for several digitally modulated signals under different modulations schemes: quadrature phase-shift keying, 16-quadrature amplitude modulation, 16-amplitude and phase-shift keying, and 32-amplitude and phase-shift keying. Moreover, a coarse method based on the envelope integration to determine the RF multipactor voltage threshold when involving arbitrary digital modulations is also presented. These results are also compared with the "20-gap-crossing" rule used in the space standard document ECSS-E20-1A. In order to validate the theoretical results, a test campaign was performed for realistic modulated signals, finding good agreement between theoretical predictions and experimental data.

4.7. Multipactor effect in a parallel-plate waveguide partially filled with magnetized ferrite

4.7.1. Bibliography record

- Authors: D. González-Iglesias, B. Gimeno. V. E. Boria, Á. Gómez, A. Vegas
- Publication: IEEE Transactions on Electron Devices, vol. 61, no. 7
- Year: 2014
- Pages: 2552-2557
- Keywords: Ferrite components, multipactor effect, parallel-plate waveguide, radio frequency (RF) breakdown

4.7.2. Abstract

The aim of this paper is the analysis of the multipactor effect in a parallel-plate waveguide when a ferrite slab, transversally magnetized by a static magnetic field parallel to the waveguide walls, is present. Employing an in-house developed code, numerical simulations are performed to predict the multipactor radio frequency voltage

threshold in such a ferrite-loaded waveguide. Variations of the ferrite magnetization field strength and the ferrite slab height are analyzed. Effective electron trajectories are also shown for a better understanding of the breakdown phenomenon, finding different multipactor regimes.

4.8. Analysis of multipactor RF breakdown in a waveguide containing a transversely magnetized ferrite

4.8.1. Bibliography record

- Authors: D. González-Iglesias, Á. Gómez, B. Gimeno, Ó. Fernández, A. Vegas, F. Casas, S. Anza, C. Vicente, J. Gil, R. Mata, I. Montero, V. E. Boria, D. Raboso
- Publication: IEEE Transactions on Electron Devices, vol. 63, no. 12
- Year: 2016
- Pages: 4939-4947
- Keywords: ferrite devices, magnetic field, multipactor effect, parallel-plate waveguide, RF breakdown.

4.8.2. Abstract

In this paper, the multipactor RF breakdown in a parallel-plate waveguide partially filled with a ferrite slab magnetized normal to the metallic plates is studied. An external magnetic field is applied along the vertical direction between the plates in order to magnetize the ferrite. Numerical simulations using an in-house 3-D code are carried out to obtain the multipactor RF voltage threshold in this kind of structures. The presented results show that the multipactor RF voltage threshold at certain frequencies becomes considerably lower than for the corresponding classical metallic parallel-plate waveguide with the same vacuum gap.

Chapter 5

Article list

Publication I

Multipactor in a coaxial line under the presence of an axial DC magnetic field

IEEE Electron Device Letters, vol. 33, no. 5, pp. 727-729, May 2012

Multipactor in a Coaxial Line Under the Presence of an Axial DC Magnetic Field

D. González-Iglesias, A. M. Pérez, S. Anza, J. Vague, B. Gimeno, *Member, IEEE*, V. E. Boria, *Senior Member, IEEE*, D. Raboso, C. Vicente, J. Gil, F. Caspers, *Senior Member, IEEE*, and L. Conde

***Abstract*—The main goal of this letter is the analysis of the multipactor effect within a coaxial waveguide structure when an external axial dc magnetic field is applied. We have designed and manufactured a coaxial waveguide sample that has been immersed within a long solenoid. Numerical and experimental results confirm a significant change in the RF breakdown behavior with regard to the case without the axial dc magnetic field, as well as the existence of single- and double-surface multipactor regimes. Good agreement between theory and experimental data has been found.**

***Index Terms*—Coaxial transmission line, dc magnetic field, multipactor effect, RF breakdown.**

I. Introduction

MULTIPACTOR breakdown is a phenomenon that takes place on devices operating under vacuum conditions and high-power RF electromagnetic fields [1]. The multipactor effect is present in different environments such as satellite passive components used for space communications, klystrons, cyclotrons, and particle accelerators, where it is named electron cloud phenomenon [2]. The multipactor breakdown occurs when the trajectories of free electrons, existing inside the device, are synchronized with the RF electric field. This phenomenon produces an exponential growth of the electron population, generating several negative effects that degrade the device performance.

Multipactor phenomenon has been deeply studied for different kinds of waveguides. In particular, multipactor analysis in coaxial lines has attracted the interest of many researchers [3]–[7]. In this context, the presence of dc magnetic fields has been recently used for the partial or total discharge mitigation, as reported in [8], where the direction of the magnetic field remains in the transverse propagation plane of a coaxial geometry, and in [9] and [10], where an axial magnetic field is inserted within a rectangular waveguide for multipactor suppression.

In this letter, we have studied the effect of an axial dc magnetic field in the multipaction existing within a standard coaxial transmission line. In the first section, we discuss the theoretical model employed for simulations. Next, we have designed, manufactured, and tested a simple coaxial sample, as well as a long solenoid for dc magnetic field generation. An experimental test bed for multipactor detection has been developed. Finally, the comparison between experimental data and theory proves the existence of different multipactor regimes under the presence of an external dc magnetic field.

Manuscript received January 23, 2012; accepted January 31, 2012. Date of publication March 16, 2012; date of current version April 20, 2012. This work was supported in part by the Spanish Government through R&D project TEC2010-21520-C04-01. The review of this letter was arranged by Editor E. A. Gutiérrez-D.

D. González-Iglesias, A. M. Pérez, J. Vague, and V. E. Boria are with the Departamento de Comunicaciones-iTEAM, Universidad Politécnica de Valencia, 46022 Valencia, Spain.

B. Gimeno is with the Departamento de Física Aplicada-ICMUV, Universidad de Valencia, 46100 Valencia, Spain (e-mail: benito.gimeno@uv.es).

S. Anza, C. Vicente, and J. Gil are with AURORASAT, 46022 Valencia, Spain.

D. Raboso is with the European Space Agency/European Space Research and Technology Centre, 2200 AG Noordwijk, The Netherlands.

F. Caspers is with CERN, 1211 Geneva, Switzerland.

L. Conde is with the Departamento de Física Aplicada, E.T.S.I. Aeronáuticos, Universidad Politécnica de Madrid, 28040 Madrid, Spain.

Color versions of one or more of the figures in this letter are available online at http://ieeexplore.ieee.org.

Digital Object Identifier 10.1109/LED.2012.2186952

II. Theory

The commercial FEST3D software [11] was used to perform the simulations of multipactor within the coaxial line. Indeed, this code is based on the 3-D tracking of a set of electrons governed by electric and magnetic external fields. To proceed, the Lorentz force equation is numerically solved by means of the leap-frog algorithm, as described in [12]. The considered fields are the superposition of the time-harmonic electric and magnetic coaxial TEM mode fields of frequency f, and the external axial uniform dc magnetic field B_{DC}. Following the Monte Carlo technique, when an electron hits on the inner or the outer metallic walls, the code allows absorbing the electron or releasing secondary electrons depending on the impact conditions. This is done by using the secondary-electron-yield coefficient δ (SEY) [13] of the material. Thus, the SEY model for copper is described in [14] with a first crossover $W_1 = 25$ eV, $\delta_{\max} = 2.25$, and an incident electron energy value for $\delta_{\max}$ given by $W_{\max} = 175$ eV. A Maxwellian distribution for computing the secondary electrons' velocities has been used, considering a mean of 4 eV and a standard deviation of 2 eV. The multipactor onset criterion used by FEST3D is based on the detection of an exponential growth rate.

III. Experimental Setup

The coaxial sample for multipactor test is shown in Fig. 1. The inner and outer radius dimensions are $a = 1.515$ mm and $b = 3.490$ mm, respectively; the length of the total sample is 90.4 mm. Both conductors were made of copper, and the existing gap between them is $d = b - a = 1.975$ mm.

An external dc magnetic field is applied to the coaxial sample by means of a long solenoid, with dimensions selected to ensure

Fig. 1. Manufactured coaxial sample for multipactor test.

a uniform magnetic field in the central region, where the coaxial sample is inserted. According to these specifications, we have designed and manufactured a solenoid formed by around 8250 turns with 30-cm length and 1.905-cm radius, being its electrical resistance is 71.8 Ω. This solenoid was calibrated by means of a magnetic probe mounted in a translation linear stage, which moves along the axis of symmetry of the solenoid. The linear relation between the solenoid dc current $I_{\rm DC}$ and the magnetic field in the center of the solenoid gives $B_{\rm DC} = 3.8$ mT when $I_{\rm DC} = 100$ mA.

An experiment to validate FEST3D simulations was carried out at the European Space Agency Val Space Consortium Laboratory [15]; the experimental setup is the standard one, commonly employed in multipactor measurements (see [14]). The coaxial sample was placed centered inside the solenoid, and three detection methods were used, i.e., the measurement of nulling between the input and the reflected waves at the carrier frequency, the third-harmonic frequency detection of the transmitted signal, and the measurement of the secondary electrons generated in the discharge with an electron probe. During the measurements, a pressure vacuum chamber was in an interval $10^{-5}-10^{-7}$ mbar.

Measurements were performed at an RF frequency of $f = 1.145$ GHz, which corresponds to a frequency gap of $f \times d = 2.261$ GHz $\cdot$ mm. The RF signal generator operated in pulsed mode with a pulse width of 20 μs and a duty cycle of 2%. An optical fiber connected to an ultraviolet mercury lamp (254 nm) was used to generate photoelectrons, which was inserted into the coaxial sample through a venting hole. Multipactor RF power threshold was measured for several dc magnetic field strengths. Both experimental and theoretical results are shown in Fig. 2.

IV. Discussion

As we can see in Fig. 2, there is good agreement between experimental and computed points. Small differences can be related to the inaccuracy of the SEY model used in the theoretical simulations. According to both experiment and theory, the presence of the dc magnetic field has minimized and maximized the RF power threshold a factor of 84% and 23% in comparison to the zero magnetic field case, respectively.

In order to have a better understanding of the obtained results, electron trajectories have been represented for some significant points, which have been marked in Fig. 2 as A, B, C, D, and E. In Table I, we have summarized the most relevant results, including cyclotron frequency f_c, Larmor radius r_L, and mean SEY value on the inner i and the outer o surfaces. For point A, we find a hybrid double-surface multipactor mode of order 1 for the inner-to-outer conductor path and order 3 for the outer-to-inner case, as shown in Fig. 3. (Note that we define the multipactor order in terms of the number of RF semiperiods.) Due to the presence of the magnetic field, for point B, we have observed a mixing between double- and single-surface multipactor regimes. This effect is due to the increase in the dc magnetic field, which tends to bend the electron orbits around the magnetic field flux lines, as shown in Fig. 3.

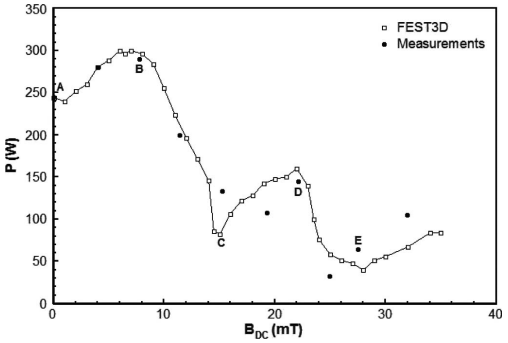

Fig. 2. Multipactor RF input power threshold as a function of the dc magnetic field strength. Experimental and theoretical results are shown. Experimental errors associated with both magnitudes have been estimated in ± 2 W and ± 1 mT, respectively.

TABLE I
Summary of the Results Showed in Fig. 2

Point	B_{DC}(mT)	P(W)	f_c(MHz)	$r_L(\mu m)$	SEY_i	SEY_o
A	0	245	0	∞	2.0	1.1
B	8	290	216	875	2.9	2.9
C	15	86	420	449	1.2	0.5
D	22	145	620	305	0.4	1.1
E	27	65	770	245	2.2	0.9

For point C, the dc magnetic field is strong enough to avoid electrons reaching the opposite conductor so that there are only single-surface orbits, as illustrated in Fig. 3. Indeed, electron trajectories are confined near the conductor where electrons are launched, but the discharge is generated only on the inner wall. Electrons starting around the central region of the gap and near the outer conductor impact on the outer wall with too low kinetic energy values to generate true secondaries; hence, they do not contribute to the discharge (see Table I). However, electrons starting from the inner conductor produce a single-sided multipactor regime of order 4. The variation of the RF electric field of the TEM fundamental mode with $1/r$ (r being the cylindrical radial coordinate) produces an asymmetric behavior in both inner and outer walls, providing more kinetic energy to the electrons emitted from the internal wall than those launched from the external one. Thus, when the RF power is increased above the threshold for the same value of magnetic field, we observe discharges on both surfaces, which enhance multipactor effect in comparison with point C.

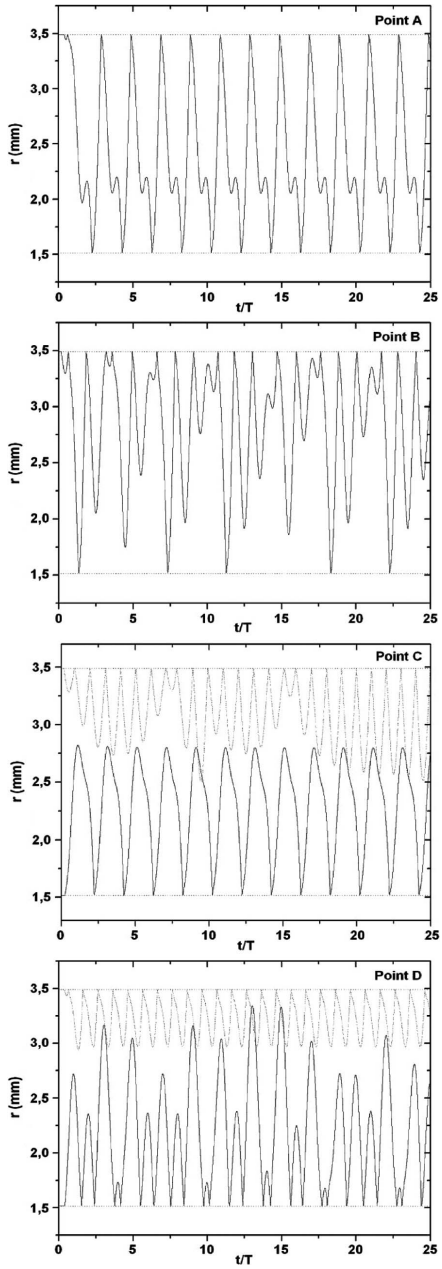

Fig. 3. Electron trajectories of points A, B, C, and D in Fig. 2. The cylindrical radial coordinate of the effective electron r has been plotted as a function of the normalized time t/T, T being the RF period ($T = 1/f$). The inner and outer radii of the coaxial sample have been marked with horizontal lines. In points C and D, the continuous and dashed lines represent an electron launched from the inner and outer walls, respectively.

In the range from point C to point D, we have observed that multipactor cannot occur on the inner wall because of a lack of resonance, as depicted in Fig. 3 for point D. However, a stable single-surface discharge of order 2 can be generated on the outer metal. Thus, the significant local increase in the threshold of point D is again explained in terms of the variation with the radial coordinate of the applied RF electric field.

For point E, a single-surface discharge of order 2 has been found on the inner surface, which directly supposes a reduction of the RF power threshold. In this case, electron dynamics is similar to point C.

V. Conclusion

In this letter, we have studied the multipactor effect in coaxial transmission lines when an external axial dc magnetic field is applied. A significant modification of the RF power threshold as a function of the magnetic field has been observed, finding an increase and a reduction (with regard to the zero magnetic field case) of 23% and 84%, respectively. Simulations performed with commercial software FEST3D have demonstrated the existence of both double- and single-sided multipactor regimes. An experiment has been designed and performed, obtaining good agreement between measurements and theoretical data.

References

[1] J. R. M. Vaughan, "Multipactor," *IEEE Trans. Electron Dev.*, vol. 35, no. 7, pp. 1172–1180, Jul. 1988.

[2] S. De Santis, J. M. Byrd, F. Caspers, A. Krasnykh, T. Kroyer, M. T. F. Pivi, and K. G. Sonnad, "Measurement of electron clouds in large accelerators by microwave dispersion," *Phys. Rev. Lett.*, vol. 100, no. 9, p. 094801, Mar. 2008.

[3] R. Woo, "Multipacting discharges between coaxial electrodes," *J. Appl. Phys.*, vol. 39, no. 3, pp. 1528–1533, Feb. 1968.

[4] E. Somersalo, P. Ylä-Oijala, and D. Proch, "Electron Multipacting in RF Structures," Hamburg, Germany, TESLA Rep. 94-14, Jul. 1994.

[5] T. P. Graves, B. LaBombard, S. Wukitch, and I. Hutchinson, "The coaxial multipactor experiment (CMX): A facility for investigating multipactor discharges," *Rev. Sci. Instrum.*, vol. 77, no. 1, pp. 014701-1–014701-4, Jan. 2006.

[6] R. Udiljak, D. Anderson, M. Lisak, V. Semenov, and J. Puech, "Multipactor in a coaxial transmission line. Part I: Analytical study," *Phys. Plasmas*, vol. 14, no. 3, pp. 033508-1–033508-11, Mar. 2007.

[7] A. M. Pérez, C. Tienda, C. Vicente, S. Anza, J. Gil, B. Gimeno, and V. E. Boria, "Prediction of multipactor breakdown thresholds in coaxial transmission lines for traveling, standing, and mixed waves," *IEEE Trans. Plasma Sci.*, vol. 37, no. 10, pp. 2031–2040, Oct. 2009.

[8] G. Becerra, *Studies of Coaxial Multipactor in Presence of a Magnetic Field*. Cambridge, MA: MIT, May 2007, PSFC/RR-07-6, DOE/ET-54512-359.

[9] R. L. Geng, H. Padamsee, S. Belomestnykh, P. Goudket, D. M. Dykes, and R. G. Carter, "Suppression of multipacting in rectangular coupler waveguides," *Nucl. Instrum. Methods Phys. Res. A, Accel. Spectrom. Detect. Assoc. Equip.*, vol. 508, no. 3, pp. 227–238, Aug. 2003.

[10] A. Henry and Y. Acediran, "Suppression of multipactor breakdown in satellite rectangular waveguides using DC magnetic fields," in *Proc. IC-CAE*, Feb. 2010, vol. 1, pp. 766–770.

[11] FEST3D, ESA/ESTEC, Valencia, Spain, [Online]. Available: www.fest3d.com

[12] S. Anza, C. Vicente, D. Raboso, J. Gil, B. Gimeno, and V. E. Boria, "Enhanced prediction of multipaction breakdown in passive waveguide components including space charge effects," in *Proc. IEEE MTT-S Microw. Symp. Dig.*, 2008, pp. 1095–1098.

[13] J. R. M. Vaughan, "Secondary emission formulas," *IEEE Trans. Electron Dev.*, vol. 40, no. 4, p. 830, Apr. 1993.

[14] Multipaction Design and Test, ECSS-E-20-01A, 2003.

[15] Val Space Consortium-European Space Agency RF High-Power Laboratory, Valencia, Spain. [Online]. Available: www.val-space.com

Publication II

Multipactor mitigation in coaxial lines by means of permanent magnets

IEEE Transactions on Electron Devices, vol. 61, no. 12, pp. 4224-4231, December 2014

Multipactor Mitigation in Coaxial Lines by Means of Permanent Magnets

Daniel González-Iglesias, Antonio M. Pérez, Sergio Anza, Joaquín Vague Cardona, Benito Gimeno, *Member, IEEE*, Vicente E. Boria, *Senior Member, IEEE*, David Raboso, Carlos Vicente, *Member, IEEE*, Jordi Gil, *Member, IEEE*, Fritz Caspers, *Senior Member, IEEE*, and Luis Conde

***Abstract*— The main aim of this paper is the analysis of the feasibility of employing permanent magnets for the multipactor mitigation in a coaxial waveguide. First, the study of a coaxial line immersed in a uniform axial magnetic field shows that multipactor can be suppressed at any RF if the external magnetic field is strong enough. Both theoretical simulations and experimental tests validate this statement. Next, multipactor breakdown of a coaxial line immersed in a hollow cylindrical permanent magnet is analyzed. Numerical simulations show that multipactor can be suppressed in a certain RF range. The performed experimental test campaign demonstrates the capability of the magnet to avoid the multipactor electron multiplication process.**

***Index Terms*— Coaxial waveguide, dc magnetic field, multipactor effect, multipactor mitigation, permanent magnet, RF breakdown.**

I. Introduction

THE multipactor effect is a resonant vacuum electron discharge that appears in components operating with RF high-power electromagnetic fields [1]. This phenomenon is present in many different environments, such as RF satellite payloads, particle accelerators, klystrons, or cyclotrons. When certain conditions are satisfied, the free electrons synchronize with the RF electric field, and impact against the metallic walls releasing secondary electrons. Thus, the increase of the electron population in the device leads to an electrical discharge that degrades the component performance and can physically damage the structure.

This RF breakdown effect has been the subject of a number of studies addressed to designing multipactor-free RF components. Several techniques are applicable for avoiding this undesirable effect, such as chemical polishing, groove insertions in the metal surface, surface coatings, or changes in the gap dimensions. However, surface treatments degrade in time, surface grooves impair the RF performance, and geometrical modifications are unpractical in most microwave components. Recently, some authors proposed the use of dc magnetic fields for the partial or total discharge mitigation. Sometimes, the direction of the applied magnetic field is oriented along the transverse plane for a coaxial geometry [2], while an axial magnetic field is inserted for multipactor suppression in rectangular waveguides [3]–[7].

The multipactor effect in a coaxial line under the presence of a uniform axial static magnetic field was investigated in [8]. These results evidence that RF power thresholds (the lowest RF power value at which the multipactor discharge appears) are strongly influenced by the magnitude of the magnetic field. These results were obtained for a fixed RF. In this paper, we extend this previous study by analyzing the effect of the RF signal, as well as the magnetic field strength. As we shall see, the total suppression of multipactor breakdown can be obtained regardless of the RF signal frequency for magnetic field strengths over a onset. In addition, we discuss about the feasibility of multipactor suppression by means of the realistic nonuniform magnetic field pattern of neodymium permanent magnets.

This paper is structured as follows. Section II-A describes the physical model used in our simulation code to perform the numerical calculations of multipactor breakdown. In Section II-B, we derive analytical expressions for the magnetic field strength produced by a magnetized hollow cylinder. Section III-A analyzes the effect of a uniform dc magnetic field on the multipactor power threshold showing both theoretical simulations and experimental results. Next, in Section III-B, the implementation of a nonuniform magnetic field along the coaxial line by means of a hollow neodymium magnet is investigated. According to the required specifications, a neodymium magnet has been designed and manufactured to carry out experimental tests to validate the theoretical results. Finally, the conclusion is drawn in Section IV.

Manuscript received June 12, 2014; revised July 30, 2014, September 4, 2014, and September 11, 2014; accepted September 26, 2014. Date of publication October 16, 2014; date of current version December 9, 2014. This work was supported by the European Regional Development Fund—A Way of Making Europe. The review of this paper was arranged by Editor R. Carter.

D. González-Iglesias and B. Gimeno are with the Department of Applied Physics, Institute of Materials Science, University of Valencia, Valencia 46010, Spain (e-mail: daniel.gonzalez-iglesias@uv.es; benito.gimeno@uv.es).

A. M. Pérez, J. V. Cardona, and V. E. Boria are with the Departamento de Comunicaciones-iTEAM, Universidad Politécnica de Valencia, Valencia 46021, Spain (e-mail: antonio.perez@uv.es; jvague@dcom.upv.es; vboria@dcom.upv.es).

S. Anza, C. Vicente, and J. Gil are with AURORASAT, Valencia 46022, Spain (e-mail: sergio.anza@aurorasat.es; carlos.vicente@aurorasat.es; jordi.gil@aurorasat.es).

D. Raboso is with the European Space Research and Technology Centre, European Space Agency, Noordwijk 2201 AZ, The Netherlands (e-mail: david.raboso@esa.int).

F. Caspers is with the European Organization for Nuclear Research, Geneva CH-1217, Switzerland (e-mail: fritz.caspers@cern.ch).

L. Conde is with the Department of Applied Physics, E.T.S.I. Aeronáuticos, Technical University of Madrid, Madrid 28040, Spain (e-mail: luis.conde@upm.es).

Digital Object Identifier 10.1109/TED.2014.2361172

II. THEORY

A. Multipactor Algorithm

In this paper, we use a Monte Carlo code to perform the simulations of multipactor in coaxial transmission lines using the traditional single effective electron model [10], [11]. This technique is based on the 3-D tracking of a set of effective electrons governed by the electromagnetic field. The trajectory of the effective electron is found numerically solving its equation of motion (expressed in Cartesian coordinates) by means of the velocity Verlet algorithm [12]. Each effective electron describes a particular electronic population that evolves in time by colliding with the coaxial metallic walls of the waveguide. The secondary electron yield (SEY) function (δ) is computed after each impact as a function of the impact kinetic energy and impinging angle by means of the SEY model formulated in [13] and [14]. After that, the colliding electron is reemitted from the impact place with random initial velocity given by a Maxwellian distribution with a mean average energy of 3 eV. The velocity launching angle is given by the cosine law [15].

The total driving electromagnetic field experienced on each effective electron is the sum of three contributions: 1) the excited RF fields; 2) the electric field due to the Coulombian repulsion among electrons; and 3) an applied external dc magnetic field. The excited RF fields are those related to the fundamental mode of the coaxial guide at frequency f. The electric field caused by the electron cloud is modeled by means of a single electron sheet, following the same procedure proposed in [16]. Two different kinds of external dc magnetic field will be considered in this paper. First, in Section III-A, a uniform magnetic field is oriented along the axial direction of the coaxial line. Second, in Section III-B, the coaxial sample is immersed into a hollow cylindrical permanent magnet. In this case, the nonuniform magnetic field has radial and axial components.

The effective electron dynamics is governed by the nonrelativistic Lorentz force expression leading to [17]

$$\frac{dv_r}{dt}=\frac{d^2r}{dt^2}-r\left(\frac{d\phi}{dt}\right)^2=-\frac{e}{m}\left[E_{\mathrm{RF}}(\vec{r},t)+E_{sc}(\vec{r},t) -+B_{\mathrm{RF}}(\vec{r},t)\,v_z+B_{\mathrm{ext},z}(\vec{r})\,v_\phi\right] \tag{1}$$

$$\frac{dv_\phi}{dt}=r\frac{d^2\phi}{dt^2}+2\frac{dr}{dt}\frac{d\phi}{dt}=-\frac{e}{m}\left[-B_{\mathrm{ext},z}(\vec{r})\,v_r+B_{\mathrm{ext},r}(\vec{r})\,v_z\right] \tag{2}$$

$$\frac{dv_z}{dt}=\frac{d^2z}{dt^2}=-\frac{e}{m}\left[-B_{\mathrm{ext},r}(\vec{r})\,v_\phi+B_{\mathrm{RF}}(\vec{r},t)\,v_r\right] \tag{3}$$

where $-e$ and m are the electron charge and electron mass at rest, respectively; $\vec{r}$ is the vector position, t is the time, and $(r,\ \phi,\ z)$ are the cylindrical coordinates; $(v_r\ =\ dr/dt,\ v_\phi\ =\ r\,(d\phi/dt),\ v_z\ =\ dz/dt)$ are the corresponding components of the electron velocity; $\vec{E}_{\mathrm{sc}}=E_{\mathrm{sc}}\,\hat{r}$ is the electric field that considers the space charge effect; $\vec{E}_{\mathrm{RF}}=E_{\mathrm{RF}}\,\hat{r}$ and $\vec{B}_{\mathrm{RF}}=B_{\mathrm{RF}}\,\hat{\phi}$ are the electric and magnetic fields of the TEM coaxial mode; and $\vec{B}_{\mathrm{ext}}\ =\ B_{\mathrm{ext},r}\,\hat{r}\ +\ B_{\mathrm{ext},z}\,\hat{z}$ is the external magnetic field.

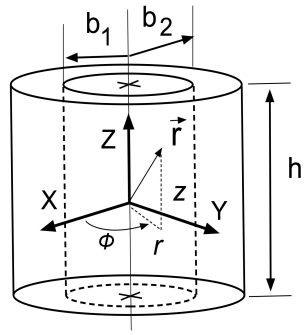

Fig. 1. Scheme of the hollow magnet with height h, and b_1 and b_2 radii.

B. Magnetic Field Produced by a Hollow Cylindrical Magnet

In this section, we present the procedure to compute the magnetic field of an homogenously magnetized hollow cylinder in terms of the expressions of a simple homogenously magnetized cylinder. In Fig. 1, the magnetized hollow cylinder under consideration is shown, whose dimensions are b_1 and b_2 for the inner and outer radius of the cylinder, respectively, and h is the height. As indicated, the reference frame is centered in the midheight of the cylinder.

First of all, we are going to present the magnetic field generated by a uniform cylinder with radius r_0. Static magnetic field of a homogenously magnetized cylinder can be derived using the equivalent volume and surface currents [18] determined as $\vec{J}_M\ =\ \nabla\times\vec{M}$ and $\vec{K}_M\ =\ \vec{M}\times\vec{n}$, with $\vec{J}_M$ and $\vec{K}_M$ being the volume and the surface currents, respectively, $\vec{n}$ the unitary vector normal to the surface, and $\vec{M}=M\hat{z}$ the volume magnetization. Once the equivalent currents are obtained, the static magnetic field inside and outside the magnet can be calculated by means of the Ampere's law [18], resulting in the following expressions:

$$B_r(r,z)=\frac{\mu_0 M}{4\pi}\sqrt{\frac{16\,r_0}{r}}\left[\frac{E(k_2)}{k_2}-\frac{E(k_1)}{k_1}+\frac{1}{k_1^2}\left(1-\frac{k_1^2}{2}\right)\times K(k_1)-\left(1-\frac{k_2^2}{2}\right)K(k_2)\right] \tag{4}$$

$$B_z(r,z)=\frac{\mu_0\,M}{2\pi\sqrt{r\,r_0}\left(1+\frac{r}{r_0}\right)^2}\left[\left(z+\frac{h}{2}\right)k_2\Pi\,(k_2,\sigma) +-\left(z-\frac{h}{2}\right)k_1\Pi\,(k_1,\sigma)\right]-\frac{r}{r_0}B_r(r,z) \tag{5}$$

$$\sigma\equiv\frac{4\,r\,r_0}{(r+r_0)^2}$$

$$k_1\equiv\sqrt{\frac{4\,r\,r_0}{(r+r_0)^2+\left(z-\frac{h}{2}\right)^2}}$$

$$k_2\equiv\sqrt{\frac{4\,r\,r_0}{(r+r_0)^2+\left(z+\frac{h}{2}\right)^2}}$$

where μ_0 is the magnetic permeability of vacuum; $K(k)$, $E(k)$, and $\Pi(k,\sigma)$ are the complete elliptic integrals of the first, the

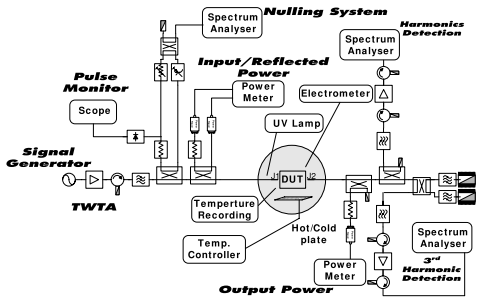

Fig. 2. Standard setup used for multipactor measurements. In our experiment, three detection methods were employed: nulling system, third harmonic detection, and electron probe. Pressure was in an interval 10^{-5}–10^{-7} mbar during the experiments. RF signal generator operated in pulsed mode with a pulsewidth of 20 μs and a duty cycle of 2%.

second, and the third kind, respectively [19]. Note that the azimuthal magnetic field component is zero due to symmetry.

Finally, magnetic field expression for a hollow cylinder can be obtained by considering the superposition of the magnetic fields generated by two homogeneously magnetized cylinders with different radii, the same magnetization strength, and opposite magnetization direction.

III. Simulation and Experimental Results

A. Uniform Static Axial Magnetic Field

The coaxial dimensions for multipactor simulations, as well as the testing sample, are as those employed in [8]. The experimental setup is the standard one and commonly employed in multipactor measurements, which is shown in Fig. 2 (for a full detailed description [9]). The inner and outer radius dimensions are $a = 1.515$ mm and $b = 3.490$ mm, respectively, the gap length is $d = b - a = 1.975$ mm, the characteristic impedance is $Z_0 = 50\ \Omega$, and the length of the total sample is 90.4 mm. Both conductors were made of copper, with the following SEY parameters: first crossover $W_1 = 25$ eV, the maximum SEY coefficient $\delta_{\max} = 2.25$, and an incident electron energy for $\delta_{\max}$ given by $W_{\max} = 175$ eV. The uniform static axial magnetic field is applied by means of a long solenoid, where the sample is inserted.

The theoretical results show that multipactor resonant electron trajectories are disturbed by the presence of an external uniform axial dc magnetic field [8]. In this case, the equations of motion of the effective electron are simplified since $B_{\text{ext},r} = 0$. The effect of such an axial magnetic field in the electron motion is the appearance of an azimuthal acceleration in (2). This component of the acceleration bends the electron trajectories around the magnetic field flux lines, pushing the electron back to the departure conductor, allowing the presence of single-surface multipactor modes. Thus, the external magnetic field influences the electron flight time between successive impacts with the coaxial walls. In the numerical simulations, it has been found that the ratio between the cyclotron frequency $f_c = (eB_{\text{dc}})/(2\pi m)$ and the frequency of the RF electromagnetic field plays a crucial role in the multipactor behavior, as reported in [4]. Fig. 3 reproduces this effect, where the multipactor RF power thresholds against the ratio of the cyclotron frequency to the microwave frequency are represented. The theoretical results predict that no multipactor discharge occurs when the ratio f_c/f exceeds a certain limit that varies depending on the RF signal frequency. For the investigated range, the numerical calculations show that this critical quotient is within the range $f_c/f \in [0.7, 1]$. It should be remarked that the analyzed RF range is wide enough to cover the most suitable frequency gap zone for the multipactor discharge.

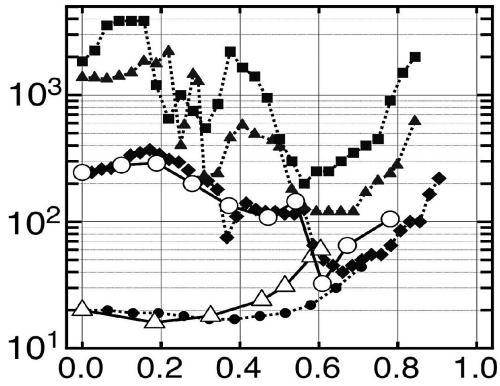

Fig. 3. Comparison of the experimental multipactor power threshold levels in watts (solid lines) with the numerical simulations (dashed lines) against the ratio f_c/f. Numerical simulations: $f = 0.435$ GHz, solid circle; $f = 1.145$ GHz, solid diamond; $f = 2.000$ GHz, solid triangle; and $f = 3.000$ GHz, solid square. Experimental data: $f = 0.435$ GHz, open triangle, and $f = 1.145$ GHz, open circle. It covered the f_c/f range where multipactor is expected to trigger.

Multipactor mitigation phenomenon can be understood in terms of the electron resonant trajectories. The classical theory of multipactor states that the time between two successive impacts must be an odd (even) number of RF semiperiods for double (single) surface multipactor modes. In numerical simulations, it has been found that the electron flight time between successive impacts decreases as the ratio f_c/f increases. If the flight time is too short, the electron will never be able to synchronize with the RF electric field and, consequently, the electron kinetic energy at the impacts will be too low to release secondaries. In [8], the case of $f = 1.145$ GHz in Fig. 3 was analyzed by examining the electron trajectories at some relevant points of the multipactor power threshold curve. It was found that as the external axial magnetic field increases for a fixed RF (i.e., the ratio f_c/f grows), the multipactor order diminishes. Moreover, the applied magnetic field introduces single-sided multipactor modes. According to classical resonance modes, the lower multipactor single-surface order possible is two. If the ratio f_c/f is such that the flight time of the electron is below two RF semiperiods, the resonance between the electron and the RF electric field cannot be achieved, and consequently, no multipactor discharge is possible.

Experimental measurements were performed at RFs of $f = 1.145$ GHz and $f = 0.435$ GHz to validate the previous

TABLE I
MEASURED POINTS FOR $f = 1.145$ GHz WHERE NO MULTIPACTOR DISCHARGE WAS FOUND UP TO P_{Max}

B_{DC} (mT)	f_c/f	P_{max} (W)
34.25	0.837	1450
37.56	0.918	1450
68.43	1.673	1450

TABLE II
MEASURED POINTS FOR $f = 0.435$ GHz WHERE NO MULTIPACTOR DISCHARGE WAS FOUND UP TO P_{Max}

B_{DC} (mT)	f_c/f	P_{max} (W)
10.0	0.644	120
11.5	0.710	120
13.3	0.856	120
14.8	0.952	120
15.2	0.978	120
18.9	1.216	120

theoretical simulations. These results are shown in Fig. 3 together with the theoretical ones. It should be mentioned that although some experimental measurements for $f = 1.145$ GHz were previously presented in [8], new measurements have been performed to explore the multipactor-free zone for higher f_c/f values. These new measurements are summarized in Table I, where the magnitude of the static axial magnetic field B_{DC}, the corresponding ratio f_c/f, and the maximum level of RF input power available in the experimental test-bed P_{max} are indicated. No multipactor discharge was found up to P_{max}, as well as in Table II for $f = 0.435$ GHz. Two additional checks were performed at $f = 0.435$ GHz to confirm that large f_c/f ratios hinder the multipactor breakdown. First, the RF input power was fixed at 60 W, and the axial magnetic field was ranged from 8.9 mT ($f_c/f = 0.572$) to 19.0 mT ($f_c/f = 1.223$). Second, the RF input power was fixed at 120 W, and the axial magnetic field was swept from 15.1 mT ($f_c/f = 0.972$) to 57.0 mT ($f_c/f = 3.668$). No multipactor discharge was observed in any of the two aforementioned tests.

Our experimental data and numerical calculations are in good agreement and suggest that electron multiplication is precluded over an f_c/f threshold. This fact proves the multipactor discharge suppression by a uniform dc magnetic field along the waveguide axis. However, small discrepancies exist between the theoretical values and the experimental f_c/f thresholds that delimit the multipactor-free domain. These small discrepancies between the experimental data and numerical simulations would be basically caused by the inaccuracy of the SEY model as well as the assumed velocity distribution for the secondary electrons.

B. Nonuniform Magnetic Field

The results discussed in the previous section evidence that a strong enough magnetic field prevents the multipactor multiplication in coaxial lines. However, the experimental implementation that requires heavy coils and power supplies is unpractical in most cases [8]. Alternatively, the multipactor breakdown might be attenuated or mitigated using the inhomogeneous magnetic field produced by a set of permanent magnets. To explore this possibility, the coaxial sample was introduced into a hollow cylindrical neodymium permanent magnet. Its magnetization and dimensions were determined to hinder the multipactor multiplication within the required microwave frequency range.

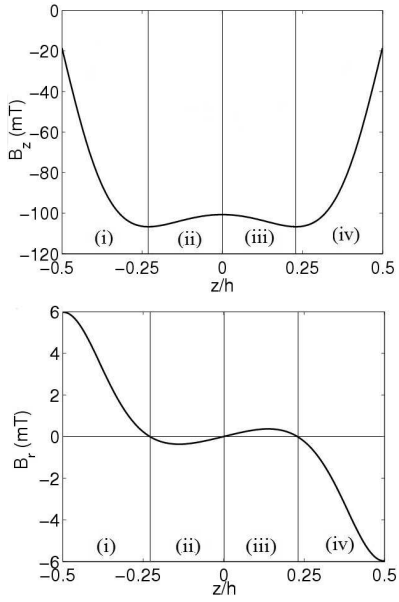

Fig. 4. Axial B_z and radial B_r components of Fig. 1 given by (4) and (5) as a function of the normalized coordinate z/h. The value of the radial cylindrical coordinate has been chosen in the center of the coaxial gap, $r = 2.044$ mm. Magnet dimensions and properties: $b_1 = 12.5$ mm, $b_2 = 16.5$ mm, $h = 44$ mm, and $M = 1.153 \times 10^6$ A/m.

In our case, the inner and outer coaxial radii are $a = 1.238$ mm and $b = 2.850$ mm, respectively, the gap between conductors is $d = b - a = 1.612$ mm, the characteristic impedance is $Z_0 = 50\,\Omega$, and the sample length is 41.0 mm. Both conductors were made of copper, with the following SEY parameters: $W_1 = 19.5$ eV, $\delta_{\text{max}} = 2.61$, and $W_{\text{max}} = 219.7$ eV.

The inner radius was selected to hold inside the coaxial sample leaving an small gap to allow the outgassing of the system. Later, a parametrical study was performed to study the effect of the variation of the outer radius in the magnetic field structure. The main effect of increasing the cylinder thickness (for a fixed magnetization value) is to enlarge the strength of the magnetic field inside the gap of the magnet. In our case, a thickness in the range 2–4 mm is desirable (the minimum thickness is 2 mm due to manufacturing considerations). Therefore, the inner and outer radii for our prototype were $b_1 = 12.5$ mm and $b_2 = 16.5$ mm. In Fig. 4, the axial and radial magnetic field components of a hollow cylindrical magnet are represented,

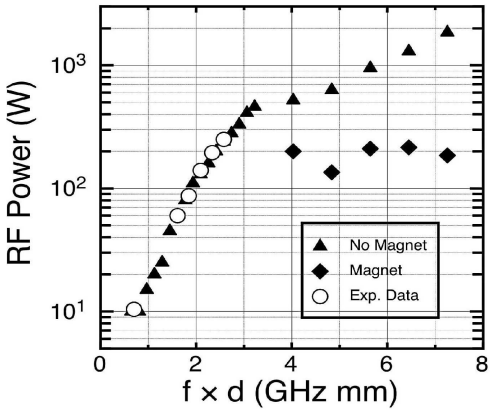

Fig. 5. Comparison of the numerical calculations (solid symbols) with the experimental data (open symbols) without external magnetic field. The RF power thresholds are represented against the frequency gap (gap remains fixed). Note that multipactor discharge was not experimentally detected in the presence of the permanent magnet in the explored frequency range.

as a function of the axial coordinate normalized to the magnet height, using the expressions derived in Section II-B. It is seen that the axial (radial) magnetic field component is symmetrical (antisymmetrical) with respect to the plane $z = 0$. Moreover, it is also noticed that the axial magnetic field presents a local minimum (in absolute value) in the center of the magnet. When we move toward the magnet edge, there is a local maximum and then the strength drops to zero. As shown in Section III-A, the higher the axial component B_z is, the better multipactor suppression is achieved. As a consequence, it is desirable that the axial magnetic field over the coaxial sample is as high as possible. It is evident that a long magnet would provide a very high homogeneous central magnetic field region, but in practical implementation, this prototype might disturb other microwave components and electronic circuits surrounding the coaxial sample. Thus, we have preferred to design a permanent magnet with the minimum height. To achieve that, the coaxial waveguide center must be axially aligned with the magnet geometrical center, since the highest axial magnetic field is reached approximately in the region described by $z/h \in [-0.3, 0.3]$, and it becomes weaker as we approach to the magnet edges. To avoid these low axial magnetic field zones, the magnet height is selected to be 5%–10% higher than the coaxial length. Finally, the height of the magnet has been chosen to be $h = 44$ mm.

In Fig. 5, the multipactor RF input power threshold as a function of the frequency gap (gap remains fixed) is plotted for two configurations of the coaxial waveguide just described in this section. The first configuration corresponds to the coaxial line without the magnet; the second case is for the coaxial waveguide immersed in the neodymium magnet. These numerical calculations evidence the multipactor mitigation within a certain frequency gap range using the permanent magnet. The magnet inhibits the discharge below $f \times d = 4.030$ GHz $\cdot$ mm ($f = 2.5$ GHz), which corresponds to $f_c/f = 1.12$ (f_c has been calculated in $z = 0$, $r = (b-a)/2$, and the coaxial gap point where the axial magnetic field is maximum). It should be mentioned that multipactor appears above such frequency gap value with an RF power threshold lower than for the case without magnet. This fact is due to the appearance of single-surface multipactor mode that may have a multipactor threshold even lower than the classical double-surface multipactor resonance [8], [20].

Despite the nonuniform magnetic field, the multipactor threshold for a coaxial waveguide immersed in a hollow cylindrical magnet is similar to those of that in Section III-A. Next, we analyze the electron trapping in the waveguide under the inhomogeneous magnetic field. First, from Fig. 4, the radial component $B_r \ll B_z$ and therefore the axial magnetic field strength B_z is dominant for the electron motion. This fact allows to neglect the term $B_{\text{ext},r}\, v_z$ with respect to $B_{\text{ext},z}\, v_r$ in (2). In addition, for the considered RF power range, the microwave magnetic field B_{RF} is also negligible compared with B_z. Thus, the terms $v\, B_{\text{RF}}$ could be dropped from 1 and 3. Typical values of the aforementioned terms obtained in the numerical simulations are $B_{\text{ext},r}\, v \sim 10^4$ T m/s, $B_{\text{ext},z}\, v \sim 10^5$ T m/s, and $v\, B_{\text{RF}} \sim 10^3$ T m/s. Equations (1)–(3) for the earlier stages of the electron multiplication become

$$\frac{dv_r}{dt} \approx -\frac{e}{m}[E_{\text{RF}}(\vec{r}, t) + B_{\text{ext},z}(\vec{r})\, v_\phi] \tag{6}$$

$$\frac{dv_\phi}{dt} \approx \frac{e}{m} B_{\text{ext},z}(\vec{r})\, v_r \tag{7}$$

$$\frac{dv_z}{dt} \approx \frac{e}{m} B_{\text{ext},r}(\vec{r})\, v_\phi. \tag{8}$$

For this electron trapping argumentation, we do not consider the electron acceleration caused by the microwave electric field. For this situation [21], the electron trajectories are found to spin around magnetic field lines with an angular frequency of $\vec{\omega}_c = (e/m)\vec{B}$. If the axial magnetic field is oriented along the $-z$-direction, the electron will spin clockwise leading to $v_\phi < 0$ since $v_\phi = r\,(d\phi/dt)$ (and $d\phi/dt < 0$ for clockwise rotation). Despite the presence of the RF electric field in our case, we can assume that the electron will still spin with $v_\phi < 0$. As a consequence, the axial acceleration approximated by (8) will be positive or negative depending only on the value of B_r. If $B_r > 0$, then $B_r\, v_\phi < 0$ and $dv_z/dt < 0$. Otherwise, if $B_r < 0$, then $B_r\, v_\phi > 0$ and $dv_z/dt > 0$. As it can be noted from observing Fig. 4, the radial magnetic field has zeros at the points $z = -z_c$, $z = 0$, and $z = z_c$. According to this, we can delimit four regions for the axial electron cynematics as follows:

1) $z < -z_c$, $B_r > 0$, $(dv_z/dt) < 0$;
2) $-z_c < z < 0$, $B_r < 0$, $(dv_z/dt) > 0$;
3) $0 < z < z_c$, $B_r > 0$, $(dv_z/dt) < 0$;
4) $z > z_c$, $B_r < 0$, $(dv_z/dt) > 0$.

Thus, an electron starting from zone 1) will be pushed toward $-z$, and will eventually leave the coaxial waveguide inhibiting the multipactor discharge. However, if the electron is initially in region 2), it will be pushed toward $+z$, and may reach region 3). Now, in zone 3), the electron will be

accelerated toward $-z$, back to zone 2). It is clear that an electron starting from zone 2) will tend to move between zones 2) and 3) indefinitely, and therefore, it will remain inside the coaxial line. Similar argumentation applies for an electron starting in region 3). Finally, an electron initially placed in zone 4) will be pushed toward $+z$ and will eventually leave the coaxial waveguide. In these conditions, only electrons starting from regions 2) and 3) will contribute to the multipactor discharge. This point is crucial since, if no radial magnetic field was present, multipactor would appear in regions 1) and 4) at lower RF than in regions 2) and 3) [this is because the axial magnetic field is weaker in zones 1) and 4) than in regions 2) and 3)], and thus the multipactor mitigation efficiency would be reduced. This fact is explained in accordance to the analysis of the uniform magnetic field in Section III-A. The multipactor mitigation takes place when the empirical condition $f_c/f > [0.7, 1]$ is roughly fulfilled. If we take the worst case in the previous condition, we have that the multipactor should be mitigated for RFs below f_c. In our case, the lowest axial magnetic field in regions 2) and 3) (in absolute value) is 100 mT (Fig. 4), which gives a cyclotron frequency of $f_c = 2.8$ GHz ($f \times d = 4.5$ GHz $\cdot$ mm). By inspecting Fig. 5, it is noted that in fact no multipactor discharge is expected for RFs below $f = 2.5$ GHz ($f \times d = 4.0$ GHz $\cdot$ mm). However, in regions 1) and 4), the axial magnetic fields are lower than in regions 1) and 3). Actually, the axial magnetic field in the borders of the coaxial waveguide is around 40 mT, which gives $f_c = 1.1$ GHz. Therefore, if the radial magnetic field was not present to expel the electron from the coaxial waveguide, multipactor would appear for RFs above $f = 1.1$ GHz ($f \times d = 1.77$ GHz $\cdot$ mm), which is not the case.

We assessed this analysis by inspecting typical electron trajectories calculated in the numerical simulations of the multipactor breakdown. The microwave frequency was fixed within the multipactor mitigation range, and electrons were launched from different axial initial positions. It was found that an electron released from zone 1), it was pushed out of the coaxial waveguide in few RF periods. It is also noted that the growth rate in time of the electron population in the simulations is low enough to prevent the multipactor breakdown. On the other hand, if an electron starts its movement near the axis center, it remains within the central region, as discussed before. Although the electron does not leave the waveguide, the cumulative population quickly diminishes, so no multipactor discharge occurs.

Finally, the numerical simulations of Fig. 5 were assessed against a set of experimental tests. Coaxial and magnet properties are the same as described above in this section. The experimental setup for multipactor measurements is similar to that described in Section III-A. The multipactor breakdown was detected without the permanent magnet within the P-band test at $f = 0.435$ GHz ($f \times d = 0.701$ GHz $\cdot$ mm). These results are shown in Fig. 5 and are in agreement with the theoretical predictions. On the contrary, no electron multiplication was detected when the coaxial sample was placed inside the hollow magnet up to the maximum RF power available of 100 W. The second test series were carried out within the L-band for the frequencies: $f = 1.0$ GHz ($f \times d = 1.612$ GHz $\cdot$ mm), $f = 1.145$ GHz ($f \times d = 1.845$ GHz $\cdot$ mm), $f = 1.3$ GHz ($f \times d = 2.096$ GHz $\cdot$ mm), $f = 1.45$ GHz ($f \times d = 2.337$ GHz $\cdot$ mm), and $f = 1.6$ GHz ($f \times d = 2.579$ GHz $\cdot$ mm). Again, the multipactor discharges trigger for RF power levels in agreement with the theoretical simulations, as evidenced from the results of Fig. 5. When the magnet is present, no multipactor breakdown appeared (in this case, the maximum available RF input power was 360 W), in good concordance with the theory. Despite that theoretical simulations explore frequency values up to 4.96 GHz (8 GHz $\cdot$ mm, Fig. 5), the return losses of the coaxial sample increase at RF frequencies above the L-band. If the return loss increases, we will have a considerable fraction of the input RF power being reflected by the coaxial sample, and as a consequence, the RF amplifier might be damaged during the multipactor test. To avoid this, the frequency range of the multipactor measurements presented is restricted to P-band and L-band, both in the magnet and without magnet configurations.

IV. Conclusion

In this paper, we have studied the possible mitigation of the multipactor discharge in coaxial waveguides by means of an external magnetic field. First, we have analyzed the most simple scenario of a coaxial line immersed into an axial static magnetic field. The numerical simulations evidence that no multipactor discharge triggers when a strong enough external magnetic field is applied. Our experimental results are in good agreement with the theoretical calculations. Next, we have analyzed the case of a coaxial line immersed in a hollow cylindrical magnet. The multipactor simulations predicted the suppression of the discharge for RFs below a certain value that depends on the specific magnetic field properties. Finally, a strong magnetized neodymium magnet was designed and manufactured. A multipactor test campaing was performed to validate the theoretical results. The experimental measurements in P-band and L-band are in good agreement with the simulations, demonstrating the capability of permanent magnets for multipactor suppression.

References

[1] J. Vaughan, "Multipactor," *IEEE Trans. Electron Devices*, vol. 35, no. 7, pp. 1172–1180, Jul. 1988.

[2] G. Becerra, "Studies of coaxial multipactor in presence of a magnetic field," M.S. thesis, Dept. Nucl. Sci. Eng., MIT, Cambridge, MA, USA, Dissertation nos. PSFC/RR-07-6, DOE/ET-54512-359, May 2007.

[3] R. L. Geng, H. Padamsee, S. Belomestnykh, P. Goudket, D. M. Dykes, and R. G. Carter, "Suppression of multipacting in rectangular coupler waveguides," *Nucl. Instrum. Methods Phys. Res. A, Accel., Spectrometers, Detectors Assoc. Equip.*, vol. 508, no. 3, pp. 227–238, 2003.

[4] V. E. Semenov *et al.*, "Reduction of the multipactor threshold due to electron cyclotron resonance," *IEEE Trans. Plasma Sci.*, vol. 40, no. 11, pp. 3062–3069, Nov. 2012.

[5] S. Riyopoulos, D. Chernin, and D. Dialetis, "Theory of multipactor in crossed fields," *Phys. Plasmas*, vol. 2, no. 8, pp. 3194–3212, Aug. 1995.

[6] E. C. A. Akoma Henry, D. A. Ogundele, O. Agboola, and Y. A. Adediran, "Matlab analysis of the DC magnetic fields multipactor suppression model for rectangular waveguides," in *Proc. 3rd Int. Conf. Adv. Comput. Theory Eng. (ICACTE)*, vol. 4. Aug. 2010, pp. V4-97–V4-101.

[7] A. Henry and Y. Acediran, "Suppression of multipactor breakdown in satellite rectangular waveguides using DC magnetic fields," in *Proc. 2nd Int. Conf. Comput. Autom. Eng. (ICCAE)*, vol. 1. Feb. 2010, pp. 766–770.
[8] D. Gonzalez-Iglesias *et al.*, "Multipactor in a coaxial line under the presence of an axial DC magnetic field," *IEEE Electron Device Lett.*, vol. 33, no. 5, pp. 727–729, May 2012.
[9] *Multipaction Design and Test*, document Rec. ECSS-E-20-01A, 2003.
[10] E. Somersalo, P. Ylä-Oijala, D. Proch, and J. Sarvas, "Computational methods for analyzing electron multipacting in RF structures," *Particle Accel.*, vol. 59, pp. 107–141, Aug. 1998.
[11] A. M. Pérez *et al.*, "Prediction of multipactor breakdown thresholds in coaxial transmission lines for traveling, standing, and mixed waves," *IEEE Trans. Plasma Sci.*, vol. 37, no. 10, pp. 2031–2040, Oct. 2009.
[12] L. Verlet, "Computer 'experiments' on classical fluids. I. Thermodynamical properties of Lennard-Jones molecules," *Phys. Rev.*, vol. 159, no. 1, pp. 98–103, Jul. 1967
[13] C. Vicente *et al.*, "Multipactor breakdown prediction in rectangular waveguide based components," in *IEEE MTT-S Int. Microw. Symp. Dig.*, pp. 1055–1058, Jun. 2005.
[14] R. Vaughan, "Secondary emission formulas," *IEEE Trans. Electron Devices*, vol. 40, no. 4, pp. 830–839, Apr. 1993.
[15] J. Greenwood, "The correct and incorrect generation of a cosine distribution of scattered particles for Monte-Carlo modelling of vacuum systems," *Vacuum*, vol. 67, no. 2, pp. 217–222, Sep. 2002.
[16] T. P. Graves, "Experimental investigation of electron multipactor discharges at very high frequency," Ph.D. dissertation, Dept. Nucl. Sci. Eng., MIT, Cambridge, MA, USA, 2006.
[17] J. W. Gewartowski and H. A. Watson, *Principles of Electron Tubes: Including Grid-Controlled Tubes, Microwave Tubes, and Gas Tubes*. Princeton, NJ, USA: Van Nostrand, 1965.
[18] D. J. Griffiths, *Introduction to Electrodynamics*, 3rd ed. London, U.K.: Pearson, 2008.
[19] M. Abramowitz and I. Stegund, *Handbook of Mathematical Functions With Formulas, Graphs, and Mathematical Tables*. New York, NY, USA: Dover, 1972.
[20] D. González-Iglesias, B. Gimeno, V. E. Boria, A. Gomez, and A. Vegas, "Multipactor effect in a parallel-plate waveguide partially filled with magnetized ferrite," *IEEE Trans. Electron Devices*, vol. 61, no. 7, pp. 2552–2557, Jul. 2014.
[21] R. K. Wangsness, *Electromagnetic Fields*, 2nd ed. New York, NY, USA: Wiley, 1986.

Daniel González-Iglesias received the Licenciado degree in physics and the master's degree in advanced physics from the University of Valencia, Valencia, Spain, in 2010 and 2011, respectively, where he is currently pursuing the Ph.D. degree in physics.

His current research interests include multipacting simulation of RF high-power passive components.

Antonio M. Pérez was born in Valencia, Spain, in 1977. He received the Degree in Physics from the University of Valencia, Valencia, in 2001.

He received a fellowship through the European Union at the Universita degli Studi di Pavia, Pavia, Italy, as a Researcher in 2003. Since 2005, he has been a Researcher with the Department of Communications, Universidad Politécnica de Valencia, Valencia.

Sergio Anza was born in Madrid, Spain, in 1978. He received the B.S. degree in telecommunications engineering from the Universidad Politécnica de Valencia, Valencia, Spain, in 2002.

His current research interests include theoretical and numerical techniques of nonlinear phenomena in RF high-power devices for space applications, as multipactor effect.

Joaquín Vague Cardona was born in Valencia, Spain, in 1979. He received the Electronics Engineering degree from the Universidad Politécnica de Valencia (UPV), Valencia, Spain, in 2003.

He is currently a Technical Researcher in charge of several laboratories with the Department of Communications, UPV.

Benito Gimeno (M'01) received the Licenciado degree in physics and the Ph.D. degree from the University of Valencia, Valencia, Spain, in 1987 and 1992, respectively.

He became a Full Professor at the University of Valencia in 2010. His current research interests include the electromagnetic analysis and design of microwave passive components and RF breakdown high-power effects.

Vicente E. Boria (S'91–A'99–SM'02) received the Ph.D. degree in telecommunications engineering from the Universidad Politécnica de Valencia, Valencia, Spain, in 1997.

He is currently a Full Professor with the Universidad Politécnica de Valencia. His current research interests include the electromagnetic analysis and design of microwave passive components and RF breakdown high-power effects.

David Raboso was born in Alcázar de San Juan, Spain, in 1967. He received the master's degree in physics from the University Autónoma of Madrid, Madrid, Spain, in 1992.

He has been the Manager of the European High-Power RF Laboratory, Valencia, Spain, since 2010. He is currently with the European Space Research and Technology Center, European Space Agency, Noordwijk, The Netherlands.

Carlos Vicente (M'08) was born in Elche, Spain, in 1976. He received the Diploma degree in physics from the University of Valencia, Valencia, Spain, in 1999, and the Dr.Ing. degree in engineering from the Technical University of Darmstadt, Darmstadt, Germany, in 2005.

His current research interests include the analysis of passive components for communications satellites.

Jordi Gil (M'08) was born in Valencia, Spain, in 1977. He received the Licenciado degree in physics from the University of Valencia, Valencia, in 2000, and the Ph.D. degree in telecommunications engineering from the Universidad Politécnica de Valencia, Valencia, in 2010.

His current research interests include the analysis of microwave passive components, and nonlinear phenomena appearing in high-power microwave subsystems for space applications.

Fritz Caspers (M'76–SM'91) received the Dipl.-Ing degree in electrical engineering from RWTH Aachen University, Aachen, Germany, in 1975, and the Dr.Ing (Hons.) degree from Ruhr University Bochum, Bochum, Germany, in 1982.

He has been a CERN Fellow with the European Organization for Nuclear Research, Geneva, Switzerland, since 1982, where he is involved in different fields of RF-technology, stochastic beam cooling, EMC, electron cloud, and material measurements.

Luis Conde received the Degree in physics from the Universidad Autónoma de Madrid, Madrid, Spain, in 1983, and the Ph.D. Degree in Physics from the Universidad Nacional de Educación a Distancia, Madrid, in 1988.

He is currently a Professor of Physics with the School of Aeronautical and Space Engineering, Technical University of Madrid, Madrid. His current research interests include plasma physics, with an emphasis on space applications as plasma propulsion and low-pressure electric discharges.

Publication III

Multipactor susceptibility charts for ridge and multiridge waveguides

IEEE Transactions Electron Devices, vol. 59, no. 12, pp. 3601–3607, December 2012

Multipactor Susceptibility Charts for Ridge and Multiridge Waveguides

Daniel González-Iglesias, Pablo Soto, *Member, IEEE*, Sergio Anza, Benito Gimeno, *Member, IEEE*, Vicente E. Boria, *Senior Member, IEEE*, Carlos Vicente, *Member, IEEE*, and Jordi Gil, *Member, IEEE*

***Abstract*—The aim of this paper is to study the multipactor radio-frequency breakdown voltage in several ridge and multiridge waveguide configurations. First, multipactor susceptibility charts for several types of ridged waveguides have been computed using the commercial software FEST3D. Next, these charts have been used to predict multipactor threshold values for a bandpass filter and a quasi-low-pass filter both containing ridge waveguide sections. Furthermore, multipactor simulations using FEST3D are carried out to calculate the multipactor threshold of the aforementioned structures. A good agreement between predictions and simulations has been found for both filter examples.**

***Index Terms*—Multipactor effect, multiridge waveguide, radio frequency (RF) breakdown, ridge waveguide.**

I. Introduction

MULTIPACTOR is a vacuum discharge phenomenon that takes place on devices operating under high-power radio frequency (RF) electromagnetic fields [1]. It can appear in a wide variety of scenarios, such as satellite communication devices, klystrons, and accelerator structures [2], [3]. The multipactor effect occurs when an RF electric field accelerates free electrons inside the device, impacting on the metallic walls of the device. When electron impact energy is such that the secondary emission yield (SEY) coefficient of the material, δ, is higher than unity, new secondary electrons are released [4]. Under certain resonant conditions, new secondaries get synchronized with the RF electric field producing an exponential growth of the electron population. Once the number of electrons becomes very high, an electrical current is established between the walls of the component. This RF discharge can produce several negative effects that degrade the device performance: increase of signal noise and reflected power, heating up of the device walls, outgassing, detuning of resonant cavities, vacuum window failure, and even the total destruction of the component.

Multipactor has been deeply studied for many different kinds of geometries such as parallel-plate [5]–[9], coaxial [10]–[13], rectangular [14], [15], microstrip [16], circular [17], [18], and elliptical [19] waveguides. Despite all these past efforts, and to the authors' knowledge, multipactor in ridge and multiridge waveguides has not been studied yet.

Single- and multiridged waveguides have found many applications in microwave and millimeter-wave devices. Among their main advantages, we find large single-mode broadband operation, large dominant cutoff wavelength, and low-impedance characteristics. They are widely used for both high-power and low-power applications such as bandpass and quasi-low-pass filters [20]. These filters are very appropriate candidates for some space and terrestrial communication applications due to their compact size and good stop-band performance. For instance, they can be used as preselector filters before the input multiplexer, or as harmonic suppression filters after RF transmitters or amplifiers, particularly as onboard satellite components.

In this paper, we have computed multipactor susceptibility charts for several ridge and multiridge waveguide configurations. In most of them, the gap height is much less compared to the transverse dimensions, which means that the simulated structures are very close to a parallel-plate waveguide. Despite this, we cover a wide range of gap heights which are interesting for practical applications. First, Section II describes the procedure carried out to perform the requested multipactor simulations in order to generate the susceptibility charts. In Section III, ridge, double-ridge, and multiridge waveguide multipactor charts are presented for both symmetrical and asymmetrical configurations. All susceptibility charts are valid for a single-carrier signal. These results are used in Section IV for predicting the multipactor threshold values of an evanescent-mode filter and of a waffle-iron filter, both containing ridge waveguide sections. In addition, and with the aim of verifying the derived susceptibility charts, a complete FEST3D multipactor analysis has been performed for both filter structures. Finally, in Section V, some relevant conclusions are outlined.

II. Multipactor Analysis Methodology

The commercial software tool FEST3D [21] has been used to perform multipactor simulations within the analyzed ridged waveguides. This code allows the 3-D tracking of a set of electrons immersed into a region under RF electric and magnetic

Manuscript received July 13, 2012; revised August 3, 2012 and August 20, 2012; accepted August 22, 2012. Date of publication September 21, 2012; date of current version November 16, 2012. The review of this paper was arranged by Editor M. Thumm.

D. González-Iglesias and B. Gimeno are with the Departamento de Física Aplicada y Electromagnetismo, Instituto de Ciencia de Materiales, Universidad de Valencia, 46100-Burjasot, Spain (e-mail: Daniel.Gonzalez-Iglesias@uv.es; benito.gimeno@uv.es).

P. Soto and V. E. Boria are with the Departamento de Comunicaciones, Instituto de Telecomunicaciones y Aplicaciones Multimedia, Universidad Politécnica de Valencia, 46022-Valencia, Spain (e-mail: pabsopac@dcom.upv.es; vboria@dcom.upv.es).

S. Anza, C. Vicente and J. Gil are with the Aurora Software and Testing, S.L., Business Development Building, Universidad Politécnica de Valencia, 46022-Valencia, Spain (e-mail: sergio.anza@aurorasat.es; carlos.vicente@aurorasat.es; jordi.gil@aurorasat.es).

Digital Object Identifier 10.1109/TED.2012.2215611

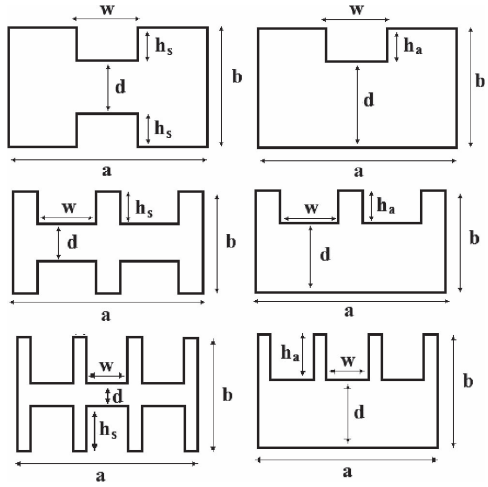

Fig. 1. Symmetrical structures on the left column and asymmetrical structures on the right column. From top to bottom: Ridge, double-ridge, and multiridge waveguides.

fields. An electromagnetic solver based on full-wave modal techniques [22] and microwave network theory calculates these fields with high accuracy and efficiency, even for complex passive microwave components. All simulations have been carried out in the running wave regime. Thus, the presence of the higher order modes has not been considered in the simulations performed to generate the susceptibility charts. However, such modes are accounted for in both the electromagnetic and multipactor analyses of the complex structures studied in this paper. Differential equations of electron motion are numerically solved using a Leap-Frog method, as described in [23]. The interactions of the electrons with the metal boundaries are modeled to consider electron elastic reflection, absorption, or creation of secondaries after each primary electron impact. The SEY is modeled using a modified version of the Vaughan's formula [14]. All simulated structures are silver plated. The SEY parameters for silver, which are described in [6], are as follows: the first crossover, $W_1 = 30$ eV; the maximum SEY coefficient, $\delta_{\max} = 2.22$; and the impact kinetic energy for $\delta_{\max}$, $W_{\max} = 165$ eV. The secondary electron velocities have been computed using a 4-eV mean and 2-eV standard deviation Maxwellian distribution.

III. Multipactor Susceptibility Charts

Ridge, double-ridge, and multiridge waveguides (see Fig. 1) with housing dimensions of a standard WR75 rectangular waveguide ($a = 19.05$ mm and $b = 9.525$ mm) have been analyzed. Symmetrical and asymmetrical configurations have been considered. In susceptibility charts, the RF multipactor voltage threshold is depicted as a function of the frequency gap $f \times d$.

Multipactor discharge is always expected to occur in the narrowest waveguide zone, where electric field becomes higher.

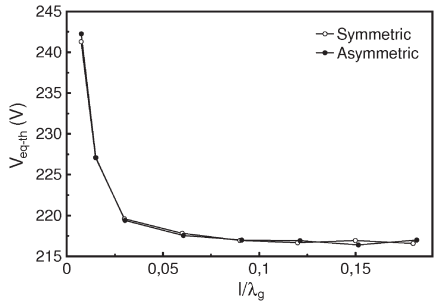

Fig. 2. Multipactor voltage threshold as a function of the normalized waveguide length for symmetrical and asymmetrical single-ridge waveguides. The gap is $d = 0.5$ mm ($d/b = 0.052$), $b/a = 0.5$, and $w/a = 0.4$. RF frequency is 5 GHz, and λ_g is the wavelength in the guide.

According to this, the existing gap between metal ridges is the critical zone for the appearance of a multipactor discharge. Thus, an equivalent voltage is numerically computed using the following expression:

$$V_{\text{eq}} = \left| \int_0^d \vec{E} \cdot \vec{dl} \right| \tag{1}$$

where $\vec{E}$ is the RF electric field of the fundamental mode in the ridge gap and $\vec{dl}$ is the differential vector parallel to the transversal component of the electric field. The integration line is located in the center of the ridge width. It can be checked numerically that, for double-ridge waveguides, the equivalent voltage is the same at both symmetrical ridges, whereas for multiridge waveguides (with an odd number of ridges), the voltage is higher at the central one.

Fig. 2 shows the voltage threshold as a function of the waveguide length for both symmetrical and asymmetrical single-ridge waveguides. Multipactor simulations show that the multipactor threshold strongly depends on the waveguide length value, i.e., l/λ_g in Fig. 2. In fact, the voltage threshold raises up for short waveguide lengths as a result of the axial drift that allows electrons leaving the ridge gap. Thus, in order to counteract the lost electrons, a higher rate of generation of secondaries is needed, which is obtained by means of an increase of the RF power. Similar results were obtained for the different multiridge topologies. In the next multipactor susceptibility charts, a waveguide length in the flat zone of the graphic has been always considered (i.e., $l/\lambda_g > 0.1$).

Two different kinds of charts are presented. First, the RF voltage threshold for several ridge widths is shown in Fig. 3 for both symmetrical and asymmetrical configurations. As it can be shown, there are slight variations on the voltage threshold with the ridge width for each figure. However, it can be observed that the narrower the ridge, the higher the voltage threshold. An explanation of this phenomenon is that lower w/a values allow electrons to escape from the gap region, so an extra voltage is needed in order to compensate this phenomenon. Similar multipactor behavior is found for waveguide irises [24]–[26], where the power threshold increases when the h/l ratio is

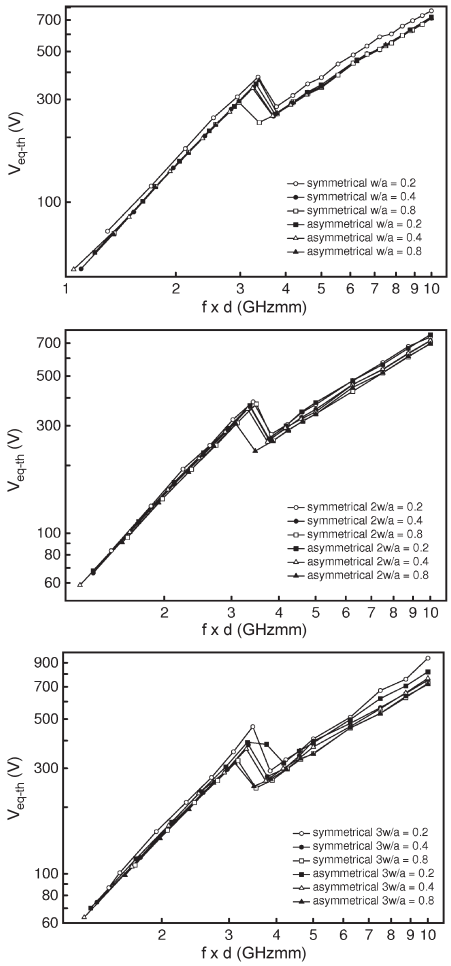

Fig. 3. Multipactor voltage threshold for several ridge widths in both symmetrical and asymmetrical configurations. From top to bottom: Ridge, double-ridge, and multiridge waveguides. The gap height is $d = 0.5$ mm, $d/b = 0.052$, and $b/a = 0.5$.

higher (h is the gap height, and l is the iris length). Two different mechanisms for electron loss were proposed for an iris scenario. On the one hand, fringing electric field accelerates electrons out of the iris. On the other hand, a random drift due to the axial component of the initial velocity of the secondary emitted electrons may push many electrons away from the gap region. In our ridge waveguide case, both effects are supposed to act but in the transverse plane to the wave propagation direction, specifically parallel to the ridge width of value w. For a better understanding of the fringing phenomenon in ridged waveguides, a study of the voltage threshold dependence with the ratio of ridge width to gap, w/d, has been performed. It covers a wider range of w/d values than the previous

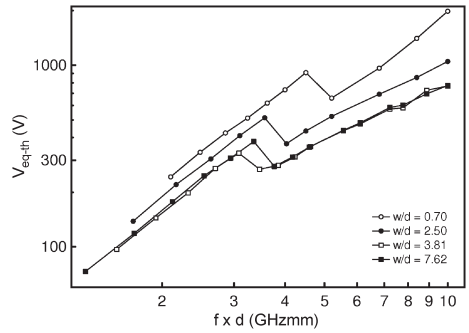

Fig. 4. Multipactor voltage threshold for several values of ridge-width-to-gap ratio for single-ridge symmetrical waveguide. The gap height is $d = 0.5$ mm, $d/b = 0.052$, and $b/a = 0.5$.

w/a analysis. Results are presented in Fig. 4 for a symmetrical single-ridge waveguide, but similar behavior can be found for asymmetrical and/or multiridge waveguides. It is observed that fringing effect raises up the voltage threshold as the w/d ratio reduces. This behavior becomes more important when w/d is close to unity or lower. On the other hand, for w/d values higher than unity, threshold variations become slighter.

Next, the effect of ridge gap variation on the voltage threshold was also studied for both symmetrical and asymmetrical topologies (see Figs. 5 and 6, respectively). Like in the previous performed studies, a very slight variation of the voltage threshold in terms of the gap for higher d/b values considered is observed. Multipactor voltage threshold comparison among single, double, and multiridge waveguides is presented for the symmetrical case in Fig. 7. As it was pointed out in Fig. 3, the RF voltage threshold increases as the ridge width becomes smaller. The multiridge waveguide has the narrowest ridges and, therefore, the higher threshold values, as it can be expected.

Finally, the effect of rounding off the sharp edges of the ridges has been analyzed in the case of a symmetric ridge waveguide. In Fig. 8, the equivalent voltage threshold as a function of the $f \times d$ parameter is plotted for different radii of curvature of the external ridge corners. For low radii of curvature, we have not observed significant variations. However, as a consequence of the inhomogeneity of the electric field pattern, a small increase of the voltage threshold has been obtained for high curvature radii which round almost all the ridge wall.

IV. Multipactor Prediction Using Susceptibility Charts

In this section, a simple multipactor prediction method for complex microwave devices containing ridge waveguide sections is presented. This procedure does not require any additional multipactor simulation. Only the electromagnetic field distribution inside the structure at the operating frequency is needed. Once the electromagnetic fields are computed, the electric field must be integrated in order to calculate the voltage across the ridge gap sections using (1). As the electric field

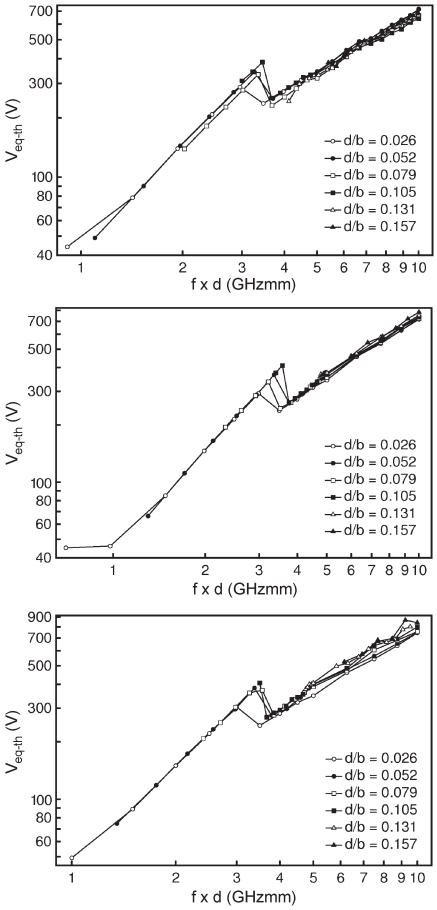

Fig. 5. Multipactor voltage threshold for several gap heights in symmetrical topologies. From top to bottom: Ridge (width $w/a = 0.4$), double-ridge ($2w/a = 0.4$), and multiridge ($3w/a = 0.4$) waveguides. In all cases, $b/a = 0.5$.

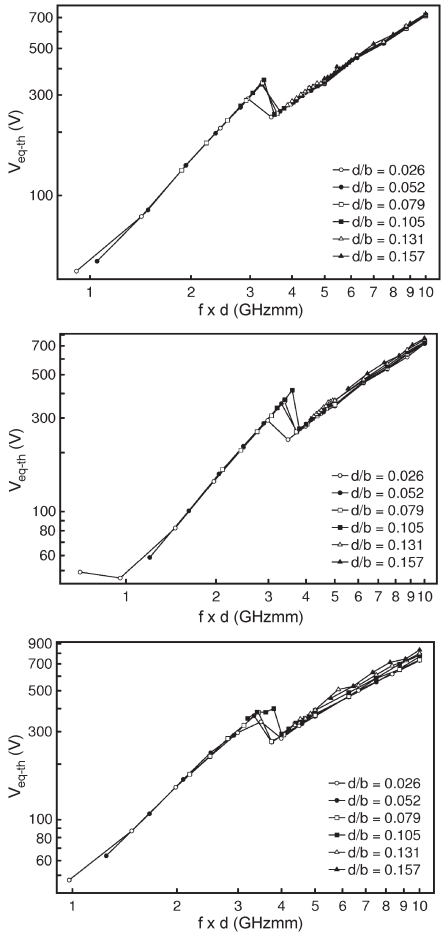

Fig. 6. Multipactor voltage threshold for several gap heights in asymmetrical topologies. From top to bottom: Ridge (width $w/a = 0.4$), double-ridge ($2w/a = 0.4$), and multiridge ($3w/a = 0.4$) waveguides. In all cases, $b/a = 0.5$.

typically varies with the axial direction [27], such voltage must be evaluated for several axial points along the ridge length. As a result, the highest voltage $V'_{\rm eq}$ at each ridge in the structure for an RF power input excitation, i.e., $P_{\rm in} = 1$ W, is found. For each frequency value, the device input power is proportional to the square of the ridge voltage. Accordingly, the multipactor input power threshold $P_{\rm th}$ at the input port of the device related to a particular ridge section will be

$$P_{\rm th} = \left| \frac{V_{\rm eq-th}}{V'_{\rm eq}} \right|^2 P_{\rm in} \tag{2}$$

where the voltage threshold $V_{\rm eq-th}$ depends on the frequency gap $f \times d$ of each particular section, which can be extracted from the previously computed multipactor susceptibility charts. The multipactor power threshold in the full structure is the lowest power value obtained among all studied ridges. We detail this method through the two following examples.

A. Evanescent-Mode Filter

The first analyzed structure is an evanescent-mode filter extracted from [28]. Fig. 9 shows the filter topology, and its dimensions are summarized in Table I. Input and output ports are implemented with a WR137 waveguide ($a_{\rm in} = 34.85$ mm and $b_{\rm in} = 15.80$ mm).

The operation frequency is chosen to be centered in the passband of the filter, namely, $f = 9.78$ GHz. Since the considered structure consists of five identical ridges, the frequency gap product is $f \times d = 3.08$ GHzmm for all of them. First,

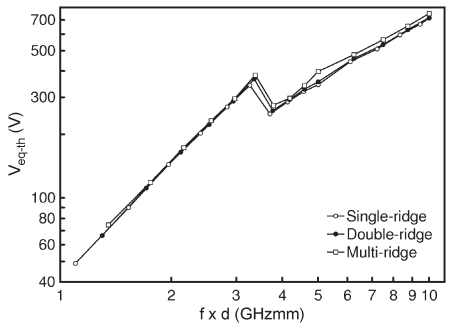

Fig. 7. Multipactor voltage threshold for symmetrical ridged waveguides. Singe-ridge $w/a = 0.4$, double-ridge $2w/a = 0.4$, and multiridge $3w/a = 0.4$. The gap is 0.5 mm $(d/b = 0.052)$, and $b/a = 0.5$.

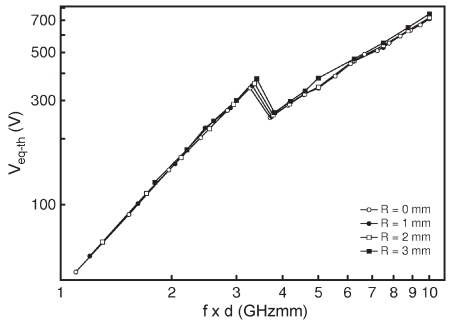

Fig. 8. Multipactor voltage threshold in symmetrical ridged waveguides for different radii of curvature of the external ridge corners. The gap is 0.5 mm $(d/b = 0.052)$, $b/a = 0.5$, and $w/a = 0.4$.

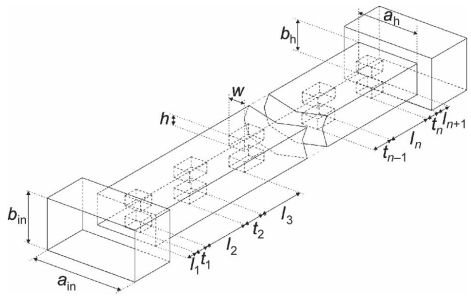

Fig. 9. Symmetrical evanescent-mode ridge waveguide filter under consideration.

the electromagnetic analysis of the complete structure is performed, assuming $P_{\rm in} = 1$ W excitation at the input port. The equivalent voltage over the gap has been computed for several axial points along the ridge sections (see Fig. 10). Ridges are numbered from the input port to the output port as indicated in Table I. From these results, the multipactor threshold can be predicted as follows. Since the ridge sections have the very same gap values, the voltage threshold $V_{\rm eq-th}$ will be the same

TABLE I
DIMENSIONS OF THE EVANESCENT-MODE FILTER SHOWN IN Fig. 9

a_h	6.790 mm
b_h	5.275 mm
w	3.050 mm
h	2.480 mm
d	0.315 mm
$l_1 = l_6$	0.250 mm
$t_1 = t_5$	0.901 mm
$l_2 = l_5$	7.785 mm
$t_2 = t_4$	1.411 mm
$l_3 = l_4$	8.278 mm
t_3	1.411 mm

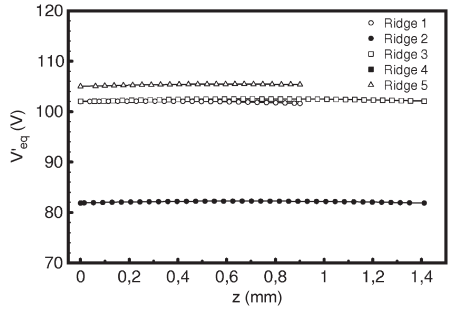

Fig. 10. Equivalent voltage over the gap for $P_{\rm in} = 1$ W on several axial points of the filter.

TABLE II
SUMMARIZED MULTIPACTOR RESULTS FOR THE EVANESCENT-MODE FILTER

Ridge	V'_{eq} (V)	P_{pred} (W)	$P_{\rm FEST3D}$ (W)
5	105.4	8.65	9.09

for all of them. Therefore, the greatest voltage among all the ridge sections must be found. From such a voltage value and the voltage threshold extracted from symmetrical waveguide charts, the multipactor power threshold at the input port can be obtained. Ridge sections have the following dimensions: $w/a = 0.45$ and $d = 0.315$ mm. The most similar situation in previously computed susceptibility charts is found in Fig. 5 for $w/a = 0.4$ and $d/b = 0.026$. From there, the voltage threshold for the working frequency is $V_{\rm eq-th} = 310$ V. Moreover, the multipactor input power threshold is also computed using FEST3D [23]. Results obtained from both methods are summarized in Table II. The first column indicates the number of the ridge section providing the highest voltage (and consequently where breakdown is expected to occur); the second column gives the highest voltage value for $P_{\rm in} = 1$ W, $V'_{\rm eq}$; the third column is the predicted input power threshold, $P_{\rm pred}$; and the fourth column provides the input power threshold computed by FEST3D, $P_{\rm FEST3D}$.

It is observed that both simulation and prediction match up with the ridge section where the multipactor appears. In addition, power thresholds obtained by two different procedures are very similar, thus demonstrating the feasibility of the prediction method. Note that the predicted threshold value is always expected to be less than the simulated one due to

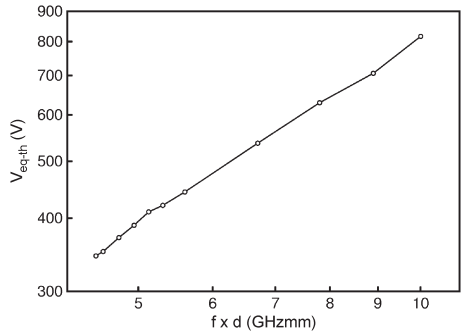

Fig. 11. Multipactor voltage threshold for the symmetrical multiridge waveguide of the waffle-iron filter under consideration manufactured in copper.

the fact that, in the susceptibility charts, the ridge waveguides have uniform fields along the axial direction. In a realistic case, the waveguide is connected to the adjacent discontinuities, and the voltage along the waveguide varies, as shown in Fig. 10. This effect raises the multipactor threshold above the uniform axial case.

Finally, the advantage of using the new computed charts instead of the parallel-plate model charts must be pointed out. From the ECSS Multipactor Tool version 1.1 [6], the power threshold for the considered gap at the working frequency is 3.44 W (192.5 V). Comparing this value with the predicted one using the new generated charts, it is found that the free-multipactor power handling capability of the filter can be increased in 4 dB. In fact, it is well known that the parallel-plate model is rather conservative for more complex waveguide geometries.

B. High-Power S-Band Filter

The last analyzed structure is a high-power S-band filter whose topology and dimensions are detailed in [29, Fig. 2]. The filter consists of seven equal multiridge sections, and each multiridge transversal cross section has five symmetrical ridges with $d = 2.413$ mm gap. The filter was constructed in copper.

First, multipactor susceptibility charts are computed for a single five-symmetrical-multiridge waveguide with transversal cross-sectional dimensions of the filter. Results for copper are shown in Fig. 11. For the copper SEY simulations we have the following: $W_1 = 35$ eV, $\delta_{\max} = 2.3$, and $W_{\max} = 165$ eV.

After that, an electromagnetic analysis of the whole device is performed. Input and output ports are implemented with rectangular waveguides of the following dimensions: $a = 72.1360$ mm and $b = 6.4516$ mm. The operation frequency has been chosen to be 2.78 GHz, and the frequency gap product is $f \times d = 6.71$ GHzmm for all the ridge sections. The equivalent voltage between ridges was calculated for the central ridge (where the electric field is higher), according to Fig. 12. From the susceptibility chart in Fig. 11, the voltage threshold for the working frequency is $V_{\mathrm{eq-th}} = 530$ V. With these data, multipactor power threshold prediction can be done. Table III

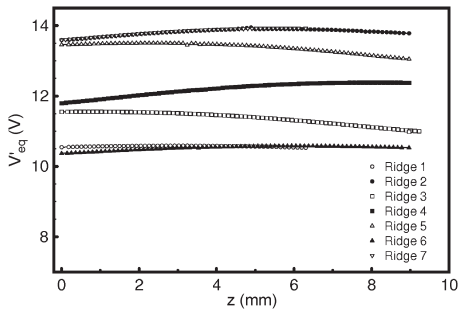

Fig. 12. Equivalent voltage over the gap of the filter ridges for $P_{\mathrm{in}} = 1$ W on several axial points.

TABLE III
SUMMARIZED MULTIPACTOR RESULTS FOR THE WAFFLE-IRON FILTER

Ridge	V'_{eq} (V)	P_{pred} (W)	P_{FEST3D} (W)
7	13.921	1449	1532

summarizes the main results ($V'_{\mathrm{eq}}, P_{\mathrm{pred}}, P_{\mathrm{FEST3D}}$ already defined in the previous section).

Good agreement has been found between our predicted value and the one provided by FEST3D. Comparing the predicted power threshold value with the one corresponding to the parallel-plate model (676 W), there is a relevant difference of 3.3 dB between them.

V. CONCLUSION

In this paper, we have studied the multipactor effect in ridged waveguides. Multipactor susceptibility charts have been computed by means of the commercial software FEST3D for several ridge and multiridge configurations. For each configuration, the variation of the voltage threshold as a function of the different waveguide dimensions is presented, and a qualitative explanation of such behaviors in terms of the fringing effect is outlined. Afterward, developed multipactor susceptibility charts have been used to predict the RF input power threshold for an evanescent-mode filter and for a high-power S-band filter, both containing ridges. Predicted multipactor values have been compared with FEST3D simulations of the entire structures, and a very good agreement has been found in both cases.

REFERENCES

[1] J. Vaughan, "Multipactor," *IEEE Trans. Electron Devices*, vol. 35, no. 7, pp. 1172–1180, Jul. 1998.
[2] F. Zimmermann, "A Simulation Study of Electron Cloud Instability and Beam Induced Multipacting in the LHC," CERN, Geneva, Switzerland, CERN LHC Project Rep. 95, Feb. 1997.
[3] M. A. Furman, "The Electron-Cloud Effect in the ARCS of the LHC," CERN, Geneva, Switzerland, CERN LHC Project Rep. 180, May 1998.
[4] J. R. M. Vaughan, "Secondary emission formulas," *IEEE Trans. Electron Devices*, vol. 40, no. 4, p. 830, Apr. 1993.
[5] A. Woode and J. Petit, "Diagnostic Investigations Into the Multipactor Effect, Susceptibility Zone Measurements and Parameters Affecting a Discharge," Noordwijk, The Netherlands, Tech. Rep. ESA/ESTEC Working Paper 1556, Nov. 1989.
[6] *Space Engineering: Multipacting Design and Test.* Noordwijk, ESA Publ. Div., May 2003, ECSS-20-01A, edited by ESA-ESTEC.

[7] A. J. Hatch and H. B. Williams, "Multipactor modes of high-frequency gaseous breakdown," *Phys. Rev.*, vol. 112, no. 3, pp. 681–685, Nov. 1958.
[8] J. Lara, F. Pérez, M. Alfonseca, L. Galán, I. Montero, E. Román, and D. Raboso, "Multipactor prediction for on-board spacecraft RF equipment with the MEST software tool," *IEEE Trans. Plasma Sci.*, vol. 34, no. 2, pp. 476–484, Apr. 2006.
[9] R. A. Kishek, Y. Y. Lau, L. K. Ang, A. Valfells, and R. M. Gilgenbach, "Multipactor discharge on metals and dielectrics: Historical review and recent theories," *Phys. Plasmas*, vol. 5, no. 5, pp. 2120–2126, May 1998.
[10] A. M. Pérez, C. Tienda, C. Vicente, S. Anza, J. Gil, B. Gimeno, V. E. Boria, and D. Raboso, "Prediction of multipactor breakdown thresholds in coaxial transmission lines for traveling, standing, and mixed waves," *IEEE Trans. Plasma Sci.*, vol. 37, no. 10, pp. 2031–2040, Oct. 2009.
[11] R. Udiljak, D. Anderson, M. Lisak, V. Semenov, and J. Puech, "Multipactor in a coaxial transmission line. Part I: Analytical study," *Phys. Plasmas*, vol. 14, no. 3, pp. 033508-1–033508-11, 2007.
[12] V. Semenov, N. Zharova, R. Udiljak, D. Anderson, M. Lisak, and J. Puech, "Multipactor in a coaxial transmission line. Part II: Particle-in-cell simulations," *Phys. Plasmas*, vol. 14, no. 3, pp. 033509-1–033509-7, 2007.
[13] E. Somersalo, P. Yl-Oijala, and D. Proch, "Electron Multipacting in RF Structures," Deutsches Elektronen-Synchrotron DESY, Hamburg, Germany, TESLA Rep. 94-14, Jul. 1994.
[14] C. Vicente, M. Mattes, D. Wolk, B. Mottet, H. L. Hartnagel, J. R. Mosig, and D. Raboso, "Multipactor breakdown prediction in rectangular waveguide based components," in *Proc. IEEE MTT-S Int. Microw. Symp. Dig.*, Jun. 2005, pp. 12–17.
[15] V. E. Semenov, E. I. Rakova, D. Anderson, M. Lisak, and J. Puech, "Multipactor in rectangular waveguides," *Phys. Plasmas*, vol. 14, no. 3, pp. 033501-1–033501-8, 2007.
[16] V. E. Semenov, E. I. Rakova, A. G. Sazontov, I. M. Nefedov, V. I. Pozdnyakova, I. A. Shereshevskii, D. Anderson, M. Lisak, and J. Puech, "Simulations of multipactor thresholds in shielded microstrip lines," *J. Phys. D, Appl. Phys.*, vol. 42, no. 20, p. 205 204, Oct. 2009.
[17] V. E. Semenov, N. A. Zharova, D. Anderson, M. Lisak, and J. Puech, "Simulations of multipactor in circular waveguides," *Phys. Plasmas*, vol. 17, no. 12, pp. 123503-1–123503-7, 2010.
[18] A. M. Pérez, V. E. Boria, B. Gimeno, S. Anza, C. Vicente, and J. Gil, "Multipactor analysis in circular wave-guides," *J. Electromagn. Waves Appl.*, vol. 23, no. 11/12, pp. 1575–1583, 2009.
[19] A. Frotanpour, G. Dadashzadeh, M. Shahabadi, and B. Gimeno, "Analysis of multipactor RF breakdown thresholds in elliptical waveguides," *IEEE Trans. Electron Devices*, vol. 58, no. 3, pp. 876–881, Mar. 2011.
[20] J. Uher, J. Bornemann, and U. Rosenberg, *Waveguide Components for Antenna Feed System: Theory and CAD*. Norwood, MA: Artech House, 1993.
[21] FEST3D, ESA/ESTEC, Valencia, Spain. [Online]. Available. www.fest3d.com
[22] G. Conciauro, M. Guglielmi, and R. Sorrentino, *Advanced Modal Analysis*. New York: Wiley, 2000.
[23] S. Anza, C. Vicente, D. Raboso, J. Gil, B. Gimeno, and V. E. Boria, "Enhanced prediction of multipactor breakdown in passive waveguide components including space charge effects," in *Proc. IEEE MTT-S Microw. Symp. Dig.*, 2008, pp. 1095–1098.
[24] D. Wolk, C. Vicente, H. L. Hartnagel, M. Mattes, J. R. Mosig, and D. Raboso, "An investigation on the effect of fringing fields on multipactor breakdown," in *Proc. 5th Int. Workshop Multipactor, Corona Passive Intermodul.*, Sep. 2005, pp. 93–99.
[25] R. Udiljak, D. Anderson, M. Lisak, J. Puech, and V. E. Semenov, "Multipactor in a waveguide iris," *IEEE Trans. Plasma Sci.*, vol. 35, no. 2, pp. 388–395, Apr. 2007.
[26] V. E. Semenov, E. Rakova, R. Udiljak, D. Anderson, M. Lisak, and J. Puech, "Conformal mapping analysis of multipactor breakdown in waveguide irises," *Phys. Plasmas*, vol. 15, no. 3, pp. 033501-1–033501-8, 2008.
[27] P. Sarasa, A. González, H. Esteban, P. Mader, K. Tossou, and P. Lepeltier, "Comparative study of the power handling capability of space broadband antenna filters in Ku-band," in *Proc. 5th Int. Workshop Multipactor, Corona Passive Intermodul.*, Noordwijk, The Netherlands, Sep. 2005.
[28] P. Soto, D. de Llanos, V. E. Boria, E. Tarín, B. Gimeno, A. Oñoro, I. Hidalgo, and M. J. Padilla, "Performance analysis and comparison of symmetrical and asymmetrical configurations of evanescent mode ridge waveguide filters," *Radio Sci.*, vol. 44, pp. RS6 010-1–RS6 010-16, 2009.
[29] H. Guthart, "A high-power S-band filter," *IRE Trans. Microw. Theory Tech.*, vol. 10, no. 2, pp. 148–149, Mar. 1962.

Daniel González-Iglesias received the Licenciado Degree in Physics and the Master on Advanced Physics from the University of Valencia, Valencia, Spain, in 2010 and 2011, respectively.

He is currently with the University of Valencia.

Pablo Soto (S'01–M'06) received the M.S. and Ph.D. degrees from the Universidad Politécnica de Valencia, Valencia, Spain, in 1999 and 2012, respectively.

He is currently with the Universidad Politécnica de Valencia.

Sergio Anza was born in Madrid, Spain. He received the M.S. degree in aerospace science and technology from the Universidad Politécnica de Cataluña, Barcelona, Spain, in 2006.

He is currently with Universidad Politécnica de Valencia, Valencia, Spain.

Benito Gimeno (M'01) received the Licenciado degree in physics and the Ph.D. degree from the University of Valencia, Valencia, Spain, in 1987 and 1992, respectively.

He became a Full Professor with the University of Valencia in 2010.

Vicente E. Boria (S'91–A'99–SM'02) received the Doctor Ingeniero de Telecomunicación degree from the Universidad Politécnica de Valencia, Valencia, Spain, in 1997.

He is currently with the Universidad Politécnica de Valencia.

Carlos Vicente (M'08) was born in Elche, Spain, in 1976. He received the Dr. Ing. degree in engineering from the Technical University of Darmstadt, Darmstadt, Germany, in 2005.

He is currently with Universidad Politécnica de Valencia, Valencia, Spain.

Jordi Gil (M'08) received the Licenciado degree from the Universidad de Valencia, Valencia, Spain, in 2000 and the Ph.D. degree from the Universidad Politécnica de Valencia, Valencia, in 2010.

He is currently with Universidad Politécnica de Valencia.

Publication IV

Analysis of multipactor effect using a Phase-Shift Keying single-carrier digital modulated signal

IEEE Transactions on Electron Devices, vol. 60, no. 8, pp. 2664-2670, August 2013

Analysis of Multipactor Effect Using a Phase-Shift Keying Single-Carrier Digital Modulated Signal

Daniel González-Iglesias, Maria Pilar Belloch Rodríguez, Òscar Monerris Belda, Benito Gimeno, *Member, IEEE*, Vicente E. Boria, *Senior Member, IEEE*, David Raboso, and Vladimir E. Semenov

***Abstract*— The main aim of this paper is the analysis of the multipactor effect within a coaxial waveguide structure excited by a phase-shift keying single-carrier digital modulated signal. To reach this aim, we developed in-house a software code which is able to predict the RF multipactor input voltage threshold. This code is based on the single effective electron model, and considers the space charge effect. Numerical simulations are performed for binary phase-shift keying and quadrature phase-shift keying modulated signals. In addition, an experiment is carried out to validate the proposed theoretical model. We have demonstrated that the digital modulation of the single-carrier signal may modify the RF voltage threshold in comparison to the nonmodulated scenario. Good agreement between theory and experimental data is found.**

***Index Terms*— Binary phase-shift keying (BPSK), coaxial waveguides, digitally modulated signals, multipactor effect RF breakdown, quadrature phase-shift keying (QPSK), space charge.**

I. Introduction

MULTIPACTOR breakdown is an electron avalanche-like discharge occurring in components operating under vacuum conditions and high-power RF electromagnetic fields [1]. The phenomenon occurs when free electrons in the device get synchronized with the RF electric field, and impact against the metallic walls of the component with enough energy to release secondary electrons from the surface. The growth in the electron population in the device can lead to one or several discharges. These discharges have several negative effects that degrade the component performance; increase of signal noise and reflected power, heating up of the device walls, detuning of resonant cavities, vacuum window failure, and even physical damages in the device structure. This RF breakdown effect appear in a wide range of different environment, such as satellite passive components for space communications, klystrons and travelling-wave tubes, or particle accelerators [2].

Focusing on space communications, multipactor reveals as a restrictive limitation to the power handling capabilities of many satellite RF and microwave devices. This is quite an inconvenience since the increasing number of users, requiring higher and higher bit rates, implies the necessity of increasing power levels in the RF and microwave payload equipment. For these reasons, the study of multipactor has become a crucial issue in the last 50 years.

The biggest effort of multipactor research lines is aimed to the study and characterization of the phenomenon to predict under which conditions it will appear, and thus to design multipactor-free components [3]–[6]. However, most of this work is focused on the study of nonmodulated RF signals, whereas realistic satellite communication systems are usually based on multicarrier operation and modulated carriers to use efficiently the available frequency spectrum. A typical multicarrier signal is composed of several modulated carriers with a small frequency separation, and their mix produces an RF signal with a time varying envelope [7]. As a consequence, it becomes an important issue to analyze the multipactor behavior considering modulated signals, where the main feature of the modulation is that the signal envelope stays or not constant depending on the modulation scheme. A widely used modulation scheme is the phase-shift keying (PSK), where the amplitude is constant but the phase switches on regular intervals [8].

Traditionally, the multipactor is associated with resonant electron trajectories coupled with the RF electric field. These trajectories must satisfy that the electron collides against the metallic walls with enough kinetic energy to release one or more secondary electrons. If the RF phase switches suddenly, the electron resonant trajectories may be disturbed, thus potentially causing an interruption in the growth of the electron population. In addition, the time between the phase shifts will be determinant in the behavior of the discharge, as if this time was short enough hence the electron avalanche could be partially mitigated or interrupted, as reported in [9].

The study presented here is mainly focused on binary phase-shift keying (BPSK) and quadrature phase-shift keying (QPSK) modulation schemes. Most of the links used in satellite communications are employing QPSK digital modulation schemes. To analyze the multipactor behavior considering QPSK-modulated signals, a digital phase modulation study based on BPSK (the simplest form of digital phase modulation) is firstly developed.

Manuscript received April 25, 2013; revised May 23, 2013; accepted May 28, 2013. Date of publication June 18, 2013; date of current version July 19, 2013. The review of this paper was arranged by Editor M. Thumm.

D. González-Iglesias and B. Gimeno are with the Departamento de Física Aplicada-ICMUV, Universidad de Valencia, Valencia 46100, Spain (e-mail: Daniel.Gonzalez-Iglesias@uv.es; benito.gimeno@uv.es).

M. P. B. Rodríguez and V. E. Boria are with the Departamento de Comunicaciones-iTEAM, Universidad Politècnica de Valencia, Valencia E46022, Spain (e-mail: mabelro1@teleco.upv.es; vboria@dcom.upv.es).

Ò. M. Belda is with the Laboratory High-Power RF, Val Space Consortium, Valencia 014459, Spain (e-mail: oscar.monerris@val-space.com).

D. Raboso is with the European Space Agency, European Space Agency/European Space Research and Technology Centre, Noordwijk 46022, The Netherlands (e-mail: david.raboso@esa.int).

V. E. Semenov is with the Institute of Applied Physics, Russian Academy of Sciences, Nizhny Novgorod 603950, Russia (e-mail: sss@appl.sci-nnov.ru).

Digital Object Identifier 10.1109/TED.2013.2266275

The main goal of this paper is to present a simulation tool which is able to predict the multipactor voltage threshold for coaxial geometries under a PSK digital modulated excitation. In Section II, the Monte-Carlo algorithm of the simulation tool is described, and the basics about the PSK digitally modulated signals is outlined. In addition, realistic pulse shaping is taking into account by considering two different types of filters. In Section III, the most relevant simulation results for the BPSK and QPSK modulation schemes are presented. In Section IV, we show some experimental results carried out to validate the proposed theoretical model. Finally, conclusions are outlined in Section V.

II. Theory

A. Monte-Carlo Algorithm

We have developed in-house a code to study multipactor phenomenon in coaxial waveguides under digitally modulated signal excitation. This code is able to compute the RF multipactor input voltage threshold within a standard coaxial line. The simulator is based on the single effective electron model [10]. This technique consists of tracking the individual trajectories of N_e effective electrons, considering the secondary electron emission when a primary electron strikes on the coaxial metal walls. Each effective electron has associated an electron population which varies with time. A brief explanation of how this software code works is outlined.

First, for each effective electron the trajectory is computed by solving numerically its nonrelativistic equation of motion. A Velocity-Verlet algorithm [11] which ensures accuracy and other important properties in physical systems (such as time-reversibility and preservation of the simplistic form on phase space) is employed. In this paper, convergent electron trajectory is found for 300 time steps per RF period.

At each integration step, the code checks if the electron collides on the inner or on the outer coaxial conductor. When an impact occurs, the electron can be either absorbed or release secondary electrons, depending on the impact conditions. This is quantified by means of the secondary electron yield (SEY) function (δ) which is computed for each impact, as a function of the impact kinetic energy and the impact angle. In this in-house developed software, we employed the SEY model formulated in [4]. After the impact, the effective electron is launched from that position with an initial velocity given by a Gaussian distribution of mean 4 eV, and standard deviation of 2 eV. The velocity launching angle is chosen normal to the departure surface.

When the code is run for a predefined number of RF periods, the code stops and the time evolution of the total population of the N_e effective electrons is shown. The total electron population $N(t)$ is obtained by adding the accumulated electron population of each individual effective electron

$$N(t) = \sum_{i=1}^{N_e} N_i(t) \tag{1}$$

where $N_i(t)$ is the accumulated electron population for the ith effective electron.

The multipactor onset criteria is based on the detection of an exponential growth rate, with a final electron population equal or higher than 10^5 times the initial population, or if saturation in the electronic population is found.

The total electromagnetic field experienced by each effective electron is the sum of two contributions: the external RF field, and the field generated by the electron cloud (i.e., the space charge effect due to the Coulombian repulsion among electrons), thus resulting in

$$\vec{E}_t = \vec{E}_{RF} + \vec{E}_{sc}, \quad \vec{B}_t = \vec{B}_{RF}. \tag{2}$$

The external RF field is the correspondent to the fundamental TEM mode supporting a digitally modulated signal

$$\vec{E}_{RF}(\vec{r},t) = \frac{V(z,t)}{r\ln(\frac{b}{a})}\hat{r}, \quad \vec{B}_{RF}(\vec{r},t) = \frac{V(z,t)}{r\,c\ln(\frac{b}{a})}\hat{\varphi} \tag{3}$$

where $V(z,t)$ is the digitally modulated signal voltage, $\hat{r}$ and $\hat{\varphi}$ are the unity vectors associated with standard cylindrical coordinates (r,φ,z), $\vec{r}$ is the position vector, c is the speed of light in the dielectric material, and b and a are the outer and inner radius of the coaxial guide, respectively.

Coulombian repulsion among electrons is modeled by means of a single electron sheet, following the same procedure proposed in [12]. This electron sheet is cylindrically shaped and remains in $r = r_s$, being $r_s = (b+a)/2$ the center of the coaxial gap. The related electrical density charge is given by the following:

$$\rho_s(t) = \frac{-eN(t)}{2\pi r_s h} \tag{4}$$

where $-e$ is the charge of an electron, h is the sheet height, and N is the number of electrons at a given time t. Thus, it can be demonstrated using the Gauss's law that the electric field due to such a density charge immersed in the metallic coaxial environment is given by the following:

$$\vec{E}_{sc}(\vec{r},t) = \begin{cases} -\frac{r_s}{r}\frac{\rho_s}{\varepsilon_0}\frac{\ln(\frac{b}{r_s})}{\ln(\frac{b}{a})}\hat{r}, & a \le r \le r_s \\ \frac{r_s}{r}\frac{\rho_s}{\varepsilon_0}\frac{\ln(\frac{r_s}{a})}{\ln(\frac{b}{a})}\hat{r}, & r_s \le r \le b. \end{cases} \tag{5}$$

It is assumed that the electron dynamics is governed by the nonrelativistic Lorentz force equation

$$\vec{F}_L = q(\vec{E}_t + \vec{v}\times\vec{B}_t) = m\,\vec{a} \tag{6}$$

where $q = -e$ and m is the electron mass at rest, $\vec{v}$ and $\vec{a}$ are the velocity and acceleration vectors, respectively.

B. Digitally Modulated Signals

In this paper, we focus on the study of the M-PSK modulation effects in the multipactor input voltage threshold of coaxial waveguides. The main characteristic of this type of modulation is that the signal envelope remains constant, but the RF phase switches at regular intervals. The phase value can vary among M different values, typically M = 2 (BPSK), 4 (QPSK), or 8 (8-PSK).

An arbitrary M-PSK signal after filtered can be represented as follows:

$$V(z,t) = V_0 \sum_{n=-\infty}^{\infty} g(t - nT_s)\cos(\omega t - \beta z + \theta_n + \phi_0) \quad (7)$$

where V_0 is the amplitude voltage, $g(t)$ is the filter function in the time domain, n is the symbol index, T_s is the symbol duration, ϕ_0 is the initial phase of the RF field at the start time ($t = 0$), $f = \omega/(2\pi)$ is the operation frequency, $\beta = \omega/c$ is the propagation constant of the fundamental TEM coaxial mode, and finally θ_n is the M-PSK modulation phase.

With regard to the filter, we are going to use two different types: a rectangular filter, and a root-raised-cosine (RRC) filter [13]. The time domain filter function for the rectangular filter is as follows:

$$g_{\text{rect}}(t) = \begin{cases} 1, & 0 \le t \le T_s \\ 0, & t > T_s, \quad t < 0. \end{cases} \quad (8)$$

Similarly, the time domain function for the RRC filter is as follows:

$$g_{\text{rrc}}(t) = \frac{4\alpha}{\pi\sqrt{T_s}} \frac{\cos\frac{(1+\alpha)\pi t}{T_s} + \frac{1}{\frac{4\alpha t}{T_{ss}}}\sin\frac{(1-\alpha)\pi t}{T_s}}{1 - (\frac{4\alpha t}{T_s})^2} \quad (9)$$

where α is the roll-off factor which takes values from 0 to 1. The modulated signal bandwidth (B_w) is related to the roll-off factor through the following simple formula $B_w = (1+\alpha)/T_s$, as reported in [13]. As a consequence, low values of α are preferred for digital communication systems to reduce the bandwidth of the employed signal.

III. Simulations

Here, we show the results of the multipactor simulations carried out with our Monte-Carlo code for a 50 Ω impedance coaxial line which was properly described in [14]. The inner and outer radius dimensions are $a = 1.515$ and $b = 3.49$ mm, respectively; the length of the total sample is 90.4 mm. Both conductors are made of copper, and the existing gap between them is $d = b - a = 1.975$ mm. Mainly, we study the variation of the multipactor voltage threshold for the modulated signals with regard to the unmodulated case. A crucial parameter in this analysis is the relation between the symbol duration T_s and the RF carrier period $T = 1/f$, which is defined as $\xi \equiv T_s/T$.

The most relevant results for BPSK and QPSK modulations are summarized next.

A. BPSK

As it was previously pointed out, the phase shift between the symbols can affect to the multipactor electron avalanche growth by perturbing the resonant electron trajectories. We are interested in considering the most disturbing scenario for the multipactor electron resonance. In BPSK modulation, this is expected to occur when the repeated sequence of transmitted bits is 101010..., which implies a phase jump of 180° at the end of each symbol.

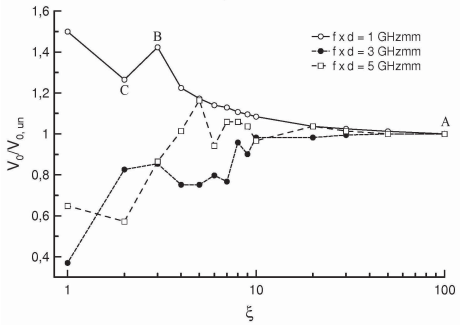

Fig. 1. Multipactor RF voltage threshold normalized to the unmodulated multipactor RF voltage threshold as a function of the ξ parameter for several frequency gap values. Signal modulated by BPSK with 101010... sequence. Rectangular filter is used. Unmodulated multipactor voltage thresholds are $V_{0,un} = 31.634$ V for $f \times d = 1$ GHzmm, $V_{0,un} = 206.227$ V for $f \times d = 3$ GHzmm, and $V_{0,un} = 231.381$ V for $f \times d = 5$ GHzmm.

1) Rectangular Filter: First, we analyze the effect of the parameter ξ in the multipactor voltage threshold for three different values of the frequency gap $f \times d$ (remaining constant the gap value and varying the frequency) considering a rectangular filter. These results are shown in Fig. 1. Note that the multipactor voltage thresholds are referred to the multipactor voltage threshold of an unmodulated scenario. From these results, it is observed that the modulated signal really affects to the multipactor voltage threshold when the time symbol is short enough, and for the considered RF frequency range this effect starts to appear at $\xi < 30$. In addition, it is observed a different behavior of the multipactor threshold with regard to the frequency gap value. For low frequency gap values (1 GHzmm), the multipactor threshold raises as ξ diminishes. Otherwise, for medium (3 GHzmm) and high (5 GHzmm) frequency gap values, it is found a general decrease in the multipactor RF voltage threshold due to the digital modulation effect.

To have a better understanding of the obtained results, the RF signal voltages and their corresponding effective electron trajectories are represented for some significant points, which are marked as A, B, C, for 1 GHzmm in Fig. 1. The most relevant results are shown in Figs. 2–4. Effective electron trajectory for each of such point is the most typical trajectory for effective electrons with an accumulative population growing with time, i.e., for those electrons which are in favorable conditions to develop the multipactor discharge. For point A, the voltage is pretty much like a sinusoidal wave, as shown in Fig. 2. This scenario is very close to the unmodulated one, and the resonant electron trajectory was not disturbed by the digital modulation, as reported in [9]. Effective electron trajectories are found to be time-periodic. In each trajectory cycle, it takes the electron 0.5 T in moving from the inner to the outer conductor, and 0.5 T in returning from the outer to the inner conductor. In the classical multipactor literature, the flight time that takes the electron from one impact to the next one is

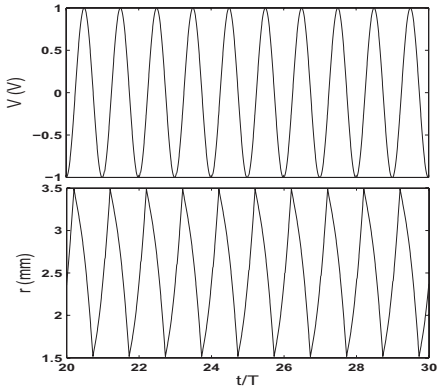

Fig. 2. RF modulated signal voltage and electron radial coordinate, as a function of the normalized time t/T. Point A from Fig. 1 for the case $f \times d = 1$ GHzmm.

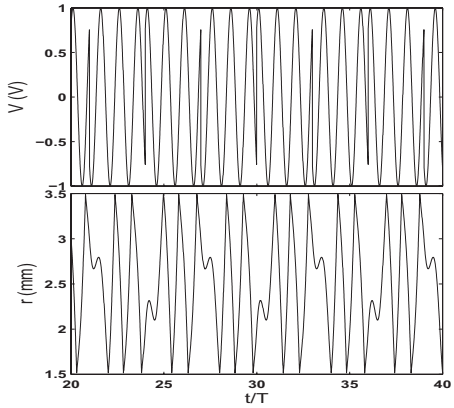

Fig. 3. RF modulated signal voltage and electron radial coordinate, as a function of the normalized time t/T. Point B from Fig. 1 for the case $f \times d = 1$ GHzmm.

usually known as the multipactor order, and it is expressed in terms of the number of RF semiperiods. According to that, the multipactor order for point A is one, which is a very common order for low frequency gap values.

For point B, $\xi = 3$ and the voltage is quite different from a sinusoidal wave. It should be noted that the voltage is periodic with period of $2T_s$ as the transmitted signal is 101010... This behavior is transmitted to the effective electron trajectories that also have a period of $2T_s$. This fact is also found for the rest of the considered modulated points with $\xi < 30$. Although effective electron trajectories in point B are periodic, multipactor order is not as well defined as in point A, appearing to be a more complex multipactor pattern, where the effective electron travels between conductors ten times before completing one trajectory cycle. A deeper analysis of

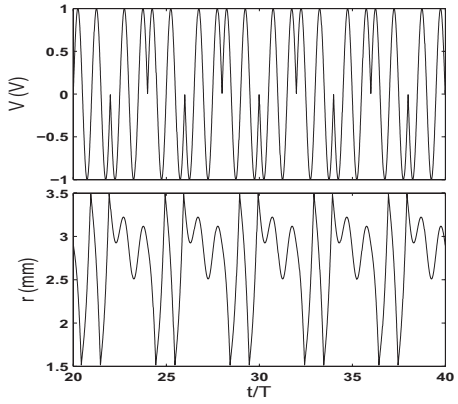

Fig. 4. RF modulated signal voltage and electron radial coordinate, as a function of the normalized time t/T. Point C from Fig. 1 for the case $f \times d = 1$ GHzmm.

the electron dynamics reveals that the SEY value for some of the impacts is below the unity, so for these ones electrons are absorbed by the metallic walls. The rest of the impacts have a SEY higher to the unity compensating the electrons lost at the former unfavorable impacts. Therefore, the multipactor voltage threshold is greater for point B than for point A, because in the latter case there is a better resonance that ensures an easy growth of the electron bunch, while in the former case an extra voltage is needed.

In point C ($\xi = 2$), we find that electron completes one cycle trajectory after only four flights between conductors. All impacts (except the last one) have SEY above unity. Therefore, this scenario is better than the described for the point B, thus observing a decrease in the multipactor voltage threshold.

2) RRC Filter: Next, we are going to analyze the effect of considering the RRC filter. Multipactor voltage threshold results, including RRC filter are quite different from those using the rectangular one, because of the significant perturbation of the single-carrier signal produced by the digital filtering process. If the rectangular filter is used, the RF signal just becomes a time harmonic cosine with constant amplitude, but with abrupt phase jumps at the end of each symbol, as shown in Fig. 3. Otherwise, when an RRC filter is applied, the modulated signal has no longer discontinuities due to sharp phase shifts. Instead of that, the modulated signal has a sinusoidal oscillation with no constant amplitude, whose envelope varies harmonically. In addition, the envelope oscillation period depends on the ξ ratio; in fact, the smaller is ξ, the faster is the envelope oscillation. Below, some voltage signals after RRC filtering will be depicted to clarify these statements.

In Fig. 5, the multipactor voltage threshold normalized to the unmodulated threshold value as a function of the ξ parameter is depicted for several $f \times d$ values, using the 101010... bit sequence with a roll-off factor of $\alpha = 0.25$. Some interesting points for the 1 GHzmm case are marked in Fig. 5

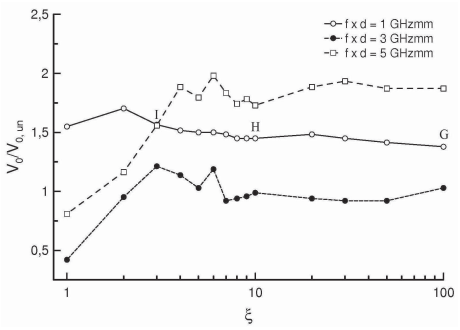

Fig. 5. Multipactor RF voltage threshold normalized to the unmodulated multipactor voltage threshold as a function of the ξ parameter for several $f \times d$ values. Signal modulated by BPSK with 101010... sequence and $\alpha = 0.25$ RRC filter is used. Same unmodulated voltage threshold as in Fig. 1.

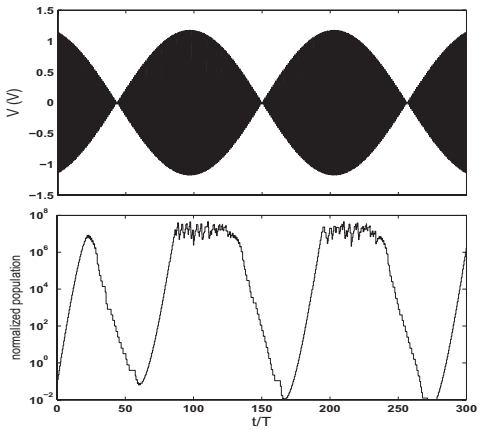

Fig. 6. (Up) RF modulated signal voltage and (down) normalized electron population as a function of the normalized time t/T for the point G from Fig. 5.

(G, H, I) for a deeper analysis of the RF signal shape, effective electron trajectory, and population evolution. Fig. 6 shows the behavior of the point G with $\xi = 100$, demonstrating that the RF voltage envelope has a slow oscillation with regard to the RF signal period. It is evident that when the envelope is close to a minimum value, the RF electric field is not strength enough to push electrons against the metallic walls with the energy necessary to deliver secondary electrons, hence electrons are absorbed decreasing the global electron population. On the other hand, when the envelope is near to a maximum value, electron impacts might be energetic enough to release secondaries and, therefore, the electron population raises up reaching the saturation level. In the electron growth region the trajectories are periodic, being the transit time of the close to the classical multipactor order one for unmodulated signals.

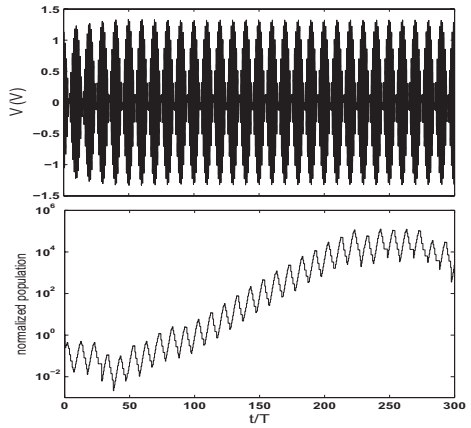

Fig. 7. (Up) RF modulated signal voltage and (down) normalized electron population as a function of the normalized time t/T for the point H from Fig. 5.

As it can be seen in Fig. 7 for point H ($\xi = 10$), the voltage amplitude envelope varies faster than the previous case, because the ξ parameter is decreased. As it happens with the previous point G, the electron population will raise or decrease depending on the envelope value. Now, the electrons are assumed to be in resonance during the maximum of the signal envelope, and, if the mean SEY is greater than one, the electron population tends to increase. However, when the amplitude of the electric field decreases electrons impact with low energy, thus diminishing the electron population. If the global electron population evolution is positive, the next envelope period will raise up the number of electrons, and finally the well-known electron accumulation phenomenon described in [15] occurs. With regard to the effective electron trajectories behavior, it looks very similar to the one shown for the previous $\xi = 100$ case. In addition, electron flight times between conductors are similar in both cases.

Finally, Fig. 8 shows the results obtained for point I ($\xi = 3$). The RF modulated signal voltage shape is now quite different from the previous points G and H, due to the low ξ value. In this case, effective electron trajectories have a wide range of flight times between conductors, resulting in a saturation of the electron population that generates a multipaction discharge.

B. QPSK

In QPSK modulation, phase can switch among four different phase values. Proceeding similarly as we did for the previous BPSK case study, we are interested in considering the potentially most disturbing scenario, which is presumed to be accomplished for a bit sequence like 11011000... This sequence involves two 180° phase jumps alternating with two 90° phase jumps. Multipactor voltage threshold curves for that sequence and the RRC filter with a roll-off factor $\alpha = 0.25$ are computed by obtaining very similar results to those shown

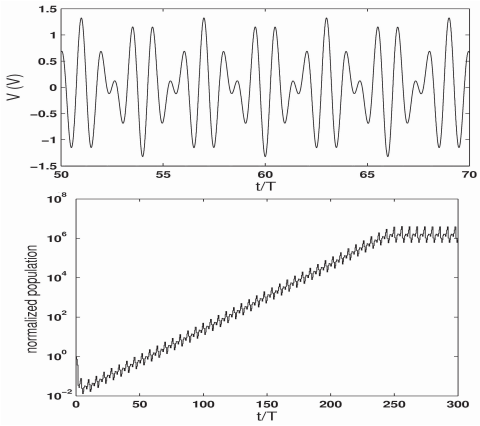

Fig. 8. (Up) RF modulated signal voltage and (down) normalized electron population as a function of the normalized time t/T for the point I from Fig. 5.

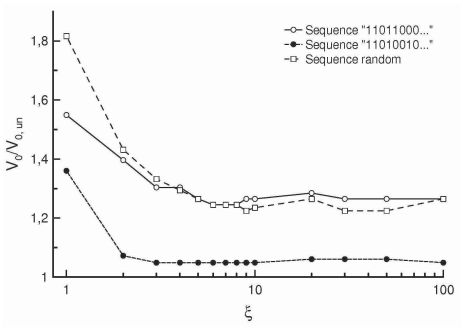

Fig. 9. Multipactor RF voltage threshold normalized to the unmodulated multipactor voltage threshold as a function of the ξ parameter for $f \times d = 1$ GHzmm. Signal modulated by QPSK with several bit sequences and $\alpha = 0.25$ RRC filter is used. Same unmodulated voltage threshold as in Fig. 1.

in Fig. 5 for the BPSK modulation scheme. However, BPSK thresholds are slightly higher than the thresholds obtained for the QPSK case, thus concluding that the BPSK modulation has a more perturbing effect on the multipactor effect.

In addition, the effect of varying the transmitted bit sequence on the multipactor threshold is considered for the case $f \times d = 1$ GHzmm. Thus, multipactor voltage thresholds are calculated for three different bit sequences: the first sequence is 11011000..., which is previously considered; the second sequence has four phase jumps of 90°, resulting in 11010010...; and the third one is a completely random sequence. Numerical results are shown in Fig. 9, observing that the threshold curve shape is not affected by the bit sequence employed. However, the lower voltage threshold variations are found for the bit sequence with four phase jumps of 90°, which is revealed as the less disturbing multipactor scenario for the QPSK modulation.

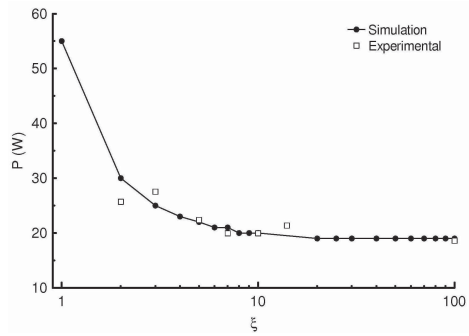

Fig. 10. Multipactor power threshold as a function of the ξ parameter at $f = 435$ MHz. Signal modulated by BPSK with rectangular filter and 101010... sequence. Simulation and experimental results.

IV. Experimental Results

An experiment to validate our formulation is performed at the RF High Power Laboratory of European Space Agency and Val Space Consortium [16]; the experimental setup is the standard one, commonly employed in multipactor measurements [17]. The coaxial sample tested in the laboratory is the same one used for the simulations in Section III. Measurements are carried out at with an RF carrier frequency of $f = 435$ MHz, which corresponds to a frequency gap of $f \times d = 0.859$ GHzmm. The RF signal is modulated with BPSK and a rectangular filter is used. The transmitted bit sequence is 101010... The multipactor RF power threshold is measured for several values of ξ. Both experimental and theoretical results are shown in Fig. 10, where a good agreement that fully validates the presented analysis algorithm is observed.

V. Conclusion

In this paper, we studied the multipactor effect in coaxial waveguides excited by a PSK digitally modulated signal. For this purpose an in-house code was developed to perform the multipactor simulations. For any of the PSK digital modulation schemes considered in this paper (i.e., BPSK and QPSK), it was demonstrated that the multipactor voltage threshold varied with regard to the multipactor voltage threshold value of a single-carrier unmodulated signal. The relation between the symbol duration and the RF carrier period was found as one of the most crucial parameters that affect the multipactor voltage threshold considering modulated signals. In addition, pulse shaping was considered for two different types of filters: the rectangular and RRC ones. Some typical electron effective trajectories were depicted for a better understanding of the multipactor phenomenon in such cases. Finally, an experiment was performed obtaining a good agreement between measurements and theoretical data.

REFERENCES

[1] J. Vaughan, "Multipactor," *IEEE Trans. Electron Devices*, vol. 35, no. 7, pp. 1172–1180, Jul. 1988.

[2] F. Zimmermann, "A simulation study of electron cloud instability and beam induced multipacting in the LHC," CERN, Geneva, Switzerland, CERN LHC Project Rep. 95, Feb. 1997.

[3] A. M. Pérez, C. Tienda, C. Vicente, S. Anza, J. Gil, B. Gimeno, and V. E. Boria, "Prediction of multipactor breakdown thresholds in coaxial transmission lines for traveling, standing, and mixed waves," *IEEE Trans. Plasma Sci.*, vol. 37, no. 10, pp. 2031–2040, Oct. 2009.

[4] S. Anza, C. Vicente, D. Raboso, J. Gil, B. Gimeno, and V. E. Boria, "Enhanced prediction of multipaction breakdown in passive waveguide components including space charge effects," in *IEEE MTT-S Microw. Symp. Dig.*, Jun. 2008, pp. 1095–1098.

[5] R. Udiljak, D. Anderson, M. Lisak, V. Semenov, J. Puech, "Multipactor in a coaxial transmission line. Part I: Analytical study," *Phys. Plasmas*, vol. 14, no. 3, p. 033508, Mar. 2007.

[6] V. Semenov, N. Zharova, R. Udiljak, D. Anderson, M. Lisak, and J. Puech, "Multipactor in a coaxial transmission line. II: Particle-in-cell simulations," *Phys. Plasmas*, vol. 14, no. 3, p. 033509, Mar. 2007.

[7] S. Anza, C. Vicente, J. Gil, M. Mattes, D. Wolk, U. Wochner, V. E. Boria, B. Gimeno, and D. Raboso, "Prediction of multipactor breakdown for multicarrier applications: The quasi-stationary method," *IEEE Trans. Microw. Theory Tech.*, vol. 60, no. 7, pp. 2093–2105, Jul. 2012.

[8] J. E. Gilley, *Digital Modulation: A Review of Basic Concepts*. Lincoln, NE, USA: Transcrypt International, Inc., Aug. 2003.

[9] V. Semenov, M. Buyanova, D. Anderson, M. Lisak, R. Udilkak, and J. Puech, "Multipactor in microwave transmission systems using quadrature phase-shift keying," *IEEE Trans. Plasma Sci.*, vol. 38, no. 4, pp. 915–922, Apr. 2010.

[10] E. Somersalo, P. Ylä-Oijala, D. Proch, and J. Sarvas, "Computational methods for analyzing electron multipacting in RF structures," *Part. Accel.*, vol. 59, pp. 107–141, Aug. 1980.

[11] L. Verlet, "Computer 'experiments' on classical fluids. I. Thermodynamical properties of Lennard-Jones molecules," *Phys. Rev.*, vol. 159, no. 1, pp. 98–103, Jul. 1967.

[12] S. Riyopoulos, "Multipactor saturation due to space-charge-induced debunching," *Phys. Plasmas* vol. 4, no. 5, pp. 1448–1462, May 1997.

[13] A. B. Carlson, P. Crilly, and P. B. Crilly, *Communication Systems*, 5th ed. New York, NY, USA: McGraw-Hill, 2009.

[14] D. González-Iglesias, A. M. Pérez, S. Anza, J. Vague, B. Gimeno, V. E. Boria, D. Raboso, C. Vicente, J. Gil, F. Caspers, and L. Conde, "Multipactor in a coaxial line under the presence of an axial DC magnetic field," *IEEE Electron Device Lett.*, vol. 33, no. 5, pp. 727–729, May 2012.

[15] S. Anza, C. Vicente, B. Gimeno, V. E. Boria, and J. Armendáriz, "Long-term multipactor discharge in multicarrier systems," *Phys. Plasmas*, vol. 14, no. 8, p. 082112, Aug. 2007.

[16] Val Space Consortium-European Space Agency RF High-Power Laboratory. Valencia, Spain [Online]. Available: http://www.val-space.com

[17] *Multipaction Design and Test*, Standard ECSS-E-20-01A, 2003.

Daniel González-Iglesias is currently pursuing the Ph.D. degree in physics with the University of Valencia, Valencia, Spain.

His current research interests include multipacting simulation of RF high-power passive components.

Maria Pilar Belloch Rodríguez received the degree in electrical engineering from Universidad Politécnica de Valencia, Valencia, Spain, in 2012.

She participated in a Trainee Program at the European Space Agency.

Òscar Monerris Belda received the Masters degree from Universidad Politécnica de Valencia, Valencia, Spain, in 2009.

His current research interests include high RF power effects in space applications, including the analysis of multicarrier and modulated signals.

Benito Gimeno (M'01) received the Ph.D. degree from the University of Valencia, Valencia, Spain, in 1992.

His current research interests include electromagnetic analysis and design of microwave passive components as well as RF breakdown high-power effects.

Vicente E. Boria (S'91–A'99–SM'02) received the Doctor Ingeniero de Telecomunicación degree from Universidad Politécnica de Valencia, Valencia, Spain, in 1997.

He is currently a Full Professor with Universidad Politécnica de Valencia.

David Raboso received the Masters degree in physics from the University Autónoma of Madrid, Madrid, Spain, in 1992.

He is currently a Chairman of European Networks and ECSS Working Groups in multipactor effect, corona, RF high power, and PIM.

Vladimir E. Semenov received the Ph.D. degree from the Institute of Applied Physics of Russian Academy of Sciences, Moscow, Russia, in 1983.

He is currently a Professor with the University of Nizhny Novgorod, Nizhny Novgorod, Russia.

Publication V

Experimental analysis of the multipactor effect with RF pulsed signals

IEEE Electron Device Letters, vol. 36, no. 10, pp. 1085-1087, October 2015

Experimental Analysis of the Multipactor Effect With RF Pulsed Signals

D. González-Iglesias, O. Monerris Belda, M. E. Díaz, B. Gimeno, *Member, IEEE*, V. E. Boria, *Senior Member, IEEE*, and D. Raboso

***Abstract*— The main goal of this letter is the analysis of the multipactor effect within a coaxial waveguide excited by an RF pulsed signal. The variation of the multipactor RF voltage threshold with the ON interval length of the pulse has been analyzed. To reach this aim, an in-house multipactor simulation code based on the Monte-Carlo algorithm has been implemented. The numerical simulations show that the multipactor RF voltage threshold increases as the ON pulse interval diminishes. In addition, an experiment was carried out to validate the proposed theoretical model, and demonstrating the excellent agreement between the theory and the experimental data. Finally, the results are compared with the 20-gap-crossing rule used in the space standard document (ECSS-E20-1A).**

***Index Terms*— Multipactor effect, RF breakdown, coaxial waveguide, RF pulse, "20-gap-crossing" rule.**

I. Introduction

MULTIPACTOR breakdown is an electron avalanche-like discharge occurring in components operating under vacuum conditions and high-power RF electromagnetic fields [1]. It can appear in a wide variety of scenarios, such as satellite passive communication devices, klystrons, and accelerator structures. The multipactor effect occurs when an RF electric field accelerates free electrons inside the device, impacting on the metallic walls of the structure. If the kinetic energy of the impacting electrons is high enough, secondary electrons may be released from the surface thus increasing the electron population inside the device. Once the number of electrons becomes very high, an electrical current is established between the walls of the component, degrading the component performance.

Focusing on space communications, multipactor reveals as a restrictive limitation to the power handling capabilities of many satellite RF and microwave devices. This is quite an inconvenience since the increasing number of users, requiring higher and higher bit rates, implies the necessity of increasing power levels in the RF and microwave payload equipment.

Multipactor has been deeply studied in many kinds of geometries, involving different surface materials (metals, dielectrics and ferrites). Most of this work has been made assuming a time harmonic excitation, i.e. continuous wave (CW) operation. However, in many microwave applications, pulsed operation involving pulses of finite length in time separated by zero power intervals is employed rather than the CW case. Even more, in telecommunication satellites, within the pulses, multicarrier operation with one or more modulated carriers is employed in order to use efficiently the limit frequency band available. Up to now, the standard adopted by the European Space Agency (ESA) for multicarrier multipactor design is based on the "20-gap-crossing" rule [2], which is used as an engineering "rule of thumb" for assessing the risk of multipactor breakdown. Understanding of the multipactor phenomenon when involving constant envelope RF pulses, seems to be the first step towards the comprehension of realistic signals, where the signal envelope varies with time within the pulse. According to the authors' knowledge, there are few studies concerning microwave pulse width effect in the multipactor discharge [3]–[5], but none of them present both theoretical and experimental results. In this manuscript, we analyze the multipactor behavior in constant envelope RF pulses from both a theoretical and experimental point of view. The numerical simulations carried out with our developed in-house multipactor code present a good match with the experimental data. Thus, it is both theoretically and experimentally demonstrated the inefficacy of the "20-gap-crossing" rule predictions and it is revealed the need of more realistic rules for the design of components operating under multicarrier regimes.

This letter analyses the effect of the ON pulse duration in the multipactor RF voltage threshold within a standard coaxial transmission line. During the ON interval of the RF pulse, the electron population in the device grows whenever the RF voltage exceeds the CW multipactor RF voltage threshold. However, during the OFF interval the electron population drops, since the electrons are mainly absorbed by the walls of the component. For the onset of a multipactor discharge a high growth of the initial electron population is required and, if the ON pulse interval is short enough, the electron population might not reach the minimum required to trigger the discharge.

Manuscript received August 4, 2015; accepted August 10, 2015. Date of publication August 13, 2015; date of current version September 23, 2015. The work of O. Monerris Belda was supported by the European Regional Development Fund. The review of this letter was arranged by Editor A. Ortiz-Conde.

D. González-Iglesias and B. Gimeno are with the Departamento de Física Aplicada, Institute of Materials Science, Universidad de Valencia, Valencia 46100, Spain (e-mail: benito.gimeno@uv.es).

O. Monerris Belda is with Val Space Consortium, Valencia 46022, Spain.

M. E. Díaz is with the Departamento de Física Aplicada, Escola Tècnica Superior d'Enginyeria, Universidad de Valencia, Valencia 46010, Spain.

V. E. Boria is with the Departamento de Comunicaciones, Instituto de Telecomunicaciones y Aplicaciones Multimedia, Universitat Politècnica de València, Valencia 46022, Spain.

D. Raboso is with the European Space Research and Technology Centre, European Space Agency, Noordwijk AZ 2201, The Netherlands.

Color versions of one or more of the figures in this letter are available online at http://ieeexplore.ieee.org.

Digital Object Identifier 10.1109/LED.2015.2468068

In this work, we focus on the analysis of low duty cycle pulses, i.e. the time elapsed between two consecutive ON intervals is long enough to ensure electron population decays to zero between consecutive pulses.

The document is organized as follows. In Section II, the theoretical model employed for multipactor simulations is discussed. Next, in Section III, numerical and experimental results are shown for a particular coaxial sample. A brief explanation of the multipactor experimental set-up is also included. Besides, the results are compared to the multipactor RF voltage thresholds derived from the "20-gap-crossing" rule. Finally, in Section IV, the conclusions are outlined.

II. Theory

To analyse the multipactor phenomenon under the excitation of pulsed and ultra short pulsed signals, a home-made software based on the individual electron model has been implemented for coaxial transmission lines. This code is based on the 3-D tracking of a set of electrons. Each electron is individually tracked. Electron motion is governed by the RF electric and magnetic fields corresponding to the fundamental coaxial TEM mode. Equation of the electron motion is derived from Lorentz force, and is solved numerically by means of the Velocity-Verlet algorithm [6]. When an electron collides with the metallic coaxial walls, the impacting electron can be absorbed, it can be elastically or inelastically backscattered, or true secondaries can be produced. Each of these possible interactions between the electron and the surface are modeled as the different contributions of the Secondary Electron Yield (SEY) function. In this work, the SEY model and formulas described in [7] and [8], which were already successfully implemented in CST Particle Studio [9], are employed.

The multipactor onset criteria is based on the detection of a high enough electron population within the component, in order to ensure that the discharge effects are noticeable from an experimental point of view. According to the multipactor literature, the electron population is expected to grow until a steady-state (saturation level) is reached [10]. At this stage the electron population is maximum (with oscillations around this value) and the detection is supposed to take place. Previous numerical simulations presented in [11] show that the saturation level is within the range of 10^9-10^{12} electrons, depending on the particular characteristics of the case (waveguide dimensions, SEY properties, RF voltage). In this work we chose the saturation level of $N_{sat} = 10^{12}$ since, after trying different levels of N_{sat}, we saw that the aforementioned value is the best one to fit the experimental data. This value has been set as the population level to determine the onset of the multipactor discharge in the simulation routine.

III. Numerical and Experimental Results

The coaxial dimensions for multipactor simulations, as well as for the test sample, are $a = 1.238$ mm and $b = 2.850$ mm for the inner and outer conductor radii, respectively; thus, the gap length is $d = b - a = 1.612$ mm. The coaxial length is 100 mm. Both conductors are made of copper and the SEY data for this material is extracted from [12]. According to the model proposed in [8], the fitting parameters for the SEY true secondaries contribution are: $\delta_m = 1.77$, $W_m = 277$ eV, and $s = 1.539$. The operational test frequency is $f = 1.145$ GHz.

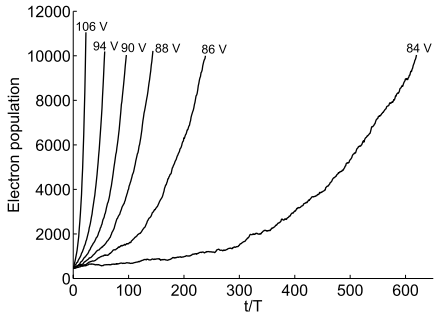

Fig. 1. Evolution of the electron population within the coaxial waveguide excited by a continuous wave signal as a function of the time normalized to the RF period for different RF voltages ($T = 1/f$).

The starting number of electrons in the simulations is $N_i = 500$, and the final number of electrons at which the code stops is $N_e = 10^4$. As stated in the previous section, the saturation level for the onset of the discharge is chosen to be $N_{sat} = 10^{12}$. However, due to computational limitations, a standard PC is not able to hold a simulation where such a number of particles is simultaneously tracked. In fact, other existing simulation codes use the called super-particles that contain a number of electrons (even fractions of them), all with the same dynamical variables. Nevertheless, using this approach, the statistical representation of the process becomes worse as the number of electrons increases while the number of super-particles becomes constant. To overcome this inconvenience, the following approach is proposed relying on the numerical results obtained from the simulations with $N_e = 10^4$ being the maximum number of simulated electrons. The electron population as a function of the RF voltage is depicted in Fig. 1. These data show that the electron population increment follows an exponential trend. For a pure continuous wave RF signal, the presence of this exponential trend in the electron population would be sufficient to ensure that the discharge will eventually occur. However, this criterion is not enough in this case, since we are dealing with pulsed signals where the RF wave is active only during the time t_{on}. Numerical results shown in Fig. 1 for different amplitudes of the RF voltage are fitted to an exponential function, and then are used to predict the time lapse that requires the electron population to reach the saturation level. If the predicted time lapse is lower than t_{on}, it is assumed that multipator can take place. This method can be used to estimate the multipactor RF voltage threshold for any length of the RF pulse.

In order to validate the theoretical model, an experimental test campaign was carried out at the ESA-VSC [13] European high power radiofrequency joint laboratory; the experimental set-up (see Fig. 2) is the standard one commonly employed in multipactor measurements (see [2] for a detailed description). Three detection methods were employed: the measurement of nulling between the incident and the reflected waves at the

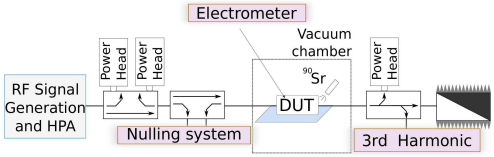

Fig. 2. Multipactor test bed diagram with the detection systems. Note that a Strontium-90 radioactive source was employed for electron seeding purpose.

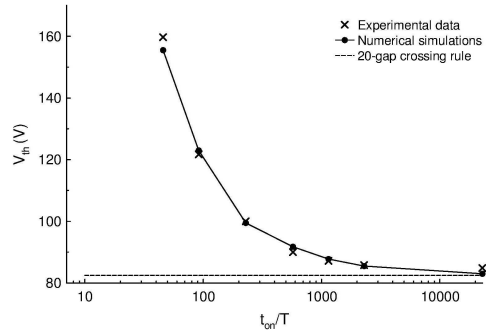

Fig. 3. Multipactor RF voltage threshold for several RF pulse lengths normalized to the RF period of the carrier signal. Experimental and theoretical results, as well as the 20-gap-crossing rule predictions, are shown.

carrier frequency, the third-harmonic frequency detection of the transmitted signal, and the measurement of the secondary electrons generated in the discharge with a biased electron probe. Following the multipactor testing ECSS standard [2], in order to determine the threshold level it is required a minimum of two detection methods simultaneously triggered. From the experimental point of view, it was observed that for pulses longer than 1μs all the detection system were monitored together. Nevertheless, for shorter pulses it was observed that only the electrometer and the harmonic system were able to detect the discharges.

Both experimental and theoretical results are shown in Fig. 3 showing good agreement between them. It is noticed that the shorter the pulse, the higher the RF multipactor voltage threshold. In Fig. 1 it was already noticed that higher RF voltage involves higher rate of growth in the electron population. Consequently, when the pulse length diminishes a faster increase in the electron population is needed to reach the same saturation level. It must also be mentioned that ultra short pulses with $t_{on}/T = 22.9$ and $t_{on}/T = 11.45$ were measured, but no multipactor discharge was detected up to 199 V, which was the maximum RF voltage delivered by the available RF power amplifier. Multipactor simulations for the two aforementioned pulses also predicted no multipactor discharge up to the voltage tested level. Measuring multipactor in pulses shorter than $t_{on}/T = 11.45$ was not possible, since considerable distortion of the RF pulse envelope was observed due to limitations in the RF power amplifier performance.

It must be also mentioned that the experimental reuslts shown in this work are consistent with those presented in [5], where the variation of the multipactor RF power threshold with the pulse width was tested. However, pulses shorter than 240 T were not considered in [5], thus not considering the very interesting region concerning pulses of very short length.

Finally, a brief comparison between our results and the predictions of the "20-gap-crossing" rule [2] is presented. Basically, this rule states that with a multi-carrier signal, multipactor events will be detectable whenever the power is maintained above the CW threshold for a time period about 20 gap crossings of the electron. For this particular case, $f \times d = 1.846$ GHzmm, so multipactor with order one is expected. Consequently, the time for 20 crossing gaps is 10 T. According to this rule, the multipactor RF voltage threshold is a flat line (see Fig. 3) at the level of the continuous wave threshold for pulses longer than 10 T, whereas no discharge would be expected below this time. It can be concluded that the "20-gap-crossing" rule is not applicable in this case, since it does not reproduce the experimental results.

IV. Conclusions

In this letter, the authors have studied the multipactor effect with RF pulsed signals within a coaxial waveguide. An in-house code was developed to perform multipactor simulations, and the results obtained from the experimental test are in excellent agreement to the theoretical predictions. Both numerical and experimental results show the increment in the multipactor RF voltage threshold as the ON pulse interval shortens. To conclude, it has been shown that the so-called "20-gap-crossing" rule reveals considerable discrepancies with the results presented in this work.

References

[1] J. R. M. Vaughan, "Multipactor," *IEEE Trans. Electron Devices*, vol. 35, no. 7, pp. 1172–1180, Jul. 1988.
[2] ECSS Secretariat, "Multipaction design and test," ESA-ESTEC Requirements & Standards Division, Noordwijk, The Netherlands, ESA-ESTEC, Tech. Rep. ECSS-E-20-01A, 2003.
[3] J. Rasch, D. Anderson, and V. E. Semenov, "Multipactor breakdown in microwave pulses," *J. Phys. D, Appl. Phys.*, vol. 46, no. 50, p. 505201, 2013.
[4] S. Anza *et al.*, "Long-term multipactor discharge in multicarrier systems," *Phys. Plasmas*, vol. 14, no. 8, p. 082112, 2007.
[5] N. Le Gallou, C. Miquel-Espanya, S. Matinfar, C. Ernst, and F. De Paolis, "Multipactor threshold and margins using realistic modulated signals," in *Proc. MULCOPIM*, Valencia, Spain, Sep. 21–23, 2011.
[6] L. Verlet, "Computer 'Experiments' on classical fluids. I. Thermodynamical properties of Lennard-Jones molecules," *Phys. Rev.*, vol. 159, no. 1, pp. 98–103, Jul. 1967.
[7] M. A. Furman and M. T. F. Pivi, "Simulation of secondary electron emission based on a phenomenological probabilistic model," Lawrence Berkeley Nat. Lab., Univ. California, Berkeley, CA, USA, Tech. Rep. LBNL-52807, Jun. 2003.
[8] J. de Lara *et al.*, "Multipactor prediction for on-board spacecraft RF equipment with the MEST software tool," *IEEE Trans. Plasma Sci.*, vol. 34, no. 2, pp. 476–484, Apr. 2006.
[9] *Computer Simulation Technology (CST)*. [Online]. Available: http://www.cst.com, accessed Jun. 2015.
[10] S. Riyopoulos, "Multipactor saturation due to space-charge-induced debunching," *Phys. Plasmas*, vol. 4, no. 5, pp. 1448–1462, 1997.
[11] E. Sorolla, A. Sounas, and M. Mattes, "Space charge effects for multipactor in coaxial lines," *Phys. Plasmas*, vol. 22, no. 3, p. 033512, 2015.
[12] V. Baglin *et al.*, "A summary of main experimental results concerning the secondary emission of copper," CERN, Geneva, Switzerland, LHC Project Rep. 472, 2002.
[13] European Space Agency RF High-Power Laboratory, Valencia, Spain. *Val Space Consortium*. [Online]. Available: http://www.val-space.com, accessed Jun. 2015.

Publication VI

Multipactor RF breakdown in coaxial transmission lines with digitally modulated signals

IEEE Transactions on Electron Devices, vol. 63, no. 10, pp. 4096-4103, October 2016

Multipactor RF Breakdown in Coaxial Transmission Lines With Digitally Modulated Signals

Daniel González-Iglesias, Óscar Monerris, Benito Gimeno Martínez, *Member, IEEE*, María Elena Díaz, Vicente E. Boria, *Senior Member, IEEE*, and Petronilo Martín Iglesias

***Abstract*— The aim of this paper is the study of the RF multipactor breakdown in coaxial transmission lines excited by a single carrier with a digitally modulated signal. Employing an in-house developed code, numerical simulations are performed to determine the RF multipactor voltage threshold for several digitally modulated signals under different modulations schemes: quadrature phase-shift keying, 16-quadrature amplitude modulation, 16-amplitude and phase-shift keying, and 32-amplitude and phase-shift keying. Moreover, a coarse method based on the envelope integration to determine the RF multipactor voltage threshold when involving arbitrary digital modulations is also presented. These results are also compared with the "20-gap-crossing" rule used in the space standard document ECSS-E20-1A. In order to validate the theoretical results, a test campaign was performed for realistic modulated signals, finding good agreement between theoretical predictions and experimental data.**

***Index Terms*— "20-gap-crossing" rule, amplitude and phase-shift keying (APSK), coaxial waveguides, digital modulations, multipactor effect, quadrature amplitude modulation (QAM), quadrature phase-shift keying (QPSK), RF breakdown, root-raised-cosine filter.**

I. Introduction

IN PRESENT and near-future space sector applications, higher power handling capabilities as well as larger component integration are being increasingly demanded. These harder requirements result in extremely high electromagnetic field densities within the devices, thus leading to major risks of RF breakdown effects. With regard to RF breakdown, two basic phenomena are meant: corona and multipactor discharge effects. Minimizing the risk of a potential failure due to any of those undesired effects is one of the major concerns in the design of the payload for the space communications satellites.

Multipactor is a breakdown discharge caused in high vacuum conditions by an electron avalanche [1]. The avalanche originates due to the release of secondary electrons when high-energy electrons collide with the walls of the device. The multipactor phenomenon can cause increasing losses and/or distortion of the RF signal, as well as potential damages on RF components and subsystems.

Therefore, it is crucial to be sure that RF breakdown does not occur during the satellite lifetime, since it can be catastrophic for its operation. Presently, the achievement of sufficient RF breakdown security margins, which are hardly achievable, implies high-cost design phase, which may result in a bigger and heavier design and expensive test campaigns for space sector companies. In addition, the lack of reliable models and software tools for the prediction of these phenomena does not help to ease the design process of components for space applications, which should minimize the risk of RF breakdown effects.

More attention is being increasingly paid to these breakdown phenomena through research and technological activities promoted either by space institutions (i.e., the European Space Agency, and specially the European Space and Research Technology Centre) or by companies devoted to design and manufacture space RF and microwave hardware.

Most of the multipactor studies do consider nonmodulated RF signals [2]–[5], whereas realistic satellite communication systems are usually based on multicarrier operation and modulated carriers to efficiently use the available frequency spectrum. These modulated RF signals are far different from the nonmodulated (or pure harmonic) case. According to the authors' knowledge, there is limited literature about multipactor with digitally modulated signals [6]–[8].

This paper can be considered as an extension of [9]. This initial work presented some hints on this topic but was constrained to single-level signals (the amplitude was changed only by the effect of the filtering). In this paper, multilevel

Manuscript received June 27, 2016; revised July 15, 2016 and July 28, 2016; accepted July 28, 2016. Date of publication August 12, 2016; date of current version September 20, 2016. This work was supported in part by the European Space Agency through the EXPRO Project entitled Development of a Software Tool for the Study of RF Breakdown for Realistic Scenarios: Multicarrier and Modulated Signals under Contract 4000111147/14/NL/GLC and in part by the European High RF Power Space Laboratory of European Space Agency and Val Space Consortium for contributing with its installations Laboratory through the European Regional Development Fund, A way of Making Europe. The review of this paper was arranged by Editor M. Thumm.

D. González-Iglesias and Ó. Monerris are with Val Space Consortium, Valencia 46022, Spain (e-mail: daniel.gonzalez-iglesias@uv.es; oscar.monerris@valspace.com).

B. G. Martínez is with Departamento de Física Aplicada, Instituto de Ciencia de Materiales, Universidad de Valencia, Valencia 46100, Spain (e-mail: benito.gimeno@uv.es).

M. E. Díaz is with the Departamento de Informática, Escuela Técnica Superior de Ingeniería, Universidad de Valencia, Valencia 46100, Spain (e-mail: elena.diaz@uv.es).

V. E. Boria is with the Departamento de Comunicaciones, Instituto de Telecomunicaciones y Aplicaciones Multimedia, Universitat Politècnica de València, Valencia 46022, Spain (e-mail: vboria@dcom.upv.es).

P. M. Iglesias is with the European Space Agency, European Space Research and Technology Centre, Noordwijk 2201, The Netherlands (e-mail: petronilo.martin.iglesias@esa.int).

Digital Object Identifier 10.1109/TED.2016.2596801

signals are considered adding an extra degree of complexity. Thus, this paper covers a wider range of digital modulations such as 16-quadrature amplitude modulation (16-QAM), 16-amplitude and phase-shift keying (16-APSK), and 32-amplitude and phase-shift keying (32-APSK), besides quadrature phase-shift keying (QPSK), which was already considered in [9]. The widespread root-raised-cosine filter is used all through this paper. Significant enhancements on the multipactor simulation software have been done with regard to the previously developed version of the code, resulting in more accurate predictions of the RF multipactor voltage threshold. In addition to the accurate simulation, a coarse method based on the envelope integration for a roughly estimation of the RF multipactor voltage threshold with an arbitrary digitally modulated signal is presented. This method, whose assumptions are similar to those of the quasi-stationary model proposed in [10], exclusively uses the results obtained from numerical simulations with a nonmodulated single carrier signal, presenting the advantage of being much faster than individual electron numerical simulations for the digitally modulated signals. Up to now, the standard adopted by the European Space Agency for multipactor design and testing when nonpure harmonic signals are involved is based on the "20-gap-crossing" rule [11], which is used as an engineering "rule of thumb" for assessing the risk of multipactor breakdown. RF multipactor voltage threshold predictions derived from the "20-gap-crossing" rule are also computed for comparison with the numerical results provided by our two developed methods. Finally, an experimental multipactor test campaign was carried out to support the theoretical results. The comparison between the measurements and simulations is very good, fully validating the presented method.

II. Theory

A. Multipactor Simulation Code

Monte Carlo software to analyze the multipactor effect in coaxial transmission lines excited by arbitrary RF signals has been developed. This algorithm combines the advantages of the individual electron and effective electron models. On the one hand, the individual electron model relies on the tracking of a set of particles, where each particle represents a real individual electron. When one of these individual electrons collides with the metallic walls of the coaxial, the impacting electron can be absorbed and backscattered or secondary electrons can be released from the surface depending on the secondary electron yield (SEY) coefficient value at the impact point. On the other hand, the effective electron model [12] is based on the tracking of a set of superparticles called effective electrons, where each of these effective electrons represents one or more electrons (or even a fraction of them) through their effective charge and mass (expressed in terms of the unitary electron charge and mass). In the effective electron model, the number of superparticles remains fixed at the start of the simulation and the emission or absorption of electrons in a collision is modeled by increasing or decreasing the cumulative charge and mass of each effective electron. The individual electron model is expected to provide more accurate results since it is closer to underlying phenomenon physics, considering the real creation or destruction of each electron throughout the simulation. However, the number of electrons required for the onset of the multipactor discharge in a typical coaxial line is very high (around 10^{12}; see [13]), and the simultaneous tracking of such a number of individual particles clearly exceeds the computational capabilities of a standard personal computer (PC). Due to this limitation, a method that combines features from both models is used: at the beginning of the multipactor simulation, the initial electron population is considered as individual electrons; if during the simulation, the electron population increases and a certain level of particles is exceeded, then the individual electrons switch into effective ones. These effective electrons start to accumulate charge and mass instead of generating new particles.

For each tracked particle, the 3-D trajectory is computed by solving the nonrelativistic differential equation of motion using the velocity Verlet algorithm [14]. The differential equation of motion that governs the electron dynamics is derived from the Lorentz force, which depends on the total electric and magnetic fields that experience the electrons. There are two contributions: the external RF electromagnetic field and the electric field due to the space charge effect that takes into account the Coulombian repulsion among the electrons. The external RF field corresponds to the fundamental coaxial TEM mode of the coaxial transmission line carrying the digitally modulated signal

$$\vec{E}_{\mathrm{RF}}(\vec{r},t)=\frac{V(z,t)}{r\ln\left(\frac{b}{a}\right)}\hat{r},\quad \vec{B}_{\mathrm{RF}}(\vec{r},t)=\frac{V(z,t)}{r\,c\ln\left(\frac{b}{a}\right)}\hat{\phi} \tag{1}$$

where $V(z,t)$ is the digitally modulated signal voltage, $\hat{r}$ and $\hat{\phi}$ are the unitary vectors associated with standard cylindrical coordinates (r,ϕ,z), $\vec{r}$ is the position vector, c is the speed of light in vacuum, and b and a are the outer and inner radius of the coaxial guide, respectively. In multilevel digital modulations, the transmitted data are usually split into their in-phase (I) and quadrature (Q) components [15]. The I and Q components are orthogonal (or in quadrature) because they modulate two pure harmonic signals shifted by 90°. Hence, the voltage of the digitally modulated signal $V(z,t)$ can be written as

$$V(z,t)=V_0 g(z,t) \tag{2a}$$

$$g(z,t)=I(t)\cos(2\pi f t-\beta z)-Q(t)\sin(2\pi f t-\beta z) \tag{2b}$$

where V_0 is the voltage amplitude, f is the frequency of the RF carrier, t is the time, and $\beta=((2\pi f)/c)$ is the propagation factor of the coaxial TEM mode. The digitally modulated signals considered throughout this paper are normalized, in order to allow an easy comparison of the RF multipactor voltage thresholds for different modulation schemes and symbol sequences. This normalization ensures that the maximum peak value of the voltage of each signal is always V_0.

Regarding the electric field due to the space charge effect, it is modeled by means of a single electron sheet, following the same procedure proposed in [16] and validated in [13].

At each integration step, the code checks if the electron collides on the inner or the outer coaxial conductor. The interactions of electrons with surfaces are considered to be different contributions of the SEY function, which in this paper have been implemented according to the Furman and Pivi formulas described in [17] and [18]. After collision, the true secondary electrons depart with a random velocity following a Maxwellian distribution with a mean average energy of 3 eV for the magnitude of the velocity vector. The elevation angle related to a local spherical coordinates system centered at the impact point is determined by means of the cosine law distribution, whereas the azimuthal angle has been calculated with a uniform probability distribution [19].

B. Coarse Method for Multipactor Prediction Based on the Envelope Integration

In this section, we present a coarse method based on the integration of the envelope used to obtain the temporal evolution of the electron population within the device for any arbitrary digital modulation scheme. This method allows estimating the RF multipactor voltage threshold without performing the exact and costly multipactor numerical simulation, relying on a pure harmonic signal oscillating at the RF carrier frequency.

In the well-studied double-sided multipactor case with a pure time-harmonic signal, the electrons get resonant with the RF electric field and cross the gap between the metallic surfaces of the device in an odd number of half-periods of the RF signal ($m = 1, 3, 5, 7\ldots$), where m is known as the multipactor order. When an electron collides with the walls of the component, the number of secondary electrons released in such impact is given by the SEY coefficient δ, which depends on the impact kinetic energy and the angle of the primary electron. Assuming that all the electrons in the multipactor resonance impact with similar velocities and angles, the SEY will have approximately the same value in all the successive impacts. Taking into account this assumption, the evolution in time of the electron population for an RF pure harmonic signal can be expressed as

$$N(t_n) = N_0 \exp\left(t_n \frac{2f}{m} \ln \delta_{\text{av}}\right) = N_0 \exp(\alpha t_n) \tag{3}$$

where $t_n = n(m/(2f))$, n represents the n-impact with the surfaces, N_0 is the initial electron population at $t_0 = 0$, δ_{av} is the average SEY in the impacts, and $\alpha = ((2f)/(m)) \ln \delta_{\text{av}}$. According to (3), the number of electrons with time increases following an exponential trend, which depends on the average SEY value, the multipactor order, and the RF frequency. In fact, this behavior is clearly observed in the results provided by numerical simulations (see [13, Fig. 1]).

For a time-harmonic signal $V = V_0 \cos(2\pi f t)$, the value of the average SEY coefficient and therefore the α factor will vary with the RF voltage amplitude V_0. Thus, the dependence of α with the RF voltage amplitude can be obtained from the multipactor simulations performed for a pure harmonic signal at the RF carrier frequency f. To do this, a setsimulations is carried out of numerical simulations is carried out for differentsimulations is carried out RF voltage amplitudes. For each V_0 value, the model proposed in (3) is fitted to match the actual electron population evolution. If (3) is expressed in the form $\ln(N(t_n)/N_0) = \alpha t_n$, then a linear fit simply provides α. Fig. 1 shows the results of the fitting for the coaxial transmission line that will be used for multipactor simulations in Section III.

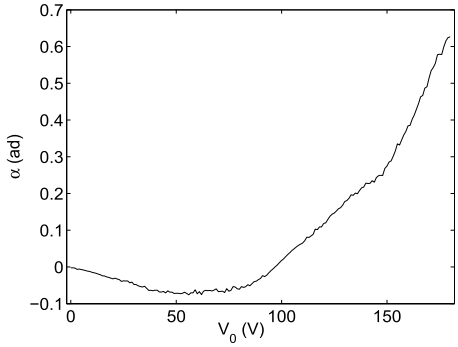

Fig. 1. Variation of α with the RF voltage amplitude for a coaxial transmission line with $a = 1.238$ mm and $b = 2.850$ mm, at an RF frequency of $f = 1.145$ GHz.

Note that in (3), the time variable t_n is discrete due to the fact that the electron population varies only at the time instant when the impact occurs. However, in a typical realistic multipactor scenario, the time required for the onset of the discharge is much greater than the time elapsed between two successive impacts, and as a consequence, it can be assumed that the time is a continuous variable. Under this consideration, the derivative of (3) is

$$\frac{dN}{N} = \frac{2f}{m} \ln \delta(t) dt. \tag{4}$$

It is well known that a digitally modulated signal given by (2) behaves like a harmonic oscillation at the RF carrier frequency whose envelope varies with time according to the sequence of transmitted symbols. Assuming that the variation of the envelope over the time interval between successive impacts is smooth, it can be considered that the electron resonant trajectories will be softly perturbed, and consequently, (4) will be still applicable. However, in the digital modulation case, the value of the average SEY coefficient will vary with time since the signal envelope, which determines the RF field strength, also does. As a consequence, in (4), the mean value of the SEY has been transformed into a time-dependent function, i.e., $\delta(t)$. If the variation of the average SEY coefficient with time is known, (4) can be integrated leading to

$$N(t) = N_0 \exp\left(\int_0^t \alpha(t)\, dt\right) \tag{5}$$

where $\alpha(t) = ((2f)/(m)) \ln \delta(t)$. Equation (5) gives the evolution of the electron population in the device for the case of considering as excitation an arbitrary digitally modulated signal. It should be emphasized that α depends on the instant

value of the RF voltage envelope, which indeed varies throughout the RF signal with time: this fact implies that α has an implicit dependence with time as seen in (5).

In order to apply this algorithm, the explicit dependence of α with time is reached in the following way. First, the envelope of the digitally modulated signal is computed by searching its maximum absolute value in each of the oscillations at the RF carrier frequency f. Then, the time variation of the signal envelope is combined with the α dependence on the RF voltage envelope, which was previously obtained from the time-harmonic signal case (recall Fig. 1). Finally, (5) can be numerically integrated obtaining the electron population evolution $N(t)$, which determines the potential existence of multipactor discharge.

This coarse method constitutes an alternative to the most accurate multipactor numerical simulations and allows obtaining roughly the RF multipactor voltage threshold for a digitally modulated signal. The main advantage of using this procedure is that it is much faster than the standard one. In fact, the computational time required to simulate the multipactor effect for a digitally modulated signal can spend several hours in a standard PC, while the proposed method reduces this time to a few minutes.

C. Conversion From Mean RF Power to RF Voltage Amplitude

When considering wideband digital modulations, the state-of-the-art power heads are not able to measure the power envelope of the signal. In these cases, thermal sensors are used instead providing an average measurement of the signal. However, the theoretical results from the multipactor analysis are often expressed in terms of RF voltage amplitude V_0. Therefore, in order to allow the comparison between them, experimental results regarding the multipactor threshold will be also presented in terms of RF voltage amplitude, rather than in terms of mean RF power. The formula that allows such a conversion is straightforward

$$V_0 = \sqrt{\frac{Z_0 \ln\left(\frac{b}{a}\right) \langle P \rangle}{2\pi \langle g(0,t)^2 \rangle}} \tag{6}$$

where $Z_0 = (\mu_0/\epsilon_0)^{1/2}$ is the impedance of free space, μ_0 is the vacuum magnetic permeability, ϵ_0 is the vacuum dielectric permittivity, $\langle g(0,t)^2 \rangle$ is the mean value of the square of $g(0,t)$, and $\langle P \rangle$ is the mean RF power measured in the laboratory, which is defined as

$$\langle P \rangle = \frac{1}{T_{\text{sig}}} \int_0^{T_{\text{sig}}} dt \int_S (\vec{E}_{\text{RF}}(\vec{r},t) \times \vec{H}_{\text{RF}}(\vec{r},t)) \cdot \vec{dS} \tag{7}$$

where T_{sig} is the digitally modulated signal duration, $\vec{H}_{\text{RF}} = \vec{B}_{\text{RF}}/\mu_0$, $\vec{dS}$ is the surface element parallel to the wave propagation direction, and S is the coaxial cross-sectional area.

III. Simulations

This section presents the simulation results carried out using both the accurate code and the coarse method. The dimensions of the coaxial line used throughout this work are $a = 1.238$ mm and $b = 2.850$ mm, and thus the gap length is $d = b - a = 1.612$ mm, and the coaxial characteristic impedance is 50 Ω. Both conductors are made of copper and the SEY data for this material are extracted from [20]. According to the model proposed in [18], the fitting parameters for the true secondaries SEY contribution are $\delta_m = 1.77$, $W_m = 277$ eV, and $s = 1.539$. For all considered modulation schemes, the RF carrier frequency is $f = 1.145$ GHz and the signal is filtered with a root-raised-cosine filter with a roll-off factor of 0.2. The criterion for the onset of the multipactor discharge is the presence of an electron population within the coaxial waveguide of 10^{12} electrons (or equivalently an electron density of 4.83×10^{17} m^{-3}; see [13]), for both the numerical simulations and the coarse method.

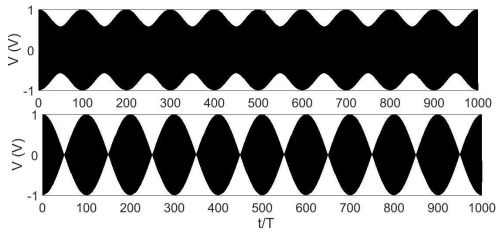

Fig. 2. Voltage of the RF signals as a function of the time normalized to the RF carrier period. Top: QPSK with Q sequence. Bottom: QPSK with X sequence. In both cases, $\xi = 100$, where $\xi = T_s/T$.

First, a QPSK digital modulation is considered, which is formed by four different symbols, with a phase shift of 90° between the neighbor symbols and 180° between opposite ones. The transmitted symbol sequence determines the shape of the RF signal and, consequently, strongly influences the RF multipactor voltage threshold. In the beginning, we consider two different simple sequences that are repeated indefinitely, and hence these signals are time periodic. The first sequence is denoted by Q and comprises a transition between two neighbor symbols. The second sequence is denoted by X and consists of a transition between opposite symbols. Besides the symbol sequence, the other modulation parameter that most influences the multipactor phenomenon is the ξ factor, which is defined as the ratio between the symbol duration T_s and the RF carrier period $T = 1/f$

$$\xi = \frac{T_s}{T}. \tag{8}$$

The RF voltage of the Q and X signals is depicted in Fig. 2. The RF multipactor voltage threshold in decibels for the Q and X signals, as a function of the ξ factor, is shown in Fig. 3. The RF multipactor voltage threshold of a digitally modulated signal, expressed in decibels, is defined according to the formula

$$V_{\text{th}}(dB) = 20 \log\left(\frac{V_{\text{th}}}{V_{\text{th,CW}}}\right) \tag{9}$$

where V_{th} is the RF multipactor voltage threshold and $V_{\text{th,CW}}$ is the RF multipactor voltage threshold of the nonmodulated case (pure harmonic signal) at the RF carrier frequency.

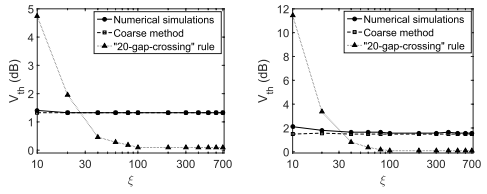

Fig. 3. RF multipactor voltage threshold as a function of the ξ factor for Q (left) and X (right) sequences. The results for both the numerical simulations and the coarse method and the "20-gap-crossing" rule are shown. Remember $\xi = T_s/T$.

In light of the results depicted in Fig. 3, it is observed that there is good agreement between the numerical simulations and the coarse method based on the envelope integration. However, there are significant discrepancies between our theoretical results and those derived from the "20-gap-crossing" rule. In fact, in both cases, the "20-gap-crossing" rule predicts a RF multipactor voltage threshold of 0 dB for a wide range of the analyzed ξ values, which implies no difference in the threshold value with regard to the nonmodulated scenario. For the two considered symbol sequences, it is evidenced that the dependence of the RF multipactor voltage threshold with the ξ factor mainly occurs for low ξ values, where an increase in the threshold for these values does appear, which is greater in the case of the X sequence. The rise in the multipactor threshold is smooth according to our theoretical predictions, whereas it is very stepped according to the "20-gap-crossing" rule. According to the numerical simulations, as well as to the coarse method, the multipactor threshold is greater for the X sequence than for the Q sequence. This can be understood by inspecting Fig. 2, where it is shown that the envelope minimum of the X signal falls to zero, while the envelope minimum of the Q sequence is quite above this value. Consequently, the form case requires having higher RF voltage amplitude to compensate for the lower amplitude regions, where electrons are mainly absorbed by the metallic surfaces.

The previous analyzed signals constitute a very simple case, where only two different symbols are periodically repeated in each case. However, the realistic transmitted signals, which involve a huge number of symbols, are far from this scenario. In order to consider realistic signals, a random symbol sequence has been generated for each of the following digital modulations: QPSK, 16-APSK, 32-APSK, and 16-QAM. The RF voltage of such signals is shown in Fig. 4.[1]

The QPSK signal has a length of 100 symbols, while the remaining signals have a length of 150 symbols. Proceeding in a similar way as the previous Q and X signals, the RF multipactor voltage threshold as a function of the ξ factor has been obtained for each of the modulations by means of numerical simulations, the coarse method, and the "20-gap-crossing" rule. These results are summarized in Fig. 5.

Good agreement is found between the results obtained from the numerical simulations and the coarse method,

[1]Telecom signals of ESA Galileo constellation provided by ESA Contract 4000111147/14/NL/GLC.

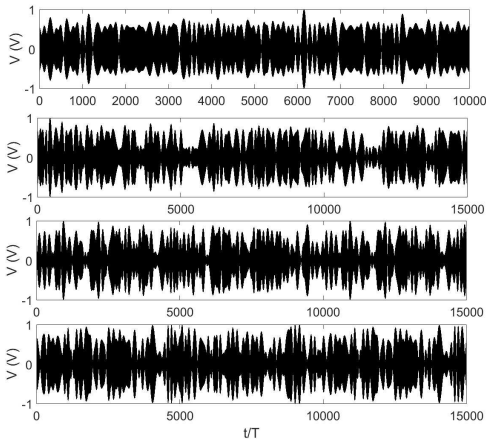

Fig. 4. Voltage of the RF signals as a function of time normalized to the RF carrier period. Top to bottom: QPSK, 32-APSK, 16-APSK, and 16-QAM. In all cases, $\xi = 100$. Remember $\xi = T_s/T$.

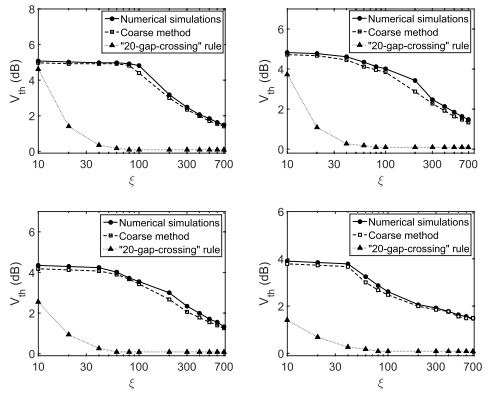

Fig. 5. RF multipactor voltage threshold in decibels as a function of the ξ factor for the random symbol sequences (remember $\xi = T_s/T$). Left to right and top to bottom: QPSK, 16-APSK, 32-APSK, and 16-QAM. The results for both the numerical simulations and the coarse method and the "20-gap-crossing" rule are shown.

while considerable discrepancies between the two aforementioned procedures and the "20-gap-crossing" rule are observed. The numerical simulations and the coarse method predict an increase in the RF multipactor voltage threshold when the ξ factor decreases. At $\xi = 700$, the RF multipactor voltage thresholds of the analyzed signals are within the interval [1.32, 1.48] dB, while at $\xi = 10$, the RF multipactor voltage threshold values are within the range from 3.90 dB (for 16-QAM) to 5.08 dB (for QPSK). Hence, a spread of RF multipactor threshold values among the different modulated signals can be observed as ξ diminishes.

In order to have a better understanding of the multipactor discharge onset when digitally modulated signals are involved,

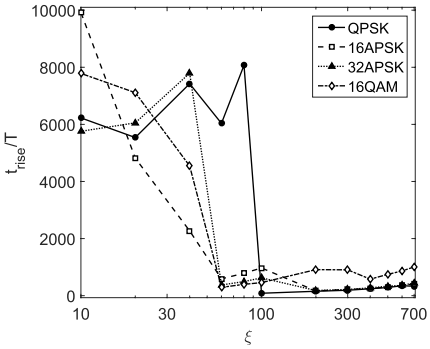

Fig. 6. Rise time for the onset of the discharge according to the multipactor numerical simulations as a function of the ξ value, for the modulations and sequences of Fig. 4. Remember $\xi = T_s/T$.

Fig. 6 displays the rise time of the discharge, i.e., the time interval that takes the electron population to evolve from a few starting electrons (500 initial electrons for these simulations) to the discharge level (10^{12} electrons), as a function of ξ factor for the modulated schemes and sequences considered in Fig. 5. Mainly, from the view of the results from Fig. 6, it is observed that the rise time for $\xi > 100$ is within the range [100, 1000] RF periods, whereas when $\xi < 100$, a sharp increase in the rise time is found, leading to rise durations well above the previous interval, reaching up to values within the range of [5000, 10 000] RF periods for the lowest ξ values that have been considered. A sharp variation in the rise time found at about $\xi \approx 100$ sets the transition between two different multipactor discharge regions. The first discharge region occurs for $\xi > 100$ and arises from a single envelope peak (in most of the cases in the main envelope peak of the RF signals). The second region (for $\xi < 100$) is a long-term discharge that takes greater time than the previous type, since it is produced throughout a large number of envelope peaks. Typically, in the middle of two consecutive envelope peaks, the RF envelope amplitude decreases below the nonmodulated RF multipactor voltage threshold, and as a consequence, there are time intervals where the electron population diminishes but does not drop to zero. Therefore, an accumulation process occurs from peak to peak that can eventually trigger the multipactor discharge [21].

IV. Experimental Results

An experimental test campaign to validate the theoretical results was performed at the ESA-VSC European High Power RF Laboratory [22]; the experimental setup is an improved version of the standard multipactor test bench described in [11]. The RF signal generator was done by means of wideband arbitrary waveform generators, which provided high-throughput IQ samples. The modulation and upconvertion was done in a Keysight PSG vector signal generator. Three detection methods for monitoring the multipactor discharge were available being tuned to capture fast events: the nulling system, third-harmonic detection, and electron probe. A 1 mCi activity Strontium-90 radioactive source was used for electron seeding purposes. The coaxial sample tested in the laboratory has the same geometry as the one used in the simulations. The SEY properties are also the same. Similarly, the RF carrier frequency for all the cases is $f = 1.145$ GHz. Measurements were performed in pulsed mode with a 40 μs (45 800 RF periods) width and a 4% duty cycle. During the measurements, the pressure in the vacuum chamber was in the level of 10^{-7} mbar.

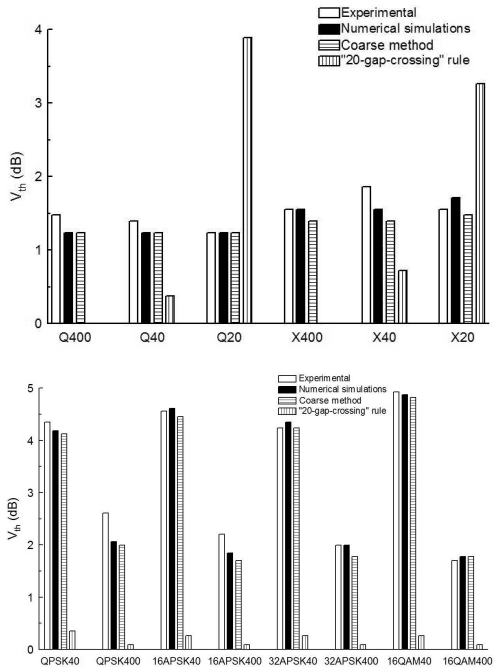

Fig. 7. RF multipactor voltage threshold in decibels for different digital modulated signals. The results from the experiment, numerical simulations, approximate method, and "20-gap-crossing" rule are presented. Top: Q and X signals. Bottom: random sequences of different modulations. In both cases, the number after the modulation name indicates the ξ value. Remember $\xi = T_s/T$.

The data obtained from the multipactor measurements have been summarized in Fig. 7, where the theoretical results from different methods described in Section III are also included. On the one hand, good concordance between the experimental results and the numerical simulations is observed, demonstrating the feasibility of the presented code to predict the RF multipactor voltage threshold with digitally modulated signals. In addition, acceptable agreement of the experimental data with the coarse method shows the capability of this faster procedure to roughly estimate the RF multipactor voltage threshold. On the other hand, it is noticed the remarkable discrepancies found between the results of the experiment and the predictions provided by the "20-gap-crossing" rule, which

in most of the cases reveals to be a very conservative approach, since the predicted RF multipactor voltage threshold is much below the real value measured in the laboratory.

V. Conclusion

In this paper, the effect of single-carrier digitally modulated signals in the RF multipactor voltage threshold for a coaxial transmission line has been studied. The QPSK, 16-APSK, 32-APSK, and 16-QAM digital modulations have been considered throughout this paper. The numerical simulations performed with the in-house developed code shows the variation in the RF multipactor voltage threshold with regard to the nonmodulated scenario. This variation in the RF multipactor voltage threshold is found to be dependent on both the ratio between the symbol time and the RF carrier period and the transmitted symbol sequence. In order to get an approximate estimation of the RF multipactor voltage threshold when digitally modulated signals are considered, an alternative method to numerical simulations has also been proposed. This procedure presents the advantage of being much faster than the accurate numerical simulations. Next, an experimental test campaign was performed to validate the theoretical predictions, finding good agreement with the numerical simulations and the coarse method based on the envelope integration. Finally, the experimental results are also compared with the application of the "20-gap-crossing" rule to these digitally modulated scenarios, finding considerable discrepancies between them. As a future research line, we propose to apply the coarse method based on the envelope integration into multicarrier analysis.

Acknowledgment

The authors would like to thank P. Angeletti and R. de Gaudenzi and D. Raboso (ESA staff member and Director of this facility) for providing the help and support.

References

[1] J. R. M. Vaughan, "Multipactor," *IEEE Trans. Electron Devices*, vol. 35, no. 7, pp. 1172–1180, Jul. 1988.

[2] A. M. Pérez *et al.*, "Prediction of multipactor breakdown thresholds in coaxial transmission lines for traveling, standing, and mixed waves," *IEEE Trans. Plasma Sci.*, vol. 37, no. 10, pp. 2031–2040, Oct. 2009.

[3] S. Anza, C. Vicente, D. Raboso, J. Gil, B. Gimeno, and V. E. Boria, "Enhanced prediction of multipaction breakdown in passive waveguide components including space charge effects," in *IEEE MTT-S Microw. Symp. Dig.*, Jun. 2008, pp. 1095–1098.

[4] R. Udiljak, D. Anderson, M. Lisak, V. E. Semenov, and J. Puech, "Multipactor in a coaxial transmission line. I. Analytical study," *Phys. Plasmas*, vol. 14, no. 3, p. 033508, Mar. 2007.

[5] V. E. Semenov, N. Zharova, R. Udiljak, D. Anderson, M. Lisak, and J. Puech, "Multipactor in a coaxial transmission line. II: Particle-in-cell simulations," *Phys. Plasmas*, vol. 14, no. 3, p. 033509, Mar. 2007.

[6] V. Semenov, M. Buyanova, D. Anderson, M. Lisak, R. Udilkak, and J. Puech, "Multipactor in microwave transmission systems using quadrature phase-shift keying," *IEEE Trans. Plasma Sci.*, vol. 38, no. 4, pp. 915–922, Apr. 2010.

[7] A. L. Sounas, J. R. Mosig, and M. Mattes, "Effect of digitally modulated signals on multipactor breakdown," in *Proc. 7th Eur. Conf. Antennas Propag. (EuCAP)*, Gothenburg, Sweden, 2013, pp. 33–36.

[8] N. Le Gallou, C. Miquel-Espanya, S. Matinfar, C. Ernst, and F. De Paolis, "Multipactor threshold and margins using realistic modulated signals," in *Proc. MULCOPIM*, Valencia, Spain, Sep. 2011.

[9] D. González-Iglesias *et al.*, "Analysis of multipactor effect using a phase-shift keying single-carrier digital modulated signal," *IEEE Trans. Electron Devices*, vol. 60, no. 8, pp. 2664–2670, Aug. 2013.

[10] S. Anza *et al.*, "Prediction of multipactor breakdown for multicarrier applications: The quasi-stationary method," *IEEE Trans. Microw. Theory Techn.*, vol. 60, no. 7, pp. 2093–2105, Jul. 2012.

[11] *Multipaction Design and Test*, document ECSS-E-20-01A, ESA-ESTEC, 2003.

[12] E. Somersalo, P. Ylä-Oijala, D. Proch, and J. Sarvas, "Computational methods for analyzing electron multipacting in RF structures," *Particle Accel.*, vol. 59, pp. 107–141, 1998.

[13] D. González-Iglesias, Ó. M. Belda, M. E. Díaz, B. Gimeno, V. E. Boria, and D. Raboso, "Experimental analysis of the multipactor effect with RF pulsed signals," *IEEE Electron Device Lett.*, vol. 36, no. 10, pp. 1085–1087, Oct. 2015.

[14] L. Verlet, "Computer 'experiments' on classical fluids. I. Thermodynamical properties of Lennard–Jones molecules," *Phys. Rev.*, vol. 159, no. 1, pp. 98–103, Jul. 1967.

[15] J. E. Gilley, *Digital Modulation: A Review of Basic Concepts*. Lincoln, NE, USA: Transcrypt International, Inc., Aug. 2003.

[16] S. Riyopoulos, "Multipactor saturation due to space-charge-induced debunching," *Phys. Plasmas*, vol. 4, no. 5, pp. 1448–1462, May 1997.

[17] M. A. Furman and M. T. F. Pivi, "Simulation of secondary electron emission based on a phenomenological probabilistic model," Lawrence Berkeley Nat. Lab., Univ. California, Berkeley, CA, USA, Tech. Rep LBNL-52807, Jun. 2003.

[18] J. de Lara *et al.*, "Multipactor prediction for on-board spacecraft RF equipment with the MEST software tool," *IEEE Trans. Plasma Sci.*, vol. 34, no. 2, pp. 476–484, Apr. 2006.

[19] J. Greenwood, "The correct and incorrect generation of a cosine distribution of scattered particles for Monte-Carlo modelling of vacuum systems," *Vacuum*, vol. 67, no. 2, pp. 217–222, Sep. 2002.

[20] V. Baglin, I. Collins, B. Henrist, N. Hilleret, and G. Vorlaufer, "A summary of main experimental results concerning the secondary electron emission of copper," CERN, Geneva, Switzerland, Tech. Rep. LHC-Project-Report-472, 2002.

[21] S. Anza, C. Vicente, B. Gimeno, V. E. Boria, and J. Armendáriz, "Long-term multipactor discharge in multicarrier systems," *Phys. Plasmas*, vol. 14, no. 8, p. 082112, 2007.

[22] European Space Agency RF High-Power Laboratory, Valencia, Spain. *Val Space Consortium*, accessed on May 2016. [Online]. Available: http://www.val-space.com

Daniel González-Iglesias received the Licenciado degree in physics and the master's degree in advanced physics from the University of Valencia, Valencia, Spain, in 2010 and 2011, respectively, where he is currently pursuing the Ph.D. degree in physics.

His current research interests include the multipacting simulation of RF high-power passive components.

Òscar Monerris Belda received the Telecommunication and M.Sc.Eng. degrees from Universitat Politècnica de València (UPV), Valencia, Spain, in 2009 and 2010, respectively, and the Economist and master's degree from the Universitat de València, Valencia, in 2014. He is currently pursuing the Ph.D. degree with UPV.

His current research interests include high power RF effects in space applications, such as multipactor and passive intermodulation.

Benito Gimeno Martínez (M'01) received the Licenciado degree in physics and the Ph.D. degree from the University of Valencia, Valencia, Spain, in 1987 and 1992, respectively.

He became a Full Professor with the University of Valencia in 2010. His current research interests include the electromagnetic analysis and design of microwave passive components, and RF breakdown high-power effects.

María Elena Díaz received the M.Sc.D. and Ph.D. degrees in physics from the University of Valencia, Valencia, Spain, in 1992 and 1997, respectively.

She held a post-doctoral fellowship with the European Molecular Biology Laboratory, Heidelberg, Germany, in 2000. She is currently a Lecturer with the Department of Computer Science, University of Valencia. Her research interests include biomedical image processing, motion analysis, discrete event simulation, and stochastic geometry.

Vicente E. Boria (S'91–A'99–SM'02) received the Doctor Ingeniero de Telecomunicación degree from the Universidad Politécnica de Valencia, Valencia, Spain, in 1997.

He is currently a Full Professor with Universidad Politécnica de Valencia.

Petronilo Martin Iglesias (M'12) was born in Cáceres, Spain, in 1980. He received the Telecommunication Engineering degree from the Polytechnic University of Madrid, Madrid, Spain, in 2002, and the master's degree from the University of Leeds, Leeds, U.K., in 2012.

His current research interests include filter synthesis theory, electromagnetic design, and high power prediction, as well as advanced manufacturing techniques for RF passive hardware.

Publication VII

Multipactor effect in a parallel-plate waveguide partially filled with magnetized ferrite

IEEE Transactions on Electron Devices, vol. 61, no. 7, pp. 2552-2557, July 2014

Multipactor Effect in a Parallel-Plate Waveguide Partially Filled With Magnetized Ferrite

Daniel González-Iglesias, Benito Gimeno, *Member, IEEE*, Vicente E. Boria, *Senior Member, IEEE*, Álvaro Gómez, *Member, IEEE*, Angel Vegas, *Member, IEEE*

***Abstract*— The aim of this paper is the analysis of the multipactor effect in a parallel-plate waveguide when a ferrite slab, transversally magnetized by a static magnetic field parallel to the waveguide walls, is present. Employing an in-house developed code, numerical simulations are performed to predict the multipactor radio frequency voltage threshold in such a ferrite-loaded waveguide. Variations of the ferrite magnetization field strength and the ferrite slab height are analyzed. Effective electron trajectories are also shown for a better understanding of the breakdown phenomenon, finding different multipactor regimes.**

***Index Terms*— Ferrite components, multipactor effect, parallel-plate waveguide, radio frequency (RF) breakdown.**

I. Introduction

MULTIPACTOR is a high-power radio frequency (RF) electromagnetic field phenomenon that appears on devices operating under vacuum conditions [1]. It is present in a wide range of different scenarios, such as passive components of satellite communication payloads, travelling-wave tubes or particle accelerators. In a vacuum environment, free electrons inside a microwave device are accelerated by the RF electric field, impacting against its metallic walls. If the electron impact energy is high enough, one or more secondary electrons may be released from the surface. When some resonant conditions are satisfied, secondary electrons get synchronized with the RF electric field, and the electron population inside the device grows exponentially leading to a multipactor discharge. The onset of a multipactor discharge in a device has negative effects that degrade its performance.

Multipactor research lines are aimed to study and characterize the phenomenon to predict under which conditions it will appear [2]–[6]. Some RF devices, such as filters, gyrators, circulators, isolators, and phase shifters, use ferrite components which are magnetized by means of an external permanent field [7]–[13]. The presence of such an external magnetic field is expected to perturb the classical resonant multipactor regimes [14]–[16]. Therefore, previous multipactor studies are not useful to predict the discharge on devices involving ferrites. However, according to [17], very few contributions about multipactor on ferrite materials can be found.

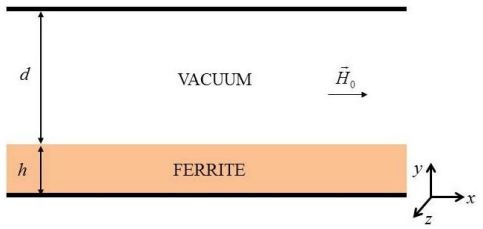

Fig. 1. Parallel-plate waveguide filled in part with a ferrite slab transversally magnetized by a static magnetic field.

In this paper, we are interested on the multipactor analysis of a metallic parallel-plate waveguide partially filled with a ferrite slab, placed just above the metal bottom wall, and transversally magnetized by a static (dc) magnetic field parallel to the waveguide walls (see Fig. 1). This paper might be used for a preliminary analysis of multipactor phenomenon in the aforementioned devices containing ferrite, specially, some kind of isolators (resonance isolator) and phase shifters (nonreciprocal latching phase shifters) [18]–[20]. This paper is organized as follows. First, in Section II, the theoretical model employed for the simulations is discussed. Next, in Section III, some multipactor susceptibility charts and the effects of the variation of some fundamental parameters, such as ferrite height and ferrite magnetization field strength, are introduced. Finally, in Section IV, the conclusions of this paper are outlined.

II. Theory

In this paper, the magnetization field is oriented along the x-axis, parallel to the waveguide walls. The waveguide structure under study is shown in Fig. 1, where d is the vacuum gap length, h is the ferrite slab height, and ε_r is its relative dielectric permittivity. The RF electromagnetic field is assumed to propagate along the positive direction of the z-axis. For the sake of simplicity, in this model the waveguide

Manuscript received March 24, 2014; revised April 15, 2014; accepted May 2, 2014. Date of publication May 22, 2014; date of current version June 17, 2014. The review of this paper was arranged by Editor M. Thumm.

D. González-Iglesias and B. Gimeno are with the Departamento de Fisica Aplicada–ICMUV, Universidad de Valencia, Valencia 46100, Spain (e-mail: daniel.gonzaleziglesias@uv.es; benito.gimeno@uv.es).

V. E. Boria is with the Departamento de Comunicaciones–ITEAM, Universidad Politécnica de Valencia, Valencia 46022, Spain (e-mail: vboria@dcom.upv.es).

Á. Gómez and A. Vegas are with the Department of Engineering of Information and Communications, Universidad de Cantabria, Cantabria 39005, Spain (e-mail: alvaro.gomez@unican.es; angel.vegas@unican.es).

Color versions of one or more of the figures in this paper are available online at http://ieeexplore.ieee.org.

Digital Object Identifier 10.1109/TED.2014.2322395

is supposed to be infinite in the z and x directions. In this paper, an $e^{j\omega t}$ time-dependence is implicitly assumed, ω being the angular frequency and t the time.

In any actual microwave device involving ferrites, an external static magnetic field H_0 must be applied to magnetize the ferrite. As a first approach, this external magnetic field is assumed to be uniform over the entire waveguide. When the applied magnetic field is strong enough, the ferrite reaches the saturation magnetization and behaves like a magnetic medium, described by a gyrotropic permeability tensor $\overleftrightarrow{\mu}$ (see [21, Formula 9.26]).

The RF electromagnetic fields supported by a waveguide with the aforementioned characteristics can be obtained analytically. In this situation, two family of electromagnetic field modes are found: TM^z ($H_z = 0$) and TE^z ($E_z = 0$). Following the same procedure outlined in [21], it can be analytically demonstrated that the TE^z modes have no vertical electric field component along the gap, so they are not suitable to hold a multipactor discharge and, as a consequence, they are not considered in our analysis. Otherwise, the TM^z modes do have vertical electrical component, so they may lead to a multipactor discharge. After imposing the boundary conditions on the significant surface interfaces of the problem, the propagation factor β of the TM^z modes is found by solving numerically the following characteristic equation:

$$\varepsilon_r k_1 \sinh(k_1 d)\, \cos(k_2 h) - k_2 \cosh(k_1 d)\, \sin(k_2 h) = 0$$

where $k_1^2 \equiv \beta^2 - \omega^2 \mu_0 \varepsilon_0$, $k_2^2 \equiv \omega^2 \mu_0 \varepsilon_0 \varepsilon_r - \beta^2$, μ_0, and ε_0 are the magnetic susceptibility and the dielectric permittivity of vacuum, respectively; $f = \omega/(2\pi)$ is the frequency of the RF electromagnetic field. The nonzero TM^z modal field components of the RF electromagnetic field in the vacuum region are given by

$$E_y(y,z,t) = \frac{V_0 k_1}{\sinh(k_1 d)} \cosh\left[k_1((d+h)-y)\right] \cos(\omega t - \beta z) \quad (1a)$$

$$E_z(y,z,t) = -\frac{V_0 k_1^2}{\beta \sinh(k_1 d)} \sinh\left[k_1((d+h)-y)\right] \sin(\omega t - \beta z) \quad (1b)$$

$$H_x(y,z,t) = -\frac{\omega \varepsilon_0}{\beta} E_y(y,z,t) \quad (1c)$$

where V_0 is the equivalent voltage obtained from the path integration of the RF electric field E_y along the vacuum gap from $y = h$ to $y = d + h$ at $z = 0$ plane and $t = 0$

$$V_0 = \int_h^{d+h} E_y(y,0,0)dy.$$

Note that for the considered TM^z modes the characteristic equation does not depend on the magnetic properties of the ferrite.

To obtain the numerical solution for our problem (a parallel-plate waveguide filled in part with a ferrite layer), a multipactor simulator code based on the Monte-Carlo algorithm has been developed to compute the RF voltage threshold. The software code, similar to the one described in [22], employs the single effective electron model [23], which consists of tracking the individual trajectories of a certain number of effective electrons. Individual electron trajectories are computed by solving numerically its nonrelativistic equation of motion derived from the Lorentz force

$$\vec{F}_L = q(\vec{E} + \vec{v} \times B) = m\vec{a}.$$

where $q = -e$ is the electron charge, m is the electron mass at rest, $\vec{v}$ is the velocity, $\vec{a}$ is the acceleration, and $\vec{E}$ and $\vec{B} = \mu_0 \vec{H}$ are the total electric and total magnetic field (RF and dc contributions) experienced by the electron, respectively.

When one of the effective electrons hits the waveguide walls, secondary electrons may be released from the surface depending on the primary electron impact conditions. The emission of secondary electrons is modeled by the secondary electron yield (SEY) coefficient as formulated in [24]. Initial launching energies for secondary electrons are given by a Gaussian distribution of mean 4 eV and standard deviation 2 eV. The departure angle is selected to be normal to the impacting surface [25].

The current multipactor simulation model includes the space charge effect, that takes into account the Coulombian interaction among electrons [26], [27], as well as the dielectric polarization effect of the ferrite that leads to the presence of a dc electric field, as reported in [27] and [28].

III. Simulations

The simulation model previously described in Section II is now used to compute the multipactor RF voltage threshold of the ferrite-loaded parallel-plate waveguide shown in Fig. 1. In the considered case, the waveguide walls are made of silver, whose SEY parameters are: first crossover $W_1 = 30$ eV, the maximum SEY coefficient, $\delta_{\max} = 2.22$; and the impact kinetic energy for $\delta_{\max}$, $W_{\max} = 165$ eV. Regarding to the ferrite slab, its relative dielectric permittivity is $\varepsilon_r = 15.5$, the saturation magnetization is $4\pi M_s = 1790$ G, and the SEY parameters are $W_1 = 29$ eV, $\delta_{\max} = 2.40$, and $W_{\max} = 288$ eV [29].

First of all, we have analyzed the multipactor effect when no external magnetic field is applied to magnetize the ferrite ($H_0 = 0$ Oe, see Fig. 2). We have compared this case with the results presented in [28]–[30], finding good agreement between them. Furthermore, it has also been noticed that in some particular cases the polarization electric field is able to turn the multipactor discharge OFF, as it was reported in [27] and [28].

Next, we have studied the ferrite magnetization field effect in the multipactor RF voltage threshold. In Fig. 2, multipactor susceptibility charts are shown for several typical values of the magnetization field. It is noticed that the presence of such an external magnetic field really changes the multipactor behavior. First, when the magnetization field is present, the multipactor susceptibility regions are shifted to higher frequency gap values. In fact, the starting frequency gap value for the multipactor zones becomes higher if the magnetization field strength is increased. For $H_0 = 500$ Oe multipactor breakdown does not appear for frequency gap values less

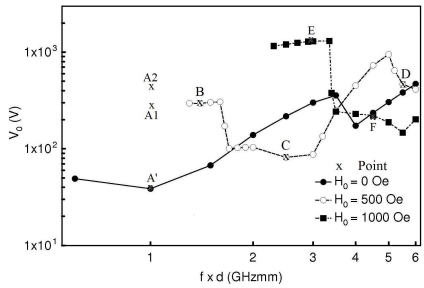

Fig. 2. Multipactor voltage threshold for several values of the external ferrite magnetization field. Waveguide dimensions: $d = 1$ mm and $h = 3$ mm.

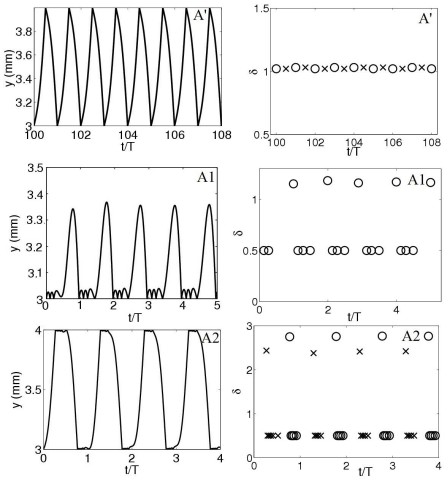

Fig. 3. Vertical coordinate (left column) and SEY impact coefficient (right column) of the effective electron for several points in Fig. 2. SEY coefficient for the impacts with the bottom (upper) wall are denoted by circles (crosses).

than 1.3 GHzmm, while for $H_0 = 1000$ Oe no multipactor discharge is observed below 2.4 GHzmm. Besides, it can be seen in Fig. 2 that there is a frequency gap interval (for both $H_0 = 500$ Oe and $H_0 = 1000$ Oe situations) where the multipactor voltage threshold is even less than for the nonmagnetized ferrite case. These results are consistent with [14] and [31], wherein it is experimentally demonstrated that the presence of an external dc magnetic field may lead to an enhancement of the multipacting effect for certain values of the external static magnetic field strength.

To have a better understanding of the multipactor behavior, the effective electron trajectories, as well as the SEY coefficient value at the electron impacts, have been plotted for several significant points marked in Fig. 2. Points A1, A2, B, C, and D belong to the $H_0 = 500$ Oe case; points E and F to $H_0 = 1000$ Oe, whereas point A' corresponds to the $H_0 = 0$ Oe situation.

First, we are going to compare the effective electron trajectories behavior for the frequency gap value of 1 GHzmm. If we examine the point A' (Figs. 2 and 3) it corresponds to the $H_0 = 0$ case, where no external magnetization field is applied. It is observed that the electron takes one semiperiod of the RF signal between successive impacts with the waveguide walls, which corresponds with the well-known classical double-surface multipactor of order one. It is also noticed that the mean SEY is slightly above the unity, so the electron population in the device will grow resulting into a multipactor discharge.

In contrast, when the external magnetization field is present, the multipactor effect has not been observed at that frequency gap (1 GHzmm), as it can be seen in Fig. 2. On inspecting point A1 for $H_0 = 500$ Oe (see Fig. 3), it is noticed that the SEY mean value is below one (despite the fact that at some of the impacts the SEY exceeds the unity), implying that there is no discharge. Indeed, as the external dc magnetic field bends the electron trajectories around the magnetic field lines (in our case H_0 is oriented along the x-direction), it will tend to impinge a circular motion in the transverse yz plane pushing the electron back to the departure wall. This fact destroys the electron resonant trajectories, forcing many low energetic impacts in which the electron is not favored by the RF electric field polarity, and it is pushed back to the departure wall. Both the electron orbit radius and the orbital velocity due to the external dc magnetic field depend on the magnetic field strength, the amplitude of the RF voltage, the ratio between the cyclotron frequency ($f_c = (e\mu_0 H_0)/(2\pi m)$) and the frequency of the RF electromagnetic field [14]. Thus, when the radius of this circular motion is shorter than the waveguide gap value d, the electron will not be able to reach the opposite conductor, as it happens with point A1. Of course, if the RF voltage is increased then the electron will be able to cross the gap, as it is shown for point A2 (see Fig. 3). However, owing to the lack of resonance between the electron orbits and the RF electric field, it is found that the SEY mean value remains below the unity, so no multipactor discharge occurs. Points A1 and A2 evidence that it is not only necessary that the electrons impact kinetic energy is enough to release secondaries (SEY values above the unity), but their flight time between successive impacts has to be synchronized with the RF electric field, to avoid the electrons being pushed back at the departure instant. In points A1 and A2, the electron flight time between successive impacts is too short (always below the RF semiperiod) to allow a good resonance of the trajectory with the RF electric field. It should be remarked that classical theory of multipactor states that the time between successive impacts must be an odd (even) number of RF semiperiods for double (single)-surface multipactor modes. Moreover, we have found that the electron flight time strongly depends on the ratio between the RF frequency and the cyclotron one. Specifically, for a fixed value of the cyclotron frequency, the flight time increases as the RF frequency does. This fact is shown analyzing effective electron trajectories for the points B, C, and D corresponding to the $H_0 = 500$ Oe case.

If we focus our attention in point B (Figs. 2 and 4), it can be found a multipactor double-surface regime of order one,

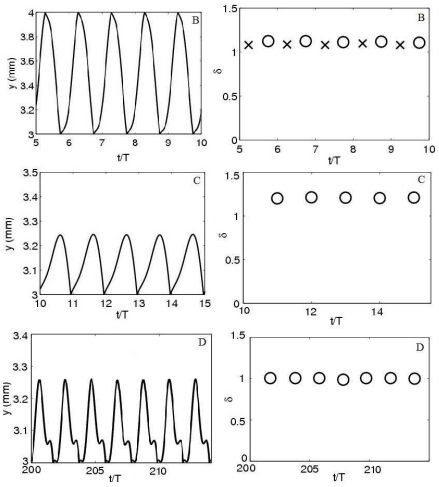

Fig. 4. Vertical coordinate (left column) and SEY impact coefficient (right column) of the effective electron for several points shown in Fig. 2. SEY coefficient for the impacts with the bottom (upper) wall are denoted by circles (crosses).

which presents a mean SEY higher than one. Now, the ratio between the RF and the cyclotron frequencies is higher than for points A1 and A2 and, consequently, the electron flight time has become greater with regard to points A1 and A2. Moreover, the orbital radius has also become greater (note that the RF voltage is very similar to point A1, see Fig. 2). As a consequence, electron is allowed to get resonant with the RF electric field.

For point C (see Fig. 2), single surface multipactor resonance of order two can be seen in Fig. 4, where the SEY is slightly higher than one. In the same way as point B, the increment in the RF frequency related to the cyclotron one allows the electron to increase the flight time impacting over the walls, which gives rise to the appearance of higher order mode resonance. It should also be noticed that in point C the RF multipactor voltage threshold is lower than for point B (see Fig. 2), because this single surface resonance does not need the electron to cross the whole gap. Therefore, less energy provided by the RF field is required to produce the discharge.

Next, for point D (see Fig. 2), a single-surface regime with order four is shown (the mean SEY is also above the unity). It should be emphasized that the behavior of the RF voltage threshold increases for high values of the frequency gap parameter, in a similar way as it does for the nonmagnetized case (see Fig. 2). Despite this, the presence of the external H_0 field allows the presence of single surface multipactor modes and, for nearby frequencies of these resonant modes, the RF voltage threshold shows local minimums as it can be noticed for points C and D.

In Fig. 5, the electron trajectories and the SEY coefficients for the points E and F corresponding to the $H_0 = 1000$ Oe case (see Fig. 2) are plotted. There is a

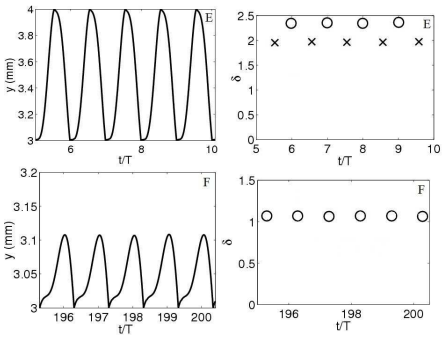

Fig. 5. Vertical coordinate (left column) and SEY impact coefficient (right column) of the effective electron for several points shown in Fig. 2. SEY coefficient for the impacts with the bottom (upper) wall are denoted by circles (crosses).

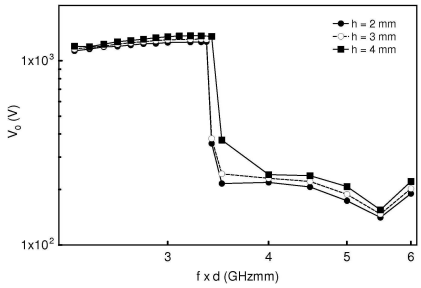

Fig. 6. Multipactor susceptibility charts for silver partially ferrite-filled parallel-plate waveguide. Multipactor voltage threshold for several values of the ferrite slab height. Gap distance is $d = 1$ mm and $H_0 = 1000$ Oe.

clear correspondence between points E and F, and points B and C of the $H_0 = 500$ Oe case, respectively. Point E shows a double-surface multipactor regime of order one (just the same as for point B), whereas for point F a single surface multipactor resonance of order two (the same as for point C) is found. Indeed, the shape of the voltage threshold variation with the frequency gap for the $H_0 = 1000$ Oe case seems to be very similar to the $H_0 = 500$ Oe one, but shifted to higher frequency gap values and voltages. This is because, as mentioned before, the electron flight time is strongly affected by the ratio between the RF frequency and the cyclotron one. Thus, electron flight time determines which resonance order is available at each frequency gap value. Therefore, the same multipactor orders are found for similar values of the ratio between the RF frequency and the cyclotron one.

Finally, the effect of changing the ferrite slab height in the multipactor RF voltage threshold for a fixed value of the gap and the ferrite magnetization field, is analyzed as shown in Fig. 6. As it can be observed, there is a small shift in the voltage threshold, although the general behavior and shape of the multipactor curves remain unchanged for the considered slab height range.

IV. Conclusion

In this paper, we have studied the multipactor effect in a ferrite-loaded parallel-plate waveguide. Multipactor simulations made with an in-house code show the multipactor RF voltage threshold in several different scenarios. The effect of the variation of the ferrite magnetization field strength has been considered, finding important deviations from the behavior of the simple metallic parallel-plate structure. In addition, several heights of the ferrite slab have been also considered. Finally, the analysis of some effective electron trajectories reveals the presence of single and double surface multipactor regimes. Thus, it has been found that the apparition of such multipactor modes strongly depends on the ratio between RF frequency and the cyclotron one.

References

[1] J. Vaughan, "Multipactor," *IEEE Trans. Electron Devices*, vol. 35, no. 7, pp. 1172–1180, Jul. 1988.

[2] V. E. Semenov *et al.*, "Simulations of multipactor thresholds in shielded microstrip lines," *J. Phys. D, Appl. Phys.*, vol. 42, no. 20, pp. 205204-1–205204-7, 2009.

[3] A. M. Pérez *et al.*, "Prediction of multipactor breakdown thresholds in coaxial transmission lines for traveling, standing, and mixed waves," *IEEE Trans. Plasma Sci.*, vol. 37, no. 10, pp. 2031–2040, Oct. 2009.

[4] R. Udiljak, D. Anderson, M. Lisak, V. E. Semenov, and J. Puech, "Multipactor in a coaxial transmission line. I. Analytical study," *Phys. Plasmas*, vol. 14, no. 3, p. 033508, Mar. 2007.

[5] V. E. Semenov, N. Zharova, R. Udiljak, D. Anderson, M. Lisak, and J. Puech, "Multipactor in a coaxial transmission line. II. Particle-in-cell simulations," *Phys. Plasmas*, vol. 14, no. 3, pp. 033509-1–033509-7, Mar. 2007.

[6] C. Vicente *et al.*, "Multipactor breakdown prediction in rectangular waveguide based components," in *IEEE MTT-S Int. Microw. Symp. Dig.*, Jun. 2005.

[7] C. L. Hogan, "The ferromagnetic Faraday effect at microwave frequencies and its applications: The microwave gyrator," *Bell Syst. Tech. J.*, vol. 31, no. 1, pp. 1–31, Jan. 1952.

[8] C. E. Fay and R. L. Comstock, "Operation of the ferrite junction circulator," *IEEE Trans. Microw. Theory Techn.*, vol. 13, no. 1, pp. 15–27, Jan. 1965.

[9] W. J. Ince and E. Stern, "Nonreciprocal remanence phase shifters in rectangular waveguide," *IEEE Trans. Microw. Theory Techn.*, vol. 15, no. 2, pp. 87–95, Feb. 1967.

[10] W. P. Clark, "A high power phase shifter for phased-array systems," *IEEE Trans. Microw. Theory Techn.*, vol. 13, no. 6, pp. 785–788, Nov. 1965.

[11] R. A. Stern and P. Agrios, "A 500 kW X-band air-cooled ferrite latching switch," *IEEE Trans. Microw. Theory Techn.*, vol. 16, no. 12, pp. 1034–1037, Dec. 1968.

[12] J. D. Adam, L. E. Davis, G. F. Dionne, E. F. Schloemann, and S. N. Stitzer, "Ferrite devices and materials," *IEEE Trans. Microw. Theory Techn.*, vol. 50, no. 3, pp. 721–737, Mar. 2002.

[13] Ü. Özgür, Y. Alivov, and H. Morkoç, "Microwave ferrites, part 2: Passive components and electrical tuning," *J. Mater. Sci., Mater. Electron.*, vol. 20, no. 10, pp. 911–952, Oct. 2009.

[14] V. E. Semenov *et al.*, "Reduction of the multipactor threshold due to electron cyclotron resonance," *IEEE Trans. Plasma Sci.*, vol. 40, no. 11, pp. 3062–3069, Nov. 2012.

[15] S. Riyopoulos, D. Chernin, and D. Dialetis, "Theory of electron multipactor in crossed fields," *Phys. Plasmas*, vol. 2, no. 8, pp. 3194–3212, 1995.

[16] L. Cai, J. Wang, X. Zhu, Y. Wang, C. Xuan, and H. Xia, "Suppression of multipactor discharge on a dielectric surface by an external magnetic field," *Phys. Plasmas*, vol. 18, no. 7, pp. 073504-1–073504-6, 2011.

[17] V. E. Semenov *et al.*, "Preliminary results on the multipactor effect prediction in RF components with ferrites," in *Proc. IEEE 14th Int. IVEC*, Paris, France, May 2013.

[18] W. E. Hord, "Microwave and millimeter wave ferrite phase shifters," *Microw. J.*, vol. 32, pp. 81–89, Sep. 1989.

[19] A. Vegas, A. Prieto, and M. A. Solano, "Rigorous analysis of scattering by partial height magnetised ferrite posts in rectangular waveguides," *Electron. Lett.*, vol. 18, no. 10, pp. 913–915, May 1992.

[20] A. Abuelma'atti, J. Zafar, I. Khairuddin, A. Gibson, A. Haigh, and I. Morgan, "Variable toroidal ferrite phase shifter," *IET Microw., Antennas Propag.*, vol. 3, no. 2, pp. 242–249, Mar. 2009.

[21] D. M. Pozar, *Microwave Engineering*, 4th ed. New York, NY, USA: Wiley, 2012.

[22] D. González-Iglesias *et al.*, "Analysis of multipactor effect using a phase-shift keying single-carrier digital modulated signal," *IEEE Trans. Electron Devices*, vol. 60, no. 8, pp. 2664–2670, Aug. 2013.

[23] E. Somersalo, P. Ylä-Oijala, D. Proch, and J. Sarvas, "Computational methods for analyzing electron multipacting in RF structures," *Particle Accel.*, vol. 59, pp. 107–141, Jan. 1998.

[24] S. Anza, C. Vicente, D. Raboso, J. Gil, B. Gimeno, and V. E. Boria, "Enhanced prediction of multipaction breakdown in passive waveguide components including space charge effects," in *IEEE MTT-S Microw. Symp. Dig.*, Jun. 2008, pp. 1095–1098.

[25] J. Greenwood, "The correct and incorrect generation of a cosine distribution of scattered particles for Monte-Carlo modelling of vacuum systems," *Vacuum* vol. 67, no. 2, pp. 217–222, Sep. 2002.

[26] S. Riyopoulos, "Multipactor saturation due to space-charge-induced debunching," *Phys. Plasmas*, vol. 4, no. 5, pp. 1448–1462, May 1997.

[27] A. Coves, G. Torregrosa-Penalva, C. Vicente, B. Gimeno, and V. E. Boria, "Multipactor discharges in parallel-plate dielectric-loaded waveguides including space-charge effects," *IEEE Trans. Electron Devices*, vol. 55, no. 9, pp. 2505–2511, Sep. 2008.

[28] G. Torregrosa, Á. Coves, C. Vicente, A. M. Pérez, B. Gimeno, and V. E. Boria, "Time evolution of an electron discharge in a parallel-plate dielectric-loaded waveguide," *IEEE Electron Device Lett.*, vol. 27, no. 7, pp. 619–621, Jul. 2006.

[29] I. Montero, F. Caspers, L. Aguilera, L. Galán, D. Raboso, and E. Montesinos, "Low-secondary electron yield of ferromagnetic materials and magnetized surfaces," in *Proc. IPAC*, Kyoto, Japan, May 2010.

[30] G. Torregrosa-Penalva, A. Coves, B. G. Martinez, I. Montero, C. Vicente, and V. E. Boria, "Multipactor susceptibility charts of a parallel-plate dielectric-loaded waveguide," *IEEE Trans. Electron Devices*, vol. 57, no. 5, pp. 1160–1166, May 2010.

[31] R. L. Geng, H. Padamsee, S. Belomestnykh, P. Goudket, D. M. Dykes, and R. G. Carter, "Suppression of multipacting in rectangular coupler waveguides," *Nucl. Instrum. Methods A*, vol. 508, no. 3, pp. 227–238, Aug. 2003.

Daniel González-Iglesias received the Licenciado degree in physics and the master's degree in advanced physics from the University of Valencia, Valencia, Spain, in 2010 and 2011, respectively, where he is currently pursuing the Ph.D. degree in physics.

His current research interests include multipacting simulation of RF high-power passive components.

Benito Gimeno (M'01) received the Licenciado degree in physics and the Ph.D. degree from the University of Valencia, Valencia, Spain, in 1987 and 1992, respectively.

He became a Full Professor at the University of Valencia in 2010. His current research interests include the electromagnetic analysis and design of microwave passive components, and RF breakdown high-power effects.

Vicente E. Boria (S'91–A'99–SM'02) received the Doctor Ingeniero de Telecomunicación degree from the Universidad Politécnica de Valencia, Valencia, Spain, in 1997.

He is currently a Full Professor with the Universidad Politécnica de Valencia. His current research interests include the electromagnetic analysis and design of microwave passive components, and RF breakdown high-power effects.

Álvaro Gómez (M'08) was born in Santander, Spain, in 1976. He received the Licenciado en Ciencias Físicas and Ph.D. degrees from the Universidad de Cantabria, Santander, in 2000 and 2005, respectively.

He joined the Departamento de Ingeniería de Comunicaciones at Universidad de Cantabria in 2000, where he became a Profesor Contratado Doctor in 2011. His current research interests include electromagnetic propagation in complex materials and numerical methods in electromagnetics.

Angel Vegas (M'98) received the Ph.D. degree in physical sciences from the University of Cantabria, Santander, Spain, in 1983.

He is a Full Professor of Electromagnetics with the University of Cantabria, where he is the Head of the Electromagnetics Group. His current research interests include the electromagnetics of complex materials, computer methods in electromagnetism, and microwave measurements.

Publication VIII

Analysis of multipactor RF breakdown in a waveguide containing a transversely magnetized ferrite

IEEE Transactions on Electron Devices, vol. 61, no. 7, pp. 4939-4947, December 2016

Analysis of Multipactor RF Breakdown in a Waveguide Containing a Transversely Magnetized Ferrite

Daniel González-Iglesias, Álvaro Gómez, Benito Gimeno, *Member, IEEE*, Óscar Fernández, Angel Vegas, *Member, IEEE*, Fernando Casas, Sergio Anza Hormigo, Carlos Vicente, *Member, IEEE*, Jordi Gil, Rafael Mata, Isabel Montero, Vicente E. Boria, *Senior Member, IEEE*, and David Raboso

***Abstract*— In this paper, the multipactor RF breakdown in a parallel-plate waveguide partially filled with a ferrite slab magnetized normal to the metallic plates is studied. An external magnetic field is applied along the vertical direction between the plates in order to magnetize the ferrite. Numerical simulations using an in-house 3-D code are carried out to obtain the multipactor RF voltage threshold in this kind of structures. The presented results show that the multipactor RF voltage threshold at certain frequencies becomes considerably lower than for the corresponding classical metallic parallel-plate waveguide with the same vacuum gap.**

***Index Terms*— Ferrite devices, magnetic field, multipactor effect, parallel-plate waveguide, RF breakdown.**

I. Introduction

MULTIPACTOR discharge is an undesired phenomenon that takes place on devices operating under vacuum conditions and high-power RF electromagnetic fields [1], [2]. When certain conditions arise, free electrons in the device are driven by the RF electric field toward the walls. If the kinetic energy of the impacting electrons is high enough, secondary electrons may be released from the surface. As a consequence, a chain reaction leading to an exponential growth of the electron population inside the component is started. The onset of the multipactor discharge degrades the device performance by several negative effects, such as increasing the signal noise and reflected power, heating up the device walls, outgassing, detuning of resonant cavities, vacuum window failure, and even resulting in the total destruction of the component. Due to that, multipactor phenomenon is revealed as a crucial limitation in the maximum RF power handling. Multipactor occurs in different environments, such as passive components of satellite communication payloads, particle accelerators, and klystrons.

Special attention must be paid to multipactor in satellite components, where replacement of damaged devices is not possible. Therefore, in order to ensure that the RF component will not suffer this undesirable phenomenon during operation, it is extremely important to take into account this effect in the design process. In fact, restrictive specifications have been imposed by the space agencies about this issue [3].

Multipactor has been extensively analyzed in the case of metallic surfaces so far [4], [5], [6]. Recently, some studies have focused their attention to the case wherein dielectric surfaces are involved [7], [8], [9]. However, very little literature about multipactor effect in devices containing ferrites can be found [10], [11]. Ferrites are ferromagnetic materials which exhibit magnetic anisotropy when are brought under a dc magnetic bias field. When an external dc magnetic field is applied multipactor discharge can be either suppressed [12] or enhanced [13], depending on the specific magnitude and direction of the external field. The induced anisotropy in the ferrite has been used to produce a wide range of RF passive devices, such as circulators, isolators, and phase shifters [14]–[17]. Until now, the high power handling of this kind of components can only be analyzed by rough approximations whose validity is not clear.

The main aim of this paper is the study of the multipactor effect in an ideal uniform parallel-plate waveguide (as shown in Fig. 1) of infinite length along the x- and z-axes, z being the propagation direction of the electromagnetic wave,

Manuscript received May 13, 2016; revised August 3, 2016; accepted September 22, 2016. Date of publication October 13, 2016; date of current version November 22, 2016. This work was supported in part by the European Space Agency under Novel Investigation in Multipactor Effect in Ferrite and other Dielectrics used in high power RF Space Hardware under Contract AO 1-7551/13/NL/GLC, in part by the Spanish Government under Coordinated R&D Project TEC2013- 47037-5-R and Project TEC2014-55463-C3-3-P, and in part by the European Commission (ERDF). The review of this paper was arranged by Editor R. Carter.

D. González-Iglesias, B. Gimeno, and R. Mata are with the Departamento de Física Aplicada, Universidad de Valencia, 46100 Valencia, Spain (e-mail: daniel.gonzaleziglesias@uv.es; benito.gimeno@uv.es; rafael.mata@uv.es).

Á. Gómez, Ó. Fernández, and A. Vegas are with the Departamento de Ingeniería de Comunicaciones, Universidad de Cantabria, 39005 Santander, Spain (e-mail: alvaro.gomez@unican.es; oscar.fernandez@unican.es; angel.vegas@unican.es).

F. Casas is with the Instituto Universitario de Matemáticas y Aplicaciones, Universidad Jaume I, 12071 Castellón de la Plana, Spain (e-mail: casas@uji.es).

S. Anza Hormigo, C. Vicente, and J. Gil are with AURORASAT, 46001 Valencia, Spain (e-mail: sergio.anza@aurorasat.es; carlos.vicente@aurorasat.es; jordi.gil@aurorasat.es).

I. Montero is with the Instituto de Ciencia de Materiales de Madrid, Consejo Superior de Investigaciones Científicas, 28049 Madrid, Spain (e-mail: imontero@icmm.csic.es).

V. E. Boria is with the Departamento de Comunicaciones, Instituto de Telecomunicaciones y Aplicaciones Multimedia, Universidad Politécnica de Valencia, 46022 València, Spain (e-mail: vboria@dcom.upv.es).

D. Raboso is with the European Space Research and Technology Centre, European Space Agency, 2201 AZ Noordwijk, The Netherlands (e-mail: david.raboso@esa.int).

Digital Object Identifier 10.1109/TED.2016.2614370

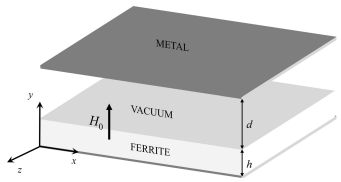

Fig. 1. Parallel-plate waveguide (considered to be infinite along the x- and z-axes, z being the propagation direction of the electromagnetic wave) partially loaded with a ferrite slab magnetized along the waveguide gap direction by a static magnetic field $\vec{H}_0$.

thus resulting an electromagnetic field which does not depend on the x-coordinate. Transmission of the fundamental TEM like mode is considered in this analysis. The waveguide contains a lossless ferrite slab, which is magnetized along the direction perpendicular to the metallic walls, i.e., $\vec{H}_0 = H_0\,\hat{y}$. When the ferrite is saturation magnetized, it can be electromagnetically characterized by the constitutive relations $\vec{D} = \varepsilon\vec{E}$ and $\vec{B} = [\mu]\vec{H}$, wherein ε is the dielectric permitivitty and $[\mu]$ is the Polder's tensor corresponding to the aforementioned magnetization [14, eq. 9.27]. The effective field H_{ef} which magnetizes the ferrite is $H_{\text{ef}} = H_0 - M_s$ [14], where M_s is the saturation magnetization. There is a gyromagnetic resonance of the ferrite at the Larmor frequency $\omega_0 = \gamma\,\mu_0 H_{\text{ef}}$, where μ_0 is the free space permeability, and $\gamma = e/m$ is the gyromagnetic ratio of the electron ($-e$ and m are the electron charge and electron mass at rest, respectively).

In a previous authors' work [11], which at first glance could be seen similar to the current one, the external magnetization field was oriented parallel to the ferrite slab. Since the magnetic permeability of the ferrite is anisotropic and depends on the bias magnetic field H_0 direction, the RF behavior of the ferrite in both cases is completely different. Moreover, the effect on the electron orbits due to changing the direction of the external magnetic field employed to magnetize the ferrite is crucial. Therefore, the present analysis is not only a straightforward extension of the previous one, and it is worthy of being studied.

This paper is structured as follows. First, in Section II, it is described both the multipactor algorithm and the method employed to compute the RF electromagnetic fields in such ferrite loaded waveguide. Next, Section III presents and analyzes the results of the multipactor simulations. Finally, the main conclusions of our study are summarized in Section IV.

II. Theory

A. Multipactor Algorithm

The simulation code developed for the study of the multipactor is based on the single effective electron model [4]. This method consists of tracking the individual trajectories of a set of effective electrons. Each effective electron has associated a cumulative electron population that takes into account the emission or absorption of secondary electrons by the device walls. This is done by computing the value of the secondary electron yield (SEY) function (δ) at each impact, which depends on the electron kinetic energy and impacting angle [18], [19]. After the impact, the colliding effective electron is launched back to the waveguide with random velocity given by a Maxwellian distribution with a mean certain kinetic energy (3 eV in our simulations). The velocity angle follows the cosine law distribution [20]. When the software has run for a predefined number of RF periods, the code stops and the time evolution of the total electronic population is shown.

The individual trajectories of the effective electrons are computed by solving numerically their nonrelativistic equations of motion derived from the Lorentz Force. The total electromagnetic field experienced by the electron is the superposition of the RF electric E_{RF} and magnetic B_{RF} fields, the electric field due to the space charge effect E_{sc}, the dc electric field appearing because of the charging of the ferrite surface E_{dc}, and the external magnetic field H_0 employed to magnetize the ferrite. Both E_{sc} and E_{dc} have been computed following the procedure reported in [7].

For the numerical integration of the differential equations of the electron trajectories, we use a conveniently modified velocity-Verlet method. This particular scheme has very favorable properties concerning the error propagation in time, both in the energy and the position and velocity. We choose the time step size so that the relative error in position and in energy is less than 1% after a time of 200 RF periods.

B. RF Electromagnetic Field Computation

The RF electromagnetic field inside the structure under study has been obtained with the aid of the coupled mode method (CMM). This well-known numerical method, formulated in the frequency domain, has been widely and successfully used in the analysis of the electromagnetic wave propagation inside uniform waveguides that contain any isotropic, anisotropic, or complex material [21], [22], [23].

In few words, the CMM is a method of moments, which consists on expanding the electromagnetic field components inside the structure under analysis in terms of a set of base functions previously defined [21]. In many cases, these base functions correspond to the electric or magnetic field components of the TE and TM modes of the empty waveguide. Therefore, they are called basis modes. According to this idea, any component of the electromagnetic field of the structure under test can be expressed as a linear combination of the basis modes.

Once the electromagnetic fields inside the waveguide are obtained, the calculation of the equivalent voltage V_0 is done by integrating the vertical RF electric field along the vacuum gap.

III. Simulations

In order to compute the multipactor RF voltage threshold for the parallel-plate ferrite loaded waveguide shown in Fig. 1, numerical simulations have been performed. For all the considered cases, the ferrite thickness h and the vacuum gap d have been selected to match with the height of a WR-90 rectangular waveguide, i.e., $b = d + h = 10.16$ mm. The saturation

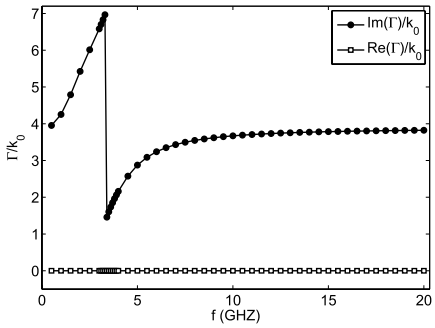

Fig. 2. Real and imaginary parts of the propagation factor for the fundamental mode of a ferrite loaded waveguide (with $d = 1$ mm) as a function of the RF frequency. Note that gyromagnetic resonance, given by Larmor frequency, occurs at 3.34 GHz.

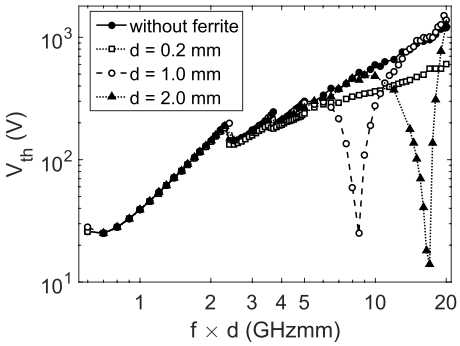

Fig. 3. Multipactor RF voltage threshold as a function of the frequency gap. Results are presented for parallel-plate ferrite loaded waveguides with different gap lengths and ferrite thicknesses (but maintaining the height of a WR-90 waveguide), and also for a metallic parallel-plate waveguide ("without ferrite").

magnetization of the ferrite is $4\pi M_s = 1806$ G, its relative dielectric permittivity $\varepsilon_r = 15$, and its SEY parameters are: first crossover energy for SEY coefficient equal to unity, $W_1 = 19$ eV, maximum SEY coefficient $\delta_{\max} = 2.88$, and impact kinetic energy for $\delta_{\max}$, $W_{\max} = 289$ eV [24]. For simplicity, the same SEY parameters are selected for the top metallic wall. The external magnetic field employed to magnetize the ferrite is $H_0 = 3000$ Oe. Consequently, the effective biasing field inside the ferrite is $H_{\text{ef}} = 1194$ Oe. The considered fields are those corresponding to the fundamental mode of the ferrite loaded waveguide (i.e., $l = 1$). For all calculations of the electromagnetic field components with the CMM, a total number of 75 TE and 75 TM basis modes are used. These basis modes have been included by increasing their cutoff frequencies.

We are interested in analyzing the effect of the variation of the ferrite thickness and the vacuum gap length in the multipactor RF voltage threshold. First, for the fundamental mode, the propagation factor dependence with frequency it is obtained, as shown in Fig. 2. It can be observed that the real part of the propagation factor is zero within the plotted frequency range, which corresponds to a propagative mode.

In Fig. 3, the variation of the multipactor RF voltage threshold as a function of the frequency gap value (i.e., the multipactor susceptibility chart) is shown for several ferrite loaded parallel-plate waveguides. Note that for each curve, the gap remains fixed. Moreover, the results for a classical metallic parallel-plate waveguide with no ferrite slab, a gap of $d = 0.2$ mm and $H_0 = 0$ (henceforth referred as without ferrite case) has been included for comparison purpose. Remember that according to the well-known multipactor theory [2] for a classical metallic parallel-plate waveguide, the multipactor phenomenon depends only on the frequency gap product, and as a consequence, the same multipactor RF voltage threshold curve would be obtained for metallic parallel-plate waveguides with other gaps while maintaining the same frequency gap range. From the results (recall Fig. 3), it is noticed that there is considerable difference between the multipactor RF voltage threshold of the ferrite loaded waveguides and the corresponding to the without ferrite case. It is found that this discrepancy increases with the gap value. In fact, the maximum difference in the multipactor RF voltage threshold between the $d = 0.2$ mm waveguide and the without ferrite case is of 6.5 dB, while in the $d = 1$ mm and $d = 2$ mm, the difference becomes of 26 and 37 dB, respectively. It is also observed that the multipactor behavior of the ferrite loaded waveguides remains very close to the without ferrite case for low-frequency gap values (below 2.5 GHzmm). In general terms, the multipactor RF voltage threshold of the ferrite loaded waveguide cases tends to be equal or below the without ferrite multipactor threshold.

In order to have a better understanding of the behavior of the different multipactor susceptibility curves, a detailed analysis of the RF electromagnetic fields (spatial distribution, scale analysis of the different electric, and magnetic spatial components), and electron dynamics (resonant trajectories and multipactor order) has been performed for both the ferrite loaded waveguides and the classical unloaded metallic parallel-plate waveguide.

An exhaustive inspection of the RF electromagnetic field pattern of the three ferrite loaded waveguide cases has revealed that the RF magnetic field has very little influence in the electron motion, and thus, the contribution of the terms $v_i\ B_{\text{RF},j}$ (being $i, j = x, y, z$) can be neglected in the differential equations of the electron motion. Regarding the RF electric field components, it has been found that all of them have noticeable effects in the electron trajectories. In Fig. 4 (left), it has been depicted the quotient between the maximum absolute value along the gap of the $E_{\text{RF},x}$ and $E_{\text{RF},y}$ components for the different considered ferrite waveguides. In a similar way in Fig. 4 (right), it has been plotted the same quotient for the $E_{\text{RF},z}$ and $E_{\text{RF},y}$ components. From these figures, it is extracted that the $E_{\text{RF},y}$ is the greater RF electric field component for low-frequency gap values. As the frequency

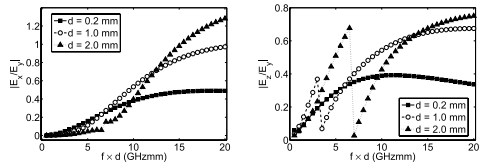

Fig. 4. Left (right): quotient between the maximum absolute value along the gap of the $E_{\mathrm{RF},x}$ ($E_{\mathrm{RF},z}$) and $E_{\mathrm{RF},y}$ components for the ferrite loaded waveguides.

gap increases the components, $E_{\mathrm{RF},x}$ and $E_{\mathrm{RF},z}$ also grow with regard to the $E_{\mathrm{RF},y}$ component. This increment is found to be more notorious for the ferrite loaded waveguides with higher gaps. In fact, it can be observed that $E_{\mathrm{RF},x}$ becomes the dominant component in the $d = 2$ mm waveguide for values above 15 GHz mm.

Taking the previous statements into account, the differential equations of motion can be approximated in the following way for the earlier stages of the electron multiplication:

$$\frac{dv_x}{dt} \simeq \omega_c v_z - \frac{e}{m} E_{\mathrm{RF},x} \cos(\omega t + \phi) \tag{1}$$

$$\frac{dv_y}{dt} \simeq -\frac{e}{m} E_{\mathrm{RF},y} \cos(\omega t + \phi) \tag{2}$$

$$\frac{dv_z}{dt} \simeq -\omega_c v_x - \frac{e}{m} E_{\mathrm{RF},z} \sin(\omega t + \phi) \tag{3}$$

where $E_{\mathrm{RF},x}$, $E_{\mathrm{RF},y}$, and $E_{\mathrm{RF},z}$ are the x, y, and z RF electric field components, respectively, which only depend on the y-coordinate; $\omega_c = (e/m)\mu_0 H_0$ is the cyclotron angular frequency, $\omega = 2\pi f$ is the RF angular frequency (f being the RF frequency), v_x, v_y, and v_z are the x-, y-, and z-components of the velocity vector, respectively, and ϕ is the phase of the RF electromagnetic field. It is remarkable that in such conditions, the equation of motion for the y-coordinate gets decoupled from the remaining x- and z-coordinates. Indeed, the approximated y-equation of motion becomes the corresponding one of the analytically well-studied classical case without ferrite [1], [2]. The effect of the external field H_0 is to spin the electron orbits in the xz plane. In addition, the $E_{\mathrm{RF},x}$ and $E_{\mathrm{RF},z}$ components accelerate the electron along the directions x and z, respectively. Manipulating the expressions (1) and (3), the following differential equations arise for the v_x and v_z velocities:

$$\frac{d^2 v_x}{dt^2} + \omega_c^2 \, v_x = A_1 \, \sin(\omega t + \phi) \tag{4}$$

$$\frac{d^2 v_z}{dt^2} + \omega_c^2 \, v_z = A_2 \, \cos(\omega t + \phi) \tag{5}$$

where $A_1 = (e/m)(E_{\mathrm{RF},x,0}\,\omega - E_{\mathrm{RF},z,0}\,\omega_c)$ and $A_2 = (e/m)$ $(E_{\mathrm{RF},x,0}\,\omega_c - E_{\mathrm{RF},z,0}\,\omega)$. The above differential equations can be solved analytically provided that the amplitude of the RF electric field components is uniform along the gap. Although this is not true in our case, we will take this assumption in order to obtain some analytical expressions that can give us a certain qualitative insight of the multipactor phenomenon. After some calculations, the following expressions arise for

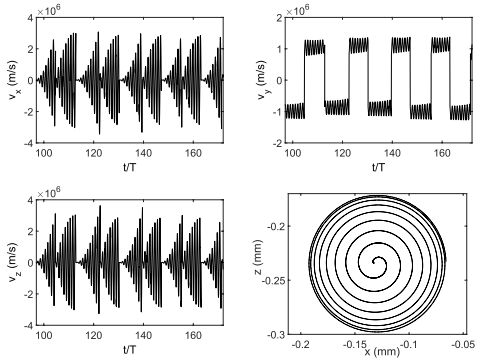

Fig. 5. From left to right, and up to down: effective electron velocity components as a function of the time normalized to the RF period (T is the RF period), and xz plane electron trajectory. All for a ferrite waveguide with $d = 1$ mm, $f \times d = 8.5$ GHzmm, $V_0 = 25$ V.

the v_x and v_z velocities (it is assumed zero initial velocity for both coordinates):

$$v_x = \frac{A_1}{\omega_c^2 - \omega^2} \sin(\omega t + \phi) - \frac{A_1 \sin(\phi)}{\omega_c^2 - \omega^2} \cos(\omega_c t) - \frac{A_2 \cos(\phi)}{\omega_c^2 - \omega^2} \sin(\omega_c t) \tag{6}$$

$$v_z = \frac{A_2}{\omega_c^2 - \omega^2} \cos(\omega t + \phi) - \frac{A_2 \cos(\phi)}{\omega_c^2 - \omega^2} \cos(\omega_c t) + \frac{A_1 \sin(\phi)}{\omega_c^2 - \omega^2} \sin(\omega_c t). \tag{7}$$

Note that (6) and (7) are valid for all the RF frequencies except for $\omega = \omega_c$. For both velocities, there are oscillatory terms at both the RF frequency and at the cyclotron frequency. It is easily noticed that the amplitude of these oscillations becomes maximum when the RF frequency equals the cyclotron one ($\omega = \omega_c$). Consequently, the velocity gain in the plane xz is maximum in the neighborhood of such resonance. In our case, the cyclotron frequency is 8.4 GHz and the corresponding frequency gap is 8.4 GHz mm for the $d = 1$ mm waveguide and 16.8 GHz mm for the $d = 2$ mm waveguide. This cyclotron resonance allows to understand the sharp minimums observed for the multipactor RF voltage thresholds of the ferrite loaded waveguides with $d = 1$ mm and $d = 2$ mm in the surroundings of such frequency gap values. Due to the enhance in kinetic energy gain of the electron in the xz plane, less RF voltage amplitude is necessary to achieve that the total kinetic impact energy of the electron exceeds the W_1 of the material. To illustrate the cyclotron resonance effect, in Fig. 5, we have plotted the v_x, v_y, and v_z velocities of an effective electron in the $d = 1$ mm ferrite loaded waveguide, for a frequency gap value close to the resonance and an RF voltage value corresponding to the multipactor threshold. It is noticed the increment of the v_x and v_z maximum amplitude in the successive oscillations between one impact and next, while for the v_y velocity, it is not observed such maximum

amplitude increment. In Fig. 5, it has also been depicted the xz plane electron trajectory, which seems very similar to that of a cyclotron accelerator, where the radius of the electron circular trajectory tends to increase as the kinetic energy gain process is ongoing.

The above statements justify the presence of a sharp minimum in the multipactor RF voltage threshold for the frequency gap values in the vicinity of the cyclotron resonances for the $d = 1$ mm and $d = 2$ mm ferrite loaded waveguide cases. However, it is notorious that such multipactor RF voltage threshold minimum is not observed for the $d = 0.2$ mm waveguide (which should be expected at 1.68 GHz mm). To understand this point, we will briefly recall some aspects of the classic multipactor theory for parallel-plate waveguides. As it is well known, for the onset of a multipactor discharge, it is required that the electron becomes synchronized with the RF electric field (it implies the apparition of stable resonant trajectories, also known as multipactor modes), and an electron impact kinetic energy with the waveguide walls above the W_1 parameter of the material (which ensures the release of secondary electrons). The classical multipactor modes that guarantee the electron synchronization with the RF electric field consist on electron trajectories that take an odd number of RF semiperiods to cross the gap (the multipactor order N is defined as that number of RF semiperiods).

In our ferrite loaded waveguide case, we have argued previously that the y motion becomes decoupled from the x- and z-coordinates, resulting in the same y differential equation of motion that for the classical metallic parallel-plate waveguide. The only difference in the y equation of motion between the unloaded ferrite waveguide and the ferrite waveguide is that, in the latter case, the $E_{\mathrm{RF},y}$ is inhomogeneous along the gap. However, we can take the assumption of spatial homogeneity as a first approach to our problem. When such consideration is done, we can use the classical multipactor modes and formulas to qualitatively explain the ferrite loaded waveguide. We will rely on two expressions to reach this aim. The first expression, $V_{0,\min}$, gives the minimum RF voltage that guarantees a resonant multipactor of order N. To deduce such equation we have imposed that an electron starting from $y = 0$ arrives to $y = d$ in a time $(NT/2$, then we have searched the starting phase of the RF field (ϕ) that gives the lowest RF value [1], [2]

$$V_{0,\min} = \frac{m}{e}\frac{(\omega d)(\omega d - v_{0y}\pi N)}{2\sqrt{1+\left(\frac{\pi N}{2}\right)^2}} \tag{8}$$

where v_{0y} is the y-component of the initial velocity. It must be remarked that the RF voltage calculated with (8) does not ensure that the kinetic energy due to v_y is above the W_1 parameter. The second expression is for the RF voltage that ensures a resonant multipactor mode of order N with an electron impacting with a kinetic energy of W_1, i.e., $V_{0,W1}$. In some cases, the values given by expressions of $V_{0,W1}$ or $V_{0,\min}$ may not correspond to valid resonant trajectories. The procedure to deduce $V_{0,W1}$ consists of imposing the two aforementioned conditions in the equations of the y trajectory and the v_y velocity. Finally, it is obtained that

$$V_{0,W_1} = \frac{m}{e}\frac{(\omega d)(\omega d - v_{0y}\pi N)}{\pi N \sin\phi_{W_1} - 2\cos\phi_{W_1}}$$
$$\phi_{W_1} = \operatorname{arc\,cot}\left(\frac{\pi N}{2} - \frac{\omega d - v_{0y}\pi N}{v_{iy}}\right) \tag{9}$$

where v_{iy} is the y impacting velocity that is set to match with the W_1 kinetic energy. Note that expressions (8) and (9) depend on the frequency gap product. For each frequency gap value, it can be estimated the minimum RF voltage at which each of the multipactor modes appears.

TABLE I
MULTIPACTOR MODES FOR $f \times d = 8.4$ GHz mm

N	V_{0,W_1} (V)	$V_{0,min}$ (V)	$W_{i,V_{0,min}}$ (eV)
1	7111	4043	1579
3	5487	1390	280
5	3864	743	95
7	2244	459	43
9	656	300	23
11	x	199	14
13	x	129	8.4
15	x	77	5.4
17	x	37	3.5
19	x	6	2.3

The first multipactor modes at a frequency gap value of 8.4 GHz mm are shown in Table I. The first column indicates the order of the multipactor mode N; second column gives the RF voltage to ensure the resonant electron impacts with a kinetic energy equal to the W_1 (19 eV in our case) of the material, V_{0,W_1}; third column provides the minimum RF voltage at which the resonant trajectories appear, $V_{0,\min}$, and fourth column is for the electron impact kinetic energy when the RF voltage is $V_{0,\min}$ and $W_{i,V_{0,\min}}$. If $W_{i,V_{0,\min}}$ is equal or above W_1 then $V_{0,\min}$ is the multipactor RF voltage threshold for the N mode, if not the multipactor RF voltage threshold is $V_{0,W1}$. At the view of the results summarized in Table I, the $N = 9$ multipactor mode appears at an RF voltage threshold lower than the other available modes ($N = 1, 3, 5, 7$), which appear at higher RF voltages than the multipactor threshold. Electron resonant trajectories with $N = 11, 13, 15, \ldots$ may appear but cannot contribute to the eventual onset of the discharge since their impacting energies are below W_1. The results of the multipactor numerical simulations for the without ferrite waveguide are in concordance with the theoretical predictions of Table I. Indeed, in Fig. 6 (left), it is depicted the effective electron vertical trajectory at 8.4 GHz mm in the multipactor RF voltage threshold, revealing the presence of a resonant multipactor with $N = 9$. In Fig. 6 (right), it is depicted the effective electron vertical trajectories at the same frequency gap in the multipactor RF voltage threshold for the ferrite loaded waveguide with $d = 1$ mm. Note that at this frequency gap, the cyclotron resonance occurs and the multipactor RF voltage threshold is clearly below the without ferrite value. For this case, it cannot be found a well-defined multipactor order, instead a hybrid multipactor than ranges from order

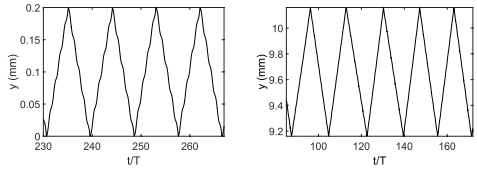

Fig. 6. Vertical coordinate effective electron trajectories as a function of the time normalized to the RF period, $f \times d = 8.4$ GHz mm. Left: metallic parallel-plate waveguide (without ferrite case), $V_0 = 518$ V. Right: ferrite loaded waveguide with $d = 1$ mm and $V_0 = 25$ V.

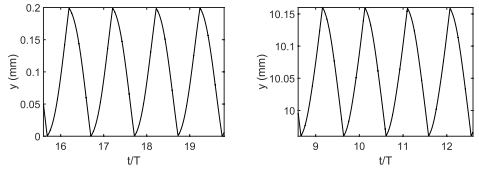

Fig. 7. Vertical coordinate effective electron trajectories as a function of the time normalized to the RF period, $f \times d = 1.68$ GHz mm. Left: metallic parallel-plate waveguide (without ferrite case), $V_0 = 104$ V. Right: ferrite loaded waveguide with $d = 0.2$ mm and $V_0 = 103$ V.

TABLE II
MULTIPACTOR MODES FOR $f \times d = 1.68$ GHz mm

N	V_{0,W_1} (V)	$V_{0,min}$ (V)	$W_{i,V_{0,min}}$ (eV)
1	162	126	55
3	x	15	5.2
5	x	11	0.7

15 to 19 appears [see Fig. 6 (right)]. According to Table I, for such multipactor modes, there are no RF voltages that give an impact kinetic energy of the electron equal or above the W_1 of the material. Although resonant trajectories can appear (when the RF voltage exceeds $V_{0,\min}$), their impacting energies are quite below the W_1 (5.4 and 3.5 eV for the multipactor orders 17 and 19, respectively). However, these impacting energies have been obtained for the classical metallic parallel-plate waveguide (without ferrite), where there is only vertical RF electric field that accelerates the electron along that spatial direction. In the ferrite loaded case, the RF electric fields in the transverse xz plane induce an acceleration, which is uncoupled from the vertical dynamics of the electron but contributes to its total kinetic energy. Indeed, after analyzing the different spatial contributions to the electron total kinetic energy, it is noticed that the xz plane contribution notoriously exceeds the vertical contribution (recall Fig. 5). This occurs because the xz plane acceleration is maximum at the frequency gap value that fits the cyclotron resonance. This fact allows to reduce the multipator RF voltage threshold in the ferrite case with regard to the without ferrite case, thus moving from a multipactor order 9 (without ferrite case) to a 17–19 multipactor order (ferrite case).

In the same way that for Table I, the first resonant modes for $f \times d = 1.68$ GHz mm are shown in Table II. At this frequency gap value, only the multipactor mode with $N = 1$ can contribute to the multipactor discharge in the unloaded ferrite waveguide. Resonant trajectories with orders 3 and 5 may exist, but their impacting energies are insufficient to release secondary electrons. In Fig. 7 (left), it is depicted the effective electron vertical trajectory at 1.68 GHz mm in the multipactor RF voltage threshold for the without ferrite case; it can be observed the presence of the predicted multipactor mode of order 1. In Fig. 7 (right), it is also shown the effective electron vertical trajectory at the same frequency gap value for the ferrite waveguide with $d = 0.2$ mm; it is noticed the presence of the same multipactor mode ($N = 1$) that in the without ferrite case. Although for the ferrite case the frequency gap value matches the cyclotron resonance, the other available multipactor modes ($N = 3$ and $N = 5$) have too short flight time between successive impacts with the device walls, preventing the energy gain in the xz plane due to the cyclotron resonance. This fact justifies that the multipactor RF voltage thresholds are equal in the loaded and unloaded ferrite cases.

As it is well stated in the classical multipactor theory, the number of multipactor modes available for a multipactor discharge grows as the frequency gap increases [2]. In the same way, the flight time between successive electron impacts rises up as the multipactor order does. Thus, low-frequency gap values imply low crossing gap times for the electrons. This fact justifies similarity in the multipactor RF voltage threshold between the ferrite waveguide and the without ferrite cases for the low-frequency gap values (remember Fig. 3). Despite the presence of the accelerating RF electric field in the xz plane, the contribution to the electron kinetic energy is quite low due to short transit time. However, when the frequency gap increases the flight time also does, allowing higher gain in the transverse plane kinetic energy, and so reducing the multipactor RF voltage threshold regarding the without ferrite case (recall Fig. 3).

Previously, we have analyzed ferrite waveguides with the vacuum gaps of 0.2, 1, and 2 mm, and a total height equal to the standard WR-90 waveguide. For completeness, we try a ferrite loaded waveguide with a gap of $d = 5$ mm. According to the above statements, for the frequency gap value that matches the cyclotron resonance (in this case 42 GHzmm), it is expected a sharp minimum in the multipactor RF voltage threshold. Indeed, the results from the numerical simulations for the multipactor RF voltage threshold in the $d = 5$ mm ferrite waveguide shown in Fig. 8 confirm this statement. It should be remarked that for a classical metallic parallel-plate waveguide, no multipactor discharge is expected at such high-frequency gap values at the RF voltage levels employed in the RF satellite telecommunication systems.

Finally, it has been analyzed the case of having different SEY coefficients for the ferrite and the metal surface. The SEY parameters for the ferrite remain the same that were described previously in this section, while the SEY coefficients for the metal are those from the ECSS silver [3], i.e., $W_1 = 30$ eV, $W_{\max} = 165$ eV, and $\delta_{\max} = 2.22$. In Fig. 9, it is shown the multipactor RF voltage threshold for the ferrite waveguide

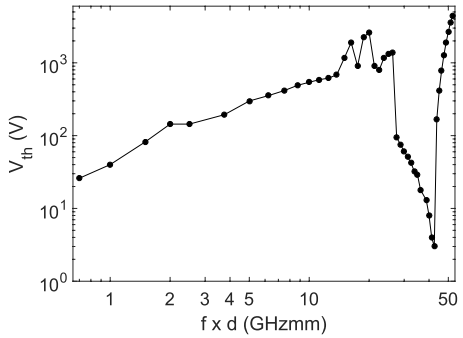

Fig. 8. Multipactor RF voltage threshold as a function of the frequency gap for a ferrite waveguide with $d = 5$ mm and $b = 10.16$ mm.

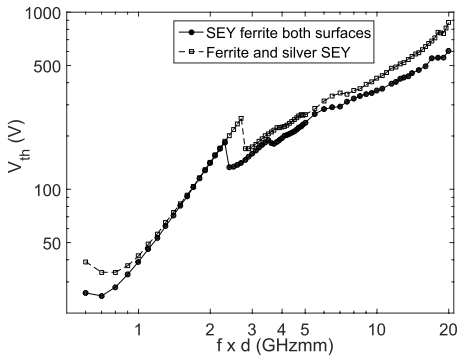

Fig. 9. Multipactor RF voltage threshold as a function of the frequency gap for a ferrite waveguide with $d = 0.2$ mm and $b = 10.16$ mm, considering the same SEY properties for both surfaces and considering different SEYs for ferrite and metal (silver) surfaces.

with $d = 0.2$ mm considering the ferrite and silver SEY properties, as well as the results considering the same SEY properties for both surfaces. It is observed slight differences between both cases. Note that the multipactor RF voltage threshold in the ferrite and silver SEY case tends to be greater than in the case with the same SEY in both surfaces, this is because the W_1 for silver is above the W_1 for the ferrite, and more RF voltage amplitude is required in the former case to reach the multipactor threshold.

IV. Conclusion

In this paper, the multipactor effect in a parallel-plate waveguide containing a magnetized ferrite slab has been studied. In order to magnetize the ferrite, an external static magnetic field oriented along the vertical direction was assumed. A home-made 3-D code based on the effective electron model was developed to carry out numerical simulations that allowed to compute the multipactor RF voltage threshold. The multipactor susceptibility charts obtained show that the multipactor RF voltage threshold changes with regard to the classical metallic parallel-plate situation with neither ferrite slab nor external magnetic field. In fact, a considerable reduction threshold with respect to the classic parallel-plate case has been found at some frequency gap ranges. Moreover, the analysis of the effective electron trajectories has led to a better understanding of the multipacting phenomenon in waveguides loaded with magnetized ferrites.

References

[1] J. Vaughan, "Multipactor," *IEEE Trans. Electron Devices*, vol. 35, no. 7, pp. 1172–1180, Jul. 1988.

[2] A. J. Hatch and H. B. Williams, "Multipacting modes of high-frequency gaseous breakdown," *Phys. Rev.*, vol. 112, no. 3, pp. 681–685, Nov. 1958.

[3] *Multipaction Design and Test*, document ECSS-E-20-01A, ESA-ESTEC, 2003.

[4] A. M. Pérez *et al.*, "Prediction of multipactor breakdown thresholds in coaxial transmission lines for traveling, standing, and mixed waves," *IEEE Trans. Plasma Sci.*, vol. 37, no. 10, pp. 2031–2040, Oct. 2009.

[5] V. E. Semenov, E. I. Rakova, D. Anderson, M. Lisak, and J. Puech, "Multipactor in rectangular waveguides," *Phys. Plasmas*, vol. 14, no. 3, p. 033501, 2007.

[6] V. E. Semenov, N. A. Zharova, D. Anderson, M. Lisak, and J. Puech, "Simulations of multipactor in circular waveguides," *Phys. Plasmas*, vol. 17, no. 12, p. 123503, 2010.

[7] A. Coves, G. Torregrosa-Penalva, C. Vicente, B. Gimeno, and V. E. Boria, "Multipactor discharges in parallel-plate dielectric-loaded waveguides including space-charge effects," *IEEE Trans. Electron Devices*, vol. 55, no. 9, pp. 2505–2511, Sep. 2008.

[8] L. K. Ang, Y. Y. Lau, R. A. Kishek, and M. Gilgenbach, "Power deposited on a dielectric by multipactor," *IEEE Trans. Plasma Sci.*, vol. 26, no. 3, pp. 290–295, Jun. 1998.

[9] R. A. Kishek, Y. Y. Lau, L. K. Ang, A. Valfells, and R. M. Gilgenbach, "Multipactor discharge on metals and dielectrics: Historical review and recent theories," *Phys. Plasmas*, vol. 5, no. 5, p. 2120, May 1998.

[10] V. E. Semenov *et al.*, "Preliminary results on the multipactor effect prediction in RF components with ferrites," in *Proc. 14th IEEE Int. Vac. Electron. Conf. (IVEC)*, May 2013, pp. 1–2.

[11] D. González-Iglesias, B. Gimeno, V. E. Boria, A. Gómez, and A. Vegas, "Multipactor effect in a parallel-plate waveguide partially filled with magnetized ferrite," *IEEE Trans. Electron Devices*, vol. 61, no. 7, pp. 2552–2557, Jul. 2014.

[12] R. L. Geng, H. Padamsee, S. Belomestnykh, P. Goudket, D. M. Dykes, and R. G. Carter, "Suppression of multipacting in rectangular coupler waveguides," *Nucl. Instrum. Methods Phys. Res. A*, vol. 508, no. 3, pp. 227–238, 2003.

[13] V. E. Semenov *et al.*, "Reduction of the multipactor threshold due to electron cyclotron resonance," *IEEE Trans. Plasma Sci.*, vol. 40, no. 11, pp. 3062–3069, Nov. 2012.

[14] M. David Pozar, *Microwave Engineering*, 4th ed. New York, NY, USA: Wiley, 2012.

[15] A. J. B. Fuller, *Ferrites at Microwave Frequencies* (IEE Electromagnetic Waves Series). London, U.K.: IET, 2008, p. 280.

[16] J. Helszajn, *Waveguide Junction Circulators Theory and Practice*. New York, NY, USA: Wiley, 1998.

[17] R. E. Collin, *Foundations for Microwave Engineering*. 2nd ed. New York, NY, USA: McGraw-Hill, 1992.

[18] S. Anza, C. Vicente, D. Raboso, J. Gil, B. Gimeno, and V. E. Boria, "Enhanced prediction of multipaction breakdown in passive waveguide components including space charge effects," in *IEEE MTT-S Int. Microw. Symp. Dig.*, Jun. 2008, pp. 1095–1098.

[19] R. M. Vaughan, "Secondary emission formulas," *IEEE Trans. Electron Devices*, vol. 40, no. 4, p. 830, Apr. 1993.

[20] J. Greenwood, "The correct and incorrect generation of a cosine distribution of scattered particles for Monte-Carlo modelling of vacuum systems," *Vacuum*, vol. 67, no. 2, pp. 217–222, Sep. 2002.

[21] S. A. Schelkunoff, "Generalized telegraphist's equations for waveguides," *Bell Labs Tech. J.*, vol. 31, no. 4, pp. 784–801, Jul. 1952.

[22] A. Gómez, J. S. Ipiña M. A. Solano, A. Prieto, and A. Vegas, "Improving the coupled-mode method by means of step functions: Application to partial-height isotropic or anisotropic dielectric parallel-plate waveguides," *Microw. Opt. Techn. Lett.*, vol. 33, no. 6, pp. 408–414, Jun. 2002.

[23] A. Gómez, A. Lakhtakia, A. Vegas, and M. A. Solano, "Hybrid technique for analysing metallic waveguides containing isotropic chiral materials," *IET Microw. Antennas Propag.*, vol. 4, no. 3, pp. 305–315, Mar. 2010.
[24] I. Montero, F. Caspers, L. Aguilera, L. Galán, D. Raboso, and E. Montesinos, "Low-secondary electron yield of ferromagnetic materials and magnetized surfaces," in *Proc. IPAC*, Kyoto, Japan, May 2010, pp. 23–28.

Daniel González-Iglesias received the Licenciado degree in physics and the master's degree in advanced physics from the Universidad de Valencia, Valencia, Spain, in 2010 and 2011, respectively, where he is currently pursuing the Ph.D. degree in physics.

His current research interests include multipacting simulation of RF high-power passive components.

Álvaro Gómez was born in Santander, Spain, in 1976. He received the Licenciado en Ciencias Físicas and Ph.D. degrees from the Universidad de Cantabria, Santander, Spain, in 2000 and 2005, respectively.

He joined the Departamento de Ingeniería de Comunicaciones, Universidad de Cantabria, in 2000, where he became a Profesor Contratado Doctor in 2011. His current research interests include electromagnetic propagation in complex materials and numerical methods in electromagnetics.

Benito Gimeno (M'01) received the Licenciado degree in physics and the Ph.D. degree from the Universidad de Valencia, Valencia, Spain, in 1987 and 1992, respectively.

He became a Full Professor with the Universidad de Valencia in 2010. His current research interests include the electromagnetic analysis and design of microwave passive components and RF breakdown high-power effects.

Óscar Fernández was born in Santander, Spain, in 1976. He received the Degree in telecommunications engineering and the Ph.D. degree from the University of Cantabria, Santander, in 2001 and 2007, respectively. He joined the Department of Communication Engineering, University of Cantabria, in 2001. His current research interests include numerical methods in electromagnetism and microwave measurements.

Angel Vegas (M'98) received the Ph.D. degree in physical sciences from the University of Cantabria, Santander, Spain, in 1983.

He is currently a Full Professor of Electromagnetics with the University of Cantabria, where he is the Head of the Electromagnetics Group. His current research interests include the electromagnetics of complex materials, computer methods in electromagnetism, and microwave measurements.

Fernando Casas received the Ph.D. degree in theoretical physics from the University of Valencia, Valencia, Spain, in 1992.

He has been a Professor of Applied Mathematics with the Universitat Jaume I, Castellon, Spain, since 2009. His current research interests include geometric numerical integration, including the design and analysis of splitting and composition methods for differential equations and their applications, Lie group methods, perturbation techniques, and the algebraic issues involved.

Sergio Anza Hormigo received the B.S. degree in telecommunications engineering and the Ph.D. degree from the Universidad Politecnica de Valencia, Valencia, Spain.

He is currently with Aurora Software and Testing SL, Valencia. His current research interests include the areas of theory and numerical techniques for the modelling and prediction of nonlinear phenomena in RF high power devices for space applications.

Carlos Vicente (M'08) received the Diploma degree in physics from the Universidad de Valencia, Valencia, Spain, in 1999, and the Dr.Ing. degree in engineering from the Technical University of Darmstadt, Darmstadt, Germany, in 2005.

In 2006, he co-founded Aurora Software and Testing SL, Valencia, which is devoted to telecommunications sector. His research concerns the analysis and design of passive components for communications satellites with a special emphasis on high-power practical aspects.

Jordi Gil received the Licenciado degree in physics from the Universidad de Valencia, Valencia, Spain, in 2000, and the Ph.D. degree in telecommunications engineering from the Universidad Politécnica de Valencia, Valencia, in 2010.

In 2006, he co-founded Aurora Software and Testing SL, Valencia, which is devoted to the space sector. His current research interests include numerical methods in computer-aided techniques for the analysis and design of microwave passive components.

Rafael Mata received the Degree in physics and the Ph.D. degree from the Universidad de Valencia, Valencia, Spain, in 2006 and 2011, respectively.

He held a researcher/technician position with the Val Space Consortium, Valencia, in 2012. His current research interests include secondary electron emission properties, outgassing, and venting processes in RF high power space materials.

Isabel Montero is currently a Research Professor with the Spanish National Research Council (CSIC), Madrid, Spain. She is the Head of the Group Surface Nanostructuring for Space and Terrestrial Communications, Materials Science Institute of Madrid (ICMM-CSIC), Madrid. She is also the Director of Spanish Laboratory on secondary electron emission, CSIC.

Vicente E. Boria (S'91–A'99–SM'02) received the Doctor Ingeniero de Telecomunicación degree from the Universidad Politécnica de Valencia, Valencia, Spain, in 1997.

He is currently a Full Professor with the Universidad Politécnica de Valencia. His research interests include the electromagnetic analysis and design of microwave passive components and also RF breakdown high-power effects.

David Raboso received the Degree in physics from the Autonomous University of Madrid, Madrid, Spainand the master's degree in space engineering from the University of Delft, Delft, The Netherlands.

In 1992, he joined the European Space Agency, The Netherlands, where he became responsible for all activities related to RF breakdown in space microwave components. He has co-authored over 100 articles in prestigious journals and a Co-Inventor of nine patents.

Chapter 6

General discussion

The articles presented in the Chapter 5 constitute the core of the research done in this PhD Thesis. These papers cover a wide range of different scenarios concerning to the multipactor phenomenon in RF waveguides and transmission lines. Basically, the contents of the articles can be submitted in four different topics that correspond to the following sections in which this Chapter has been splitted, namely: multipactor mitigation by means of static magnetic fields (section 6.1), multipactor in ridge waveguides (section 6.2), multipactor with digital modulated signals (section 6.3), and multipactor in a ferrite-loaded waveguide (section 6.4).

This chapter will give an overview of the aforementioned articles, detailing the motivation, objectives, main results and conclusions for each analyzed problem.

6.1. Multipactor mitigation by means of static magnetic fields

It is well-known that the multipactor discharge addresses several negative effects that degrade the performance of a realistic microwave component. Due to this, multipactor mitigation techniques, encouraged to prevent the appearance of the multipactor discharge during the component operation, have been subject of a number of studies with the purpose of designing multipactor-free RF devices. Several techniques for avoiding this undesirable effect have been attempted. On the one hand, surface treatments such as chemical polishing, groove insertions in the metal surface, or surface coatings are aimed to the modification of the SEY properties in order to reduce the amount of emitted secondary electrons [38]-[42]. However, surface treatments degra-

de in time and surface grooves impair the RF performance. On the other hand, some authors propose the use of DC magnetic fields for the partial or total discharge mitigation. Sometimes, the direction of the applied magnetic field is oriented along the transverse plane for a coaxial geometry [47], whilst an axial magnetic field is inserted for multipactor suppression in rectangular waveguides [43]-[46]. Alternatively, a DC electric field can be applied for mitigation purposes, as reported in [48] for coaxial transmission lines.

In this section, the feasibility of using an axial static magnetic field to mitigate the multipactor discharge in a coaxial transmission line is explored. To reach this aim, in a first stage it is analyzed the multipactor effect assuming that the coaxial line is immersed in a uniform axial static magnetic field over all the sample length (see subsection 6.1.1). The results obtained both from theory and experiment revealed that the discharge could be mitigated under certain circumstances. However, the implementation of such axial and uniform magnetic field was found to be very unpractical from an experimental point of view. Due to this, in a second stage, it was explored the multipactor mitigation using the more realistic magnetic field pattern generated by a permanent magnet (see subsection 6.1.2). In this case, the magnetic field had also a radial component besides the axial one, and both of them were spatially non uniform over the coaxial sample. Fortunately, numerical simulations predicted that the mitigation effects of such magnetic field were comparable to the results of the ideal pure DC axial magnetic field case. This statement was also confirmed by experimental measurements, demonstrating the feasibility of using permanent magnets to achieve multipactor mitigation in a coaxial transmission line.

6.1.1. Uniform axial DC magnetic field

The application of a static magnetic field oriented along the axial direction of a coaxial transmission line causes the appearance of an azimuthal acceleration that bends the electron trajectories across the magnetic field flux lines, pushing electrons trajectories back to the departure conductor, thus disturbing the multipactor resonant electron trajectories and possibly inhibiting the onset of the discharge.

First, numerical simulations were performed for a particular coaxial sample in order to explore the variation of the multipactor RF power threshold with the external magnetic field applied at a fixed value of the RF frequency. Afterwards, this procedure is repeated for other RF frequencies. The presented numerical simulations have been

performed with the Monte-Carlo algorithm based on the effective electron model. The coaxial sample inner and outer radius dimensions are $a = 1.515 \pm 0.001$ mm and $b = 3.490 \pm 0.001$ mm, respectively; the gap length is $d = b - a = 1.975 \pm 0.001$ mm, the characteristic impedance is $Z_0 = 50\,\Omega$, and the length of the total sample is 90.4 ± 0.1 mm. The material for both conductors is copper, with the following SEY parameters of the modified Vaughan's model: $W_1 = 25 \pm 1$ eV, $\delta_{max} = 2.25 \pm 0.01$, and $W_{max} = 175 \pm 1$ eV.

For the multipactor measurements the coaxial sample was inserted in a long solenoid which provides an axial uniform static magnetic field when it is fed by a DC current. The solenoid designed and manufactured for such purpose is formed by around 8250 turns with 30 cm length and 1.905 cm internal radius (see Fig. 6.1). The solenoid was calibrated by means of a magnetic probe mounted in a translation linear stage, which moves along the axis of symmetry of the solenoid. This set-up was carried out at the Laboratory of Electromagnetics of the Faculty of Physics at the University of Valencia. The calibration is based on the electromagnetic induction phenomenon. After the calibration the linear relation between the feeding current I_{DC} and the magnetic field strength induced in the center of the solenoid B_{DC} was established, which is $B_{DC} = 3.8 \pm 0.1$ mT when $I_{DC} = 100$ mA.

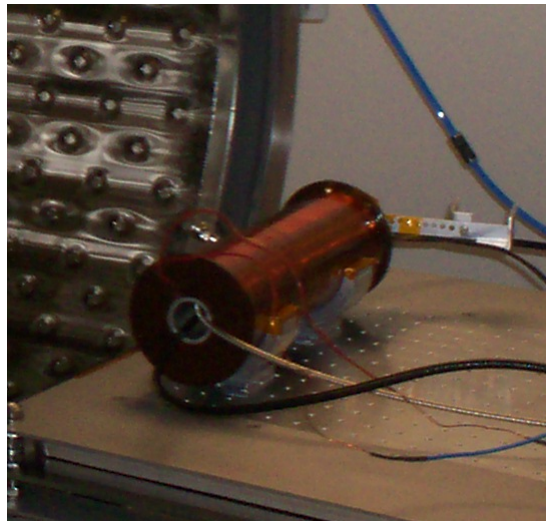

Figura 6.1: Picture of the solenoid placed with the coaxial sample immersed inside.

In Fig. 6.2 the results for both the numerical simulations and the experimental measurements are shown. Each plot depicts the multipactor RF power threshold as a function of the external magnetic field amplitude, expressed in terms of the cyclotron frequency ($f_c = \frac{1}{2\pi}\frac{e}{m_e}B_{DC}$) normalized to the RF frequency f. It must be mentioned that experimental data are available for $f = 0.435$ GHz and $f = 1.145$ GHz. In both of these two cases, good agreement between simulations and measurements is found.

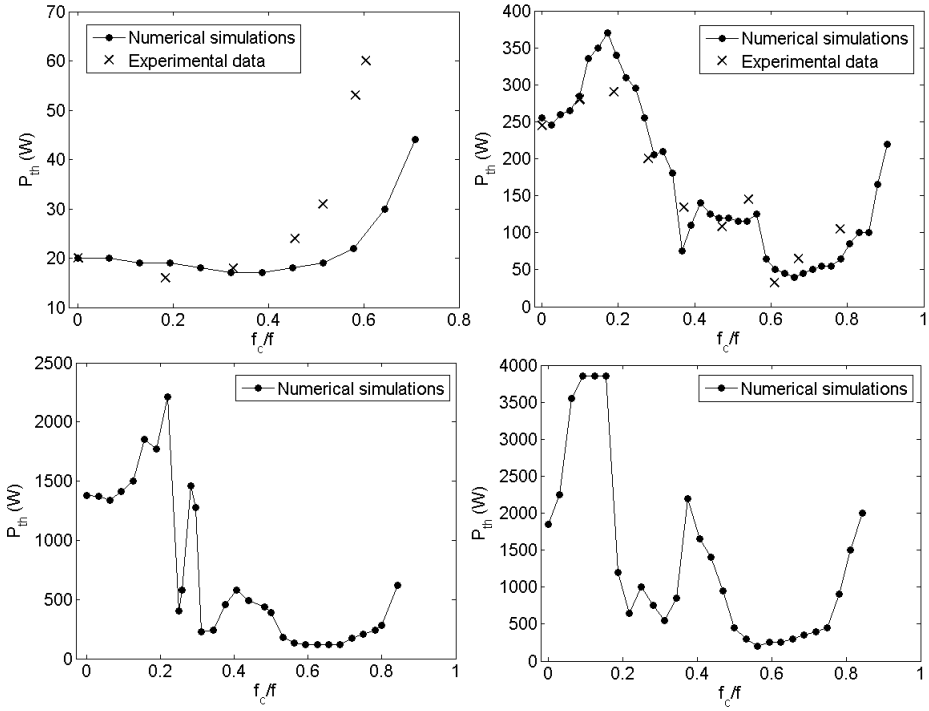

Figura 6.2: Multipactor RF voltage threshold as a function of the external magnetic field (in terms of the cyclotron frequency normalized to the RF frequency). From left to right, and top to bottom: $f = 0.435$ GHz, $f = 1.145$ GHz, $f = 2.000$ GHz, $f = 3.000$ GHz.

The most relevant conclusion that can be extracted from results presented in Fig. 6.2 is that the multipactor discharge can be inhibited provided that a strong enough magnetic field is applied. In fact, the minimum magnetic field that prevents the onset of the discharge is within the range $f_c/f \in [0.7, 1]$. Although simulations explored a

wide range of f_c/f values above the mitigation discharge limit, no multipactor was found, even for high values of the f_c/f ratio. From the experimental point of view, the measurement of situations with high f_c/f was restricted. The reason for this limitation is that the higher the magnetic field the higher the current that feeds the solenoid and, consequently, the Joule heating effect due to the ohmic resistance of the solenoid wire becomes greater. Since the solenoid is placed inside the vacuum chamber, no heat dissipation by means of convective process is possible, resulting in a continuous warming of the coil during the evolution of the experiment. The local increase of the solenoid temperature was revealed to promote the outgassing of the dielectric cover surrounding the metallic wires, leading to a reduction of the vacuum level inside the tested device, thus disturbing the measurement. Taking into account this limitation, for the $f = 0.435$ GHz case, the values of f_c/f equal to 0.644, 0.710, 0.856, 0.952, 0.978, and maximum 1.216 were measured, sweeping the RF power up to a maximum of 120 W (the maximum value deliverable by the RF power amplifier) without detecting any discharge. Similarly it was proceeded at $f = 1.145$ GHz, measuring the points of f_c/f equal to 0.837, 0.918, 1.673 up to a maximum power of 1450 W.

Multipactor mitigation phenomenon can be understood in terms of the electron resonant trajectories. The classical multipactor theory for parallel-plate waveguides (described in section 2.1) predicts the presence of double-surface electron resonant trajectories, taking the electron an odd number of RF semiperiods in crossing the gap between the plates. However, as it was reported in [25], when an external static electric or magnetic field is applied, it is possible the appearance of single-surface multipactor modes, in which the electron collides in the successive impacts with the departure wall in a time equal to an even number of RF semiperiods. In the numerical simulations, it was noticed the presence of such single-surface multipactor modes that become predominant as the f_c/f ratio increases. In fact, the bending effect in the electron trajectories grows together with f_c/f, pushing back the electron to the departure conductor and preventing it from reaching the opposite conductor. In addition, a reduction of the electron flight time between successive collisions is produced. The reduction of this time lapse is critical. If the transit time is too short, the electron might not be able to get resonant with the RF electric field, which is a necessary condition for starting the multipactor discharge. Moreover, very short flight times implies a reduction of the amount of kinetic energy that the electron can extract from the RF electric field between consecutive impacts.

In order to give a picture of the effect of the static magnetic field in the electron

motion, in Fig. 6.3 we have plotted the cylindrical radial coordinate of the effective electron as a function of the time normalized to the RF period, for some characteristic points of the multipactor RF power threshold curve corresponding to an RF frequency of 1.145 GHz (recall Fig. 6.2). The data for the considered points are outlined in the Table 6.1.

Table 6.1: Summary of the analyzed points for the $f = 1.145$ GHz case in Fig. 6.2

Point	f_c/f	P (W)
A	0	245
B	0.197	290
C	0.367	86
D	0.538	145
E	0.660	65

For point A, which corresponds with the zero external magnetic field case, it is found a hybrid double-surface multipactor mode of order 1 from the inner-to-outer conductor and 3 from the outer-to-inner case (see Fig. 6.3). For point B, the presence of the magnetic field bends the electron trajectories, resulting in a mix between double- and single- surface multipactor regimes. At the point C, the DC magnetic field has become strong enough to avoid electrons reaching the opposite conductor so that there are only single-surface orbits. It is observed a different behavior for electrons launched from the inner and outer conductor. In fact, multipactor discharge is only produced in the inner conductor, where a single-sided multipactor regime of order 4 appears. With regard to electrons starting from the outer conductor, they do not have a well-defined order of resonance, and besides their impacting energies are below the first-cross over point of the material. This asymmetric behavior between the inner and outer walls is due to the spatial variation of the RF electric field of the TEM fundamental mode as $1/r$ (r being the radial coordinate). For point D, it is obtained that the multipactor is generated in the outer metal with a single-surface discharge of order 2. Now, in the inner conductor, there is a lack of resonance in the electron trajectories and the discharge cannot occur. Finally, for point E, the discharge is expected again only in the inner conductor, with a multipactor of order 2. It is worth to mention that the single-surface multipactor theory establishes that the minimum order that ensures resonance between the electron and the RF electric field is 2. Taking into

consideration that as the magnetic field is increased the flight time of the electron between successive impacts diminishes, it is straightforward that a magnetic field with an amplitude higher to that corresponding to point E (which has the lowest available order of single-surface) will result in the total inhibition of the discharge.

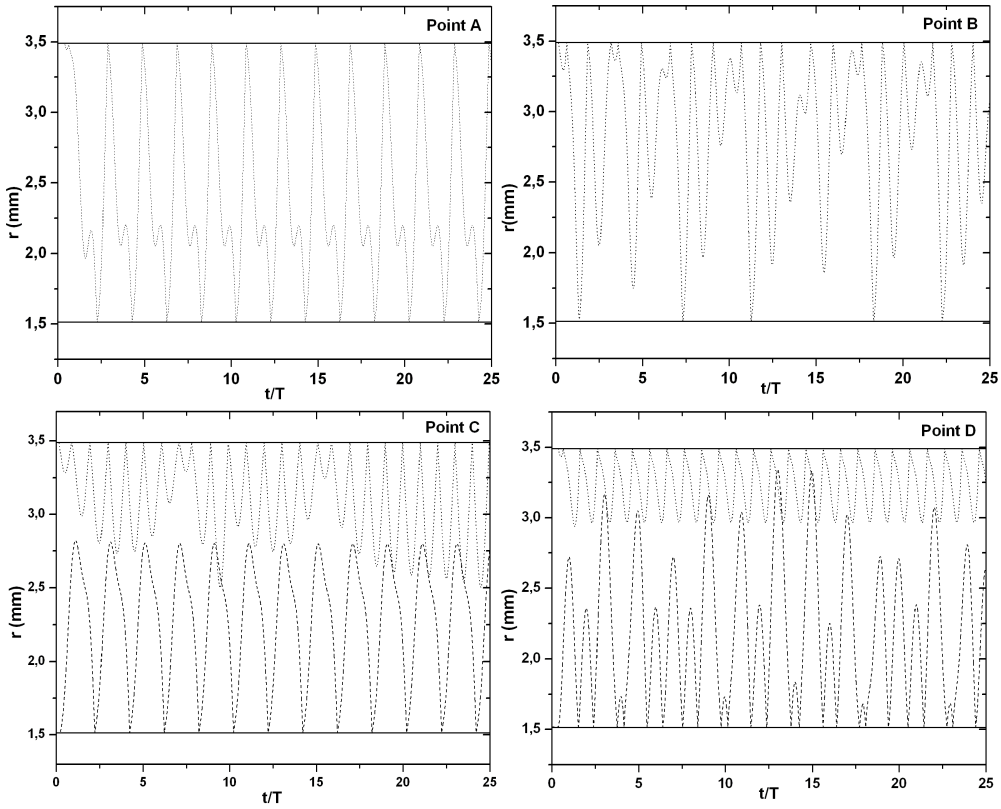

Figura 6.3: Electron trajectories of points A, B, C, and D; for case $f = 1.145$ GHz of Fig. 6.2. The cylindrical radial coordinate has been plotted as a function of the normalized time. The inner and outer radius of the coaxial cable have been marked with horizontal lines. In points C and D, two electrons are launched: one from the inner conductor and other from the external one.

6.1.2. Non-uniform magnetic field generated with permanent magnets

As shown in the previous section for the uniform axial DC magnetic field case, it is possible to avoid the multipactor discharge provided a strong enough magnetic field is applied over the coaxial sample. However, the experimental implementation of such uniform axial magnetic field requires the use of a solenoid, which is unpractical in most cases since it presents some problems such as heavy weight, big size, requirement of a DC power supply, and outgassing caused by the overheating due to ohmic losses. An alternative that overcomes the inconveniences that presents the coil is the use of a permanent magnet. Proceeding in a similar way as in the coil case, the coaxial sample was inserted inside of a hollow cylindrical neodymium permanent magnet. The magnet was acquired in [59].

First of all, we needed to obtain the mathematical expressions that provide the magnetic field generated by a hollow permanent magnet, in order to compute the electron trajectories within the coaxial waveguide. The hollow cylindrical magnet under consideration is shown in Fig. 6.4, whose dimensions are b_1 and b_2 for the inner and outer radius of the cylinder, respectively, and h is the height. As indicated, the reference frame is centered in the mid-height of the cylinder.

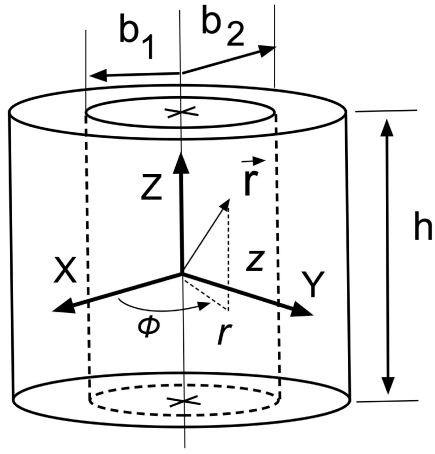

Figura 6.4: The scheme of the hollow magnet with height h, and b_1 and b_2 radii.

A prior step to the obtaining of the magnetic field of the hollow cylinder is the

calculus of the magnetic field of an homogenously magnetized cylinder with radius r_0. The magnetic field of such uniform magnetized cylinder can be derived from the equivalent volume and surface magnetization currents [60]

$$\begin{aligned} \vec{J}_M &= \nabla \times \vec{M} \\ \vec{K}_M &= \vec{M} \times \vec{n} \end{aligned} \tag{6.1}$$

$\vec{J}_M$ and $\vec{K}_M$ being the volume and the surface equivalent currents, respectively; $\vec{n}$ is the unitary vector normal to the surface, and $\vec{M}$ the volume magnetization. In this case, we have that $\vec{M} = M\hat{z}$, and consequently

$$\vec{J}_M = \vec{0}$$

$$\vec{K}_M = M\hat{\phi}, \quad \text{for the lateral surface } (r = r_0) \tag{6.2}$$

$$\vec{K}_M = \vec{0}, \quad \text{for the top and bottom surfaces } (z = \pm h/2) \tag{6.3}$$

Once the equivalent currents are obtained, the static magnetic field inside and outside the magnet can be calculated by means of the Ampere's Law [60],

$$\vec{B}(\vec{r}) = \frac{\mu_0}{4\pi} \int_{S'} \frac{\vec{K}_M \times \vec{R}}{R^3} dS' \tag{6.4}$$

where μ_0 is the magnetic permeability of vacuum, dS' is the differential surface element containing the source current $\vec{K}_M$, $\vec{R} = \vec{r} - \vec{r}'$, $\vec{r}$ being the position vector where the field is calculated and $\vec{r}'$ the vector position of the current source. After integrating (6.4) for our case the following expressions arise:

$$B_r(r,z) = \frac{\mu_0 M}{4\pi} \sqrt{\frac{16\, r_0}{r}} \left[\frac{E(k_2)}{k_2} - \frac{E(k_1)}{k_1} + \frac{1}{k_1^2} \left(1 - \frac{k_1^2}{2}\right) K(k_1) - \left(1 - \frac{k_2^2}{2}\right) K(k_2) \right] \tag{6.5}$$

$$B_z(r,z) = \frac{\mu_0\, M}{2\pi \sqrt{r\, r_0} \left(1 + \frac{r}{r_0}\right)^2} \left[\left(z + \frac{h}{2}\right) k_2 \Pi\left(k_2, \sigma\right) + - \left(z - \frac{h}{2}\right) k_1 \Pi\left(k_1, \sigma\right) \right] - \frac{r}{r_0} B_r(r,z) \tag{6.6}$$

$$\sigma \equiv \frac{4\,r\,r_0}{(r+r_0)^2}$$

$$k_1 \equiv \sqrt{\frac{4\,r\,r_0}{(r+r_0)^2+\left(z-\frac{h}{2}\right)^2}}$$

$$k_2 \equiv \sqrt{\frac{4\,r\,r_0}{(r+r_0)^2+\left(z+\frac{h}{2}\right)^2}}$$

where $K(k)$, $E(k)$ and $\Pi(k,\sigma)$ are the complete elliptic integrals of the first, the second and the third kind, respectively [61]-[64]. Note that the azimuthal magnetic field component is zero due to symmetry.

Finally, the magnetic field expression for the hollow cylinder can be obtained by considering the superposition of the magnetic fields generated by two homogeneously magnetized cylinders with different radii, the same magnetization strength, and opposite magnetization direction:

$$\vec{B}_{hollow}(\vec{r}) = \vec{B}_{r_0=b,M}(\vec{r}) + \vec{B}_{r_0=a,-M}(\vec{r})$$

In this subsection, we will focus on the mitigation of the multipactor for a specific coaxial sample with the following dimensions: inner and outer coaxial radius are $a = 1.238 \pm 0.001$ mm and $b = 2.850 \pm 0.001$ mm, respectively; the gap between conductors is $d = b - a = 1.612 \pm 0.001$ mm, the characteristic impedance is $Z_0 = 50\,\Omega$, and the sample length is $l = 41.0 \pm 0.1$ mm. Both conductors were made of copper, with the following SEY properties: $W_1 = 19.5 \pm 0.1$ eV, $\delta_{max} = 2.61 \pm 0.1$, and $W_{max} = 219.7 \pm 0.1$ eV. According to these parameters, the design of a hollow cylindrical magnet prototype is accomplished with the aim of achieving the maximum multipactor mitigation range, while minimizing the weight and size of the magnet. Taking into account these specifications the following considerations arise:

- Since the multipactor mitigation requires strong magnetic fields, the maximum magnetization strength of the magnet is preferred.
- The inner radius of the cylinder must be large enough to ensure that the coaxial sample can be inserted inside, leaving a small gap to allow the outgassing of the whole structure.

- A small cylinder thickness is desirable to reduce weight and size. However, it is found that increasing the thickness (for a fixed magnetization value) enlarges the magnetic field inside the magnet. The minimum thickness of the magnet is 2 mm due to manufacturing considerations. After some parametric analysis it was found that a thickness in the range $2 - 4$ mm could be enough to provide the required magnetic fields for mitigation purposes.

- The magnet height must be high enough to generate a quasi-uniform axial magnetic field component. At the same time, minimizing the height as much as possible is required for the device compactness.

According to these considerations and the specifications provided by the manufacturer of the magnet, we choose $M = 1.153 \times 10^6$ A/m, $b_1 = 12.5$ mm, $b_2 = 16.5$ mm. In order to select the proper height of the cylinder, which is the last remaining dimension, we show in Fig. 6.5 the axial and radial magnetic field components of the hollow cylindrical magnet as a function of the axial coordinate normalized to the magnet height, using the expressions (6.5) and (6.6).

It is observed that the axial (radial) magnetic field component is symmetrical (antisymmetrical) with respect to the plane $z = 0$. Moreover, it is also noticed that the axial magnetic field presents a local minimum (in absolute value) in the center of the magnet. When we move towards the magnet edge there is a local maximum and then the strength drops to zero. The highest axial magnetic field is reached approximately in the region described by $z/h \in [-0.3, 0.3]$, and it becomes weaker as we approach to the magnet edges. In order to avoid these low axial magnetic field zones, the magnet height is selected to be $5 - 10\,\%$ higher than the coaxial length. Finally, the height of the magnet has been chosen to be: $h = 44$ mm. In Fig. 6.6 we can see a picture of the hollow cylindrical magnet prototype with the coaxial sample inserted inside.

In order to explore the multipactor mitigation capabilities of the magnet prototype, multipactor numerical simulations were performed with the Monte-Carlo code based on the effective electron model described in subsection 3.6. Two different configurations for the coaxial waveguide were considered. The first configuration corresponds to the coaxial line without the magnet; the second case is for the coaxial waveguide immersed in the hollow magnet. For each configuration, the multipactor RF power threshold was obtained as a function of the RF frequency value. In addition, a set of multipactor experiments were carried out in order to compare with the theoretical results. A summary of the results obtained both from simulations and tests is pre-

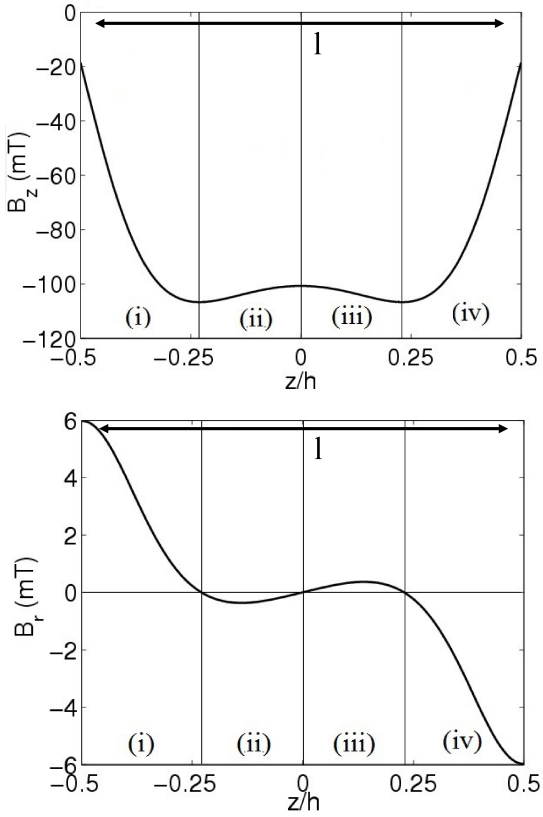

Figura 6.5: The axial B_z and radial B_r components of Fig. 6.4, given by expressions (6.6) and (6.5), as a function of the normalized coordinate z/h. It is also indicated the length (l) of the coaxial sample immersed in the magnet. The value of the radial cylindrical coordinate has been chosen in the center of the coaxial gap, $r = 2.044$ mm. Magnet dimensions and properties: $b_1 = 12.5 \pm 0.1$ mm, $b_2 = 16.5 \pm 0.1$ mm, $h = 44.0 \pm 0.1$ mm, and $M = 1.153 \times 10^6$ A/m.

sented in Fig. 6.7. The numerical simulations predict the multipactor mitigation with the magnet below $f \times d = 4.030$ GHz mm ($f = 2.5$ GHz) which corresponds to $f_c/f = 1.12$ (f_c has been calculated in $z = 0$, $r = (b - a)/2$, the coaxial gap point where the axial magnetic field is maximum). It should be mentioned that multipac-

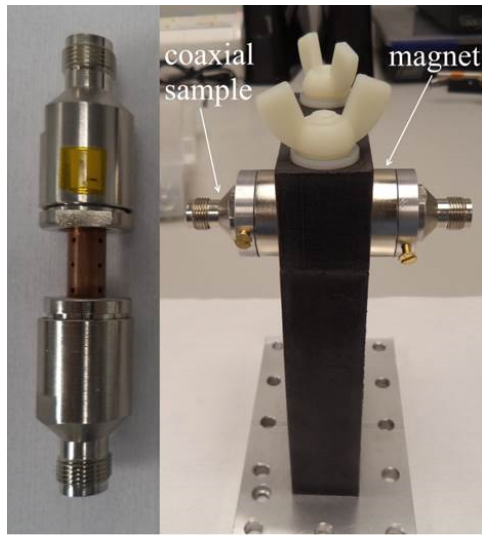

Figura 6.6: Picture of the coaxial sample (left), and the coaxial sample inserted inside the magnet (right).

tor appears above such frequency gap value with an RF power threshold lower than for the case without magnet. With regard to the experimental measurements, several RF frequencies within the range from 0.435 GHz ($f \times d = 0.701$ GHz mm) to 1.6 GHz ($f \times d = 2.579$ GHz mm) were explored, and it is noticed that the measured multipactor RF power thresholds of the without magnet case match well with the corresponding results from numerical simulations. Moreover, the same RF frequencies were tested in presence of the magnet, and then no multipactor discharge was detected, in good agreement with the theoretical results. It must be mentioned that the numerical simulations explore frequency values up to 4.96 GHz (8 GHz mm, recall Fig. 6.7), whilst experimental measurements (for both the magnet and without magnet configurations) only reach up to 1.6 GHz ($f \times d = 2.579$ GHz mm). This restriction in the experimental frequency range considered is explained in terms of the increase in the return losses of the considered coaxial sample for high RF frequencies.

It is remarkable that despite the non-uniform magnetic field, the multipactor threshold for the coaxial waveguide immersed in the hollow cylindrical magnet is similar to the uniform magnetic field case provided by the solenoid. In fact, in the uniform

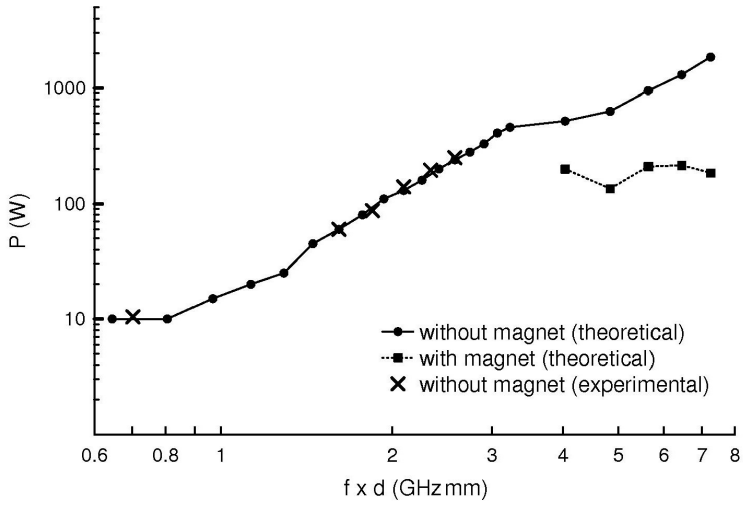

Figura 6.7: Multipactor RF input power threshold as a function of the frequency gap for the two configurations of the coaxial sample. Both theoretical and experimental results are shown. Note that multipactor discharge was not experimentally detected in the presence of the permanent magnet in the frequency range explored.

magnetic field case, the multipactor mitigation takes place when the empirical condition $f_c/f > [0.7, 1]$ is roughly fulfilled. If we take the worst case in the previous condition, we have that the multipactor should be mitigated for RF frequencies below f_c. In our case, the lowest axial magnetic field in the center of the magnet is 100 mT (see Fig. 6.5), which gives a cyclotron frequency of $f_c = 2.8$ GHz ($f_c \times d = 4.5$ GHz mm). By inspecting Fig. 6.7, it is noticed that in fact no multipactor discharge is expected for RF frequencies below $f = 2.5$ GHz ($f \times d = 4.0$ GHz mm). Thus, the multipactor mitigation range of the uniform magnetic field case can be used as a rough approximation for the mitigation when the hollow cylindrical magnet is employed. However, it must be noted that as we approach to the edges of the magnet, the axial magnetic field amplitude diminishes. In fact, in the borders of the coaxial wave-

guide is around 40 mT, which gives $f_c = 1.1$ GHz. This means that, according to the uniform magnetic field approximation, the discharge should appear near the borders of the coaxial line for RF frequencies near above $f = 1.1$ GHz ($f \times d = 1.77$ GHz mm), although this does not occur.

In order to understand a bit more the multipactor mitigation phenomenon in the hollow magnet case, the equations of the electron dynamics as well as the effective electron trajectories have been analyzed. First, from Fig. 6.5 it stated that the radial component $B_r \ll B_z$ and therefore the axial magnetic field strength B_z is dominant for the electron motion. This fact allows to neglect the term $B_{ext,r}\, v_z$ with respect to $B_{ext,z}\, v_r$ in the electron equations of motion. Additionally, for the considered RF power range the microwave magnetic field B_{RF} is also negligible compared with B_z. Thus, the terms $v\, B_{RF}$ can also be neglected. Under these assumptions, for the earlier stages of the electron multiplication, the differential equations can be approximated as follows,

$$\frac{dv_r}{dt} \approx -\frac{e}{m}\left[E_{RF}(\vec{r},t) + B_{ext,z}(\vec{r})\, v_\phi\right] \tag{6.7}$$

$$\frac{dv_\phi}{dt} \approx \frac{e}{m} B_{ext,z}(\vec{r})\, v_r \tag{6.8}$$

$$\frac{dv_z}{dt} \approx \frac{e}{m} B_{ext,r}(\vec{r})\, v_\phi \tag{6.9}$$

For the next argumentation, we do not consider the electron acceleration caused by the microwave electric field. For this situation [65], the electron trajectories are found to spin around magnetic field lines with an angular frequency of $\vec{\omega}_c = (e/m)\vec{B}$. If the axial magnetic field is oriented along the $-z$ direction, the electron will spin clockwise leading to $v_\phi < 0$ since $v_\phi = r\,(d\phi/dt)$ (and $d\phi/dt < 0$ for clockwise rotation). Despite the presence of the RF electric field in our case, we can assume that the electron will still spin with $v_\phi < 0$. As a consequence, the axial acceleration approximated by (6.9) will be positive or negative depending only on the value of B_r. If $B_r > 0$, then $B_r\, v_\phi < 0$ and $dv_z/dt < 0$. Otherwise, if $B_r < 0$, then $B_r\, v_\phi > 0$ and $dv_z/dt > 0$. As it can be noticed from observing Fig. 6.5, the radial magnetic field has zeros at the points $z = -z_c$, $z = 0$, and $z = z_c$. According to this, we can delimit four regions for the axial electron cynematics as follows:

(I) $z < -z_c$, $B_r > 0$, $(dv_z/dt) < 0$

(II) $-z_c < z < 0$, $B_r < 0$, $(dv_z/dt) > 0$

(III) $0 < z < z_c$, $B_r > 0$, $(dv_z/dt) < 0$

(IV) $z > z_c$, $B_r < 0$, $(dv_z/dt) > 0$

Thus, electrons starting from zones (i) or (iv) are pushed towards the magnet edges and eventually leave the coaxial waveguide. However, electrons starting from zone (ii) are pushed towards the zone (iii), but when they reach this region now they are pushed back to zone (ii). In this way, electrons initially released from zones (ii) and (iii) remain trapped in there. In these conditions, only electrons starting from regions (ii) and (iii) will contribute to the multipactor discharge. This point is crucial, since if no radial magnetic field were present, multipactor would appear in regions (i) and (iv) at lower RF power values than in regions (ii) and (iii) (this is because the axial magnetic field is weaker in zones (i) and (iv) than in regions (ii) and (iii)), thus degrading the multipactor mitigation capabilities of the magnet prototype.

The above statements have been confirmed by analyzing the electron trajectories. In Fig. 6.8, the time evolution of the effective electron axial position and its corresponding normalized population are shown. RF frequency has been chosen to be in the mitigation range, hence no multipactor is expected in concordance with simulations shown in Fig 6.7. Different axial launching positions have been selected for each effective electron. The first electron has been released from the zone (i), so it will be pushed out of the coaxial waveguide as indeed occurs in few RF periods. It should be mentioned that after the electron impacts the coaxial surfaces, its emission velocity is random so it can be launched with $v_z > 0$ or $v_z < 0$. Despite that, it is clearly observed that the negative axial acceleration forces the electron to drift towards $-z$. It is also noticed that although the effective electron population grows with time, the population level reached before the electron leaves the waveguide is too low to expect a multipactor discharge. The second electron is launched from the axis center. In this case, the electron remains in the central coaxial region (between regions (ii) and (iii)), as discussed before. Although the electron does not leave the waveguide, the cumulative population quickly diminishes, so no multipactor discharge occurs.

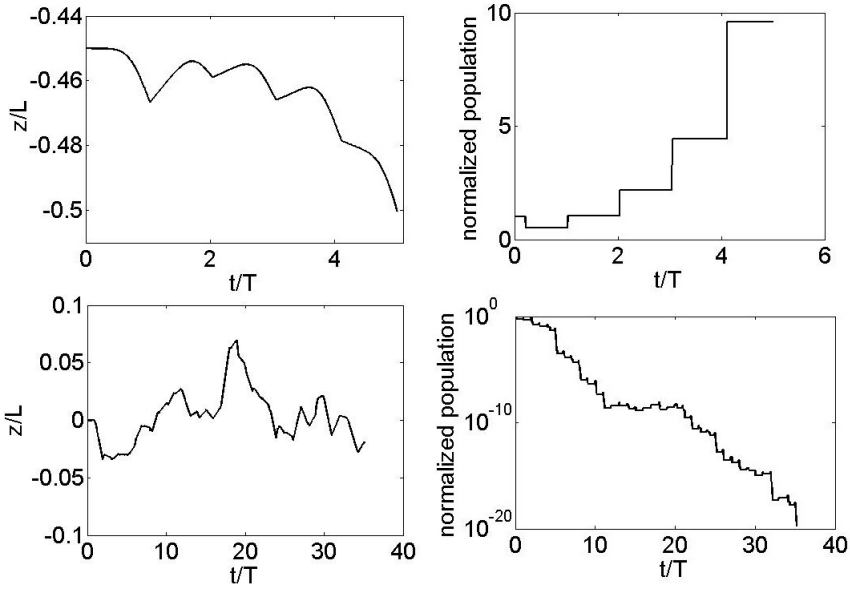

Figura 6.8: Effective electron axial position normalized to the coaxial length (left) and its normalized population (right) as a function of the time normalized to the RF period. RF frequency is $f = 1.5$ GHz ($f \times d = 2.41$ GHz mm) and RF power is 200 W. Electrons were launched from different initial axial positions for the case of the coaxial line inserted in the hollow cylindrical magnet.

6.2. Multipactor in ridge waveguides

Singe- and multi-ridged waveguides present many applications in microwave and milimeter-wave devices. For example, they are widely used for both high-power and low-power applications such as band-pass and quasi low-pass filters [66]-[69]. These filters are very appropriate candidates for some space and terrestrial communication applications, due to their compact size and good stop-band performance. Among their main advantages we find that they include large single-mode broad-band operation, large dominant cutoff wavelength, and low impedance characteristics. Some applications of these filters are, for instance, as preselector filters before the input multiplexer, or as harmonic suppression filters after RF transmitters or amplifiers, particulary as

on board satellite components.

In this section, multipactor susceptibility charts has been computed for several ridge and multi-ridge waveguide configurations. In the present form, the susceptibility charts are plots of the multipactor RF voltage threshold as a function of the frequency gap product (typically the gap is fixed and the RF frequency is swept). The multipactor simulations performed to compute the susceptibility charts have been carried out using the commercial software FEST3D [70]. This tool is able to analyze high RF power phenomena, such as multipactor and corona RF breakdown, in arbitrary RF waveguide structures. It relies on the individual electron model and the interaction electron-surface is taken into account by means of the modified Vaughan's model [15].

In most of the considered configurations for the ridge and multi-ridge susceptibility charts, the gap height d is much less compared to the transverse dimensions, which means that the simulated structures are very close to a parallel-plate waveguide. Despite of this, a wide range of gap heights are covered, which are interesting in practical applications. With regard to the number of ridges, three types of structures have been studied: ridge (one ridge), double-ridge (two ridges), and multi-ridge (three ridges) waveguides. In addition, two different configurations are considered: asymmetrical (the ridge is placed only at the top of the waveguide) and symmetrical (each ridge at the top has its counterpart at the bottom of the waveguide). In Fig. 6.9 the scheme of all the different ridged waveguides considered throughout this work is shown. Mainly, the susceptibility charts explore the variation of the multipactor threshold with two dimensional parameters that characterize the ridge waveguide: the gap height d and the ridge width w.

After the susceptibility charts have been computed, an approximate method for predicting the multipactor RF voltage threshold in complex microwave devices containing ridge and multi-ridge sections is presented. This method uses the available susceptibility charts, presenting the advantage that no additional multipactor simulations for the whole device are required. Only the electromagnetic field distribution of the component is needed. This method is applied to two samples: an evanescent-mode filter and a waffle-iron filter. Finally, numerical simulations carried out with FEST3D have demonstrated the feasibility of this approximate method in order to obtain accurate predictions of the multipactor threshold.

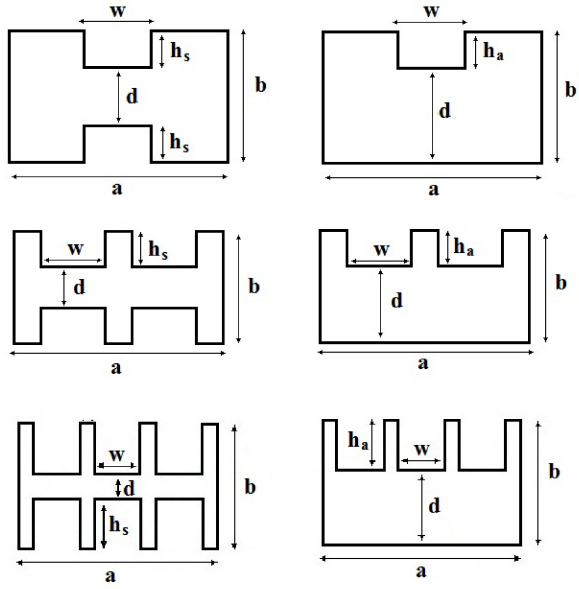

Figura 6.9: Symmetrical structures on the left column and asymmetrical structures on the right column. From top to bottom: ridge, double-ridge and multi-ridge rectangular waveguides.

6.2.1. Multipactor susceptibility charts

Ridge, double-ridge and multi-ridge waveguides (see Fig. 6.9) with housing dimensions of a standard WR75 rectangular ($a = 19.05$ mm, $b = 9.525$ mm) have been analyzed. Symmetrical and asymmetrical configurations have been considered. In susceptibility charts, the RF multipactor voltage threshold is depicted as a function of the frequency gap $f \times d$ (gap is fixed and only RF frequency changes). All simulated structures are silver-plated. The SEY parameters for silver, which are extracted from [2], are: $W_1 = 30$ eV, $\delta_{max} = 2.22$, and $W_{max} = 165$ eV.

As it is well-known, multipactor discharge is always expected to occur in the narrowest waveguide zone, where electric field becomes higher. According to this, the existing gap between metal ridges is the critical zone for the appearance of a multipactor discharge. Thus, an equivalent voltage is numerically computed with FEST3D

using the following expression:

$$V_{eq} = \left| \int_0^d \vec{E} \cdot \vec{dl} \right| \tag{6.10}$$

where $\vec{E}$ is the RF electric field of the fundamental mode in the ridge gap, and $\vec{dl}$ is the differential vector oriented along the gap direction. The integration line is located in the center of the ridge width. It can be checked numerically that for double-ridge waveguides the equivalent voltage is the same at both symmetrical ridges, whereas for multi-ridge waveguides (with an odd number of ridges) the voltage is higher at the central one.

The computed susceptibility charts cover the next range of cases:

- The effect of varying the ratio between the ridge width and the waveguide width w/a, for a fixed value of the gap between the ridge and the waveguide. In this study, a gap height of $d = 0.5$ mm is chosen, which is a typical value in RF devices affected by the multipactor discharge. This analysis is performed for both symmetrical and asymmetrical waveguide configurations, and the susceptibility charts are shown in Fig. 6.10. It is observed that the narrower the ridge, the higher the RF voltage threshold, although only slight variations are observed. This phenomenon is due to that low values of w/a allow the electrons to escape from the gap region in the transverse directions, so an extra voltage is needed to compensate these electron losses. There are two mechanisms that aid the electrons to move out from the ridge gap. On the one hand, the presence of fringing RF electric field in the boundaries of the rigde, that tends to push the electron out of the critical zone. On the other hand, a random drift due to the component transverse to the gap of the initial velocity of the secondary emitted electrons may eventually expel the electrons from the gap. Both of these two effects were also reported in the case of rectangular waveguide irises [9], [71].

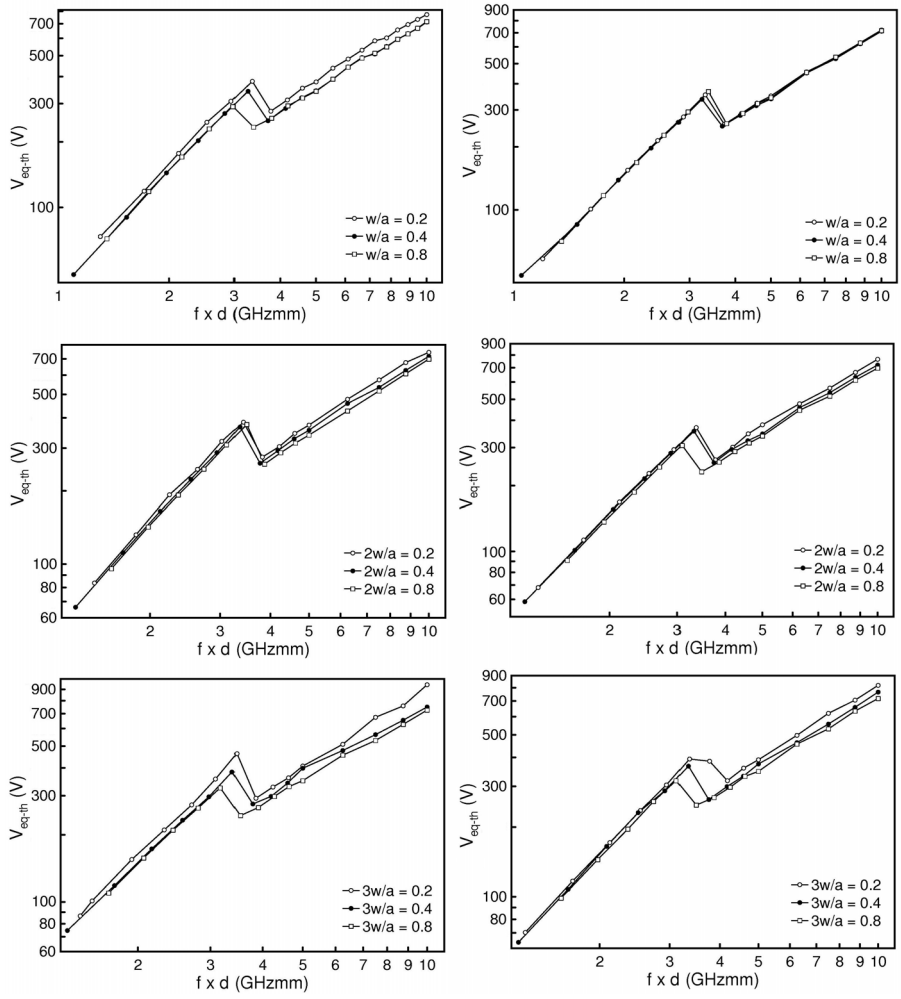

Figura 6.10: Multipactor voltage threshold for several ridge widths in symmetrical (left column) and asymmetrical (right column) configurations. From top to bottom: ridge, double-ridge and multi-ridge waveguides. Gap height is $d = 0.5$ mm, $d/b = 0.052$ and $b/a = 0.5$.

- The effect of the fringing RF electric field when the gap height is similar to the ridge width. In Fig. 6.11 the results for a symmetrical single-ridge waveguide are presented, but similar behavior can be found for asymmetrical and/or multi-ridge waveguides. It is noticed that the multipactor RF voltage threshold raises up as the ratio w/d is reduced.

- The effect of the ridge gap height variation is explored for the different values of the ridge widths, for both single- double- and multi-ridge waveguides in the symmetrical and asymmetrical configurations. The results of these susceptibility charts are summarized in Fig. 6.12. It is found very slight variation of the voltage threshold in terms of the gap within the range of d/b values considered.

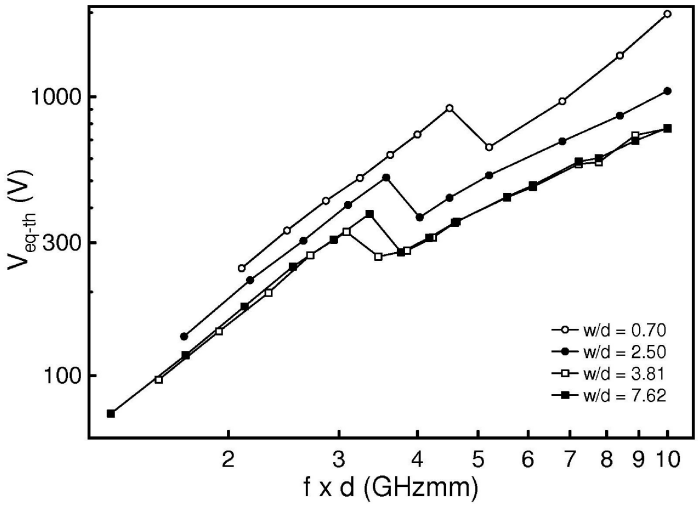

Figura 6.11: Multipactor voltage threshold for several values of ridge width to gap ratio for single ridge symmetrical waveguide. Gap height is $d = 0.5$ mm, $d/b = 0.052$ and $b/a = 0.5$.

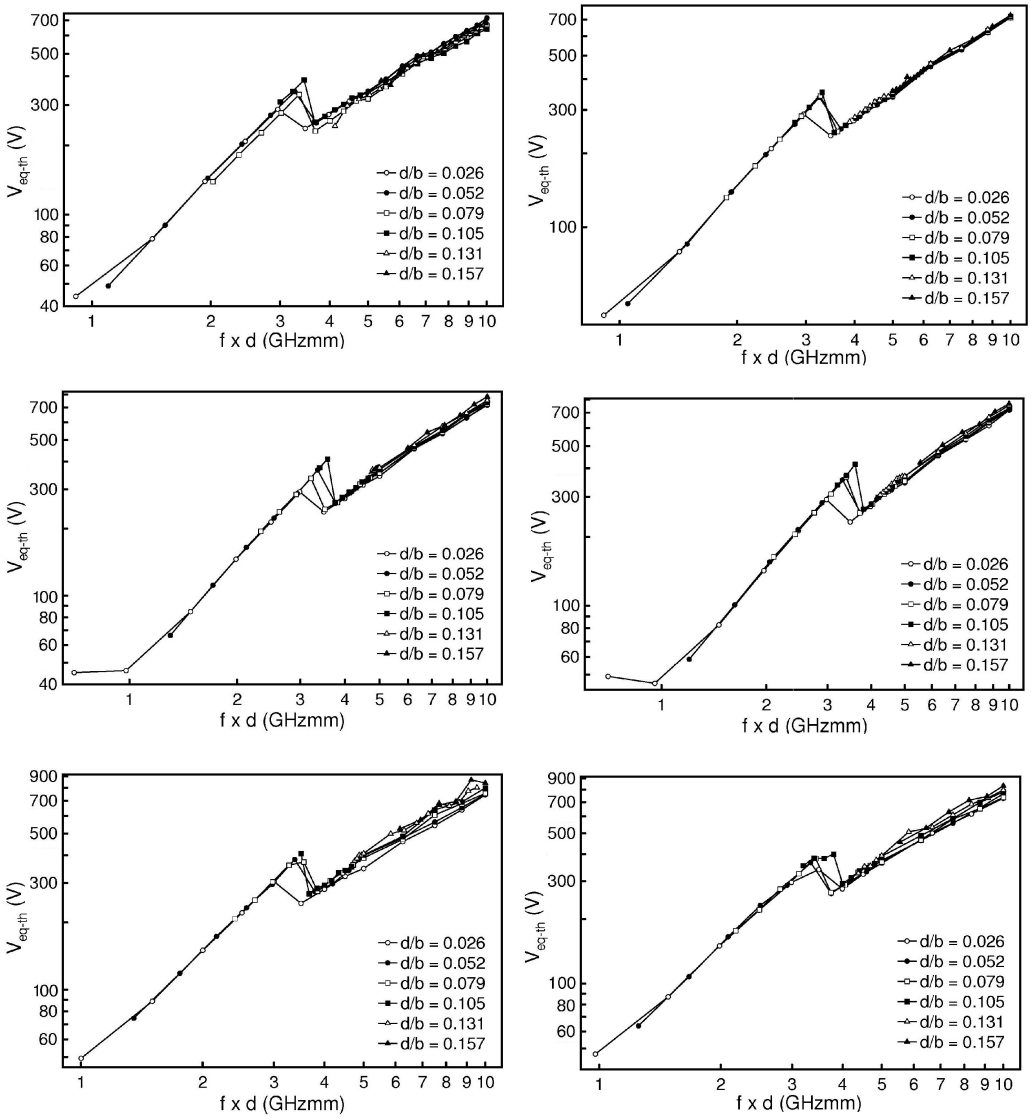

Figura 6.12: Multipactor voltage threshold for several gap heights in symmetrical and asymmetrical configurations. From top to bottom: ridge (width $w/a = 0.4$), double-ridge ($2w/a = 0.4$) and multi-ridge ($3w/a = 0.4$) waveguides. Left (right) column for symmetrical (asymmetrical) configurations. In all cases $b/a = 0.5$.

6.2.2. Multipactor prediction using susceptibility charts

The susceptibility charts presented in the previous subsection can be used to obtain an approximate prediction of the multipactor RF power threshold in complex microwave devices composed of ridged waveguide sections. The main advantage of this rough method is that no additional multipactor simulations for the specific RF device under analysis is needed. To proceed, it is required to compute the RF electromagnetic field distribution inside the device at the operating frequency. Then the RF electric field must be integrated using formula (6.10) to get the equivalent voltage $V_{eq}^{'}$ at the different ridge sections of the component. It must be also taken into account that as the RF electric field typically varies with the axial direction, it might be necessary to evaluate such voltage for several axial points along the ridge length. Afterwards, the highest equivalent voltage along the ridge section has to be selected, since the multipactor discharge will appear first at that place. For each frequency value, the power at the input port of the device is proportional to the square of the ridge voltage. Accordingly, the multipactor RF power threshold at the input port of the device P_{th} can be obtained as

$$P_{th} = \left| \frac{V_{eq-th}}{V_{eq}^{'}} \right|^2 P_{in} \tag{6.11}$$

where V_{eq-th} is the multipactor RF voltage threshold that can be extracted from the previously computed multipactor susceptibility charts, and P_{in} is the RF power at the input port of the device that corresponds to the equivalent voltage $V_{eq}^{'}$, typically an excitation with 1 W of RF power is assumed.

Next, this method is applied to a couple of filters based on ridge and multi-ridge sections.

6.2.2.1. Evanescent-mode filter

The first analyzed structure is an evanescent mode filter extracted from [72]. Basically, the filter consists of five different symmetrical ridge sections, all having the same gap ($d = 0.315$ mm) and the same ridge width ($w/a = 0.45$ with $a = 6.790$ mm). The structure of the filter is shown in Fig. 6.13. The operation frequency is chosen to be centered in the passband of the filter, namely $f = 9.78$ GHz, being the frequency gap product $f \times d = 3.08$ GHz mm for all the gaps.

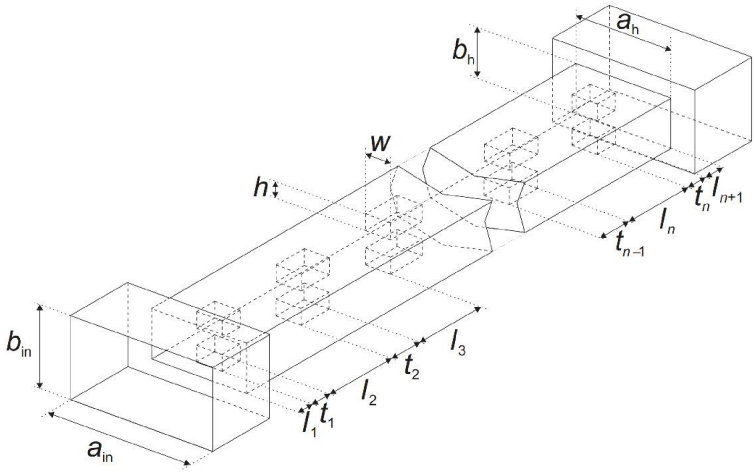

Figura 6.13: Symmetrical evanescent mode ridge waveguide filter topology (extracted from [72]).

First, the electromagnetic analysis of the full structure is performed with FEST3D. Then, equivalent voltage over the gap is computed for several axial points along the ridge sections (see Fig. 6.14). It is noticed that the highest equivalent voltage $V_{eq}^{'}$ is found in the ridge 5 (numbered from the input to the output port). After examining the susceptibility charts, it is stated that the most similar situation in previously computed susceptibility charts is given in Fig. 6.12 for $w/a = 0.4$ and $d/b = 0.026$. From there, voltage threshold for the working frequency is $V_{eq-th} = 310$ V. This voltage threshold referred to the ridge section can be converted into power threshold measured from the input port of the filter by means of expression (6.11). Finally, complete multipactor simulations with FEST3D were performed for the whole device, in order to compare with the previously predicted threshold. In Table 6.2 we summarize the multipactor power threshold results provided both for the approximated method P_{pred} , and for FEST3D simulations P_{FEST3D}. It is also indicated the number of the ridge section where the discharge is foreseen.

Table 6.2: Summarized multipactor results for the evanescent mode filter

Ridge	P_{pred} (W)	P_{FEST3D} (W)
5	8.65	9.09

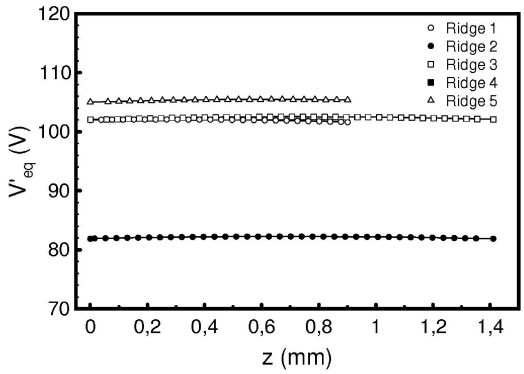

Figura 6.14: Equivalent voltage over the gap for $P_{in} = 1$ W on several axial points of the evanescent-mode filter.

It is observed that both simulation and prediction coincide with the ridge section where the multipactor appears. In addition, power thresholds obtained by two different procedures are very similar, thus demonstrating the feasibility of the prediction method. Note that the predicted threshold value is always expected to be less than the simulated one, due to the fact that in the susceptibility charts the ridge waveguides have uniform fields along the axial direction. In a realistic case the waveguide is connected to the adjacent discontinuities, and the voltage along the waveguide varies. This effect raises the multipactor threshold above the uniform axial case.

Finally, it must be pointed out the advantage of using the new computed charts instead of the parallel-plate model charts, which are commonly employed to assess the risk of a multipactor discharge when no specific multipactor simulation results are available. From ECSS Multipactor Tool version 1.1 [2], the power threshold for the considered gap at the working frequency is 3.44 W (192.5 V). Comparing this value

with the predicted one (8.65 W) using the new generated charts, it is found that the free-multipactor power handling capability of the filter can be increased in 4 dB.

6.2.2.2. High-Power S-Band Filter

The last analyzed structure is a high-power S-band filter whose topology and dimensions are detailed in Fig. 6.15 extracted from [73]. The filter consists of 7 equal multi-ridge sections, each multi-ridge transversal cross-section has 5 symmetrical ridges with $d = 2.413$ mm gap. The operating frequency is 2.78 GHz, thus $f \times d = 6.71$ GHz mm. The filter was constructed in copper.

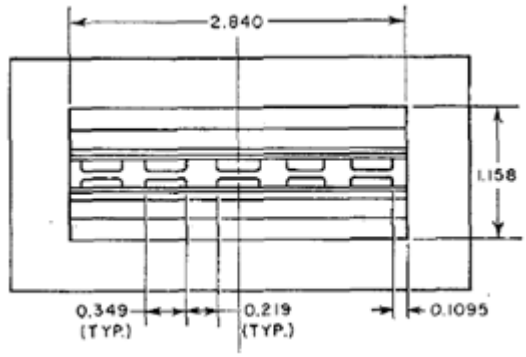

Figura 6.15: Transverse cross-section of the high-power S-band filter.

Firstly, multipactor susceptibility charts are computed for a single 5-symmetrical multi-ridge waveguide with transversal cross-section dimensions of the filter. The SEY parameters for copper are $W_1 = 35$ eV, $\delta_{max} = 2.3$, and $W_{max} = 165$ eV. Results of the susceptibility chart is shown in Fig. 6.16.

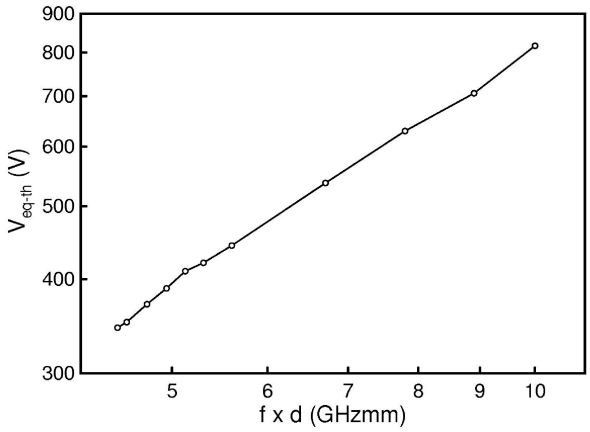

Figura 6.16: Multipactor voltage threshold for the symmetrical multi-ridge waveguide of the waffle-iron filter under consideration manufactured in copper.

After that, an electromagnetic analysis of the whole device is performed revealing that the maximum equivalent voltage is reached at the ridge 7 with a value of $V_{eq}^{'} = 13.921$ V. From the susceptibility chart, it is concluded that the voltage threshold for the working frequency is $V_{eq-th} = 530$ V. With these data, multipactor power threshold prediction can be done. Hence, multipactor simulation of the entire device is performed with FEST3D for comparison. Table 6.3 summarizes the main results.

Table 6.3: Summarized multipactor results for the waffle-iron filter

Ridge	$V_{eq}^{'}$ (V)	P_{pred} (W)	P_{FEST3D} (W)
7	13.921	1449	1532

Similarly as for the evanescent-mode filter, good agreement has been found between our predicted value and the one provided by FEST3D. Finally, comparing the predicted power threshold value with the one corresponding to the parallel plate model provided by Multipactor Tool version 1.1, which is 676 W, we conclude that there is a relevant difference of 3.3 dB between them.

6.3. Multipactor with digitally modulated signals

Most of the multipactor studies are addressed to the analysis of single-carrier time harmonic RF signals, whereas realistic satellite communication systems are usually based on multicarrier operation and modulated carriers to use efficiently the available frequency spectrum. These modulated signals are far different from the non-modulated (or pure harmonic) case and, as a consequence, multipactor results based on a single-carrier harmonic signal might not be extendible to this kind of modulated signals. Despite this, there is very few literature about multipactor with digitally modulated signals [35]-[37].

This section covers the multipactor analysis for a coaxial transmission line excited with a single-carrier digitally modulated signal. Several types of the most commonly employed digital modulation schemes are considered, such as the Phase-Shift Keying (PSK), the Quadrature Amplitude Modulation (QAM), and the Amplitude and Phase-Shift Keying (APSK). In a first stage, multipactor simulations were performed with the effective electron algorithm (described in Section 3.6) for some basic modulated signals with periodic transmitted bit sequences. The numerical results obtained were compared with experimental measurements, and good agreement between them was found in these simple scenarios. However, in a second step, signals with more complex modulation schemes and random transmitted sequences of bits were considered, revealing in this case certain inaccuracies of the effective electron model when comparing with the experimental data. In order to overcome this inconvenience, an individual electron algorithm (described in Section 3.7) was implemented to study such complex modulations scenarios. After the release of this new individual electron code, it was applied to the study of multipactor with microwave pulsed signals, which is an ideal scenario to gather information about the growth rate of the electron population during the onset of the multipactor phenomenon, as well as the minimum electron density value to trigger the discharge. Both of these data constitute a good basis towards a more detailed understanding of the multipactor phenomenon with digital modulations. An experimental test campaign in the RF pulsed scenario revealed the improved accuracy of the individual electron code for multipactor prediction in such cases. After that, the individual electron algorithm was employed to perform numerical simulations for a wide range of complex modulations and transmitted bit sequences. Moreover, a coarse method for a rough estimation of the multipactor voltage threshold in digital modulated scenarios is proposed. This method presents the

advantage of being much faster than the complete numerical simulations. Finally, some of the most representative digitally modulated signals were tested in the laboratory, demonstrating good concordance between theory and experiment.

6.3.1. Theory of modulated signals

The RF spectrum is limited and heavily populated. The increasing number of users in the telecommunication systems requires higher and higher bit rates, forcing to use efficiently the available frequency spectrum. As a solution, digital modulation schemes allow greater capacity to convey large amounts of information than analog modulation schemes. A single-carrier digital modulated signal can be defined as follows

$$V(t) = V_0\, A(t) \cos(2\pi f t + \theta(t)) \tag{6.12}$$

where $A(t)$ and $\theta(t)$ are the time-varying amplitude and phase of the RF signal, respectively, f is their frequency, and V_0 is the RF voltage amplitude. Note that $A(t)$ and $\theta(t)$ functions will be constructed in order to ensure that the maximum of the modulation signal is equal to unity. The purpose of modulating a single-carrier signal is the transmission of information encoded in terms of a finite number of different symbols M that conform the constellation modulation, each of them with specific amplitude and phase values that remain constant while that symbol is being transmitted. The symbol time T_s is the duration of each symbol of the signal, it is often expressed in terms of the RF carrier period ($T \equiv 1/f$) as the ratio $\xi = T_s/T$. There is a correspondence between the symbols in the constellation and the bit sequence that represent. Indeed, the more symbols in the constellation the more bits that are encoded for each symbol. Mainly, there are two types of digital modulation schemes. In the first kind, there is only phase variation among different symbols of the constellation. This is the case of the PSK modulations, where the phase varies among M different values. In this PhD Thesis we are interested in the cases $M = 2$, known as Binary Phase-Shift Keying (BPSK), and $M = 4$, named as Quadrature Phase-Shift Keying (QPSK). An example of a digitally modulated signal with BPSK is depicted in Fig. 6.17. In this case there are only two possibilities for the RF phase, $\theta(t) = 0$ if the transmitted bit is a "0" and $\theta(t) = \pi$ if the transmitted bit is a "1". The remaining kind of digital modulation schemes are those in which both the amplitude and phase vary among different symbols. In this work, the APSK modulation scheme with $M = 16$ and $M = 32$, named as 16-APSK and 32-APSK, respectively, as well as the QAM modulation with

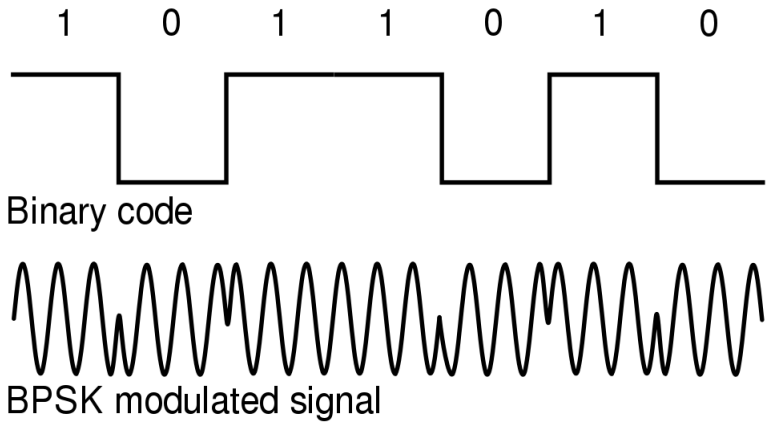

Figura 6.17: Example of a digital signal modulated with BPSK.

$M = 16$ (16-QAM) will be considered.

A simple way of analyzing this kind of signals is to separate the original signal given by (6.12) into a set of independent components or channels: I (In-phase) and Q (Quadrature). The I and Q components are considered orthogonal or in quadrature because they are separated by $90°$ degrees. In digital communications, modulation is often expressed in terms of I and Q components. On a polar diagram, the I axis lies on the zero degree phase reference, and the Q axis is rotated by $90°$ degrees. A constellation diagram shows the symbol locations in a complex signal space. As an example, Fig. 6.18 shows the constellation diagram for the BPSK, QPSK, 16-QAM, and 16-APSK modulations. The horizontal axis is the real or in-phase component, and the vertical axis is the imaginary or quadrature component. Thus, when the signal moves from one point to another (from one symbol to another), simultaneous amplitude and phase modulation usually take place.

The digital modulated signal can be expressed in terms of the I/Q components as

$$V(t) = V_0[I(t)\cos(2\pi ft) - Q(t)\sin(2\pi ft)]; \tag{6.13}$$

where:

$$I(t) = A(t)\cos(\theta(t)); \;\; Q(t) = A(t)\sin(\theta(t)) \tag{6.14}$$

After the modulation of the RF carrier, it can be observed sharp variations in the

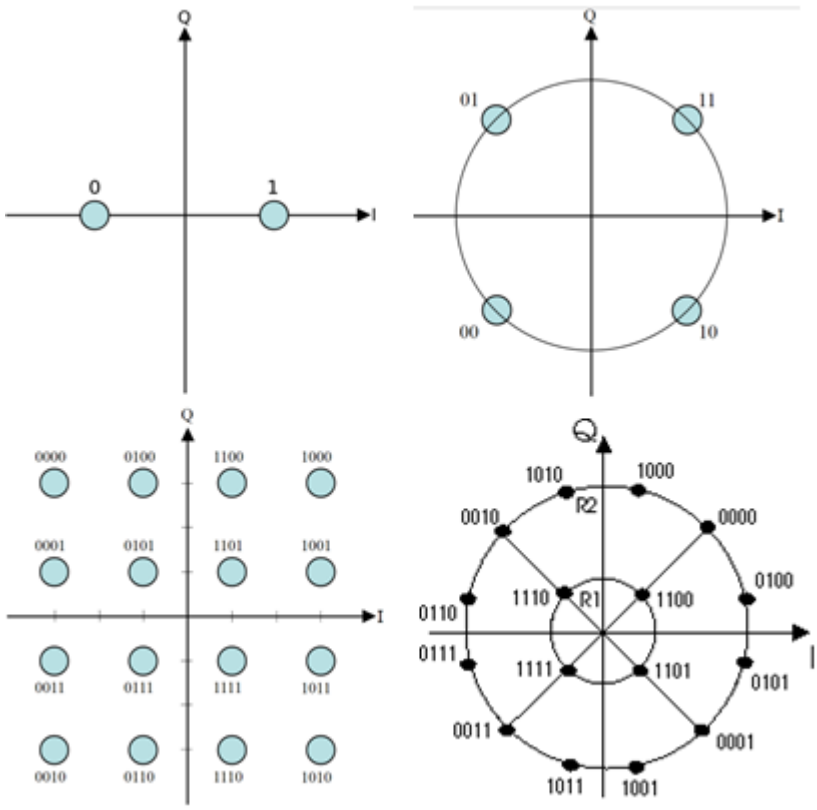

Figura 6.18: Constellation diagram for (from left to right, and top to bottom) BPSK, QPSK, 16-QAM, and 16-APSK modulations.

signal due to the transition between different symbols (see Fig. 6.17). This abrupt changes in the time-domain of the signal turn into a widening of the frequency spectrum. In order to avoid this inconvenience, a filtering process to smooth the symbol transitions is applied to the modulated signal. A digitally modulated and filtered single-carrier signal can be represented by the following expression:

$$V(t) = V_0 \sum_{n=-\infty}^{\infty} g(t - nT_s) A_n \cos(2\pi f t + \theta_n) \tag{6.15}$$

where $g(t)$ is the filter function in the time domain, n is the symbol index, and A_n and θ_n are the amplitude and phase of the *n-th*-symbol. Alternatively, the above formula (6.15) can be expressed in terms of the I/Q data with expressions (6.13) and (6.14). With regard to the specific filter function, a typical choice is the use of the Root Raised Cosine filter (RRC), whose time-domain expression is as follows [74], [75]:

$$g_{rrc}(t) = \frac{4\,\Gamma}{\pi\sqrt{T_s}} \frac{\cos\frac{(1+\Gamma)\pi\,t}{T_s} + \frac{1}{\frac{4\,\Gamma t}{T s_s}}\sin\frac{(1-\Gamma)\pi\,t}{T_s}}{1-(\frac{4\,\Gamma\,t}{T_s})^2} \tag{6.16}$$

where Γ is the roll-off factor which takes values from 0 to 1, and it is directly linked to the final signal bandwidth through the following simple formula $B_w = (1+\Gamma)/T_s$, as reported in [74]. As a consequence, low values of Γ are preferred for digital communication systems in order to reduce the signal bandwidth. In Fig. 6.19 we can see the RRC filter shape for different values of the roll-off factor.

Finally, it is worth to compare the modulated signal before and after the filtering process to give a more detailed picture of the effect of the filter. A simple BPSK modulated signal with a periodic transmitted bit sequence of "10" and $\xi = 5$ has been plotted in Fig. 6.20; it can be observed the voltage of the modulated signal before and after the filtering process. As expected, it is appreciated that the filter smoothes the sharp transition between symbols. However, the envelope of the filtered signal varies with time, despite the fact that the implemented BPSK modulation scheme is only phase-varying.

6.3.2. Simulations with the effective electron code

The coaxial transmission sample selected for multipactor simulations is the same one that was properly described in subsection 6.1.1. This analysis is focused only in the BPSK and QPSK schemes, which constitute the most simple scenarios in digital modulations. The main aim is the computation of the multipactor RF voltage threshold as a function of the ratio between the symbol duration and the RF period (ξ factor), in order to compare with the multipactor threshold corresponding to a time-harmonic signal at the RF carrier frequency (henceforth referred to as unmodulated case).

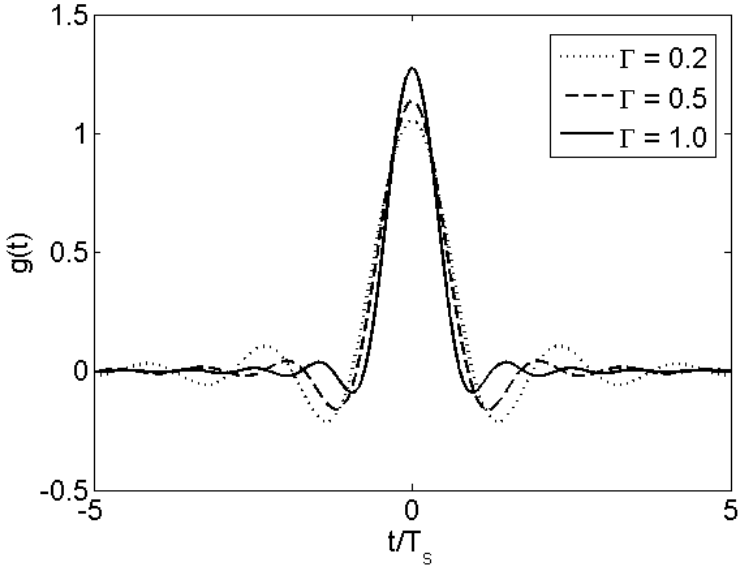

Figura 6.19: Root raised cosine filter in terms of the time normalized to the symbol duration.

6.3.2.1. BPSK

As outlined before, the BPSK modulation has only two different symbols in its constellation (recall Fig. 6.18), which correspond to RF phases of $0°$ and $180°$. Consequently, the phase shift between two successive transmitted symbols can only be of $0°$ (in the case that the two neighbor symbols are the same) or $180°$ (if the two symbols are different). In terms of the multipactor analysis, we are interested in finding the most disturbing scenario with regard to the unmodulated case, which is expected to occur when the digital modulated signal becomes far different from the time-harmonic case. For the BPSK modulation, the most perturbative case of the RF signal is the periodic sequence of "10", which involves phase changes of $180°$ at every symbol transition. In order to explore the effect of the signal filtering after the modulation process in the multipactor RF voltage threshold, both cases are taken into account.

- *without filtering*. Firstly, it is analyzed the case without any filtering after the

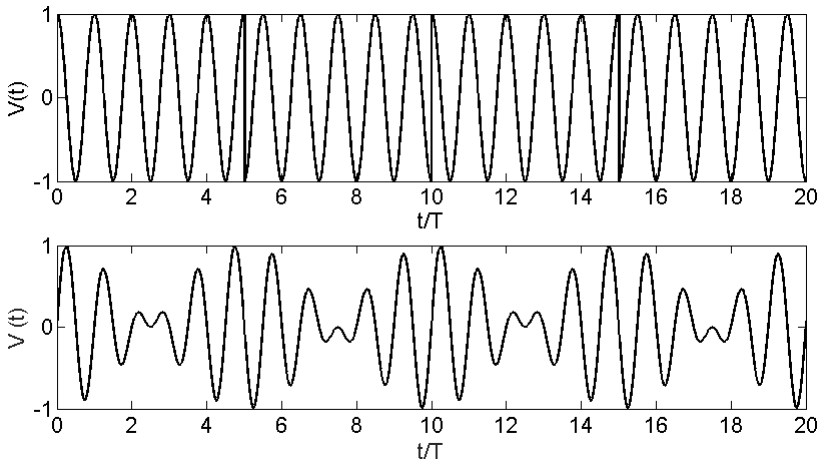

Figura 6.20: Comparative of a BPSK modulated signal before (top) and after (bottom) the filtering process with an RRC filter ($\Gamma = 0.2$). The transmitted bit sequence is periodic: "10", and $\xi = 5$.

modulation. Multipactor susceptibility charts have been obtained for different values of the frequency gap $f \times d$ (remaining the gap constant). These results are depicted in Fig. 6.21. At the view of the results, it is observed that for all frequency gap cases the multipactor voltage threshold tends to the unmodulated value for high values of ξ. However, different behavior of the multipactor curves starts to appear when $\xi < 30$. For low frequency gap values (1 GHz mm) it is noticed an increase of the multipactor RF voltage threshold. However, for the medium (3 GHz mm) and high (5 GHz mm) frequency gap values, the voltage threshold tends to diminish as the ξ decreases.

In order to achieve a better understanding of the obtained results, the radial trajectory of an effective electron has been plotted for some points of the susceptibility curves (marked as A, B and C) in Fig. 6.21. Moreover, the RF voltage of the modulated signal is also depicted with the electron trajectory, in order to visualize how the sharp phase changes affects to the electron motion. For point A (see Fig. 6.22) there is a symbol transition every 100 RF periods of the signal ($\xi = 100$), such time is much greater than the time between two successive electron impacts of the electron with the coaxial walls (typically within the ran-

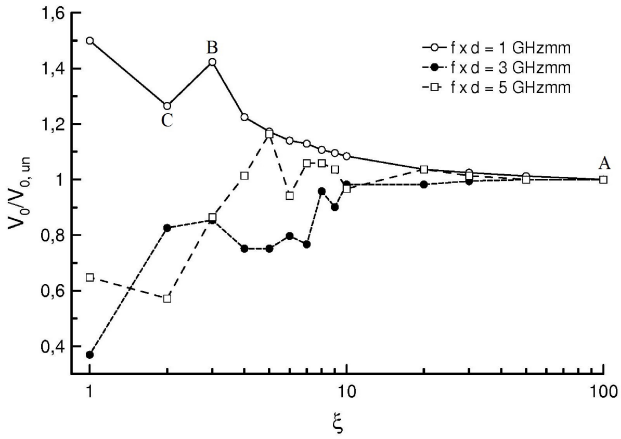

Figura 6.21: Multipactor RF voltage threshold normalized to the unmodulated multipactor RF voltage threshold as a function of the ξ parameter for several frequency gap values. Signal modulated by BPSK with "10" sequence (without filtering). Unmodulated multipactor voltage thresholds are $V_{0,un} = 31.634$ V for $f \times d = 1$ GHz mm, $V_{0,un} = 206.227$ V for $f \times d = 3$ GHz mm, and $V_{0,un} = 231.381$ V for $f \times d = 5$ GHz mm.

ge of one or a few RF semiperiods). As a consequence, the modulation does not perturb in a noticeable way the electron motion at most of the time, and hence the multipactor voltage threshold for this case is the same one than for the unmodulated scenario. In fact, a multipactor resonant trajectory of order 1 is found at this point, which is the expected value for a frequency gap of 1 GHz mm. For point B (see Figs. 6.21 and 6.23), $\xi = 3$ and the time lapse between phase jumps is now close to the transit time between impacts. This fact implies that the disturbance in the electron motion will be important now for the onset of the multipactor discharge. In fact, it is seen that the electron trajectory is altered (if compared with previous results for point A) every time that there is a phase jump. Such perturbation causes that at some of the impacts the SEY drops below unity, whereas for the impacts that are not affected by the phase shift, the SEY is still greater than one. In order to compensate the low SEY impacts, it

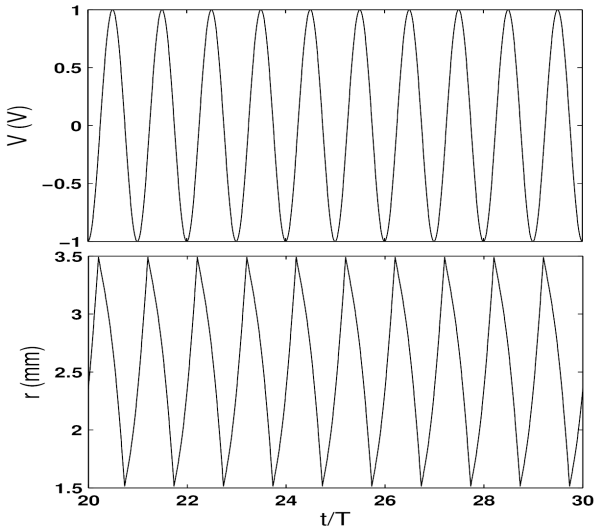

Figura 6.22: RF modulated signal voltage and electron radial coordinate, as a function of the normalized time t/T. Point A from Fig. 6.21 for the case $f \times d = 1$ GHz mm.

is required a higher RF voltage for the onset of the discharge and, due to this, the multipactor voltage threshold is higher for point B than for point A. For point C (see Figs. 6.21 and 6.24) with $\xi = 2$ it is found a similar behavior than for the previous point B. Nevertheless, it is observed a more simple periodic pattern in the electron trajectory than in the former case, as well as a reduction in the number of impacts with SEY below one. This justifies the slight decrease in the multipactor voltage threshold.

- *RRC filter*. After the modulated signal has been filtered, no sharp variations in the signal are observed in the transitions between symbols. However, as a counterpart, the signal envelope changes with time within each symbol, even if the time duration is much greater than the RF period. Due to this, it is expected a different behavior in the multipactor voltage threshold curves with regard to the previous case without filtering.

  The results of the multipactor threshold curves as a function of the ξ factor are depicted in Fig. 6.25. The same frequency gap values and bit sequence ("10")

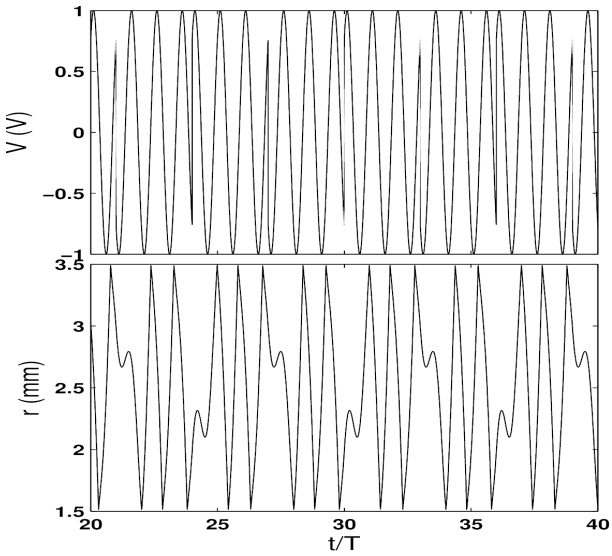

Figura 6.23: RF modulated signal voltage and electron radial coordinate, as a function of the normalized time t/T. Point B from Fig. 6.21 for the case $f \times d = 1$ GHz mm.

than in the previous "without filtering" case are considered. A roll-off factor of $\Gamma = 0.25$ is assumed for the RRC filter. At the view of the results, it is noticed that the curves corresponding to the different frequency gap cases analyzed do not converge for high ξ values as it happened in the previous "without filter" situation. It is also observed that for $\xi > 30$, there is a very slight variation of the multipactor threshold. For low ξ it is observed a similar behavior with regard to the without filtering scenario, i. e., for low frequency gap values there is a tendency in the multipactor threshold to raise as ξ diminishes, whereas for medium and high frequency gap values the trend is to have a decrease in the multipactor RF voltage threshold.

6.3.2.2. QPSK

The QPSK modulation is formed by four different symbols (recall Fig. 6.18), each of them has two neighbors with a phase difference of $90°$ and an opposite symbol with phase shift of $180°$. Firstly, in a similar way as it was done for the BPSK modulation,

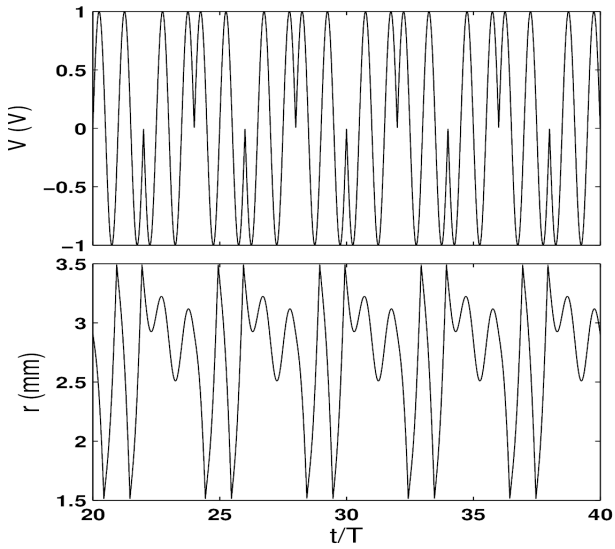

Figura 6.24: RF modulated signal voltage and electron radial coordinate, as a function of the normalized time t/T. Point C from Fig. 6.21 for the case $f \times d = 1$ GHz mm.

it is investigated the transmitted periodic sequence (using all the constellation symbols without repetition) that it is expected to perturb the multipactor threshold in a more noticeable manner. In QPSK, the corresponding bit sequence to such situation is "11011000" which involves two 180° phase jumps alternated with two 90° phase shifts. In order to compare with another periodic transmitted bit sequence, the case of four consecutive phase jumps of 90° is also considered in multipactor simulations ("11010010"). Moreover, a full-random transmitted symbol sequence, generated by means of a Matlab uniform probability distribution function, is investigated. In all three cases it is assumed the filtering with a RRC filter of $\Gamma = 0.25$. Fig. 6.26 shows the multipactor RF voltage threshold as a function of the ξ factor for the different transmitted bit sequences, at a frequency gap value of 1 GHz mm. It is appreciated that the shape of the curve is not affected by the transmitted bit sequence. The lowest multipactor threshold values are obtained in the four 90° jumps case, which is revealed as the less disturbing scenario for the multipactor. The other periodic sequence ("11011000") was supposed to be more perturbative for the multipactor, as indeed oc-

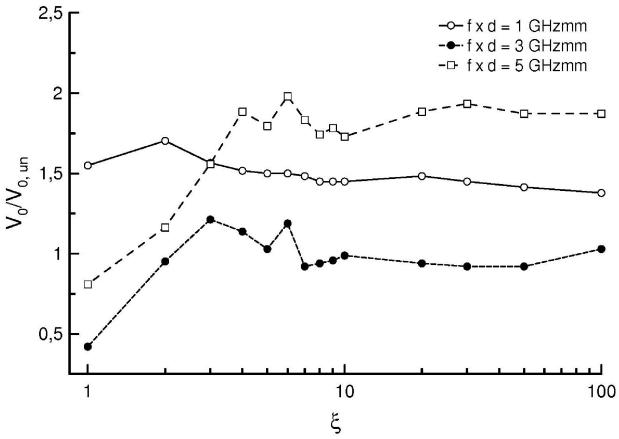

Figura 6.25: Multipactor RF voltage threshold normalized to the unmodulated multipactor voltage threshold as a function of the ξ parameter for several $f \times d$ values. Signal modulated by BPSK with "10" sequence and $\Gamma = 0.25$ RRC filter has been used. Same unmodulated voltage threshold as in Fig. 6.21.

curs since the multipactor threshold is greater. Finally, the full-random sequence has multipactor threshold values slightly above to those of the "11011000" sequence.

6.3.2.3. Experimental validation

In order to validate the previous results obtained from theoretical simulations, a multipactor experiment was performed. The coaxial sample tested in the laboratory is the same one used for the simulations, and it was already described properly above. Measurements were carried out at with an RF carrier frequency of $f = 435$ MHz, which corresponds to a frequency gap of $f \times d = 0.859$ GHz mm. The RF signal was modulated with BPSK and no filtering process. The transmitted bit sequence was "10". The multipactor RF power threshold was measured for several values of ξ. Both experimental and theoretical results are shown in Fig. 6.27, finding good agreement between them.

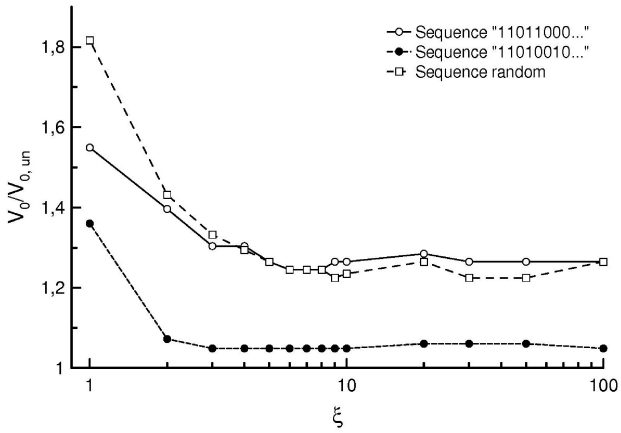

Figura 6.26: Multipactor RF voltage threshold normalized to the unmodulated multipactor voltage threshold as a function of the ξ parameter for $f \times d = 1$ GHz mm. Signal modulated by QPSK with several bit sequences and $\Gamma = 0.25$ RRC filter has been used. Same unmodulated voltage threshold as in Fig. 6.21.

6.3.3. Multipactor with RF pulsed signals

The scheme of a typical RF pulsed signal is depicted in Fig. 6.28. The signal is composed by a succession of pulses, in each of them there is an active part with a duration of t_{on} where the signal exhibits a time-harmonic pattern, followed by an OFF interval of zero amplitude voltage. If the voltage amplitude of the ON interval exceeds the multipactor voltage threshold of the harmonic case (CW), then the electron population will increase during that interval of the pulse. However, during the OFF interval, there is no RF electric field that accelerates the electrons within the waveguide and, as a consequence, the electrons will be mainly absorbed by the surfaces resulting in a decrease of the electron population. Depending on the specific ON and OFF interval durations, it is possible to have an accumulation of electrons that survive from one pulse to the next one [30]. However, if the OFF part of the pulse is chosen long enough, all the electrons will be absorbed and no accumulation effects occur. For the current study we are interested in this latter case, thus simplifying the theoretical analysis since only the active part of the first pulse is required to be considered in

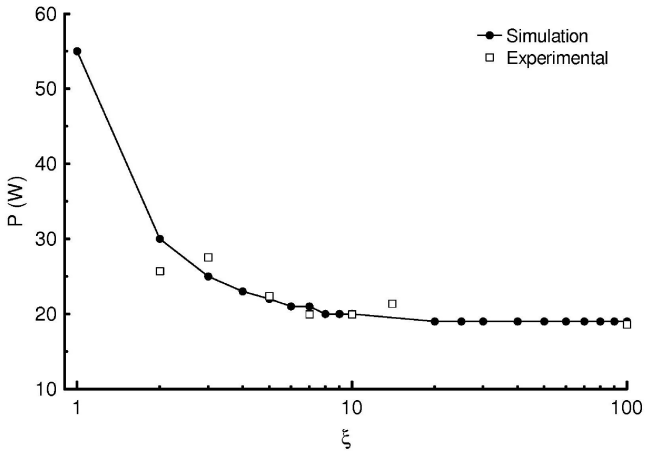

Figura 6.27: Multipactor power threshold as a function of the ξ parameter at $f = 435$ MHz. Signal modulated by BPSK without filter and "10" sequence. Simulation and experimental results.

order to obtain the multipactor RF voltage threshold. From a theoretical point of view, the discharge will occur only if a critical electron density (or its equivalent critical electron population) is exceeded at any time during the ON pulse interval. The critical electron density for the onset of the discharge is linked to the sensitivity of the multipactor detection methods implemented in the experimental set-up. The purpose of this study of the multipactor voltage threshold with pulsed signals is to correlate the results from numerical simulations with the experimental data, in order to estimate the critical electron density (according to the current experimental set-up) for the onset of the multipactor discharge. This information about the critical electron density will be crucial when analyzing multipactor in cases where the signal is not pure harmonic, as it happens with digital modulations or multi-carrier scenarios.

To proceed with the theoretical part of the study, multipactor numerical simulations were performed with an individual electron code adapted for a coaxial transmission line. The coaxial sample dimensions and material are those described in subsection 6.1.2. The RF carrier frequency is $f = 1.145$ GHz. The initial electron population in the simulations is $N_i = 500$, and the code stops when the number of electrons ex-

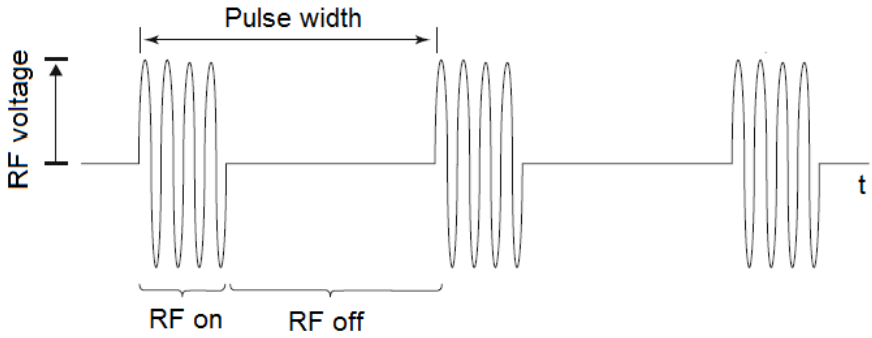

Figura 6.28: Scheme of an RF pulsed signal.

ceeds $N_e = 10^4$. This final electron number for the simulations is chosen due to computational limitations when treating with a high number of tracked particles. On the one hand, as the individual electron number raises up during the simulation, the computational time to treat all the particles quickly increases, leading to very long time simulations. On the other hand, there is even a more restrictive limit caused by the high amount of computational memory required when dealing with a huge number of individual electrons. This restricts the maximum number of tracked particles that a computer can hold in the simulations. The results of the numerical simulations performed are depicted in Fig. 6.29, where it is represented the electron population as a function of the time normalized to the RF period, for different values of the RF voltage amplitude. It is noticed that the evolution of the number of electrons follows an exponential trend, as discussed in subsection 2.1.3. Moreover, it is observed that the growth ratio increases with the RF voltage amplitude.

According to numerical simulations presented in [76], the electron saturation level in a coaxial waveguide geometry is very high, within the range of 10^9-10^{12} electrons depending on the particular characteristics of the case (waveguide dimensions, SEY properties of the surfaces, RF frequency, etc.). Since the maximum population value ($N_e = 10^4$) considered in our simulations is quite below the aforementioned saturation range suggested in [76], it is proposed the following procedure to extrapolate the results from the simulations. For each value of the RF voltage amplitude in Fig. 6.29, it is fitted the evolution of the electron population with time to an exponential function in the form $N(t) = N_0 \exp(\alpha t)$, obtaining as a result of the fit the value of the growth

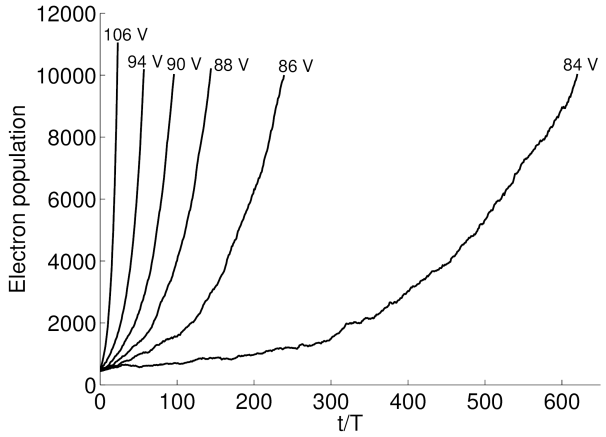

Figura 6.29: Evolution of the electron population within the coaxial waveguide excited by a continuous wave signal as a function of the time normalized to the RF period for different RF voltages.

rate α. Hence, using the previous exponential law it can be predicted the electron number within the waveguide at any time. Then, the multipactor RF voltage threshold for the pulsed signal can be obtained. To do this, it is assumed a critical population level as the multipactor criterion and, consequently, the discharge will take place if at the end of the ON pulse interval the population is equal or above the critical level value for that corresponding value of the amplitude voltage. After trying different values of the critical population level, it was found that the one that best fits the experimental results is 10^{12} electrons (or equivalently an electron density of 4.83×10^{17} m^{-3}, assuming that the electrons fill the entire vacuum coaxial volume). Fig. 6.30 shows both the theoretical and experimental results, finding good agreement between them. It is noticed that the shorter the pulse, the higher the multipactor RF voltage threshold. This makes sense since as the pulse shortens, higher electron growth rates are required to reach the discharge level, and thus higher RF voltages are needed. It must be also mentioned that ultra short pulses with $t_{on}/T = 22.9$ and $t_{on}/T = 11.45$ were measured, but no multipactor discharge was detected up to 199 V, which was the maximum RF voltage delivered by the available RF power amplifier. Multipactor simulations for the two aforementioned pulses also predicted no multipactor discharge up to the vol-

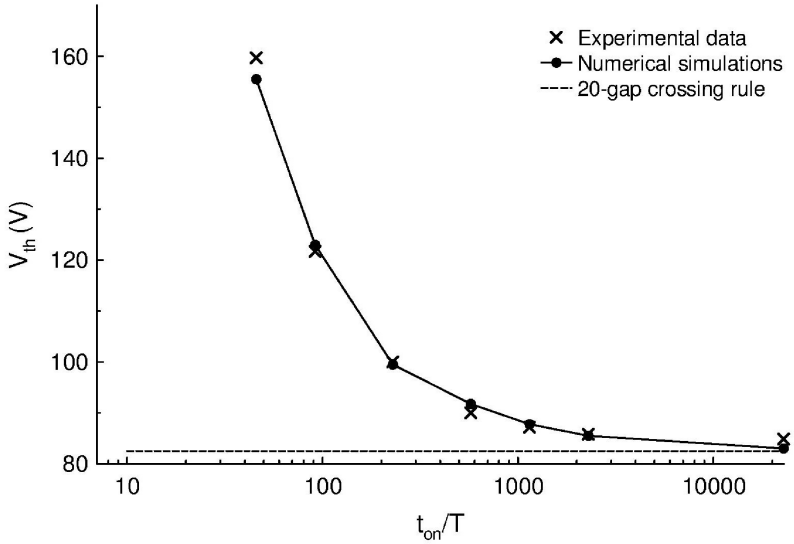

Figura 6.30: Multipactor RF voltage threshold for several RF pulse lengths normalized to the RF period of the carrier signal. Experimental and theoretical results, as well as the 20-gap crossing rule predictions, are shown.

tage tested level. Measuring multipactor in pulses shorter than $t_{on}/T = 11.45$ was not possible, since considerable distortion of the RF pulse envelope was observed due to limitations in the RF power amplifier performance. Finally, it must be also mentioned that the results from numerical simulations and the experimental data were compared with the predictions from the "20-gap-crossing" rule (recall subsection 2.2 and see Fig. 6.30) finding notorious discrepancies. It is concluded that the "20-gap-crossing" rule is not applicable in this case, since it does not reproduce well the available experimental results.

6.3.4. Coarse method

In this subsection, it is presented a coarse method based on the integration of the signal envelope, which is used to obtain the temporal evolution of the electron popu-

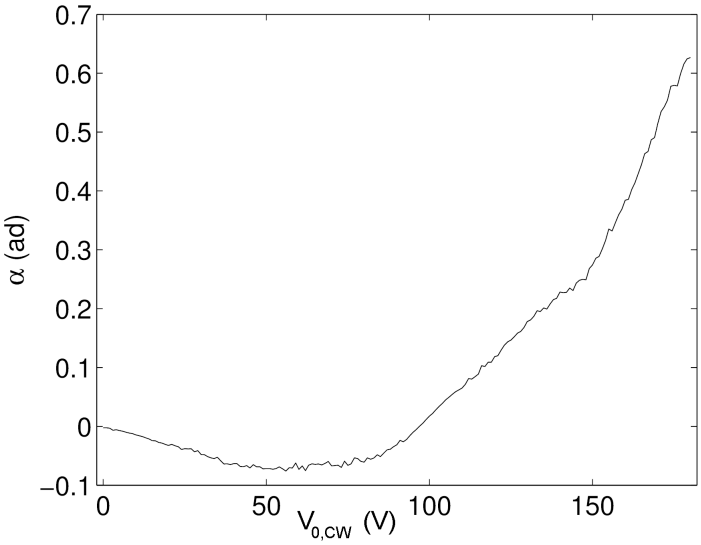

Figura 6.31: Variation of α with the RF voltage amplitude for the coaxial transmission line described in subsection 6.1.2 , at an RF frequency of $f = 1.145$ GHz.

lation within the waveguide for any arbitrary digital modulation scheme. This method allows to obtain the multipactor RF voltage threshold and constitutes a faster alternative to more accurate multipactor simulations. In fact, the computational time required to simulate the multipactor effect for a digitally modulated signal can spend several hours in a standard personal computer, whilst the proposed method reduces this time to a few minutes. The only input data for this method are the results from numerical simulations for a harmonic non-modulated signal at the RF carrier frequency.

As discussed in subsection 2.1.3, in the case of a pure-harmonic signal, the electron population grows following an exponential trend given by expression (2.17), where the growth rate α is found to depend on the mean SEY at the impacts, and hence on the value of the RF voltage amplitude. In fact, after fitting the results from numerical simulations to expression (2.17) for different values of the amplitude voltage, it is obtained the explicit dependence of the α factor with the voltage amplitude of the harmonic signal V_0 (see Fig. 6.31).

Note that in (2.17), the time variable t_n is discrete due to the fact that the elec-

tron population varies only at the time instant when the impact occurs. However, in a typical realistic multipactor scenario, the time required for the onset of the discharge is much greater than the time lapsed between two successive impacts and, as a consequence, it can be assumed that the time is a continuous variable. Under this consideration, the derivative of (2.17) is

$$\frac{dN}{N} = \alpha(t)\, dt. \tag{6.17}$$

According to expression (6.13) a digital modulated signal behaves like an harmonic oscillation at the RF carrier frequency whose envelope varies with time according to the sequence of transmitted symbols. Assuming that the variation of the envelope over the time interval between successive impacts of the electron is smooth, it can be considered that the electron resonant trajectories will be softly perturbed and, consequently, (6.17) will be still applicable at each time step.

However, in the digital modulation case, the value of the average SEY coefficient will vary with time since the signal envelope, which determines the RF electric field strength, also does. As a consequence, in (6.17), the α coefficient will be a time-dependent function, i.e. $\alpha(t)$. If this function is known, (6.17) can be integrated leading to

$$N(t) = N_0 \exp\left(\int_0^t \alpha(t)\, dt\right), \tag{6.18}$$

Equation (6.18) gives the evolution of the electron population in the device for the case of considering an arbitrary digitally modulated signal as excitation. It should be emphasized that α depends on the instant value of the RF voltage envelope, which indeed varies throughout the RF signal with time: this fact implies that α has an implicit dependence with time as seen in (6.18).

In order to apply this algorithm, the explicit dependence of α with time is reached in the following way. First, the envelope of the digitally modulated signal is computed by searching its maximum absolute value in each of the oscillations at the RF carrier frequency f. Then, the α value for each of these maximums is directly obtained from data in Fig. 6.31. Combining the time at which the maximums of the oscillations occur with the α values, it is obtained the desired function $\alpha(t)$. Then, (6.18) can be numerically integrated obtaining the electron population evolution $N(t)$ for the digitally modulated signal at the current voltage amplitude V_0 (recall (6.13)) of the

digital modulated signal. Depending on the maximum electron number reached during the transmission of the signal, it can be decided if the discharge is expected or not according to a certain multipactor criterion.

6.3.5. Simulations with the individual electron code

The coaxial transmission sample selected for multipactor simulations and measurements is the same that was properly described in subsection 6.1.1, and that was also employed for the measurements with the RF pulsed signals. The modulation schemes of QPSK, 16-QAM, 16-APSK, and 32-APSK will be also considered. The analyzed signals were generated with an in-house software developed by Petronilo Martín Iglesias under the European Space Agency Contract 4000111147/14/NL/GLC.

In all cases it is assumed the application of an RRC filter with a roll-off factor of 0.2. The RF carrier frequency is 1.145 GHz. The criterion for the onset of the multipactor discharge is the presence of an electron population of 10^{12} electrons within the coaxial waveguide (or equivalently an electron density of 4.83×10^{17} m^{-3}). The results of the multipactor RF voltage threshold for the digital modulated signals are expressed in decibels, according to the next expression

$$V_{th}(dB) = 20 \log \left(\frac{V_{th}}{V_{th,CW}} \right), \tag{6.19}$$

where V_{th} is the RF multipactor voltage threshold, and $V_{th,CW}$ is the RF multipactor voltage threshold of the non-modulated case (pure-harmonic signal) at the RF carrier frequency.

Firstly, two periodic sequences of the QPSK modulation were chosen to study the effect of the multipactor voltage threshold with the ξ factor. The first sequence, denoted as Q, is composed by a transition between two neighbor symbols, leading to a phase shift of $90°$. The second sequence, denoted as X, is formed by a transition between two opposite symbols, thus the phase shift is of $180°$. The RF voltage of the Q and X signals has been depicted in Fig. 6.32.

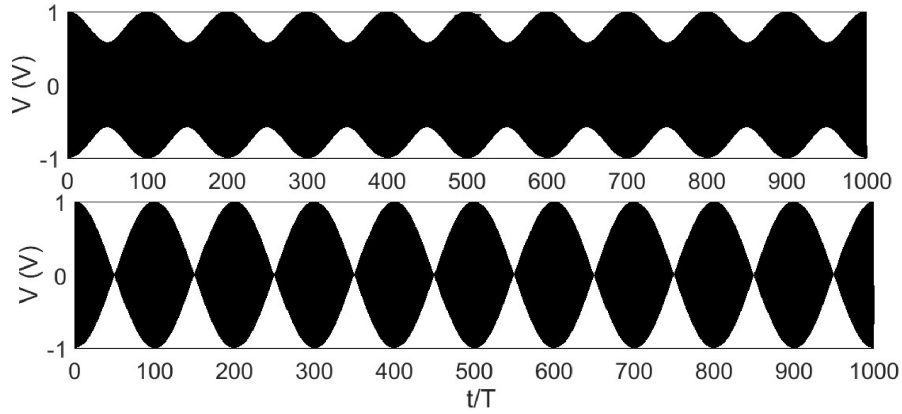

Figura 6.32: Voltage of the RF signals as a function of the time normalized to the RF carrier period. Up: QPSK with Q sequence, down: QPSK with X sequence. In both cases $\xi = 100$.

The results of the numerical simulations, the coarse method, and the "20-gap-crossing" rule are summarized in Fig. 6.33. At the view of the results, it is observed that there is good concordance between the numerical simulations and the coarse method based on the envelope integration. However, significant differences arise when comparing these results with the predictions of the "20-gap-crossing" rule. With regard to the numerical simulations and the coarse method, it is observed that there is a slight difference in the multipactor threshold as the ξ factor diminishes. In addition, it is noticed that the multipactor threshold difference is greater for the X sequence than for the Q sequence. This can be understood by inspecting Fig. 6.32, where it is shown that the envelope minimum of the X signal falls to zero, whereas the envelope minimum of the Q signal is quite above this value. Consequently, the former case requires having higher RF voltage amplitude to compensate for the lower amplitude regions, where electrons are mainly absorbed by the surfaces.

In a second stage of the study, realistic transmitted signals employed in space telecommunications, involving a large number of symbols, were considered. A random symbol sequence was generated for each of the following digital modulations: QPSK, 32-APSK, 16-APSK, and 16-QAM. The RF voltage of such signals is shown in Fig 6.34.

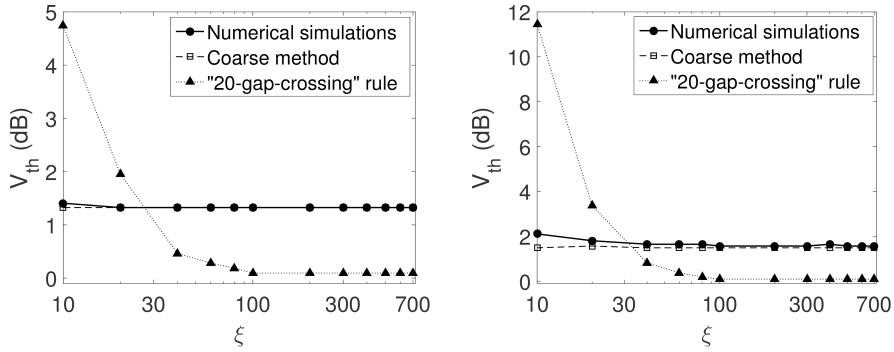

Figura 6.33: RF multipactor voltage threshold as a function of the ξ factor for Q (left) and X (right) sequences. It is shown the results for both the numerical simulations, the coarse method, and the "20-gap-crossing" rule.

These results of the multipactor voltage threshold provided by the numerical simulations, coarse method and "20-gap-crossing" rule are summarized in Fig. 6.35. It is found good agreement between the results obtained from the numerical simulations and the coarse method, whilst considerable discrepancies between the two aforementioned procedures and the "20-gap-crossing" rule are noticed. Both numerical simulations and the coarse method predict an increase in the RF multipactor voltage threshold when the ξ factor decreases. At $\xi = 700$, the RF multipactor voltage thresholds of the analyzed signals are within the interval $[1.32, 1.48]$ dB, whilst at $\xi = 10$ the RF multipactor voltage threshold values are within the range from 3.90 dB (for 16-QAM) to 5.08 dB (for QPSK). Hence, a spread in the RF multipactor threshold values among the different modulated signals can be observed as ξ diminishes.

In order to validate the theoretical framework, an experimental test campaign was carried out. The results of the measurements are shown in Fig. 6.36 together with the theoretical values. On the one hand, it is observed good concordance between the experimental results and the numerical simulations, demonstrating the feasibility of the presented code to predict the RF multipactor voltage threshold with digitally modulated signals. In addition, acceptable agreement of the experimental data with the coarse method shows the capability of this faster procedure to roughly estimate the RF multipactor voltage threshold. On the other hand, it is noticed the remarkable discrepancies found between the results of the experiment and the predictions provided

by the “20-gap-crossing” rule, which in most of the cases reveals to be a very conservative approach, since the predicted RF multipactor voltage threshold is much below the real value measured in the laboratory.

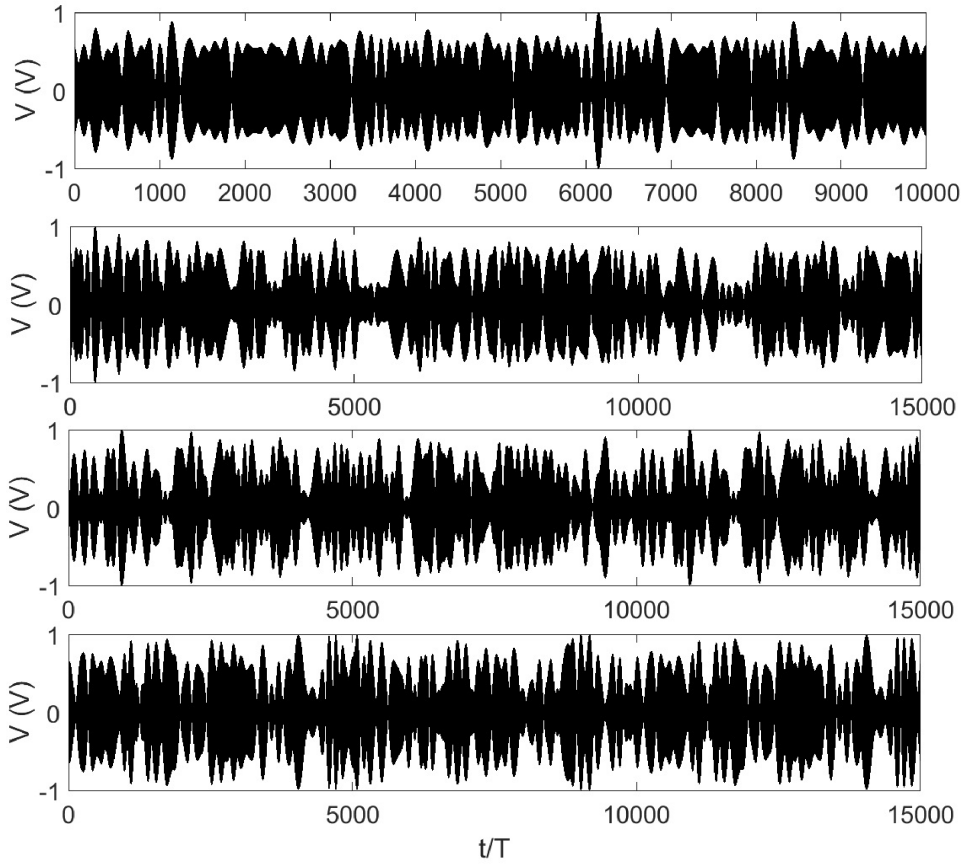

Figura 6.34: Voltage of the RF signals as a function of the time normalized to the RF carrier period. From top to bottom: QPSK, 32APSK, 16APSK, 16QAM. In all cases $\xi = 100$.

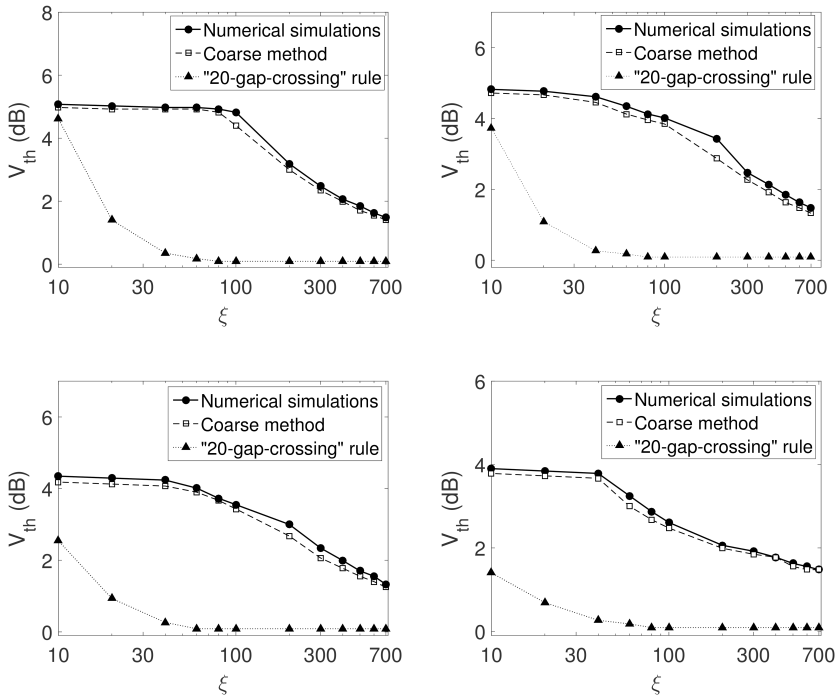

Figura 6.35: RF multipactor voltage threshold in dB as a function of the ξ factor for the random symbol sequences. From left to right and up to down: QPSK, 16-APSK, 32-APSK, and 16-QAM. It is shown the results for both the numerical simulations, the coarse method, and the "20-gap-crossing" rule.

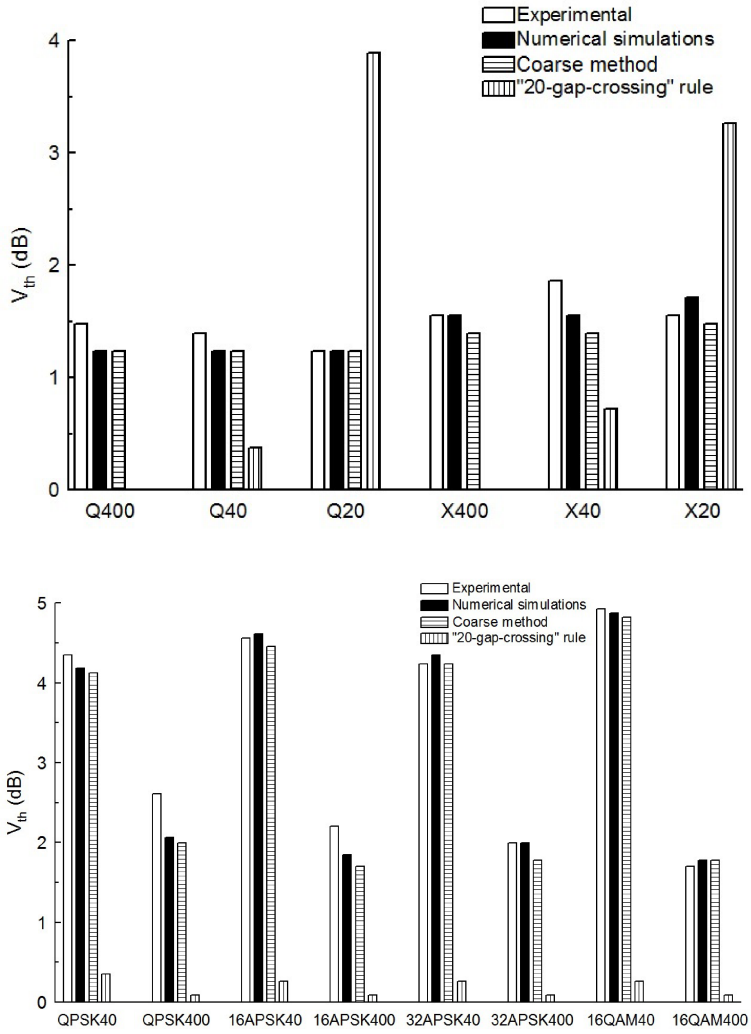

Figura 6.36: RF multipactor voltage threshold in dB for different digital modulated signals. Results from experiment, numerical simulations, approximate method and "20-gap-crossing" rule are presented. Up: Q and X signals, down: random sequences of different modulations. In both cases the number after the modulation name indicates the ξ value.

6.4. Multipactor in a ferrite-loaded waveguide

Multipactor has been extensively analyzed in the case of metallic surfaces so far. Besides, many studies have focused their attention in the study of multipactor with dielectric materials. However, the multipactor analysis in ferrite devices is a topic not covered so far. In fact, very little literature about multipactor effect in devices containing ferrites can be found [77]. This way, multipactor risk in components such as circulators, phase-shifters or isolators can only be analyzed by rough approximations whose validity is not clear.

In this section, it is analyzed the multipactor effect in an ideal uniform parallel-plate waveguide (see Fig. 6.37) of infinite length along the x and z axis, z being the propagation direction of the electromagnetic waves. The waveguide contains a lossless ferrite slab of height h, which is magnetized by means of an externally applied static magnetic field. The gap length between the ferrite and the upper metallic wall is d. Ferrites are ferromagnetic materials, which exhibit magnetic anisotropy when they are in the presence of a DC external magnetic bias field. Due to this, depending on the bias magnetic field direction, the RF behavior of the ferrite will be completely different. Here, we will consider two different orientations of the magnetization field $\vec{H}_0$: parallel to the ferrite slab (along the x-direction) and normal to the ferrite slab (along the y-direction). Thus, this study might be used for a preliminary analysis of the multipactor phenomenon within many ferrite devices such as some types of the aforementioned circulators, phase-shifters or isolators [79]-[87].

6.4.1. Computation of the RF fundamental mode

In this subsection, we describe the procedure to obtain the RF electromagnetic field pattern of the fundamental propagating mode of the parallel-plate ferrite-loaded waveguide. The multipactor simulations performed take only into account the first propagating mode, which is different for each magnetization direction of the ferrite. The magnetic permeability of the ferrite given by the Polder's tensor [78] depends on the orientation of the magnetization field. For the magnetization directions that will be considered throughout this section, i.e., $\vec{H}_0 = H_0\hat{x}$ and $\vec{H}_0 = H_0\hat{y}$, the magnetic permeability is given by

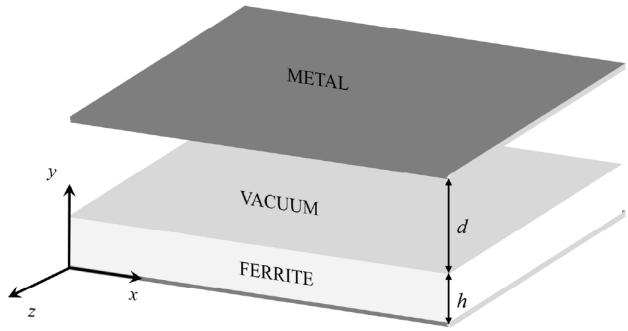

Figura 6.37: Parallel-plate waveguide (considered to be infinite along the x and z axis, z being the propagation direction of the electromagnetic wave) partially loaded with a ferrite slab.

$$[\mu] = \begin{bmatrix} \mu_0 & 0 & 0 \\ 0 & \mu & j\kappa \\ 0 & -j\kappa & \mu \end{bmatrix} (\hat{x} \text{ bias}); \quad [\mu] = \begin{bmatrix} \mu & 0 & -j\kappa \\ 0 & \mu_0 & 0 \\ j\kappa & 0 & \mu \end{bmatrix} (\hat{y} \text{ bias})$$

The elements of the permeability tensor are

$$\mu = \mu_0 \left(1 + \frac{\omega_0 \omega_m}{\omega_0^2 - \omega^2}\right)$$

$$\kappa = \mu_0 \frac{\omega \omega_m}{\omega_0^2 - \omega^2}$$

where $\omega_0 = 2\pi f_0 = \mu_0 \gamma H_{ef}$ is the Larmor angular frequency, $\omega_m = \mu_0 \gamma M_s$, M_s is the saturation magnetization, H_{ef} is the internal bias magnetic field inside the ferrite, and $\gamma = \frac{e}{m_e}$ is the gyromagnetic ratio.

It must be mentioned that the bias magnetic field H_{ef}, internal to a ferrite sample, is in general different from externally applied field H_0 because of the boundary conditions at the surface of the ferrite. For the case of the magnetization parallel to the ferrite surface, we have $H_{ef} = H_0$. However, for the case of magnetization normal to the ferrite surface, it is satisfied that $H_{ef} = H_0 - M_s$.

The procedure employed to obtain the RF electromagnetic field of the fundamental mode, as well as its propagation factor β, is different for each magnetization direction. When the bias magnetic field is oriented along the x-axis, there is analytical

expressions for the proper modes, whilst in the case of magnetization along y-axis this is not true, and numerical techniques are required.

6.4.1.1. x-magnetization proper modes

The RF electromagnetic fields supported by a waveguide with the aforementioned characteristics can be obtained analytically. In this situation two family of electromagnetic field modes are found: TM^z ($H_z = 0$) and TE^z ($E_z = 0$). Following the same mode-matching procedure outlined in [78], it can be analytically demonstrated that the TE^z modes have no vertical electric field component along the gap, so they are not suitable to hold a multipactor discharge and, as a consequence, they are not considered in our analysis. Otherwise, the TM^z modes do have vertical electrical component, so they may lead to a multipactor discharge. After imposing the boundary conditions on the significant surface interfaces of the problem, the propagation factor β of the TM^z modes is found by solving numerically the following characteristic equation,

$$\varepsilon_r k_1 \sinh(k_1 d)\, \cos(k_2 h) - k_2 \cosh(k_1 d)\, \sin(k_2 h) = 0$$

where $k_1^2 \equiv \beta^2 - \omega^2 \mu_0\, \varepsilon_0$, $k_2^2 \equiv \omega^2 \mu_0\, \varepsilon_0\, \varepsilon_r - \beta^2$. The non-zero TM^z modal field components of the RF electromagnetic field in the vacuum region are given by,

$$E_y(y,z,t) = \frac{V_0\, k_1}{\sinh(k_1\, d)} \cosh[k_1\, ((d+h) - y)]\, \cos(\omega\, t - \beta\, z) \tag{6.20a}$$

$$E_z(y,z,t) = -\frac{V_0\, k_1^2}{\beta\, \sinh(k_1\, d)} \sinh[k_1\, ((d+h) - y)]\, \sin(\omega\, t - \beta\, z) \tag{6.20b}$$

$$H_x(y,z,t) = -\frac{\omega\, \varepsilon_0}{\beta} E_y(y,z,t) \tag{6.20c}$$

where V_0 is the equivalent voltage obtained from the path integration of the RF electric field E_y along the vacuum gap from $y = h$ to $y = d + h$ at $z = 0$ plane, and $t = 0$:

$$V_0 = \int_h^{d+h} E_y(y, 0, 0)dy$$

Note that for the considered TM^z modes, the characteristic equation does not depend on the magnetic properties of the ferrite.

6.4.1.2. y-magnetization proper modes

In this case, the RF electromagnetic field inside the structure under study has been obtained with the aid of the Coupled Mode Method (CMM). This well-known numerical method, formulated in the frequency domain, has been widely and successfully used in the analysis of the electromagnetic wave propagation inside uniform waveguides that contain any isotropic, anisotropic or complex material [88]-[90]. The current version of the CCM applied to the computation of the RF electromagnetic field in the ferrite-loaded waveguide has been provided to us thanks to a collaboration with a research group of the Universidad de Cantabria, under the European Space Agency project "Novel Investigation in Multipactor Effect in Ferrite and other Dielectrics used in high power RF Space Hardware" with contract number AO 1-7551/13/NL/GLC.

In few words, the Coupled Mode Method is a Method of Moments which consists on expanding the electromagnetic field components inside the structure under analysis in terms of a set of previously defined base functions [88]. In this case, these base functions correspond to the electric or magnetic field components of the TE^z and TM^z modes of the empty waveguide. Therefore, they are called basis modes. According to this idea, any component of the electromagnetic field of the structure under test can be expressed as a linear combination of the basis modes.

Once the electromagnetic fields inside the waveguide are obtained, the calculation of the equivalent voltage V_0 is done by integrating the vertical RF electric field along the vacuum gap, in the same way as for the x-coordinate magnetization case.

6.4.2. Simulations

The multipactor algorithm employed for the numerical simulations is based on the effective electron model described in section 3.6. The modified Vaughan's model was implemented for the computation of the SEY coefficient at the collisions. The current simulations take into account the space charge effect, as well as the dielectric

polarization effect of the ferrite that arises from the emission or absorption of electrons from the ferrite surface.

6.4.2.1. x-magnetization case

Multipactor simulations were performed for the ferrite-loaded parallel-plate waveguide shown in Fig. 6.37 with dimensions $h = 3$ mm and $d = 1$ mm. In the considered case, the metallic waveguide walls are made of silver, whose SEY parameters are: $W_1 = 30 \pm 1$ eV, $\delta_{max} = 2.22 \pm 0.01$, and $W_{max} = 165 \pm 1$ eV [91]. Regarding to the ferrite slab, its relative dielectric permittivity is $\varepsilon_r = 15.5 \pm 0.1$, the saturation magnetization is $4\pi M_s = 1790 \pm 1$ G, and the SEY parameters are $W_1 = 29 \pm 1$ eV, $\delta_{max} = 2.40 \pm 0.01$, and $W_{max} = 288 \pm 1$ eV.

First of all, we have analyzed the multipactor effect when no external magnetic field is applied to magnetize the ferrite ($H_0 = 0$ Oe, see Fig. 6.38). In such a case, the ferrite does not exhibit any anisotropic magnetic properties, so it behaves as a conventional dielectric and magnetic isotropic medium. In order to check our simulation code, we have compared this case with the available results in the literature for multipactor in partially dielectric-loaded waveguides [27], [29], finding good agreement between them. Furthermore, it has also been noticed that in some particular cases the polarization electric field is able to turn the multipactor discharge off, as it was reported in [27] and [28]. This is due to the disturbing effect of the electric polarization field in the multipactor resonant trajectories.

Next, we have studied the effect of the ferrite magnetization field strength in the multipactor RF voltage threshold. In Fig. 6.38 multipactor RF voltage threshold curves are shown for several typical values of the magnetization field ($H_0 = 0$ Oe, $H_0 = 500$ Oe, $H_0 = 1000$ Oe). It is noticed that the presence of such an external magnetic field really changes the multipactor behavior of the curves with regard to the without ferrite and magnetization case. Mainly, it is observed that the magnetization field tends to shift the multipactor susceptible zones towards higher values of the frequency gap product. This effect is found to be more noticeable as the strength of the magnetization field is increased. Indeed, for $H_0 = 500$ Oe multipactor breakdown does not appear for frequency gap values less than 1.3 GHz mm, whilst for $H_0 = 1000$ Oe no multipactor discharge is observed below 2.4 GHz mm. Another interesting aspect it that for some frequency gap ranges, both in the $H_0 = 500$ Oe and $H_0 = 1000$ Oe situations, the multipactor voltage threshold drops below the non-

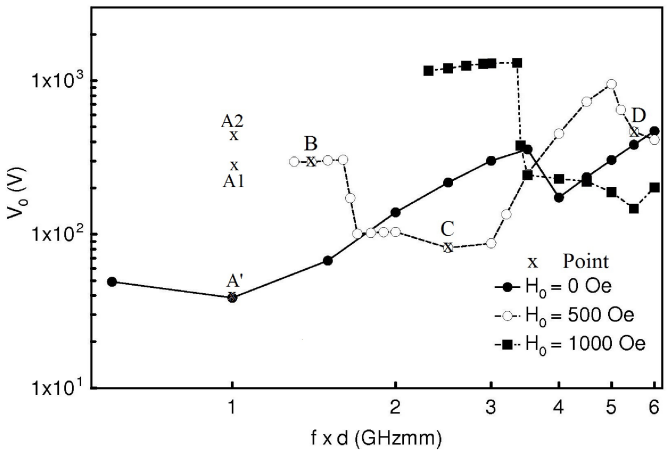

Figura 6.38: Multipactor RF voltage threshold as a function of the frequency gap for several values of the external ferrite magnetization field.

magnetized ferrite case. These results are consistent with [43] and [92], wherein it is experimentally demonstrated that the presence of an external DC magnetic field may lead to an enhancement of the multipacting effect for certain values of the external static magnetic field strength.

To have a better understanding of the multipactor behavior, the effective electron trajectories have been plotted for several significant points marked in Fig. 6.38. Points $A1$, $A2$, B, C and D belong to the $H_0 = 500$ Oe case; whereas point A' corresponds to the $H_0 = 0$ Oe situation. From the analysis of these points, it is found that the electron flight time between successive impacts strongly depends on the ratio between the RF frequency and the cyclotron one ($f_c = (e\mu_0 H_0)/(2\pi m_e)$). Note that for this direction of the magnetization field, the cyclotron and Larmor frequencies have the same value. Specifically, for a fixed value of the cyclotron frequency, the flight time increases as the RF frequency does. This fact influences the possible multipactor resonances that can arise in each case, as it will be shown next.

First, we are going to analyze the effective electron trajectories behavior for the frequency gap value of 1 GHz mm. If we examine the point A' (see Fig. 6.38 and Fig. 6.39) it corresponds to the $H_0 = 0$ case, where no external magnetization field is

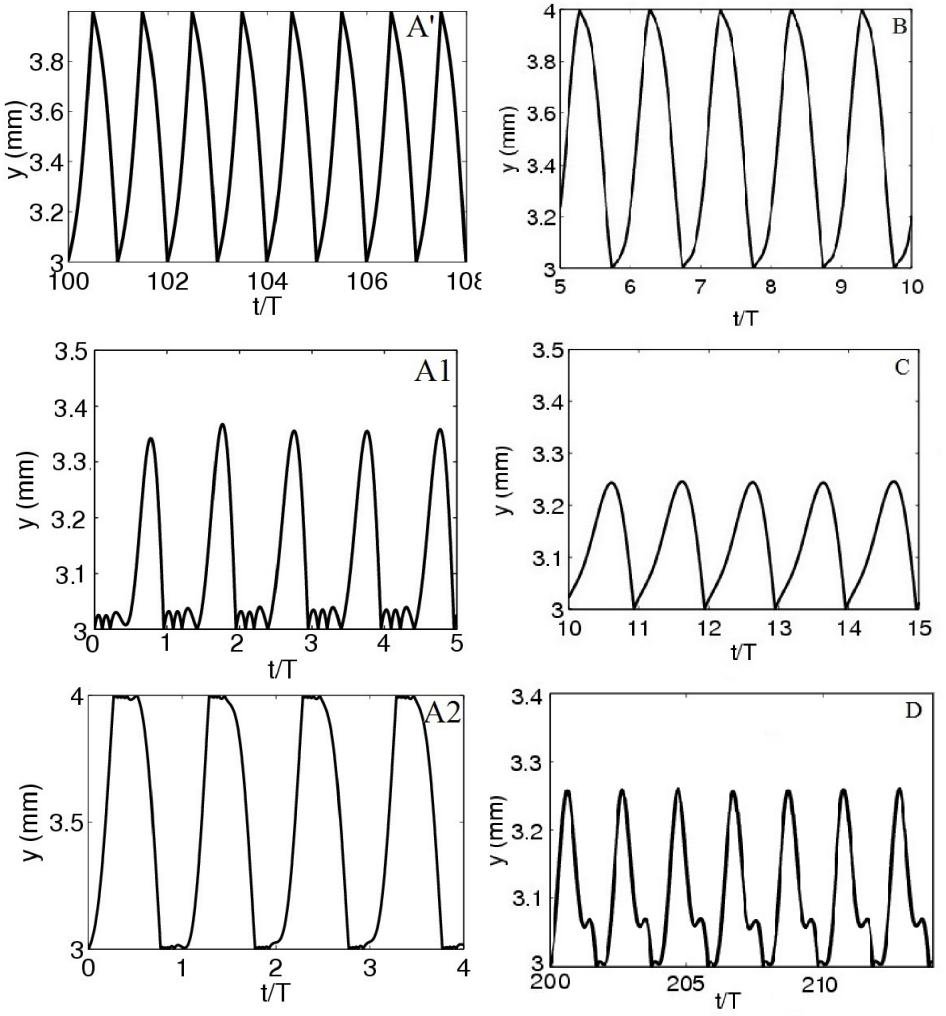

Figura 6.39: Vertical coordinate of the effective electron for several points in Fig. 6.38.

applied. It is observed that the electron takes one semiperiod of the RF signal between successive impacts with the waveguide walls, which corresponds with the well-known

classical double surface multipactor of order one. It is stated that the SEY is slightly above the unity, so the multipactor discharge will occur.

Now, for the same frequency gap value, it is examined the situation with $H_0 = 500$ Oe. In this case, no discharge is expected at any RF voltage level. At point $A1$ the RF voltage level is quite above the multipactor threshold value of the $H_0 = 0$ Oe case. However, the bending effect of the H_0 field tends to push the electron back to the departure wall, preventing it from reaching the opposite plate and leading to single-surface trajectories. Moreover, on inspecting Fig. 6.39 it is noticed the lack of resonance between the electron and the RF electric field, since there are many successive low energetic impacts (with SEY below the unity), in which the electron leaves with a non-favorable polarity of the RF electric field, and as a consequence being quickly repelled towards the initial wall. At point $A2$, it is depicted the electron trajectories for a higher RF voltage than in point $A1$. In this case, the RF electric field is strong enough to allow the electron crossing the gap. Despite this, many single-surface low energetic impacts are observed, due to the lack of resonance with the RF electric field. This lack of resonance is caused by the magnetization field H_0, which bends the electron trajectories and hence shortens the flight time between successive impacts. Notice that for point $A1$ the maximum flying time is always below two semiperiods, which is the time between impacts required to establish a single-surface resonance of order two. Below order two there are not any single-surface multipactor modes available that allow the resonance between the RF electric field and the electron and, as a consequence, the onset of the discharge is not possible. Similarly, for point $A2$, the maximum flight time does not reach the semiperiod, which is the minimum travel time of the electron in order to synchronize with the RF electric field by means of the double-surface multipactor mode with order one. In addition, the mean SEY at the impacts is below the unity.

Remaining with the analysis of the $H_0 = 500$ Oe case, we move to point B (recall Fig. 6.38) at a higher frequency gap value. In this case, there is a multipactor discharge with a double-surface multipactor of order one (see Fig. 6.39). This resonant mode is the one with the lowest order possible. It appears due to the increase of the f/f_c quotient that allows higher flying time between consecutive collisions of the electron. Note that the multipactor RF voltage threshold of the point B is quite above the corresponding value for the $H_0 = 0$ Oe case (recall Fig. 6.38). This is because the bending effect of the electron trajectories tends to force single-surface trajectories, and an extra RF voltage is needed in order to allow the electron to reach the opposite wall.

Moving towards higher frequency gap values, we find points C and D. For point C a single-surface multipactor mode with order two is established, meanwhile a single-surface resonance with order four is found for point D. Once again is observed how the increase of the f/f_c ratio allows higher flying times of the electron.

Briefly, if we examine the multipactor voltage threshold of the $H_0 = 1000$ Oe case, it is noticed that the shape of the curve is similar to the corresponding to the $H_0 = 500$ Oe situation but shifted to higher frequency gap values. In fact, when examining the multipactor resonant modes it is found that there is a clear correspondence between both curves. This is again explained in terms of the strong dependence of the flight time of the electron (and hence of the multipactor phenomenon) with the ratio f/f_c.

Finally, the effect of changing the ferrite slab height in the multipactor RF voltage threshold for a fixed value of the gap and the ferrite magnetization field is analyzed in Fig. 6.40. As it can be observed, there is a small shift in the voltage threshold, although the general behavior and shape of the multipactor curves remain unchanged for the considered slab height range.

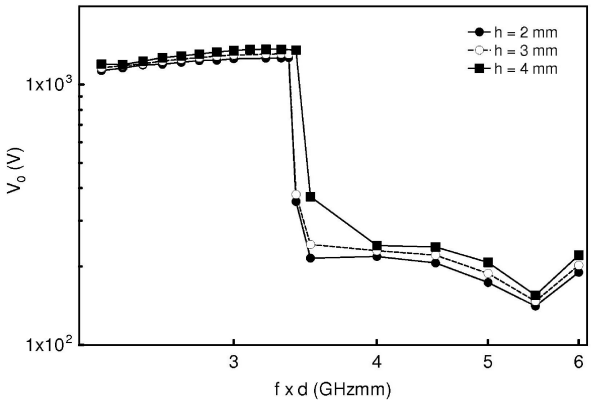

Figura 6.40: Multipactor susceptibility charts for silver partially ferrite-filled parallel-plate waveguide. Multipactor voltage threshold for several values of the ferrite slab height. Gap distance is $d = 1$ mm and $H_0 = 1000$ Oe.

6.4.2.2. y-magnetization case

In order to compute the multipactor RF voltage threshold for the parallel-plate ferrite loaded waveguide, numerical simulations have been performed. The ferrite thickness h and the vacuum gap d have been selected to match with the height of a WR-90 rectangular waveguide, i.e., $b = d + h = 10.16$ mm. The saturation magnetization of the ferrite is $4\pi M_s = 1806 \pm 1$ G, its relative dielectric permittivity $\varepsilon_r = 15.0 \pm 0.1$, and its SEY parameters are: $W_1 = 19 \pm 1$ eV, $\delta_{max} = 2.88 \pm 0.01$, and $W_{max} = 289 \pm 1$ eV. For simplicity, the same SEY parameters are selected for the top metallic wall. The external magnetic field employed to magnetize the ferrite is $H_0 = 3000$ Oe. Consequently, the effective biasing field inside the ferrite is $H_{ef} = 1194$ Oe. The considered fields are those corresponding to the fundamental mode of the ferrite loaded waveguide. For all calculations of the electromagnetic field components with the Coupled Mode Method, a total number of 75 TE^z and 75 TM^z basis modes have been used.

First, for the fundamental mode, the propagation factor dependence with frequency is obtained, as shown in Fig. 6.41. It can be observed that the real part of the propagation factor is zero within the plotted frequency range, which corresponds to a propagative mode.

We are interested in analyzing the effect of the variation of the ferrite thickness and the vacuum gap length in the multipactor RF voltage threshold. In Fig. 6.42, the variation of the multipactor RF voltage threshold as a function of the frequency gap value is shown for several ferrite loaded parallel-plate waveguides. Note that for each curve the gap remains fixed, and the constraint $d + h = 10.16$ mm is maintained. Moreover, the results for a classical metallic parallel-plate waveguide with no ferrite slab, a gap of $d = 0.2$ mm and $H_0 = 0$ (henceforth referred as without ferrite case) has been included for comparison purpose. Remember that according to the well-known multipactor theory [49] for a classical metallic parallel-plate waveguide, the multipactor phenomenon depends only on the frequency gap product and, as a consequence, the same multipactor RF voltage threshold curve would be obtained for metallic parallel-plate waveguides with other gaps while maintaining the same frequency gap range. From the results (recall Fig. 6.42) it is noticed that there is considerable difference between the multipactor RF voltage threshold of the ferrite loaded waveguides and the corresponding to the without ferrite case. It is found that this discrepancy increases with the gap value. In fact, the maximum difference in the multipactor RF voltage threshold between the $d = 0.2$ mm waveguide and the without ferrite case is of 6.5

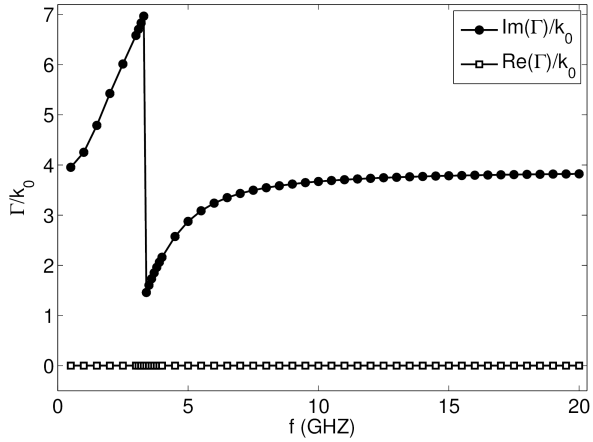

Figura 6.41: Real and imaginary parts of the propagation factor for the fundamental mode of a ferrite loaded waveguide (with $d = 1$ mm) as a function of the RF frequency. Note that gyromagnetic resonance, given by Larmor frequency, occurs at $f_0 = 3.34$ GHz.

dB, whilst in the $d = 1$ mm and $d = 2$ mm the difference becomes of 26 dB and 37 dB, respectively. It is also observed that the multipactor behavior of the ferrite loaded waveguides remains very close to the without ferrite case for low frequency gap values (below 2.5 GHz mm). In general terms, the multipactor RF voltage threshold of the ferrite loaded waveguide cases tends to be equal or below the without ferrite multipactor threshold, which might be dangerous in a realistic application.

In order to have a better understanding of the behavior of the different multipactor susceptibility curves, a detailed analysis of the RF electromagnetic fields has been performed for both the ferrite loaded waveguides and the classical unloaded metallic parallel-plate waveguide.

An exhaustive inspection of the RF electromagnetic field pattern for the fundamental mode of the three ferrite loaded waveguide cases has revealed that the RF magnetic field has very little influence in the electron motion, thus the contribution of the terms $v_i \, B_{RF,j}$ (being $i, j = x, y, z$) can be neglected in the differential equations of the electron motion (it is well known that for non-relativistic motion the RF magnetic fields can be neglected in the Lorentz Force [6]). Regarding the RF electric field

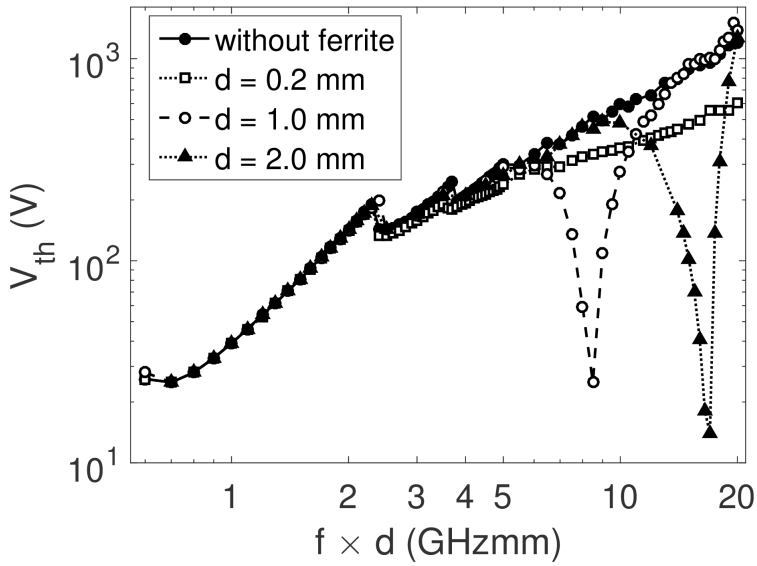

Figura 6.42: Multipactor RF voltage threshold as a function of the frequency gap. Results are presented for parallel-plate ferrite loaded waveguides with different gap lengths and ferrite thicknesses (but maintaining the height of a WR-90 waveguide, i. e. $d + h = 10.16$ mm); and also for a metallic parallel-plate waveguide ("without ferrite").

components, it has been found that all of them have noticeable effects in the electron trajectories. In Fig. 6.43 (up) it has been depicted the quotient between the maximum absolute value along the gap of the $E_{RF,x}$ and $E_{RF,y}$ components for the different considered ferrite waveguides. In a similar way in Fig. 6.43 (bottom) it has been plotted the same quotient for the $E_{RF,z}$ and $E_{RF,y}$ components. From these figures it is extracted that the $E_{RF,y}$ is the greater RF electric field component for low frequency gap values. As the frequency gap increases the components $E_{RF,x}$ and $E_{RF,z}$ are higher with regard to the $E_{RF,y}$ component. This increment is found to be more notorious for the ferrite loaded waveguides with higher gaps. In fact, it can be observed that the $E_{RF,x}$ becomes the dominant component in the $d = 2$ mm waveguide for values above 15 GHz mm.

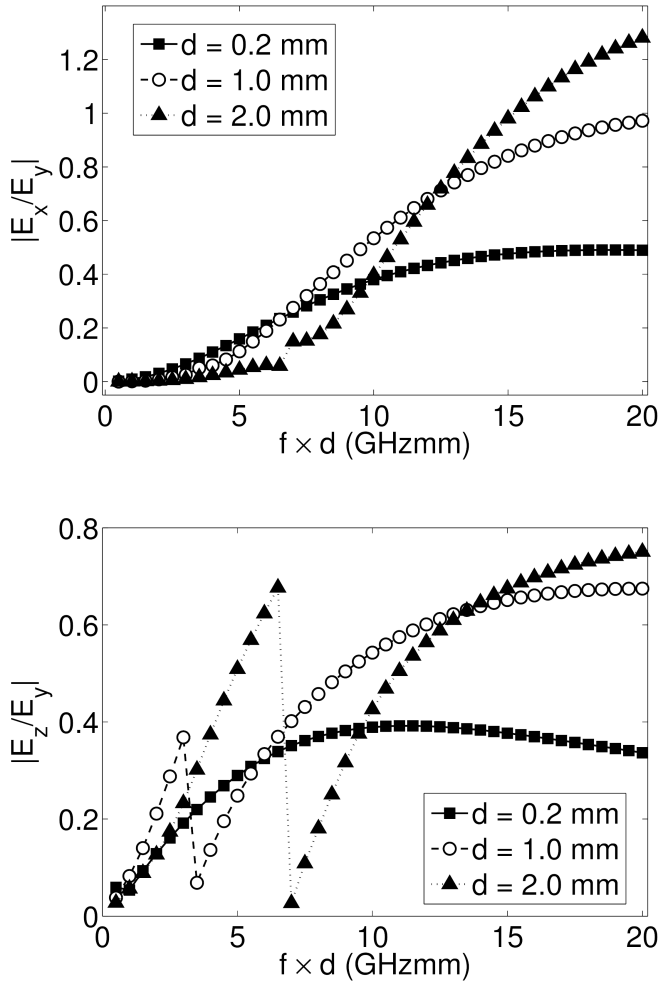

Figura 6.43: Up (bottom): quotient between the maximum absolute value along the gap of the $E_{RF,x}$ ($E_{RF,z}$) and $E_{RF,y}$ components for the ferrite loaded waveguides.

Taking the previous statements into account, the differential equations of motion can be approximated in the following way at the earlier stages of the electron multi-

plication process:

$$\frac{dv_x}{dt} \simeq \omega_c v_z - \frac{e}{m_e} E_{RF,x} \cos(\omega t + \phi) \tag{6.21}$$

$$\frac{dv_y}{dt} \simeq -\frac{e}{m_e} E_{RF,y} \cos(\omega t + \phi) \tag{6.22}$$

$$\frac{dv_z}{dt} \simeq -\omega_c v_x - \frac{e}{m_e} E_{RF,z} \sin(\omega t + \phi) \tag{6.23}$$

where $\omega_c = \frac{e}{m_e}\mu_0 H_0$ is the cyclotron angular frequency, v_x, v_y, and v_z are the x, y, z components of the velocity vector, respectively; and ϕ is the phase of the RF electromagnetic field. It is remarkable that the equation of motion for the y coordinate gets decoupled from the remaining x and z coordinates. Indeed, the approximated y-equation of motion becomes the corresponding one of the analytically well-studied classical case without ferrite [49]. The effect of the external field H_0 is to spin the electron orbits in the xz plane. In addition, the $E_{RF,x}$ and $E_{RF,z}$ components accelerate the electron along the directions x and z, respectively. Manipulating the expressions (6.21) and (6.23) the following differential equations arise for the v_x and v_z velocities

$$\frac{d^2 v_x}{dt^2} + \omega_c^2 \, v_x = A_1 \, \sin(\omega t + \phi) \tag{6.24}$$

$$\frac{d^2 v_z}{dt^2} + \omega_c^2 \, v_z = A_2 \, \cos(\omega t + \phi) \tag{6.25}$$

where $A_1 = \frac{e}{m_e}(E_{RF,x,0}\,\omega - E_{RF,z,0}\,\omega_c)$ and $A_2 = \frac{e}{m_e}(E_{RF,x,0}\,\omega_c - E_{RF,z,0}\,\omega)$. The above differential equations can be solved analytically provided that the amplitude of the RF electric field components are uniform along the gap. Although this is not true in our case, we will take this assumption in order to obtain some analytical expressions that can give us a certain qualitative insight of the multipactor phenomenon. After some calculations, the following expressions arise for the v_x and v_z velocities (it is

assumed zero initial velocity for both coordinates)

$$v_x = \frac{A_1}{\omega_c^2 - \omega^2}\sin(\omega\, t + \phi) - \frac{A_1\,\sin(\phi)}{\omega_c^2 - \omega^2}\,\cos(\omega_c\, t) - \frac{A_2\,\cos(\phi)}{\omega_c^2 - \omega^2}\,\sin(\omega_c\, t) \tag{6.26}$$

$$v_z = \frac{A_2}{\omega_c^2 - \omega^2}\cos(\omega\, t + \phi) - \frac{A_2\,\cos(\phi)}{\omega_c^2 - \omega^2}\,\cos(\omega_c\, t) + \frac{A_1\,\sin(\phi)}{\omega_c^2 - \omega^2}\,\sin(\omega_c\, t) \tag{6.27}$$

Note that (6.26) and (6.27) are valid for all the RF frequencies except for $\omega = \omega_c$. For both velocities, there are oscillatory terms at both the RF frequency and at the cyclotron frequency. It is easily noticed that the amplitude of these oscillations becomes maximum when the RF frequency equals the cyclotron one ($\omega = \omega_c$). Consequently, the velocity gain in the plane xz is maximum in the neighborhood of such resonance. In our case the cyclotron frequency is 8.4 GHz and the corresponding frequency gap is 8.4 GHz mm for the $d = 1$ mm waveguide and 16.8 GHz mm for the $d = 2$ mm waveguide. This cyclotron resonance allows to understand the sharp minimums observed for the multipactor RF voltage thresholds of the ferrite loaded waveguides with $d = 1$ mm and $d = 2$ mm in the surroundings of such frequency gap values. Due to the enhance in kinetic energy gain of the electron in the xz plane, less RF voltage amplitude is necessary to achieve that the total kinetic impact energy of the electron exceeds the W_1 of the material. To illustrate the cyclotron resonance effect, in Fig. 6.44 we have plotted the v_x, v_y, v_z velocities of an effective electron in the $d = 1$ mm ferrite loaded waveguide, for a frequency gap value close to the resonance and an RF voltage value corresponding to the multipactor threshold. It is noticed the increment of the v_x and v_z maximum amplitude in the successive oscillations between one impact and next, whilst for the v_y velocity it is not observed such maximum amplitude increment. In Fig. 6.44 it has also been depicted the xz-plane electron trajectory which seems very similar to that of a cyclotron accelerator, where the radius of the electron circular trajectory tends to increase as the kinetic energy gain process is ongoing.

The above statements justify the presence of a sharp minimum in the multipactor RF voltage threshold for the frequency gap values in the vicinity of the cyclotron resonances for the $d = 1$ mm and $d = 2$ mm ferrite loaded waveguide cases. However, it is notorious that such multipactor RF voltage threshold minimum is not observed

for the $d = 0.2$ mm waveguide (which should be expected at 1.68 GHz mm).

To understand this point we will briefly recall some aspects of the classic multipactor theory for parallel-plate waveguides since, as we argued previously, in our ferrite loaded waveguide case the y motion becomes decoupled from the x and z coordinates, resulting in the same y differential equation of motion that for the classical metallic parallel-plate waveguide. The only difference in the y equation of motion between the unloaded ferrite waveguide and the ferrite waveguide is that, in the latter case, the $E_{RF,y}$ is inhomogeneous along the gap. This fact implies that the mutipactor resonant electron trajectories in the ferrite waveguide will be almost the same than in the without ferrite case. Thus, as it is well stated in the classical multipactor theory, the number of multipactor modes available for a multipactor discharge grows as the frequency gap increases [49]. In the same way, the flight time between successive electron impacts rises up as the multipactor order does. Consequently, low frequency gap values imply low crossing gap times for the electrons. This phenomenon justifies similarity in the multipactor RF voltage threshold between the ferrite waveguide and the without ferrite cases for the low frequency gap values (remember Fig. 6.42). Despite the presence of the accelerating RF electric field in the xz-plane, the contribution to the electron kinetic energy is quite low due to short transit time. This explains the absence of the sharp decreasing peak in the multipactor RF voltage threshold of the ferrite waveguide with $d = 0.2$ mm in the vicinity of the cyclotron resonance, which occurs at 1.68 GHz mm. However, when the frequency gap increases the flight time also does, allowing higher gain of kinetic energy in the transverse plane, and so reducing the multipactor RF voltage threshold regarding the without ferrite case (recall Fig. 6.42).

An important prediction extracted from the previous analysis of the ferrite waveguides with vacuum gaps of 0.2 mm, 1.0 mm and 2.0 mm is that it is expected a sharp minimum in the multipactor RF voltage threshold when the RF frequency equals the cyclotron one, whenever that this resonance occurs at a frequency gap value high enough to allow great electron flight time between impacts. For the classical parallel-plate case, the multipactor RF voltage threshold increases monotonously with frequency gap. In fact, multipactor susceptibility curves typically do not explore frequency gap values above 20 GHz mm, since multipactor is expected to occur at very high voltage levels that exceed the operation range of the telecommunication satellite components. As a consequence, devices operating at such high frequency gap values are assumed to be out of the risk of suffering a multipactor discharge at the typical

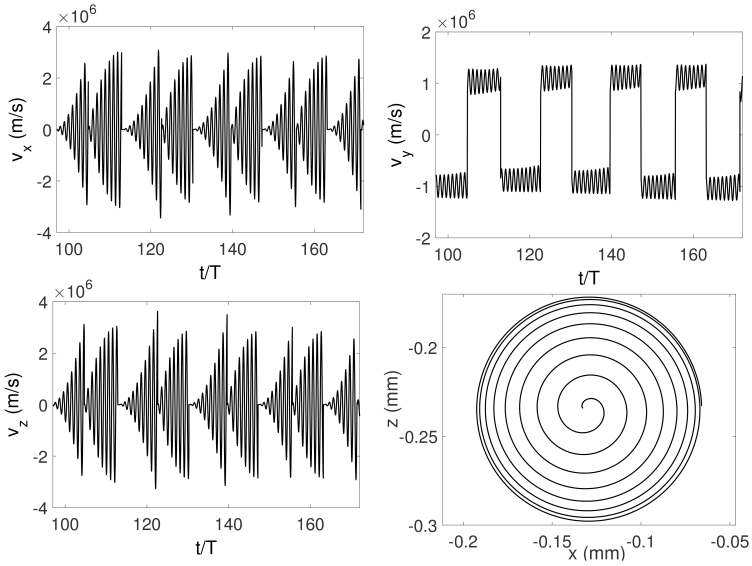

Figura 6.44: From left to right, and up to down: effective electron velocity components as a function of the time normalized to the RF period (T is the RF period), and xz-plane electron trajectory. All for a ferrite waveguide with $d = 1$ mm, $f \times d = 8.5$ GHz mm, $V_0 = 25$ V.

operation power levels. However, this assumption could be very harmful if it is extrapolated to a ferrite device, due to the lack of previous information about multipactor in ferrite components. In fact, the sharp minimum in the multipactor RF voltage threshold in the cyclotron resonance it is expected to be deeper as the cyclotron frequency gap value increases. Due to this, we carried out numerical simulations for a ferrite loaded waveguide with a gap of $d = 5$ mm (in this case the resonance conditions are fulfilled at 42 GHz mm) The results from the numerical simulations for the multipactor RF voltage threshold in the $d = 5$ mm ferrite waveguide are shown in Fig. 6.45, confirming the appearance of a very deep minimum.

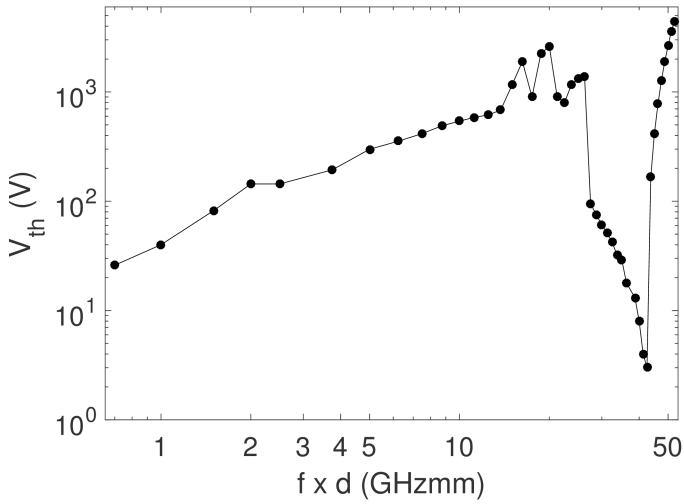

Figura 6.45: Multipactor RF voltage threshold as a function of the frequency gap for a ferrite waveguide with $d = 5$ mm and $b = 10.16$ mm.

Finally, it has been analyzed the case of having different SEY coefficients for the ferrite and the metal surface. The SEY parameters for the ferrite remain the same that were described previously in this section, whilst the SEY coefficients for the metal are those from the ECSS silver [2], i.e., $W_1 = 30$ eV, $W_{max} = 165$ eV, and $\delta_{max} = 2.22$. In Fig. 6.46 it is shown the multipactor RF voltage threshold for the ferrite waveguide with $d = 0.2$ mm considering the ferrite and silver SEY properties, as well as the results considering the same SEY properties for both surfaces. It is observed slight differences between both cases. Note that the multipactor RF voltage threshold in the ferrite and silver SEY case tends to be greater than in the case with the same SEY in both surfaces, this is because the W_1 for silver is above the W_1 for the ferrite, and more RF voltage amplitude is required in the former case to reach the multipactor threshold.

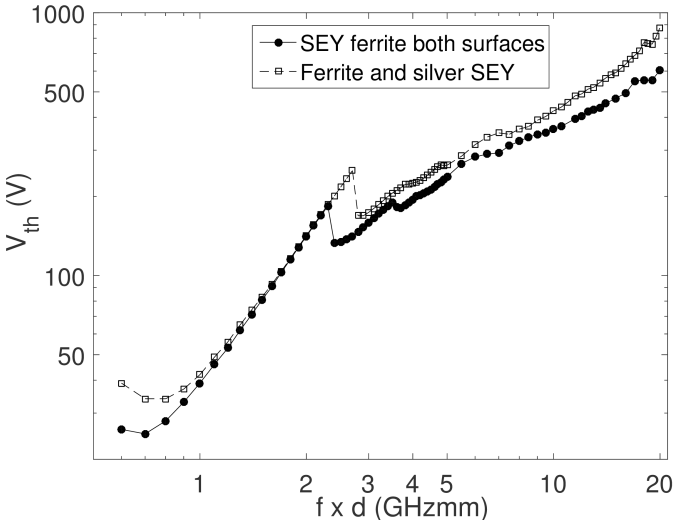

Figura 6.46: Multipactor RF voltage threshold as a function of the frequency gap for a ferrite waveguide with $d = 0.2$ mm and $b = 10.16$ mm, considering the same SEY properties for both surfaces and considering different SEY for ferrite and metal (silver) surfaces.

Chapter 7

Conclusions and future lines

7.1. Conclusions

This PhD Thesis covers the study of the multipactor effect in some specific scenarios, which are interesting for both the industry and scientific community devoted to the design and manufacturing of RF passive components in spacial telecommunications systems. In fact, there are some gaps in the multipactor literature that this works attempts to fulfill. According to this, several different topics are treated throughout this work, with the multipactor phenomenon as the common nexus to all of them. Despite the particularities of each case, the treatment given for the analysis of this RF breakdown is very similar. To proceed with the theoretical analysis, multipactor numerical simulations are carried out with an in-house developed code based on the effective or individual electron models, depending on the specific case. As a result of the numerical simulations, the time evolution of the electron population within the component is obtained. This constitutes the basic information to decide whether the discharge is expected to occur. After that, the multipactor RF voltage threshold curves are computed as a function of the most relevant parameters involved in the particular scenario. In addition, in order to achieve a deeper knowledge of the multipactor behavior, the electron trajectories and velocities are analyzed to seek multipactor resonant modes. The identification of the resonant modes, together with the analysis of the electromagnetic field pattern within the device, constitutes a great aid to understand the electron dynamics of the considered problem. Thus, the dependence of the multipactor RF voltage threshold with the parameters can be understood in terms of the

electron motion. Although the contents of this PhD Thesis are mainly focused on the numerical analysis of this phenomenon, in most of the treated scenarios experimental measurements were carried out in order to assess the presented theoretical frame.

The content of this PhD Thesis can be splitted into four different thematic areas: multipactor mitigation by means of static magnetic fields, multipactor in ridge and multi-ridged waveguides, multipactor with digitally modulated signals, and multipactor in a ferrite-loaded waveguide. For each of these topics, relevant and novel conclusions of the present study can be extracted. Next, the most remarkable findings will be outlined.

The multipactor mitigation analysis performed for coaxial transmission lines revealed the capability of a static magnetic field to suppress the discharge, provided that certain conditions are satisfied. In the investigated case, the external magnetic field is oriented along the axis direction of the coaxial waveguide, and it is spatially uniform. The presence of such DC magnetic field bends the electron trajectories that are forced to spin around the magnetic flux lines, pushing the electron back to the departure conductor, thus disturbing the classical double-surface resonant modes. In fact, single-surface multipactor modes might appear depending on the strength of the applied magnetic field. The ratio between the cyclotron frequency (which is proportional to the DC magnetic field) and the RF frequency has been found to be the parameter that most influences the electron flight time between two successive impacts with the device walls. Concretely, the higher the cyclotron to RF frequency ratio, the shorter the time lapse between collisions. When some critical value of that ratio is exceeded, the flight time becomes too short to allow the electron to synchronize with the RF electric field, resulting in very low energetic impacts that inhibit the onset of the discharge. As a consequence, it is demonstrated that a strong enough DC magnetic field is able to completely suppress the multipactor phenomenon in a coaxial transmission line. The concrete cyclotron to RF frequency ratio that mitigates the discharge depends also on the RF frequency of the signal. However, it can be taken as a rule of thumb that the discharge does not occur when the cyclotron frequency exceeds the RF frequency. In most of the cases this rough approximation constitutes a good starting point prior to performing the accurate numerical simulations. Moreover, an experimental test campaign demonstrated the validity of these theoretical results. After the axial uniform DC magnetic field case was well understood, a second study related with multipactor mitigation in non-uniform static magnetic field was performed. For this case, it was considered the magnetic field generated by a hollow cylindrical neodymium perma-

nent magnet. In such a situation, the magnetic field inside the hollow cylinder has a radial component besides the axial one, and both of them are spatially non uniform. Concretely, the axial magnetic component dependence on the axial coordinate shows that the field is rather uniform inside the cylinder, but it vanishes as the axial coordinate approaches to the borders. This point is relevant for the mitigation purposes since, as stated in the axial uniform DC case, a strong magnetic field is required in order to suppress the discharge. However, when examining the electron trajectories, it was found that the radial magnetic field component tends to push the electron out these problematic low axial magnetic field zones. Due to this phenomenon, the mitigation effect in the hollow cylindrical magnet behaves very similar to the uniform magnetic field case. This statement was also experimentally verified in a multipactor test campaign. In fact, the rough approximation of assuming that the multipactor is mitigated for RF frequencies below the cyclotron one is still valid in the case of the hollow magnet.

With regard to the multipactor analysis in ridge and multi-ridge waveguides, a bunch of multipactor susceptibility charts covering the most relevant parameters and cases have been computed. Moreover, a simple method for predicting the multipactor RF voltage threshold in complex structures containing ridge and multi-ridge waveguide sections is presented. This method is revealed as an alternative to the accurate multipactor simulation of the whole device, which can be a very time-consuming process. By means of the aforementioned susceptibility charts and the RF electromagnetic pattern of the device, it can be obtained both the multipactor RF voltage threshold at the input port of the component, as well as the location inside the device where the discharge is foreseen. This approximate method was applied for an evanescent mode filter and a high-power S-band filter, finding good agreement when the results were compared with the proper multipactor simulations of the whole devices performed with the commercial software FEST3D. As a result, the use of the ridge and multi-ridge susceptibility charts allows to increase the power handling capability of the component in comparison with the predictions given by the parallel-plate approximation, which is rather conservative for geometries that differ from that ideal scenario. In fact, according to the ridge susceptibility charts, the power thresholds for the evanescent mode filter and the high-power S-band filter are 4 dB and 3.3 dB above the predictions based on the parallel-plate calculations, respectively.

The study of the multipactor effect in coaxial transmission lines excited with digitally modulated RF signals has revealed a higher level of complexity with regard to

the other topics treated throughout this PhD Thesis. For digitally modulated signals, in contrast to the time-harmonic CW case, the signal envelope varies with time during the on-going of the energy transmission. As a consequence, the amplitude of the envelope can go above and below the time-harmonic multipactor RF voltage threshold value many times. In the time lapses where the voltage exceeds the time-harmonic threshold level, the electron population within the device will rise up. However, in the opposite case, the number of electrons will diminish, and they will be mainly absorbed by the component walls. Due to this, simulating the multipactor effect forces to consider and analyze the waveform of the full transmitted signal, which can be very long in terms of time with respect to the typical times employed for simulating multipactor with unmodulated signals. An immediate consequence is the requirement of high computational simulation times, in order to treat with long time transmitted signals. On the other hand, the theoretical criterion for the onset of the discharge becomes critical when dealing with digitally modulated signals. For the time-harmonic CW case the evolution with time of the electron population acquires a well-defined trend (exponential increase or decrease) after a short time transient. Hence, if a growing trend is observed, the population will always increase until the discharge is triggered. Taking into account that the signal extends indefinitely in time, no matter how slow the growing rate could be, the required population (or density) electron level will be eventually reached. Nevertheless, with digitally modulated signals, increasing and decreasing time lapses alternate depending on the envelope waveform, thus the choice of the electron population (or density) required for the onset of the discharge, i.e. the multipactor criterion will be critical to compute the multipactor RF voltage threshold. Despite the importance in the knowledge of the critical electron density that triggers the multipactor detection methods in the laboratory, this issue is not well understood until the present moment. In fact, only a few theoretical articles can be found in the technical literature, but there is still a lack of comparison with experimental measurements. To overcome that inconvenience, an indirect method based on multipactor RF voltage threshold measurements with pulsed RF signals is carried out to obtain the electron population density required for the detection of the discharge in the laboratory. Once established such population level as the discharge criterion, it can be applied to the analysis of the digitally modulated signals. In this work, the most common modulation schemes such as BPSK, QPSK, 16-APSK, 32-APSK, and 16-QAM have been considered, as well as a wide range of different transmitted signals. An experimental test campaign was carried out to validate the numerical results, demonstra-

ting the feasibility of the developed multipactor code to analyze properly the scenario with digitally modulated signals, thus validating the choice of the electron population level selected for the multipactor criterion. Beside this, a coarse method based on the integration of the signal envelope is presented as an alternative to the proper accurate multipactor simulations. This procedure only requires as input data the results from numerical simulations for the time-harmonic CW case at the RF carrier frequency. The main advantage of this method is that is much faster than the numerical simulations, and it can be applied to any arbitrary digitally modulated signal. Finally, it is worth to mention that up to now, the standard adopted by the European Space Agency for multipactor risk assessment, when nonpure harmonic signals are involved, was based on the engineering rule of thumb known as "20-gap-crossing" rule. Comparison between both theoretical and experimental results presented in this PhD Thesis, together with the predictions extracted from the "20-gap-crossing" rule, reveal the inefficiency of this approach when applied to digitally modulated signals.

Multipactor analysis in parallel-plate waveguides containing a ferrite slab is aimed towards the understanding of more complex RF structures involving ferrites, such as some kind of circulators, isolators and phase-shifters. Until now, a full understanding of this effect when ferrite materials are involved is still missing. Indeed, the European industry uses larger power margins (in terms of multipactor) when dielectric or ferrite materials are present in the device due to uncertainties of all type. This way, components containing ferrites can only be analyzed by rough approximations whose validity is not clear. The anisotropic magnetic properties of the ferrite, together with the magnetization field of the ferrite, are expected to have noticeable effects in the electron trajectories, and therefore in the multipactor RF voltage threshold of the device. In this work, it has been considered two different directions for the external magnetization field: parallel and normal to the ferrite slab. In both scenarios it has been found remarkable changes in the multipactor voltage threshold with regard to the classical parallel-plate waveguide with neither ferrite nor external magnetic field. Moreover, the shape of the susceptibility curves depends on the orientation of the magnetization field. On the one hand, when the magnetic field is oriented parallel to the ferrite slab, it is observed a mitigation of the discharge for low frequency gap values mainly due to the presence of the static magnetic field. However, as the frequency gap increases the multipactor breakdown does appear, and it might occur even at lower RF voltages than the corresponding to the classical without ferrite case. In addition, it is noticed that the higher the magnetization field the higher the frequency gap range in which

the discharge is suppressed. On the other hand, when the magnetic field is oriented normal to the ferrite slab, it is not observed any mitigation phenomena. In fact, for low frequency values, both the with and without ferrite curves overlap. However, as the frequency gap value increases, the ferrite curve tends to be below the without ferrite case. It is also found an important decrease in the multipactor voltage threshold when the RF frequency is close to the cyclotron one. This effect is due to the cyclotron resonance, which allows the electron to maximize its kinetic energy gain from the RF electric field when the resonant condition is fulfilled. The depth of this multipactor threshold minimum increases with the value of the frequency gap at which it is expected. To give an example, differences up to 37 dB with regard to the without ferrite multipactor threshold can be found in some cases. These values are likely to exceed even the most conservative analysis margin predictions, leading to a harmful multipactor discharge in the device if a rigorous study assessing the multipactor risk has not been performed.

7.2. Future lines

As a result of the work performed throughout this PhD Thesis, it has been achieved a deeper understanding of several specific scenarios related with the multipactor effect. Thus, the conclusions extracted are of interest for the design of many types of RF passive components devoted to satellite telecommunication systems. However, it is evident that the presented studies do not entirely cover all the possible cases, and further investigation of these topics will lead to appearance of novel results. Next, we propose briefly some topics that could be of interest as future research lines.

- *Study of the multipactor effect with digitally modulated signals propagating within frequency dispersive structures.* In this PhD Thesis, the analysis of the multipactor with digitally modulated signals was restricted to the coaxial transmission line geometry. In this kind of structure, the propagation factor of the fundamental TEM mode depends linearly on the RF frequency and, consequently, no dispersion effects arise in the propagation of a RF signal composed by a certain frequency spectral range, as it is the case of digitally modulated signals. However, there are other types of geometries commonly employed for RF passive devices, such as rectangular waveguides, where distortion while the signal is propagating throughout the structure could affect the multipactor RF

voltage threshold. This phenomenon might be more notorious in rectangular waveguide components such as band-pass filters, which only transmit frequencies within the band-pass range, rejecting the remaining side of the spectrum. Hence, a multipactor analysis of rectangular waveguide band-pass filters excited by digitally modulated signals with different spectral widths will be of great interest, in order to advance towards the understanding of multipactor effect in complex dispersive RF devices.

- *Multipactor in coaxial lines with multicarrier signals.* The simulation code developed in this PhD Thesis for the analysis of the multipactor effect in coaxial lines with digitally modulated signals could be extended to consider the case of multicarrier signals. Concretely, the determination of the parameters that conform a signal with the minimum RF voltage threshold ("worst case") for a signal composed by a certain number of carriers would be of great interest for minimizing the risk of a multipactor discharge.

- *Extension of the coarse method for multicarrier signals.* The coarse method presented for digitally modulated signals in coaxial transmission lines might be extended for the case of a multicarrier signal.

- *Parallel-plate waveguides with two magnetized ferrite slabs.* The study presented in this PhD Thesis is restricted to a parallel-plate waveguide with a single ferrite slab placed in the bottom of the waveguide. This is the most simple scenario involving a magnetized ferrite material, and it constitutes an excellent starting point towards the understanding of structures containing such complex anisotropic magnetic material. In fact, some RF ferrite circulators or isolators use a configuration with a single ferrite sheet, similar to the previously analyzed case. However, many other RF ferrite circulators do have two ferrite slabs, whose configuration is similar to the proposed case of a parallel-plate waveguide with two magnetized ferrite slabs. Due to this, considering this latter case would be of interest, since significant differences might arise in the RF electromagnetic field pattern (and hence in the multipactor phenomenon) due to the inclusion of a second ferrite sheet.

- *Mitigation of the multipactor effect in rectangular and circular waveguides.* It is proposed to extend the study of multipactor mitigation by means of a static magnetic field to rectangular and circular waveguides.

Bibliography

[1] J. Vaughan, "Multipactor", *IEEE Trans. Electron Devices*, Vol. 35, No. 7, pp. 1172-1180, July 1988.

[2] "Multipaction design and test", ECSS-E-20-01A, ESA-ESTEC, 2003.

[3] P. Farnsworth, "Television by electron image scanning", *Journal of the Franklin Institute*, vol. 218, pp. 411-444, Oct. 1934.

[4] E. W. B. Gill, A. Engel, "Starting potentials of high-frequency gas discharges at low pressure", *Proceedings of Royal Society of London*, Serie A, vol. 192, pp. 446-463, 1948.

[5] S. Riyopoulos, D. Chernin, D. Dialetis, "Theory of electron multipactor in crossed fields", *Phys. Plasmas*, vol. 2, no. 8, pp. 3194-3212, 1995.

[6] V. E. Semenov, E. I. Rakova, D. Anderson, M. Lisak, J. Puech, "Multipactor in rectangular waveguides", *Physics of Plasmas*, vol. 14, 033501, 2007.

[7] R. Udiljak, D. Anderson, M. Lisak, V. Semenov, J. Puech, "Multipactor in a coaxial transmission line. Part I: Analytical study", *Phys. Plasmas*, Vol. 14, No. 3, pp. 033 508, Mar. 2007.

[8] R. Udiljak, D. Anderson, M. Lisak, J. Puech, and V.E. Semenov, "Multipactor in a Waveguide Iris", *IEEE Transactions on Plasma Science*, vol. 35, no. 2, pp. 388-395, April 2007.

[9] V. E. Semenov, E. Rakova, R. Udiljak, D. Anderson, M. Lisak, and J. Puech, "Conformal mapping analysis of multipactor breakdown in waveguide irises", *Physics of Plasmas*, vol. 15, 033501, 2008.

[10] J. Rasch, D. Anderson, J. F. Johansson, M. Lisak, J. Puech, E. Rakova, V. E. Semenov "Microwave multipactor breakdown between two cylinders", *IEEE Transactions on Plasma Science*, 38(8) pp. 1997-2005 Aug. 2010.

[11] E. Somersalo, P. Ylä-Oijala, D. Proch, "Electron multipacting in RF structures", DESY, Hamburg, Germany, TESLA Rep. 94-14, Jul. 1994.

[12] E. Somersalo, P. Ylä-Oijala, D. Proch, and J. Sarvas, "Computational methods for analyzing electron multipacting in RF structures", *Part. Accel.,* vol. 59, pp. 107-141, 19980.

[13] S. Anza, C. Vicente, D. Raboso, J. Gil, B. Gimeno, V. E. Boria, "Enhanced Prediction of Multipaction Breakdown in Passive Waveguide Components including Space Charge Effects", *Microwave Symp. Digest, 2008 IEEE MTT-S* pp. 1095-1098.

[14] H. Bruining, *Physics and Applications of Secondary Electron Emission.* McGraw-Hill Book Company, Inc., New York, 1954.

[15] J.R.M. Vaughan "A New Formula for Secondary Emission Yield", *IEEE Trans. Electron Devices*, Vol. 36, no. 9, pp. 1963-1967, Sept. 1989.

[16] J.R.M. Vaughan "Secondary Emission Formulas", *IEEE Trans. Electron Devices*, Vol. 40, no. 4, pp. 830, April 1993.

[17] C. Vicente, M. Mattes, D. Wolk, B. Mottet, H.L. Hartnagel, J.R. Mosig and D. Raboso, "Multipactor breakdown prediction in rectangular waveguide based components", *Microwave Symposium Digest, 2005 IEEE MTT-S International*, 12-17 June 2005.

[18] M. A. Furman and M. T. F. Pivi, "Simulation of secondary electron emission based on a phenomenological probabilistic model", Lawrence Berkeley Nat. Lab., Univ. California, Berkeley, CA, USA, Tech. Rep. LBNL-52807, Jun. 2003.

[19] R. Woo, "Multipacting discharges between coaxial electrodes", *J. Appl. Phys.*, Vol. 39, No. 3, pp. 1528–1533, Feb. 1968.

[20] V. Semenov, N. Zharova, R. Udiljak, D. Anderson, M. Lisak, J. Puech, "Multipactor in a coaxial transmission line. Part II: Particle-in-cell simulations", *Physics of Plasmas*, vol. 14, 033509, 2007.

[21] E. Somersalo, P. Yla-Oijala, D. Proch, "Analysis of Multipacting in Coaxial Lines", *Proceedings of the 1995 Particle Accelerator Conference*, pp. 1500-1502, May 1-5, 1995, Dallas, TX, USA.

[22] A. M. Pérez, C. Tienda, C. Vicente, S. Anza, J. Gil, B. Gimeno, V. E. Boria, "Prediction of Multipactor Breakdown Thresholds in Coaxial Transmission Lines for Traveling, Standing, and Mixed Waves", *IEEE Trans. Plasma Science*, Vol. 37, no. 10, Oct. 2009.

[23] T.P. Graves, B.LaBombard, S. Wukitch, I. Hutchinson, "The coaxial multipactor experiment (CMX): A facility for investigating multipactor discharges", *Rev. Scient. Instrum.*, Vol. 77, pp. 014701, 2006.

[24] R. A. Kishek, Y. Y. Lau, L. K. Ang, A. Valfells, R. M. Gilgenbach, "Multipactor discharge on metals and dielectrics: Historical review and recent theories", *Physics of Plasmas*, vol. 5, no. 5, pp. 2120-2126, May 1998.

[25] G. Cheng, L. Liu, Y. Liu, C. Yuan "Monte Carlo study of the single-surface multipactor electron discharge on a dielectric", *IEEE Transactions of Plasma Science*, vol. 37, no. 10, pp. 1968-1974, Oct. 2009.

[26] L. K. Ang, Y. Y. Lau, R. A. Kishek and M. Gilgenbach, "Power deposited on a dielectric by multipactor", *IEEE Trans. on Plasma Science* vol. 26, no. 3, pp. 290-295, June 1998.

[27] G. Torregrosa, Ángela Coves, C. Vicente, A. M. Pérez, B. Gimeno, V. E. Boria, "Time evolution of an electron discharge in a parallel-plate dielectric-loaded waveguide", *IEEE Electron Device Letters*, Vol. 27, no. 7, July 2006.

[28] A. Coves, G. Torregrosa-Penalva, C. Vicente, B. Gimeno, and V. E. Boria, "Multipactor discharges in parallel-plate dielectric-loaded waveguides including space-charge effects", *IEEE Trans. on Electron Devices* vol. 55, no. 9, pp. 2505-2511, Sep. 2008.

[29] G. Torregrosa-Penalva, A. Coves, B. G. Martinez, I. Montero, C. Vicente, V. E. Boria, "Multipactor Susceptibility Charts of a Parallel-Plate Dielectric-Loaded Waveguide", *IEEE Trans. on Electron Devices* vol. 57, no. 5, pp. 1160-1166, May 2010.

[30] S. Anza, C. Vicente, B. Gimeno, V. E. Boria, and J. Armendáriz "Long-term multipactor discharge in multicarrier systems", *Phys. Plasmas*, Vol. 14, No. 8, pp. 082 112, Aug. 2007.

[31] A. J. Morrison, R. May, J. D. Sanders, A. D. Dyne, A. D. Rawlins, and J. Petit "A study of multipaction in multicarrier RF components, vol. 1", Report of ESTEC AEA/TYKB/31761/01/RP/05, AEA Technology, January 1997.

[32] S. Anza, C. Vicente, J. Gil, V. E. Boria, B Gimeno, D. Raboso, "Non-stationary statistical theory for multipactor", *Physics of Plasmas, American Institute of Physics*, vol. 17, 062110, June 2010.

[33] S. Anza, M. Mattes, C. Vicente, J. Gil, D. Raboso, V. E. Boria, B. Gimeno "Multipactor theory for multi-carrier signals", *Physics of Plasmas, American Institute of Physics*, vol. 18, 032105, March 2011.

[34] S. Anza, C. Vicente, J. Gil, M. Mattes, D. Wolk, U. Wochner, V. E. Boria, B. Gimeno, and D. Raboso, "Prediction of multipactor breakdown for multicarrier applications: the quasi-stationary method", *IEEE Trans. on Microwave Theory and Techniques* Vol. 60, no. 7, pp. 2093-2105, July 2012.

[35] V. Semenov, M. Buyanova, D. Anderson, M. Lisak, R. Udilkak, and J. Puech "Multipactor in microwave transmission systems ysing Quadrature Phase-Shift Keying", *IEEE Transactions on Plasma Science*, Vol. 38, no. 4, April 2010.

[36] A. L. Sounas, J. R. Mosig and M. Mattes, "Effect of digitally modulated signals on multipactor breakdown," Antennas and Propagation", *7th European Conference on Antennas and Propagation (EuCAP)*, pp. 33-36, Gothenburg, 2013.

[37] N. Le Gallou, C. Miquel-Espanya, S. Matinfar, C. Ernst, and F. de Paolis, "Multipactor threshold and margins using realistic modulated signals", *in Proc. MULCOPIM*, Valencia, Spain, Sep. 21-23, 2011.

[38] S. Feltham, D. Raboso, "Coatings to prevent multipactor effect in high power components for space", Final Report, ESA-ESTEC, 1989.

[39] N. Diaz, S. Casraneda, J. M. Ripalda, I. Montero, L. Galan, S. Feltham, "Materials of low secondary electron emission to prevent the multipactor effect in

high-power RF devices in space", *Proceedings of the 6th Spacecraft Charging Conference*, pp. 205-209, November 2-6, 1998. AFRL Science Center, Hanscom AFB, MA, USA.

[40] S. Michizono, A. Kinhara, Y. Saito, S. Yamaguchi, S. Anami, N. Matuda, "TiN film coatings on alumina radio frequency windows", *Journal of Vacuum Science and Tecnhology*, vol. 10, pp. 1180-1184, Jul/Aug 1992.

[41] D. Wolk, J. Damaschke, C. Vicente, B. Mottet, H.L. Hartnagel, L. Galán, I. Montero, E. Roman, M. Alfonseca, J. de Lara, D. Raboso, "Surface treatment and coating for the reduction of multipactor and passive intermodulation (PIM) effects in RF components", *MULCOPIM 2003*, Noordwijk, The Netherlands, 8-11 September, 2003.

[42] V. Nistor, L. A. González, L. Aguilera, I. Montero, L. Galan, U. Wochner, D. Raboso, "Multipactor suppression by micro-structured gold/silver coatings forspace applications", *Applied Surface Science*, vol. 315, pp. 445–453, October 2014.

[43] R.L. Geng, H. Padamsee, S. Belomestnykh, P. Goudket, D.M. Dykes, R.G. Carter, "Suppression of multipacting in rectangular coupler waveguides", *Nuclear Instrum. Methods Physics Res. A*, vol. 508, pp. 227-238, 2003

[44] R. L. Geng and H. S. Padamsee, "Exploring multipacting characteristics of a rectangular waveguide", *Proceedings of the 1999 Particle Accelerator Conference (Cat. No.99CH36366)*, vol.1, pp. 429-431, New York, NY, 1999.

[45] H. Akoma, Y. Acediran, "Suppression of multipactor breakdown in satellite rectangular waveguides using DC magnetic fields", *Comput. Automation Engin. Conf. (ICCAE) 2010*, vol. 1, pp. 766-770, Febr. 2010.

[46] H. Akoma, D. A. Ogundele, O. Agboola, Y. A. Adediran, "Matlab analysis of the DC magnetic fields multipactor suppression model for rectangular waveguides", *in Proc. 3rd Int. Conf. Adv. Comput. Theory Eng. (ICACTE)*, vol. 4, pp. 97-101, Aug. 2010.

[47] G. Becerra, "Studies of coaxial multipactor in presence of a magnetic field", PSFC/RR-07-6, DOE/ET-54512-359, M.I.T., May 2007.

[48] P. Yla-Oijala, "Suppressing electron multipacting in coaxial lines by DC voltage", *TESLA Reports 97-21*, TESLA, 1997.

[49] A. J. Hatch, H. B. Williams, "Multipacting modes of high-frequency gaseous brekdown", *The Physical Review*, Second Series, vol. 112, no. 3, pp. 681-685, November 1958.

[50] A. J. Hatch, H. B. Williams, "The secondary electron resonance mechanism of low-pressure high-frequency gap breakdown", *Journal of Applied Physics*, Second Series, vol. 25, no. 4, pp. 417-423, April 1954.

[51] R. Udiljak, "Multipactor in low pressure gas", Master's thesis, Chalmers University of Technology, Goteborg, Sweden, 2004.

[52] European Space Agency-Val Space Consortium RF High-Power Laboratory, Valencia, Spain (www.val-space.com)

[53] P. Kroese, T. Brereton, T. Taimre, I. Botev, I. Zdravko, "Why the Monte Carlo method is so important today", *Wiley Interdisciplinary Reviews: Computational Statistics*, vol. 6, pp. 386–392, 2014.

[54] L. Verlet, "Computer 'experiments' on classical fluids. I. Thermodynamical properties of Lennard-Jones molecules", *Phys. Rev.,* vol. 159, no. 1, pp. 98-103, Jul. 1967

[55] T. P. Graves, "Experimental investigation of electron multipactor discharges at very high frequency", Ph.D. dissertation, *MIT Press* Cambridge, MA, 2006.

[56] S. Riyopoulos, "Multipactor saturation due to space-charge-induced de- bunching", *Phys. Plasmas* vol. 4, no. 5, pp. 1448–1462, May 1997

[57] J. Lara, F. Pérez, M. Alfonseca, L. Galán, I. Montero, E. Román, D. Raboso, "Multipactor prediction for on-board spacecraft RF equipment with the MEST software tool", *IEEE Transactions on Plasma Science*, vol. 34, no. 2, pp. 476-484, April 2006.

[58] J. Greenwood "The correct and incorrect generation of a cosine distribution of scattered particles for Monte-Carlo modelling of vacuum systems", *Vacuum* vol. 67, no. 2, pp. 217-222, September 2002.

[59] www.supermagnete.es

[60] D. J. Griffiths, *Introduction to Electrodynamics.* Third Edition, Pearson Benjamin Cummings, 2008.

[61] M. Abramowitz, I. Stegund, *Handbook of Mathematical Functions with Formulas, Graphs, and Mathematical Tables*. Dover Publications ISBN 978-0-486-61272-0

[62] W. H. Beyer, *Table of Integrals, Series and Products*. 27th Edition, CRC Press, Boca Raton Florida, 1984.

[63] I. Gradshteyn, I. Ryzhik, *CRC Standard Math Tables*. Academic Press, New York, 1980.

[64] G. Arfken, *Mathematical Methods for Physicists*. Third Edition, Academic Press, Orlando Florida, 1985.

[65] R. K. Wangsness, *Electromagnetic Fields*. Ed. Wiley, 2th edition, 1986.

[66] J. Uher, J. Bornemann, U. Rosenberg, "Waveguide Components for Antenna Feed System: Theory and CAD", *Norwood, MA: Artech House* 1993.

[67] A. Kirilenko, L. Rud, V. Tkachenko, D. Kulik, "Design of bandpass and lowpass evanescent-mode filters on ridged waveguides", *Proc. 29th Eur. Microwave Conf.* pp. 239–242, Munich, Germany, Oct. 1999.

[68] Z. M. Liu, J. A. Ruiz-Cruz, W. Chi, K. A. Zaki, "An extremely wideband ridge waveguide filter", *IEEE MTT-S Int. Microwave Symp. Dig.* pp. 615–618, Fort Worth, TX, Jun. 2004.

[69] P. Soto, D. de Llanos, E. Tarín, V. E. Boria, B. Gimeno, A. Oñoro, I. Hidalgo, M. J. Padilla, "Efficient analysis and design strategies for evanescent mode ridge waveguide filters", *Proc. 36th Eur. Microwave Conf.* pp. 1095–1098, Manchester, UK, Sep. 2006.

[70] FEST3D, Aurora Software and Testing, S.L. on behalf of ESA/ESTEC, Valencia, Spain (www.fest3d.com)

[71] D. Wolk, C. Vicente, H.L. Hartnagel, M. Mattes, J.R. Mosig, D. Raboso "An investigation on the effect of fringing fields on multipactor breakdown", *5th International Workshop on Multipactor, Corona and Passive Intermodulation*, September 2005.

[72] P. Soto, D. de Llanos, V. E. Boria, E. Tarín, B. Gimeno, A. Oñoro, I. Hidalgo, and M. J. Padilla, "Performance analysis and comparison of symmetrical and asymmetrical configurations of evanescent mode ridge waveguide filters", *Radio Science*, vol. 44, RS6010, doi:10.1029/2008RS004034, 2009.

[73] H. Guthart, "A High-Power S-Band Filter", *IRE Transactions on Microwave Theory and Techniques*, vol. 10, pp. 148-149, 1962.

[74] A. B. Carlson, P. Crilly, P. B. Crilly, "Communication Systems", *McGraw-Hill Science*, 5th edition, 2009

[75] James E. Gilley "Digital Modulation: A Review of Basic Concepts", *Transcrypt International, Inc.*, August 7, 2003.

[76] E. Sorolla, A. Sounas, M. Mattes, "Space charge effects for multipactor in coaxial lines", *Physics of Plasmas*, vol. 22, 033512 (2015).

[77] V. E. Semenov, E. Rakova, M. Belhaj, J. Puech, M. Lisak, J. Rasch, E. Laroche, "Preliminary results on the Multipactor effect prediction in RF components with ferrites", *Vacuum Electronics Conference (IVEC), 21-23 May 2013, Paris, IEEE 14th International.*

[78] David M. Pozar, "Microwave Engineering", 4th edition, *John Wiley & Sons, Inc.*, 2012.

[79] C. L. Hogan, "The Ferromagnetic Faraday Effect at Microwave Frequencies and its Applications: The Microwave Gyrator", *Bell System Technical Journal*, vol. 31, no. 1, pp. 1-31, January 1952.

[80] C. E. Fay and R. L. Comstock, "Operation of the Ferrite Junction Circulator", *IEEE Trans. Microwave Theory Tech.*, vol. MTT-13, no. 1, pp.15-27, Jan 1965.

[81] W. J. Ince and E. Stern, "Nonreciprocal remanence phase shifters in rectangular waveguide", *IEEE Trans. Microwave Theory Tech.*, vol. MTT-15, pp. 87-95, Feb. 1967.

[82] W.P. Clark "A High Power Phase Shifter for Phased-Array Systems", *IEEE Trans. Microwave Theory Tech.*, vol. MTT-13, no. 6, pp. 785-788, Nov. 1965.

[83] R. A. Stern, P. Agrios, "A 500 kW X-band Air-Cooled Ferrite Latching Switch", *IEEE Transactions on Microwave Theory and Techniques,* vol. 16, no. 12, pp. 1034-1037, Dec 1968.

[84] J.D. Adam, L.E. Davis, Gerald F. Dionne, E.F. Schloemann, S.N. Stitzer, "Ferrite devices and materials", *IEEE Transactions on Microwave Theory and Techniques,* vol. 50, no. 3, pp. 721-737, Mar 2002.

[85] Ü. Özgür, Y. Alivov, H. Morkoç, "Microwave ferrites, part 2: passive components and electrical tuning", *Journal of Materials Science: Materials in Electronics,* vol. 20, no. 10, pp. 911-952, Oct. 2009.

[86] W. E. Hord "Microwave and millimeter wave ferrite phase shifters", *Microwave Journal* vol. 32, pp. 81-89, 1989.

[87] A. Abuelma'atti, J. Zafar, I. Khairuddin, A. Gibson, A. Haigh, I. Morgan, "Variable toroidal ferrite phase shifter", *Microwaves, Antennas & Propagation, IET,* vol. 3, no. 2, pp. 242-249, March 2009.

[88] S.A Schelkunoff, "Generalized telegraphist's equations for waveguides", *Bell Syst. Tech. J.*, vol. 3, no. 4, pp. 784-801, July 1952.

[89] Á. Gómez, J. S. Ipiña, M. A. Solano, A. Prieto, A. Vegas, "Improving the coupled-mode method by means of step functions: Application to partial-height isotropic or anisotropic dielectric parallel-plate waveguides", *Microw. Opt. Techn. Lett.*, vol. 33, no. 6, pp. 408-414, June 2002.

[90] Á. Gómez, A. Lakhtakia, A. Vegas, M. A. Solano, "Hybrid technique for analysing metallic waveguides containing isotropic chiral materials", *IET Microw., Antennas Propag.*, vol. 4, no. 3, pp. 305-315, Mar. 2010.

[91] I. Montero, F. Caspers, L. Aguilera, L. Galán, D. Raboso, and E. Montesinos, "Low-Secondary Electron Yield of Ferromagnetic Materials and Magnetized Surfaces", *Proc. IPAC'10*, Kyoto, Japan, 23-28 May, 2010.

[92] V. E. Semenov, N. A. Zharova, N. I. Zaitsev, A. K. Gvozdev, A. A. Sorokin, M. Lisak, J. Rasch, and J. Puech, "Reduction of the Multipactor Threshold Due to Electron Cyclotron Resonance", *IEEE Transactions on Plasma Science* vol. 40, no. 11, November 2012.